Istros 2013

23.-27. September

Isospin, Structure, Reactions and Energy of Symmetry 2013

1st. International Conference

Proceedings

of the ISTROS 2013 International Conference

Proceedings

of the ISTROS 2013
International Conference

Editors: *M. Veselský and M. Venhart*

INSTITUTE OF PHYSICS,
SLOVAK ACADEMY OF SCIENCES

Bratislava 2015

ISBN 978-80-971975-0-6

Dear participants,

we bring to you the proceedings of the conference ISTROS (Isospin, STructure, Reactions and energy Of Symmetry), which took place in the period between Sept 23 – Sept 27 2013 in Častá-Papiernička. The declared aim of the conference was to provide platform for meeting of international and Slovak scientists, active in the field of nuclear physics, specifically dealing with experimental and theoretical aspects of physics of exotic nuclei and states of nuclear matter, and we hope that this aim was fulfilled.

During the conference, 36 invited and contributed talks were presented, covering the open problems in the physics of exotic nuclei and of the states of nuclear matter. Part of these presentation is represented in this proceedings in the form of short articles, while other participants decided to abstain from this and thus their presentations are represented only by their abstracts. In general, present time appears to modify traditional procedures and one of the victims are the conference proceedings in their habitual form. We are still convinced that publication of proceedings is a part of our duties as organizers as a service to participants and with this in mind we bring to you these proceedings. Besides the contributed articles, we complement the proceedings with a brief summary of history of natural sciences and technology in the territory of Slovakia, which bring some interesting facts about the progress of scientific and technical knowledge in Slovakia.

As far as we can judge, you had a productive time at Častá-Papiernička, spent meaningfully discussing interesting physics, and thus we aim to bring the second edition of the ISTROS conference in the near future. We hope to see many of you in Slovakia again.

Martin Veselský and Martin Venhart

Brief summary of History of Natural Sciences and Technology in Slovakia

Dear participants,

many of you visited Slovakia for the first time during the Istros conference in Častá-Papiernička, and you may have known only some basic facts about Slovakia prior to your visit. Thus we would like to present a short summary of the history of science and specifically natural sciences and technology in Slovakia. In this brief summary, we will mention selected places and historical events in Slovakia, which are relevant for history of science in general and of natural sciences in particular, and notable persons, who either were born in Slovakia or were closely related to it or lived and worked in Slovakia and contributed to scientific progress.

Most ancient signs of technology and of exact thinking in the territory of Central Europe and of Slovakia in particular can be dated to paleolithic era. Slovakia, due to its mountainous relief with only few passages through Carpathians between fertile lowlands of Poland and Hungary was inhabited by the mammoth hunters. Archaeological finds show that mammoth hunters used large mammoth bones in analogous way as candles were used in later eras, with bone marrow gradually running out and feeding the fire for long periods of time. Such technique can be understood as a primitive tool of time measurement or at least a sign of awareness of quantitative nature of time. Paleolithic people of Central Europe hold also important priority in technology, since first documented evidence of the ceramics is the famous female clay statuette known as Venus of Dolní Věstonice, old between 25 to 30 thousand years, which was found in Dolní Věstonice, a village in Czech Republic (Moravia) just about 30 km from trijunction of Czech Republic, Slovakia and Austria.

Most ancient proof of existence of astronomical knowledge (and scientific in general) in Slovakia was demonstrated recently by collaborative work of scientists from Archaeological and Astronomical Institutes of the Slovak Academy of Sciences. Monumental neolithic settlements of round shape, attributed to neolithic Lengyel culture and dated to first half of 5th millenium B.C., with diameters from 50 to 200 meters, were identified recently using air surveillance in Slovakia (most notably in Svodín, Žlkovce and Bučany) and in neighboring countries like Czech republic, Hungary, Austria and also in Germany. Archaeologist Ján Pavúk and astronomer Vladimír Karlovský studied the shapes or these rondels and concluded that they were in fact astronomical tools, used by the predominantly agricultural Lengyel culture to determine important dates in their calendar. As one can imagine, such observatories could not be built without prior astronomical observations and accumulated knowledge. These objects, older than the famous Stonehenge (a complex analogous to Stonehenge was unearthed also in Slovakia in the city of Holíč, unfortunately it happened during construction works and when experts were notified important archaeological evidence was already destroyed), demonstrate the considerable level of civilization in the society which built them, and existence of the class, most probably priests of the cult of the Sun, who devoted their time to astronomical observations.

Another important progress in the knowledge of natural sciences was achieved when the metals started to be used, first as a valuable material and later as a material for weapons and tools. The knowledge of metallurgy arrived into Slovakia around 4000 B.C. At the time, the Lengyel culture was superseded by Corded Ware culture (known in Western Europe also as the Battle Axe culture, named after weapons made of quartz), and knowledge of metallurgy was brought from the West by the Bell Beaker culture, in the process forming the mixed Únětice and Nitra cultures in Western Slovakia and southern Moravia where Únětice site is located, and from the South-East via Balkans, forming among others the Otomani-Füzesabonyi culture, which was located in Eastern Slovakia and in neighboring countries such as Hungary, Rumania and Poland and had a trade with the region of Aegean sea (thus the name Carpathian Troy), as documented by some Minoian finds. The mountainous relief of Slovakia provided many sites where raw metals, such as copper and gold, could be found, and mining became important economical activity, which determined the civilizational and scientific progress in the territory of Slovakia ever since then. After 7th century B.C. invasion of Celts from the West lead to introduction of iron metallurgy to territory of Slovakia.

Next civilizational impulse came with expansion of the Roman empire, which established its border on the Danube river (which is a southern border of present Slovakia) and organized military campaigns and set up trade contacts across the river. Besides this general civilizational influence on immediate Celtic and later Germanic neighbors, military campaign against Germanic Markomans brought to the territory of Slovakia one of the most learned persons of his era and a great humanist, the emperor Marcus Aurelius. During the campaign, spent mostly in the vicinity of the river Granua (nowadays called Hron) in Central Slovakia he worked on his philosophical treatise Meditations, which is thus first documented scientific text, which was (partially) written on the territory of Slovakia.

After collapse of Roman empire and invasion of Huns the territory of Slovakia entered the Migration period in Europe, which resulted in arrival of Slavic tribes, most probably from the territory to the East of Vistula river. During this period of instability the knowledge and culture of the Roman era was lost and it started to reappear only after the rise of the state of Great Moravia, along the rivers Morava (which joins Danube below Devín castle in Bratislava) and Nitra. In 9th century the Great Moravian ruler Rastislav invited a mission from Byzantine empire, which brought to the territory of Slovakia one of the most learned men of that time, Constantine the Philosopher (later known as St. Cyril), together with his brother Methodius. Along with Eastern Christianity they introduced first system of writing in Slavic language (glagolitsa), used it to translate the Bible, and also founded in the city of Nitra first higher educational institution in Slavic world, teaching in Slavic language. As it is known from history, their pupils were later expelled from Great Moravia, emigrated to the Bulgarian empire, where they founded kyrillitsa writing, used nowadays by many Eastern and Southern Slavic nations.

Fall of Great Moravia and arrival of Magyar (Hungarian) tribes again led to a period of instability, which ended by the rise of the multi-ethnic Kingdom of Hungary, of which territory of Slovakia became a northern part (except for a period of about 20 years in 11th century when most of the Slovak territory belonged to Poland of the Boleslaw the Valiant) in the form of Nitra principality. Not much is known about the first period until the year 1241, when a Mongolian (known also as Tartar) invasion lead to destruction of most of the settlements, depopulation of the country, destruction of the abbeys, then centers of learning, and consequently to the loss of practically all written records. In terms of natural sciences, Mongolian invasion introduced to Europe black powder and the principle of reactive

propulsion, however other, more peaceful achievements of Chinese civilization remained obscure for Europeans until Marco Polo.

Rest of the 13th century was spent by construction of a system of fortified castles (which made Slovakia a country of castles) and re-construction of state institutions. With expiration of the Arpad dynasty and arrival of the king Charles Robert of Anjou new civilizational impulse was provided by arrival of Italian and German settlers, who settled mostly in the cities and sped up urbanization of the country (importance of cities was documented by donation of the coat of arms to the city of Košice, first such event in Europe) and established the mining industry in Slovakia (initially in Kremnica and later in Banská Bystrica and Banská Štiavnica, known in Europe also as Kremnitz, Neusohl and Schemnitz, respectively). Relative prosperity during Anjou and Luxembourg dynasties in 14th century, reflected by the booming trade and rise of the wealth of cities like Trnava in Western Slovakia or Levoča in the Spiš region, was later followed by period of instability during and after Hussite wars in Bohemia in the first half of 15th century, which was ended by ascension to the throne of the king Mathias Corvinus.

The rule of Mathias Corvinus as a King of Hungary became legendary for its (of course relative) prosperity and peace, and King Mathias (Král' Matej) became a role model of a good king, as it is documented by multitude of popular legends and fairy tales. Economical prosperity of that time can be documented by the existence of Fugger-Thurzo trade company which controlled European copper market. Copper was mined in the city of Banská Bystrica and surroundings and the first documented gun in Europe was made of that copper. The castle Červený kameň close to the conference site was later re-built by the Fugger family for a copper storage, with participation of or at least according to construction principles formulated by Albrecht Dürer. From cultural point of view, with ascension of Mathias Corvinus renaissance arrived to Slovakia, and in terms of learning, first university in the Kingdom of Hungary was founded in the year 1467 in the city of Bratislava, named Academia Istropolitana (this name was derived from the ancient name of the Danube, Istros, which also served as inspiration for the name of our conference). Among the notable professors at Academia Istropolitana, famous astronomer Regiomontanus can be singled out. While the university ceased to exist in the year 1490 and the relatively prosperous and peaceful rule of Jagellonian kings, who succeeded Mathias, ended in catastrophic defeat of the Kigdom of Hungary by Ottoman Turkish Empire at Mohács in 1526, this short period of prosperity and civilizational progress resulted in ascent of first indigenous scientists, who became active in 16th century. This trend was supported also by introduction of protestantism in the Kingdom of Hungary, what led to founding of many secondary schools in the cities and to a habit to pursue university education in Germany (most notably in Wittenberg) and thus to spreading of knowledge among secular citizens.

After the battle of Mohács the Kingdom of Hungary practically disintegrated. Most of the territory of the present Hungary fell under Ottoman rule and the Hapsburg dynasty, which succeeded Jagellonians, controlled essentially the narrow stripe of land along the present Austro-Hungarian border and the territory of Slovakia, with Bratislava (Pressburg) becoming the capital of the Kingdom of Hungary. Territory of Slovakia thus for 150 years became a buffer zone with constant warfare. Hapsburg dynasty concentrated their military activity on defense of the mining cities in central Slovakia (Kremnica, Banská Bystrica and Banská Štiavnica) using armies of Flemish mercenaries (whose active nightlife left marks in Slovak language), and the rest of the population was left to defend themselves or to pay taxes to Ottoman satraps from across the diffuse border. Situation was further complicated by erection of the counter-king and later by several anti-Hapsburg uprisings, supported by

Ottomans. Obviously in such situation the civilizational and scientific progress virtually stopped and educated people were forced to pursue their career abroad.

Probably as a reaction to persistent warfare, 16th and 17th centuries were era of polyhistors and humanists. Most notable person during 16th century was the physician, natural philosopher and humanist Ján (Johann) Sambucus (born in 1531 in Trnava, died in 1584 in Vienna). After studies in Vienna, Wittenberg, Ingolstadt, Paris and Pavia he became a court historian in Vienna. He was a collector of Latin and Greek manuscripts, which he published in Basel, Antwerp and Frankfurt. He was one of the founders of imperial library in Vienna and his personal library accounted to up to 3000 volumes. Remarkably, his poetry from the work Emblemata served as inspiration for William Shakespeare.

Another notable scientist, born in Slovakia, was Vavrinec Benedikt Nedožerský (Laurentius Benedictus Nudozerinum, born 1555 in Nedožery, died 1615 in Prague). He was a professor of mathematics, physics, arithmetics and classical languages at the Charles University in Prague, after 1611 the rector of the university. He was also active as philologist and his most notable work is a first grammar of Czech language (Grammaticae Bohemicae leges naturalis methodi conformatae .. libri due).

Charles University hosted also notable physician, natural philosopher and humanist, Johann (Ján) Jessenius. He was born in 1566 to the noble family from Turiec region in northern Slovakia, which at that time fled from Turks to Cracow. He studied philosophy in Wittenberg and medicine in Leipzig. He was personal physician of Saxonian kurfürst in Dresden, later rector of the university in Wittenberg. In 1600 he performed in Prague the first public human autopsy in central Europe, described in his work Anatomia Pragensis. Later he became personal physician of the Hapsburg ruler Mathias in Vienna and during 1617-1620 was elected a rector of Charles University. He was one of the political leaders of Czech protestant independence movement and after defeat at Bílá hora was executed on June 21 at Old Town Square in Prague, along with the cream of Czech protestant nobility. During his stay in Prague he was one of the closest friends of Tycho de Brahe (he presented his funeral speech) and he was also a friend and sponsor of Johann Kepler.

While the scientists of 16th and early 17th centuries were mostly polyhistors and humanists, a first true natural philosopher, Izák Caban (Isaacus Zabanus), was born in Slovakia in Brodzany in 1632. After studies in Wittenberg he became a director of secondary school in Brezno and later in Sibiu (Rumania). He was a critic of the Aristotelean philosophy and a supporter of the then revolutionary concept of atomisms. His views were published in 1667 in Wittenberg in his work Existencia atomarum. He died in 1707 in Sibiu (Rumania).

Despite constant warfare during 17th century, new university was founded by Jesuit order in the city of Trnava in 1635, as a part of the re-catholization campaign. This university concentrated on education of clergy and pursued Jesuit policy of spreading of learning in the native language of the people. Therefore it played key role especially in development of Slovak language and literature, what resulted in first codification of Slovak language by Anton Bernolák.

The final defeat of Ottoman Turks and liberation of the territory of the Kingdom of Hungary in 1683, followed by the defeat of last anti-Hapsburg uprising of Francis II Rakoczi, started the era of peace which lasted essentially until Napoleon wars. This again allowed acceleration of civilizational and scientific progress, especially during the era of enlightened absolutism of emperors Maria Theresa and Joseph II. This progress led in 1763 to founding of first

institution providing higher technical education, the Academy of Mines in Banská Štiavnica. This school was supported by the government with the aim of modernization of mining of precious metals, which was in decline at the time since easily accessible resources were already exhausted and new, more effective methods of exploitation of metal ores were needed. The school was unique in Europe and attracted visits from famous scientists of their time such as Alessandro Volta and Henri Lavoisier. Related scientific activity led to organization of the first international congress of chemists and metallurgists in the spa town of Sklené Teplice in 1786 and during this congress the international scientific society, La Societé de l´exploitation des mines, was founded.

Era of polyhistors and encyclopedists reached its climax in 18th century in person of Matej Bel (Mathias Belius). He was born in 1684 in Očová to the peasant family and spent his most productive years in Bratislava. He died in 1749 while returning to Bratislava from a visit of Germany. He collected the available encyclopedical knowledge about the Kingdom of Hungary in his monumental work Noticia hungariae novae historico-geographica. Already during his life his work was recognized by membership in several scientific societies (London, Berlin, Jena, Olomouc), he was donated a status of nobleman and awarded a golden medal from the Pope (while himself being Protestant !). In his recognition the university in the city of Banská Bystrica carries his name and Slovak Academy of Sciences publishes its Encyclopedia Belliana.

A close collaborator of Matej Bel was Samuel Mikovíny. He was born in 1686 in a small village of Turičky in Southern Slovakia and passed away in 1750 in the vicinity of the city of Trenčín while working on regulation of the Váh river. He distinguished himself as a geodesist and carthographer and can be considered as first Slovak engineer. He was author of first detailed maps of Slovak regions, he provided maps and plans of the cities for Noticia Hungaricae. He designed unique system of 16 water reservoirs and 60 km of dams for powering of the mining activities in Banská Štiavnica, used mostly for pumping of water from mines. He was the first director of mining school in Banská Štiavnica and helped to prepare the stage for founding of the Academy of Mines.

Other notable scientists, active during first half of 18th century, can be mentioned:

Johann Adam Reymann (1690-1770) – born in Prešov in Eastern Slovakia, studied medicine in Jena and Leyden, spent most of his life in his native city, performed first vaccination against variola in Europe (applied to his own daughter), 76 years prior to English physician Edward Jenner, also performed systematic meteorological observations.

Daniel Fischer (1695-1764) – born in Kežmarok, studied medicine in Wittenberg, attempted to publish first scientific journal Acta eruditorum Pannoniae.

After promising surge in the first half of 18th century, scientific activity in the Kingdom of Hungary and thus also on the territory of Slovakia achieved further progress in the second half of 18th century. Special mention must go to the Hell brothers, born in the center of scientific activity at the time, the city of Banská Štiavnica, a seat of the famous Academy of Mines.

Maximilian Hell (1720-1792) – astronomer of world fame, born in Banská Štiavnica, studied in Vienna, founded observatories in Trnava and and Cluj (Rumania), in 1761 and 1773 observed transition of Venus through solar disc (second time at island Vardo on special invitation by the King of Denmark), performed precise calculation of solar parallax, what

allowed calculation of distance Earth-Sun. Member of scientific societies in Paris, Kobenhavn, Bologna, Gottingen, Dortheim and London. Published 22 astronomical annals.

Joseph Karl Hell (1713-1789) – mining engineer, constructor of mining machinery, born in Banská Štiavnica, studied on mining school in Banská Štiavnica under Samuel Mikovíny, constructed unique water-pillar engines, utilizing also pressurized air, which had no equivalent in the world (copies are used for oil pumping even today), also constructed engines for pumping of fresh air into mines. Head engineer of the mines in Banská Štiavnica.

Besides Hell brothers, two famous technicians were born in Bratislava:

Johann Andreas Segner (1704-1777) – physicist in the field of hydraulics, inventor of the Segner wheel, grand-father of turbine. Born in Bratislava, studied medicine in Jena, later professor of mathematics, physics and chemistry in Jena, Gottingen, Halle. Introduced reactive force of flowing water for initiation of rotational motion, a principle later used in construction of turbines. Worked also on theory of light. Member of scientific societies in St. Petersburg, Berlin and London.

Wolfgang Kempelen (1734-1804) – legendary and enigmatic technician and inventor. Born in Bratislava, studied philosophy and law in Vienna, later gained fame as inventor of various unique mechanical apparatuses, including the world famous chess automaton, a speaking machine and many other more practical machines.

Other notable scientists of 18th century include:

Andrej Jaslinský (1715-1784) – born in Seňa (close to Košice), studied in Trnava and Vienna, professor and later rector at Trnava university, author of textbook Physica generalis (Trnava 1756), supporter of progressive ideas such as empirism and experiment, Newtonian mechanics, atomism and heliocentrism. Performed astronomical observations, most notably transition of Mercury through solar disc in 1753.

Pavol Adami (1739-1814) – veterinarian, born in Beluša, studied law and medicine in Vienna, professor of medicine in Vienna and professor veterinarian in Krakow. Performed first systematic study of diseases of cattle in central Europe.

Samel Tešedík (1742-1820) – educator of people and experimenter in agriculture, studied theology in Erlangen, evangelical priest among Slovak settlers in Szarvas (Hungary), where he founded Agricultural-industrial institute, first practical agricultural school in the world. Author of many reforms in agriculture, famous for his system of desalination of arable land. Supporter of universal education.

Monk Cyprián (Jaisge) (1724-1775) – botanist and legendary "Flying Monk". Born in Poland, since 1756 monk in the monastery in Červený Kláštor. Author of unique herbary, part of which is preserved until today, pharmacist and provider of practical herbal medicine among common people. Famous by the legend about "Flying Monk", according to which he constructed a flying apparatus and used it to sail down from the mountain Tri Koruny above Červený Kláštor. Obviously this legend lacks verification, however such a bizarre legend goes beyond usual limits of imagination of the people of that time and as a botanist Cyprian could have acquired necessary knowledge by observing flying seeds of some herbs and trees. Even during World War I airplanes (Ettrich Taube and its copies and modifications) were used, which had wings designed as enlarged copies of herbal seeds, so there is no reason to dismiss

the legend as outright baseless. In any case it makes no harm for a country to have also such kind of scientific legend.

French revolution of 1789 caused a shock for the Austrian imperial court and destroyed its belief in positive role of progress. Subsequent military defeats suffered from Napoleon shattered the reputation of the Austrian empire as a big European power. Even if independence of the empire was restored after Napoleon's defeat, weakness which Austrian empire showed emboldened secessionist tendencies inside the empire. Italians, Czechs and Hungarians started their struggle for independence, while smaller nations like Croats, Serbs, Slovaks, Rumanians started to declare their wish for some form of federalization of the empire. This resulted in unstable situation, which was countered by strict laws and tight police control. Technological gap behind industrial nations like England, France and later Prussia kept increasing and activity of the ruling class was restricted to preservation of the status quo. Revolution of 1848 and military defeats at Solferino in 1859 and in the war with Prussia (1866) further weakened the Austrian empire which ultimately ceased to exist in 1918. This situation during 19th century was reflected also in the scientific output, which was lower than in second half of 18th century. Notable scientists in physical and technical sciences with connections to territory of Slovakia, active in 19th century include:

Štefan Anián Jedlík (1800-1895) – one of the greatest pioneers of electro-technics during 19th century in Europe. Born close to the city of Komárno to poor peasant family resettled from northern Slovakia, he studied theology in Pannonhalma and mathematics and physics at the Budapest university. He teached at secondary school in Raba (Hungary) and at Royal Academy in Bratislava, and in 1840 assumed a position of professor at Budapest university. In 1828 he experimented with prototype of electromotor (four years prior to Faraday) and in 1859 invented electrical dynamo (prior to Siemens). He was author of many further patents, including apparatus for cutting fine optical grids and even apparatus for production of soda water. Unfortunately due to increasing backwardness and political instability in the Kingdom of Hungary these inventions were not brought into mass production.

Jozef Petzval (1807-1891) – mathematician and physicist, active in the field of optics. Born in Spišská Belá in northern Slovakia. Studied at Budapest university, professor in Budapest and later in Vienna. Calculated and built anastigmatic objective for daguerrotypie (photography), allowing to reduce exposition time to few seconds. This objective was mass produced by Viennese optician Voigtlander without Petzval´s permission and it allowed practical use of photography. Petzval also improved optical telescope and he is considered an author of the theather binocular.

Ján Pettko (1812-1890) – geologist. Born in Drietoma, studied at Academy of Mines in Banská Štiavnica, where he later teached. Described geology of Carpathian mountainous ridges in Slovakia and discovered a mineral called pettkoit.

Dionýz Štúr (1827-1893) - geologist. Born in Modra into family of teacher (his uncle was a Slovak political leader during revolution of 1848). Studied at Academy of Mines in Banská Štiavnica. Worked at Imperial geological institute in Vienna, where he later became a director. Systematically described geology of Alps and Carpathians. Was a member of scientific societies in Moscow, Paris, Venice, London, Dresden and Brussels.

Advent of 20th century was marked by increased activity in physical and technical sciences. Austro-Hungarian empire was still present, however its economical and military strength was already weakened and it was under influence of the recently unified and dynamically

progressing Germany. Economical problems in Austro-Hungarian empire led to mass emigration, especially to United States of America, where many scientists and inventors were able to work on their inventions. World War I handed last blow to the dying Austro-Hungarian empire and the history of Slovakia proceeded from 1918 as a part of Czechoslovakia.

Remarkably, one the founders of the new state of Czechoslovakia was also a famous scientist. Milan Rastislav Štefánik (1880-1919) was born in Košariská in the family of protestant pastor. Due to his strong Slovak patriotism he had to switch several secondary schools (Bratislava, Sopron, Szarvas). Later he moved to Prague, where he studied physics and astronomy at Charles University. After graduation he went to Paris, where he obtained a job at Observatoire de Paris-Meudon. He performed astronomical observations at Mont Blanc. Since 1908, he had been charged by the French authorities with astronomic and meteorological observations (mainly observations of sun eclipses) and political tasks in various countries all over the world including Algeria, Morocco, Turkistan, Russia, India, the USA, Panama, Brazil, Ecuador, Australia, New Zealand, Tahiti, Fiji and Tonga. In Tahiti, he also built an observatory and a network of meteorological stations (rumor has it that he spent much of his time in the Pacific spying on German positions). Štefánik dealt with astrophysics, solar physics and became well known for his spectral analysis of the sun's corona. He was involved in perfecting spectrography and has been considered a predecessor of Bernard Lyot. He also attempted to construct a machine for color photography and cinematography and had his design patented in 1911. Besides scientific activity he also performed diplomatic missions for the French Republic. During World War I Štefánik joined French army and became a pilot. He was one of the pioneers in organizing meteorological service in French air force. Due to his good contacts in French political circles he became one of the leaders of Czecho-Slovak political representation in exile and helped to convince French government to support disintegration of the Austro-Hungarian empire and formation of Czechoslovakia. Since 1917 he held a rank of general of French army and later he commanded evacuation of the Czecho-Slovak legion from Soviet Russia. After Czechoslovakia was formed in late 1918, Štefánik decided to return home. On his flight to Bratislava his airplane crashed under never satisfactorily clarified circumstances and he died.

A notable, even if controversial, scientist, born in the territory of Slovakia, is the discoverer of photo-effect and Nobel prize laureate Phillip Lenard (1862-1947). He was born in Bratislava (Pressburg) in the family of wine-makers of German origin, producers of champagne (Bratislava was the first place outside of France producing champagne, thanks to J. E. Hubert, Napoleon´s soldier from Champagne, who upon returning from Russia stopped in Bratislava, got married and started successful business). Already at gymnasium in Bratislava he experimented with cathode tube. He studied at the university of Heidelberg and worked with Heinrich Hertz. He discovered the photo-effect and was awarded Nobel prize in 1905. Based on his experiments with cathode rays (electrons) he concluded that atoms are mostly empty and formulated intermediate model of atom between Thomson and Rutherford, with pairs of opposite charges floating in mostly empty atom. He also contributed to other fields such as meteorology. His scientific activity was later in his life overshadowed by his activity in the Nazi party and contribution to persecution of Jewish scientists, including Albert Einstein.

Other notable physical and technical scientists, born in the territory of Slovakia, include:

Ján Bahýľ (1856-1916) – pioneer of aeronautics, inventor of helicopter. Born in Zvolenská Slatina, studied at Academy of Mines in Banská Štiavnica and later architecture in Vienna. Was employed as architect in Austrian army, where he was also active as inventor. Around the

turn of centuries he built a prototype of helicopter, which actually first flew in 1903 (1.5 m above ground) and in 1905 reached 4 m above ground, what was acknowledged by International Aeronautical Society.

Aurel Stodola (1859-1942) – founder of theory of gas turbines. Born in Liptovský Mikuláš, studied in Budapest and later at ETH Zurich. Afterward worked in several machinery plants in Prague before returning to Zurich as professor. His famous book Dampfturbinen und ihre Aussichten als Warmekraftmaschinen was translated into many languages and his expertise contributed to world fame of Swiss turbine-making industry. Member of many scientific societies, in 1909 awarded by Gold medal of James Watt. He was teacher and later colleague of Albert Einstein.

Jozef Murgaš (1864-1929) – pioneer of radio-technique. Born in Tajov to peasant family, he became catholic priest. Due to his progressive views he had to emigrate to USA, where he lived in Pennsylvania among Slovak emigrants. Author of several patents, invented wireless telegraphy based on frequency modulation (tone-system). Built emitter and receiver and successfully demonstrated the method over distance of 35 km, however equipment was destroyed by a gale and due to financial problems further experiments stopped. Later similar system was introduced by Marconi. At the federal court trial for priority between Marconi and other industrialist claiming the invention, priority of Murgaš was acknowledged and thus verdict did not go to either side. Besides his discoveries, Murgaš was also a notable painter.

Štefan Banič (1870-1941) – inventor of parachute. Born in Smolenice, in 1907 he emigrated to USA, where he worked in mines and later at machinery plant. In 1914 he patented a parachute of his own design (umbrella-like, mounted around waist), which was later used by the U.S. Air Force.

After 1918, Slovakia became a part of Czechoslovakia. This was reflected also in science, where Slovak scientists usually went for studies to Prague and then pursued their scientific careers there. Among them can be mentioned:

Dionýz Ilkovič (1907-1980) – physical chemist. Born in Šarišský Štiavnik in eastern Slovakia, after secondary school in Prešov he went for university studies to Prague. After graduation joined Josef Heyrovský, Nobel prize laureate for polarography. Ilkovič formulated theoretical basis for this method (Ilkovič equation) and thus significantly contributed to Heyrovský's Nobel prize. After disintegration of the first Czechoslovak republic in 1939 he returned to Slovakia, to Slovak Technical University in Bratislava. From then on he concentrated on his pedagogical activities. In 1953 he joined Slovak Academy of Sciences and in 1955 founded a Cabinet of Physics which later evolved into the Institute of Physics of Slovak Academy of Sciences.

Jozef Kvasnica (1930-1992) – theoretical physicist. Born in Tunežice, after secondary school in Trenčín he went for university studies to Prague. After graduation went to Soviet Union, where he was a PhD student of Lev Landau. After return to Prague he worked at Czech Technical University and later at Charles University. His scientific work concentrated on diffusion, specifically on inverse problem of diffusion equations.

Ľubor Kresák (1927-1994) – astronomer. Born in Topoľčany, studied astronomy at Charles University in Prague. After graduation since 1951 worked at observatory at Skalnaté pleso in High Tatras and from 1955 joined Astronomical Institute of Slovak Academy of Sciences.

Discovered two comets and theoretically explained aging and end of the life cycle of comets. Presented correct explanation of the origin of Tunguska meteorite.

Jur Hronec (1881-1959) - mathematician. Born in Gočovo, studied at university in Cluj (Rumania). After graduation in 1906 he became a teacher at gymnasium in Kežmarok, where he worked until 1922. During this time he stayed for shorter periods in Gottingen, Giessen, Berlin and elsewehere. Since 1924 became a professor at Technical University in Brno, after 1939 returned to Slovakia, where he was active as founder of higher technical education. His research activities focused primarily on differential equations. He studied problems of Erdős–Fuchs theorem of linear differential equations and their generalization.

Štefan Schwarz (1914-1996) – mathematician. Born in Nové Mesto nad Váhom, after secondary school in his native city he went for university studies to Prague. After 1939 returned to Slovak Technical University in Bratislava. His scientific activity concentrated on theory of semigroups, where he was one of the founders and leading personalitites.

From the recent activities of Slovak nuclear physicists, it is worthwhile to mention contribution of the group from Institute of Physics of Slovak Academy of Sciences (Pavel Obložinský, Igor Ribanský, Emil Běták) to theory of pre-equilibrium reactions, which was developing rapidly in 70-s and 80-s. In 90-s, Štefan Šáro and Rudolf Janík from Faculty of Mathematics, Physics and Informatics of Comenius University in Bratislava were members of the team, which synthesized several heaviest chemical elements at GSI Darmstadt. Slovak nuclear physicists have active collaboration with the Joint Institute of Nuclear Research in Dubna (Slovakia and earlier Czechoslovakia was a member state since its founding), and more recently with CERN, where after accession of Slovakia in 1994 Slovak institutions participated in large collaborations like ATLAS and ALICE and recently also active collaboration with ISOLDE RIB facility was set up.

Slovak scientists are active also in cosmic research. In relation with the flight of Slovak cosmonaut Ivan Bella, several scientific experiments were performed. Best known is the biological experiment with Japanese quails, which were reproduced under conditions of zero gravity. This activity was a result of a scientific programme, pursued at the Institute of Animal Biochemistry and Genetics of Slovak Academy of Sciences since 70-s. Another curious, even if not directly scientifically relevant fact, related to cosmic programme is that Slovak beer Zlatý bažant (Golden Pheasant) was the first beer ever brought to and consumed in space, at the Soviet orbital station Mir.

Such is the brief summary of facts, outlining the history of natural sciences and technology in the territory of Slovakia. We hope that the Istros conference and its future editions will contribute to its successful continuation.

CONTENTS

ARTICLES

ABSTRACTS

Articles

SHAPE COEXISTENCE: AN OUTLOOK

John L. Wood*

School of Physics, Georgia Institute of Technology, Atlanta, GA 30332-0430, USA
(Dated: December 24, 2014)

Abstract

Shape coexistence is a widely occurring feature of nuclear structure. It is also a topic that is undergoing rapid advances, both in experimental identification techniques and in theoretical understanding. A view of the current experimental status of nuclear shape coexistence, and suggested lines of future investigation are outlined.

INTRODUCTION

Shape coexistence has been recognized to occur in nuclei for over fifty years. From earlier reviews of the topic by Heyde et al. [1,2], which adopted the perspective that the occurrence of shape coexistence in nuclei was a relatively rare and exotic structural feature, a recent review by Heyde and Wood [3] presents the view that it probably occurs in essentially all nuclei. This raises the issue of designing future experimental programs that will critically test and advance our ideas of this facet of nuclear structure.

A GLOBAL VIEW OF SHAPE COEXISTENCE

Two dramatic manifestations of shape coexistence are well established in nuclei. The first is its occurrence in doubly closed-shell nuclei; the example of ^{40}Ca is shown in Fig. 1. The second is its occurrence in and adjacent to singly closed-shell; the example of the Hg isotopes is shown in Fig. 2.

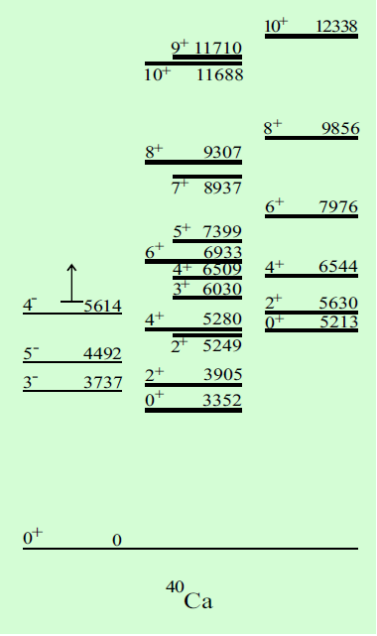

Fig. 1: Shape coexistence in ^{40}Ca (cf. Fig. 3, region A). The left-hand, middle, and right-hand columns show, respectively, spherical 1p-1h configurations, states interpreted as triaxial rotor states built on a 4p-4h (proton-pair-neutron-pair) configuration, and states interpreted as axially symmetric rotor states built on an 8p-8h configuration. The figure is adapted from Heyde and Wood [3].

*E-mail: john.wood@physics.gatech.edu

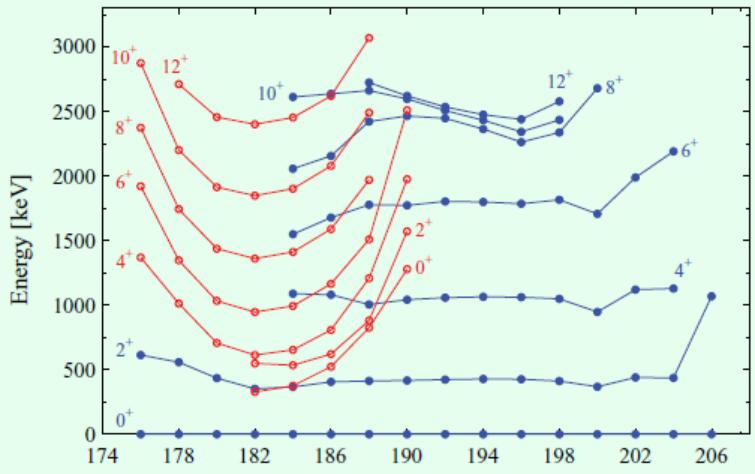

Fig. 2: Shape coexistence in the Hg isotopes (cf. Fig. 3, region L). States interpreted as strongly deformed are shown in red. Note the parabolic energy pattern. The figure is taken from Elseviers et al. [4].

Regions of shape coexistence are summarized in Fig. 3. The pattern has been established primarily by evolving experimental interest and accessibility, and does not reflect any rigorous underlying rules of occurrence. However, there is a general association of the manifestation of shape coexistence with spherical closed shells and subshells. The evidence for this view is contained in detailed spectroscopic studies, examples of which are presented in the next section.

DETAILED SPECTROSCOPIC STUDIES OF SHAPE COEXISTENCE IN NUCLEI

The association of shape coexistence with closed shells (and subshells) comes from the involvement of proton and neutron pair excitations across shell (and subshell) energy gaps, as depicted in Fig. 4. This view has its foundation in the observation of shape coexisting structures with strong population in two-nucleon

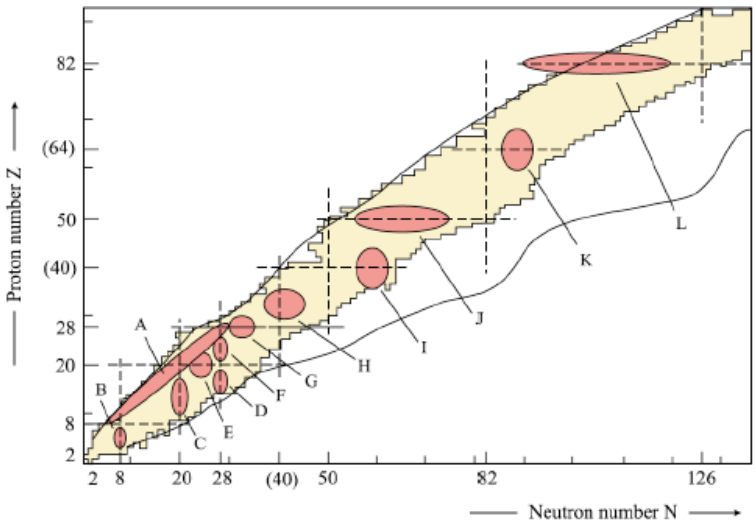

Fig. 3: The main regions of known nuclear shape coexistence are shown. The alphabetical labels are used to identify these regions and to connect to discussions in the text. The figure is taken from Heyde and Wood [3].

transfer reactions, as shown in Fig. 4. This view has its foundation in the observation of shape coexisting structures with strong population in two-nucleon transfer reactions, as shown in Fig. 4. The evidence for structures with different deformations in the Sn isotopes is embodied in B(E2) values; these are depicted for the mid-shell region in Fig. 5. Note that the 1.84 MeV state labelled in Fig. 4 corresponds to the 1757 keV state in ^{116}Sn shown in Fig. 5.

A more subtle type of evidence for structures with different deformations comes from electric monopole

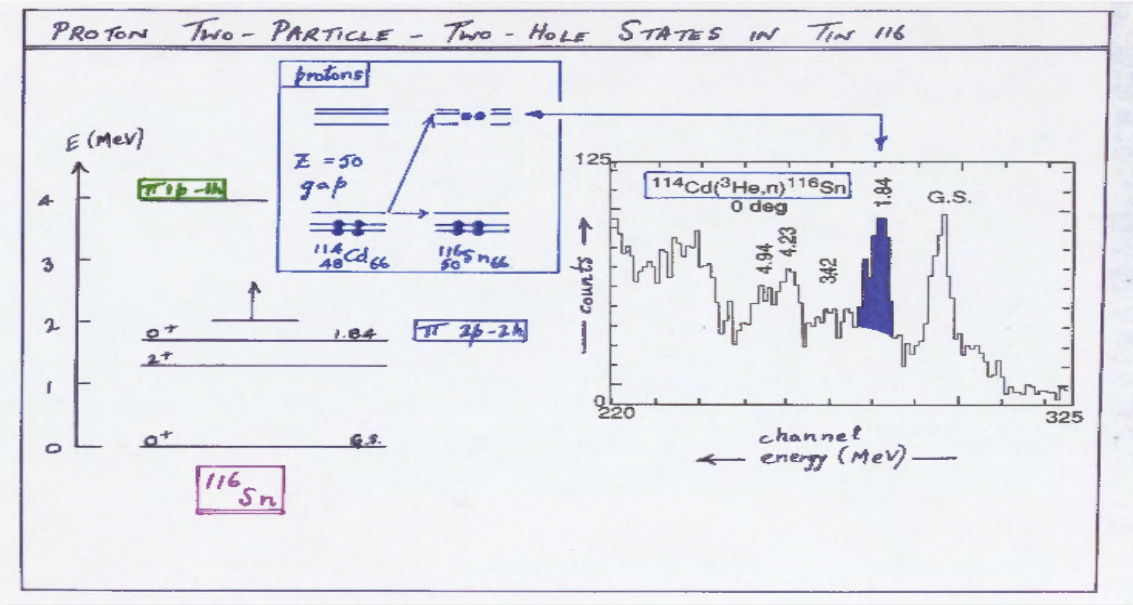

Fig. 4: The population of the candidate 0^+ deformed band head in ^{116}Sn (cf. Fig. 3, region J) by the (^{3}He,n) reaction. The spectrum is taken from Fielding et al. [5].

transition strengths, $\rho^2(\mathrm{E0})\cdot 10^3$ (conventionally quoted in milli units). Such transition strength arises from the mixing of underlying configurations with different mean-squared charge radii [6, 7] (and see Wood et al. [8] for a review of E0 strengths). Such data are shown for the mid-shell Sn isotopes in Fig. 6. Note the pattern of strength, which is greatly enhanced for the 0^+_3 state decays to the 0^+_2 (deformed) states. This is interpreted as resulting from the strong mixing of two near-degenerate 0^+ configurations. Evidence for the

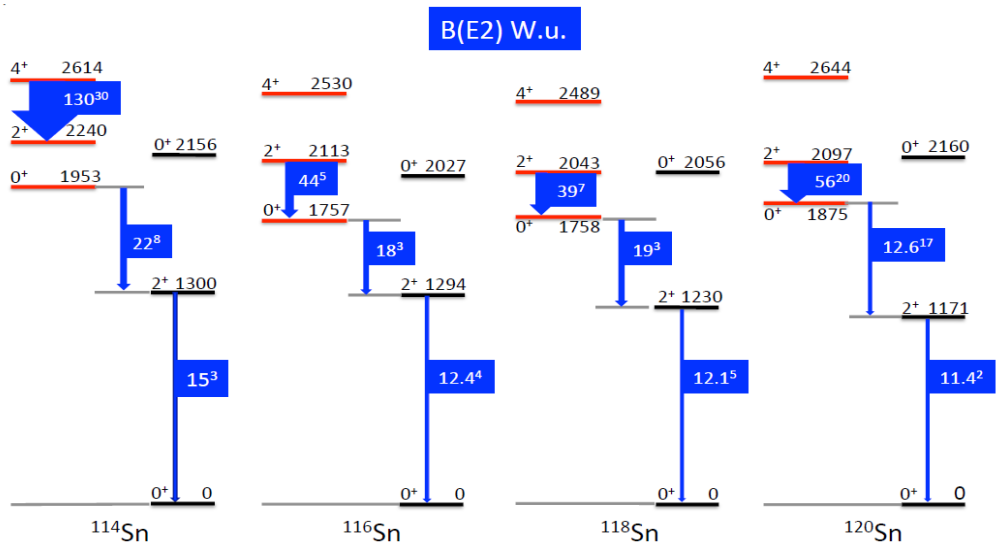

Fig. 5: The lowest three members of the deformed bands in the mid-shell Sn nuclei. Absolute B(E2) values, where known, are given in Weisskopf units. The data are taken from Nuclear Data Sheets.

occurrence of shape coexistence at subshell gaps is a more recent development. Data supporting this in the A $\sim$ 100 region are shown in Fig. 7.

The evidence for the involvement of nucleon pair excitations across subshell energy gaps is shown in Fig. 8. The evidence for shape coexistence in was recently established by the intensity measurement of an ultra-weak, high-lying, low-energy γ-ray transition, details of which are shown in Fig. 9. Combining this with lifetime data, from inelastic neutron scattering, and Doppler shifted line shapes, at the Univ. of Kentucky Accelerator Facility, yielded an enhanced B(E2) value.

The extreme difficulty of determining the intensities of ultra-weak, low-energy, high-lying, γ-ray transi-

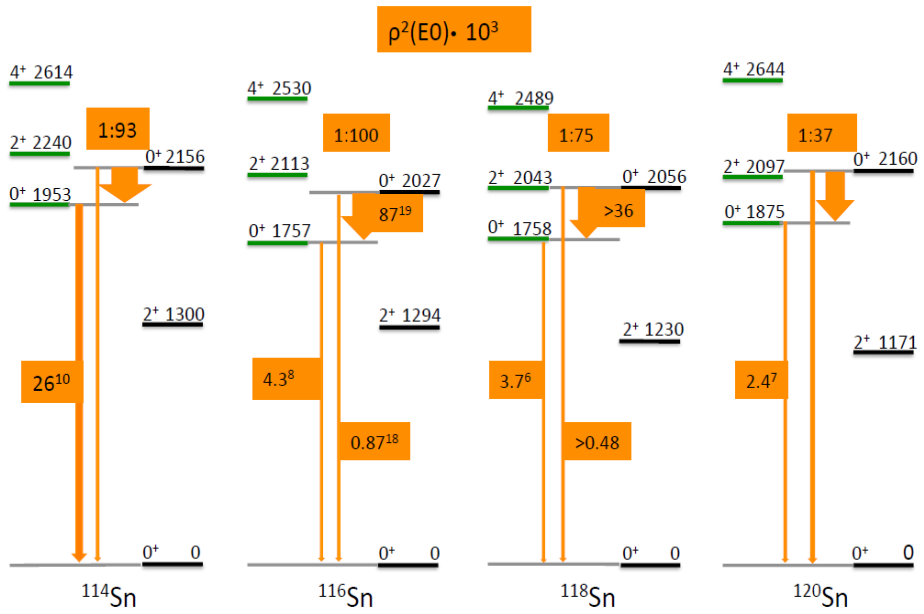

Fig. 6: Electric monopole transition strengths, $\rho^2(E0)\cdot 10^3$ associated with the low-lying excited 0^+ states in the mid-shell Sn nuclei. The data are taken from Kibedi and Spear [9].

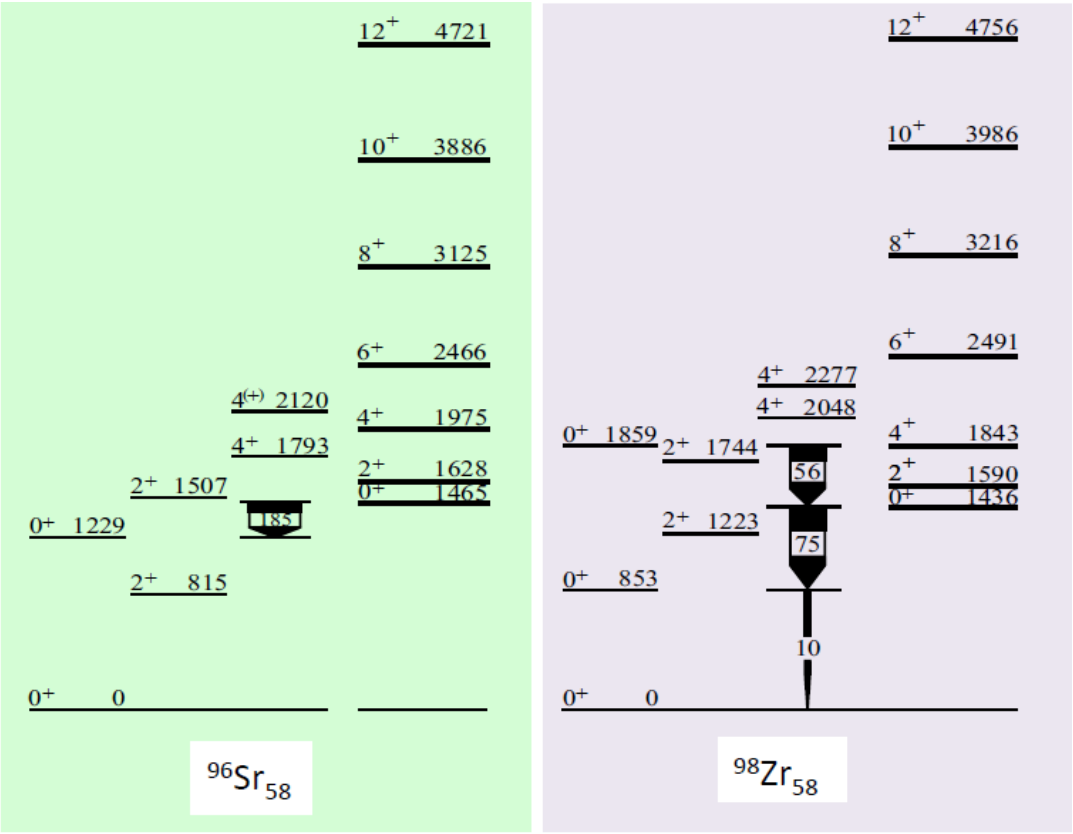

Fig. 7: Electric monopole transition strengths, $\rho^2(E0)\cdot 10^3$ associated with the low-lying excited 0^+ states in the mid-shell Sn nuclei. The data are taken from Kibedi and Spear [9].

tions has certainly kept many manifestations of shape coexistence in nuclei obscured. Recall, B(E2) values are proportional to γ-ray intensity and inversely proportional to the lifetime of the parent state and inversely proportional to the transition energy to the 5^{th} power. With the proliferation of large arrays of Compton-suppressed detectors, it is becoming possible to characterize such extraordinarily weak, but highly collective

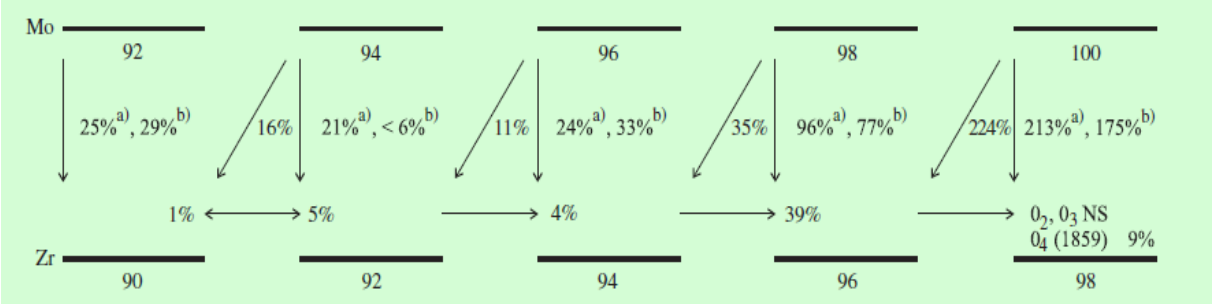

Fig. 8: Two- and multi-nucleon transfer reaction data for selected Zr isotopes (cf. Fig. 3, region I). The figure is adapted from Heyde and Wood [3].

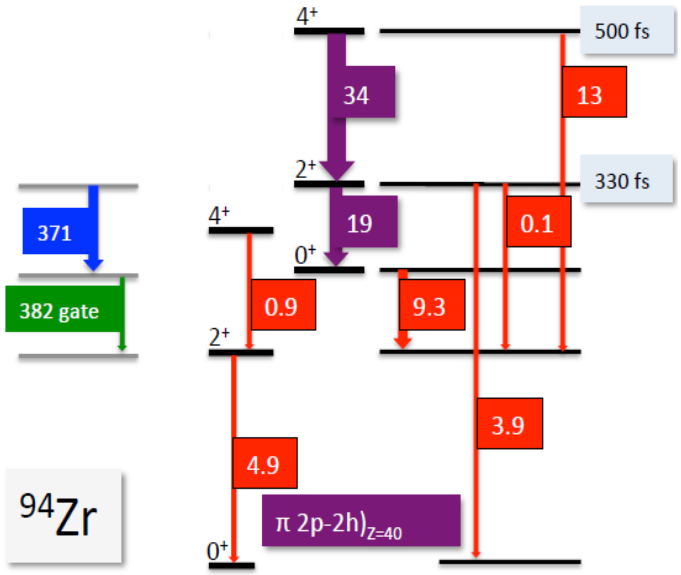

Fig. 9: Evidence for shape coexistence in (cf. Fig. 3, region I) established by combining lifetime data from Elhami et al. [10] with the measurement of the ultra-weak γ-decay branch between the 2_2^+ and 0_2^+ states. The data are taken from Chakraborty et al. [11].

transitions.

Two regions where very detailed spectroscopic data are beginning to provide exceptional detail are the Cd and Hg isotopes. These isotopic sequences have the common characteristic that they are located just below proton shell closures. They differ in that the Cd isotopes that exhibit shape coexistence are stable whereas the Hg isotopes that exhibit shape coexistence are unstable (and therefore necessitate working with radioactive beams). Electric monopole strengths for ^{114}Cd are shown in Fig. 11. One can infer that K = 0 and K = 2 bands coexist in this nucleus, based on a ΔK = 0 selection rule for the E0 operator, r^2 (which is a rank-zero spherical tensor). (But the nature of the 0^+ excited state at 1306 keV is an open question.) Electric quadrupole matrix element data, for the Hg isotopes that exhibit shape coexistence, are shown in table 1. These data are distinguished by the fact that they were obtained by Coulomb excitation of radioactive beams of Hg isotopes (at REX-ISOLDE) by Bree et al. [12]. The Worldwide emphasis of exciting new nuclear physics accessible through radioactive beams portends well for the role of Coulomb excitation in the exploration of shape coexistence in nuclei. Obtaining detailed spectroscopic data in regions away from the line of stability is generally a slow process. In consequence, if such a region exhibits shape coexistence, this can lead to misconceptions about fundamental issues of nuclear structure. The most dramatic example of this is the region centered on the closed shell nucleus ^{32}Mg. This region has come to be known as an "island of inversion". The origin of this term is related to the apparent "collapse" of the N = 20 shell closure. A useful "map" of the current extent of this region is provided by first excited 2^+ state energies, as shown in Fig. 12. The low energies for the first excited 2^+ states in the closed - shell nuclei ^{30}Ne and ^{32}Mg have been interpreted as indicating that there is a breakdown of the shell model for the N = 20 nuclei farthest from stability. A similar inference has been made for the N = 28 (closed shell) nuclei farthest from stability,

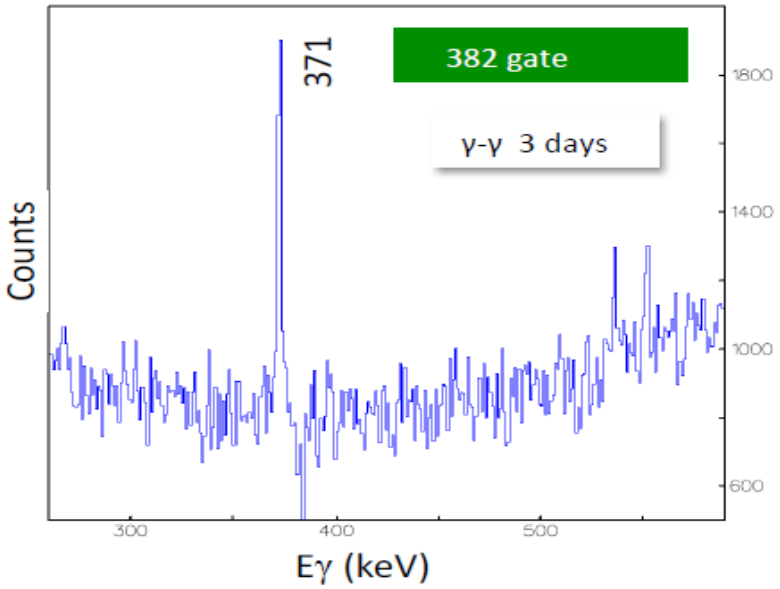

Fig. 10: Evidence for shape coexistence in ^{94}Zr established by observation of the ultra-weak 371 keV γ-ray transition between the 2_2^+ and 0_2^+ states. The spectrum is taken from Chakraborty et al. [11].

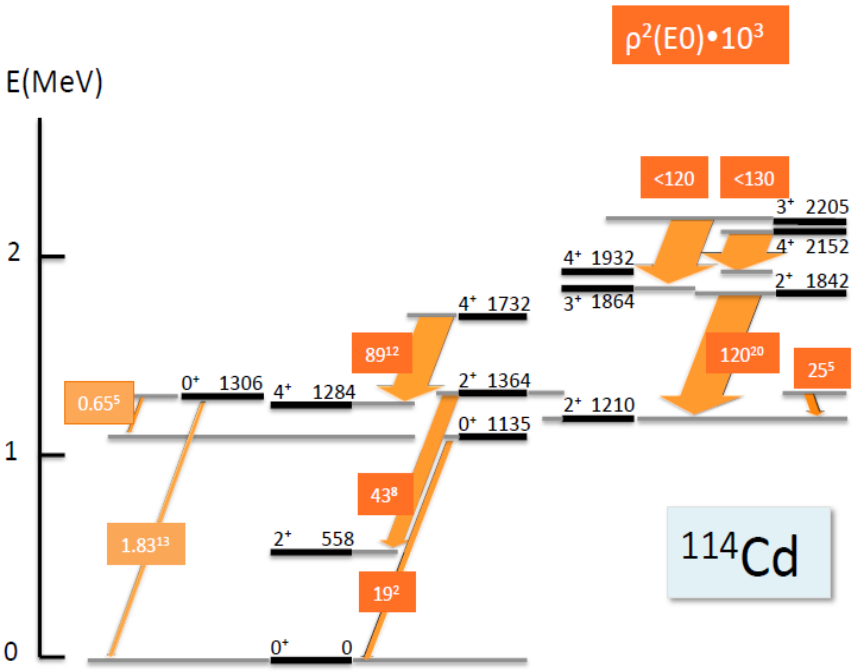

Fig. 11: Electric monopole transition strengths, $\rho^2(E0)\cdot 10^3$ in ^{114}Cd (cf. Fig. 3, region J) for all strong E0 transitions. The data are taken from [8, 9].

based on this quantity for.

Two key experiments have clarified the true nature of the nuclear structure underlying the apparent anomalies in the systematics of first excited 2^+ state energies in the N = 20 isotones. Data from the first experiment, obtained at REX-ISOLDE by Wimmer et al. [13], are shown in Fig.13. Data from the second experiment, obtained at GANIL by Rotaru et al. [14], are shown in Fig. 14. These data lead to the systematics of excited states in the N = 20 isotones shown in Fig. 15. These systematics suggest that the low-energy of the first excited 2^+ state in ^{32}Mg is due to the "intrusion" of a deformed structure below a weakly (or non-deformed) structure, i.e., the N =20 shell structure has not "collapsed" (otherwise there would not be a low-energy excited 0^+ state in ^{32}Mg that is strongly populated in a two-neutron pickup reaction on a beam of ^{30}Mg).

Tab. 1: Reduced transitional and diagonal E2 matrix elements between low-lying states in $^{182-188}$Hg (cf. Fig. 3, region J) obtained in the work of Bree et al. [12].

$\langle I_i \| E_2 \| I_f \rangle$ (eb)	^{182}Hg	^{184}Hg	^{186}Hg	^{188}Hg
$\langle 0_1^+ \| E_2 \| 2_1^+ \rangle$	$1.29^{+0.04}_{-0.03}$	1.27 (3)	$1.25^{+0.10}_{-0.07}$	1.31 (10)
$\langle 2_1^+ \| E_2 \| 4_1^+ \rangle$	3.71 (6)	3.15 (6)	3.4 (2)	2.07 (8)
$\langle 0_1^+ \| E_2 \| 2_2^+ \rangle$	-0.61 (3)	0.21 (2)	(±) 0.05 (1)	
$\langle 0_2^+ \| E_2 \| 2_1^+ \rangle$	$-2.68^{+0.15}_{-0.13}$	3.3 (8)		
$\langle 0_2^+ \| E_2 \| 2_2^+ \rangle$	-1.7 (2)	1.25 (28)	≥ 3.7 (8)	
$\langle 2_1^+ \| E_2 \| 2_2^+ \rangle$	-2.2 (4)	0.91 (14)		
$\langle 2_2^+ \| E_2 \| 4_1^+ \rangle$	3.1 (3)	5.8 (5)	$-5.3^{+1.3}_{-0.5}$	
$\langle 2_1^+ \| E_2 \| 2_1^+ \rangle$	$-0.04^{1.3}_{-1.4}$	$1.5^{+1.8}_{-1.2}$		$1.0^{+0.6}_{-0.4}$
$\langle 2_2^+ \| E_2 \| 2_2^+ \rangle$	$0.8^{+1.0}_{-0.6}$	-2.6 (20)		

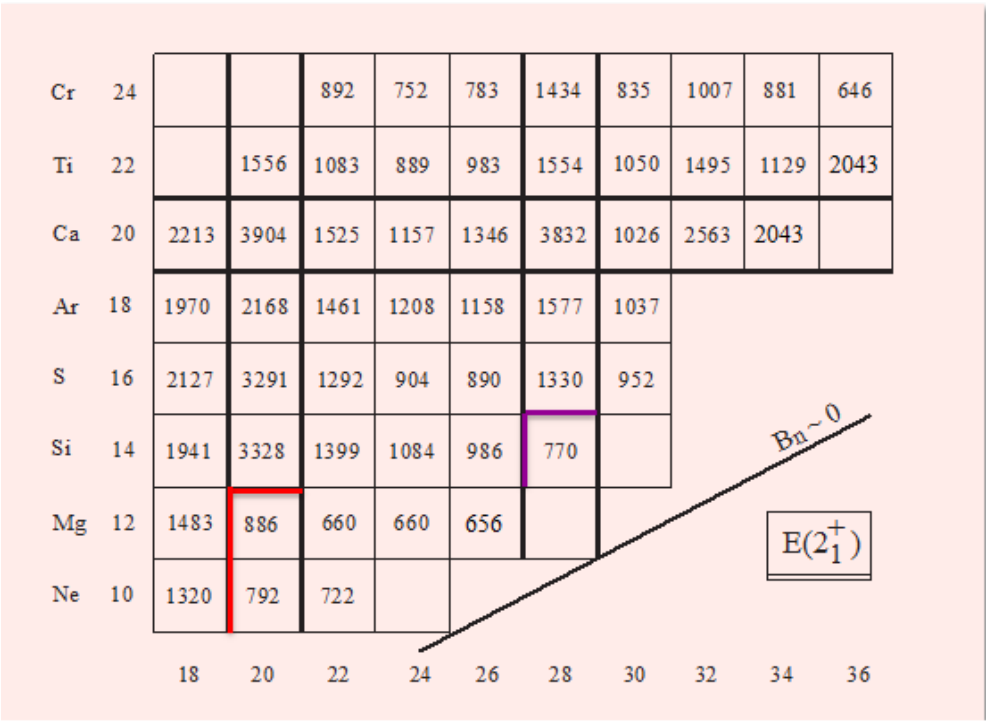

Fig. 12: First excited 2^+ state energies in the region bounded by N>16, Z<26 (cf. Fig. 3, regions C, D, E). The figure is adapted from Heyde and Wood [3].

Remarkably, shape coexisting structures are often manifested in the odd-mass nuclei that are neighbors to the doubly even nuclei manifesting shape coexistence. The example of the odd-Tl isotopes is shown in Fig. 16. The correlation of these shape coexisting structures in the odd-mass Tl isotopes with the neighboring doubly even shape coexisting structures in the Pb isotopes is shown in 17.

A pattern of shape coexistence, similar to that shown in the odd-mass Tl isotopes, is observed in the odd-mass Au isotopes and is shown in Fig. 18. The occurrence of states connected by E0 + M1 + E2 transitions correlate with the shape coexisting structures observed in the neighboring doubly even Pt isotopes, as shown for ^{184}Pt in Figs. 19, 20, 21, 22. The dramatic nature of these data is the pattern of E0 strength, namely in the $2_3^+ \rightarrow 2_1^+$ and $2_4^+ \rightarrow 2_2^+$ transitions, but not between other pairwise combinations of 2^+ states: this strongly supports the K band assignments and $\Delta K = 0$ selection rule for configuration mixing.

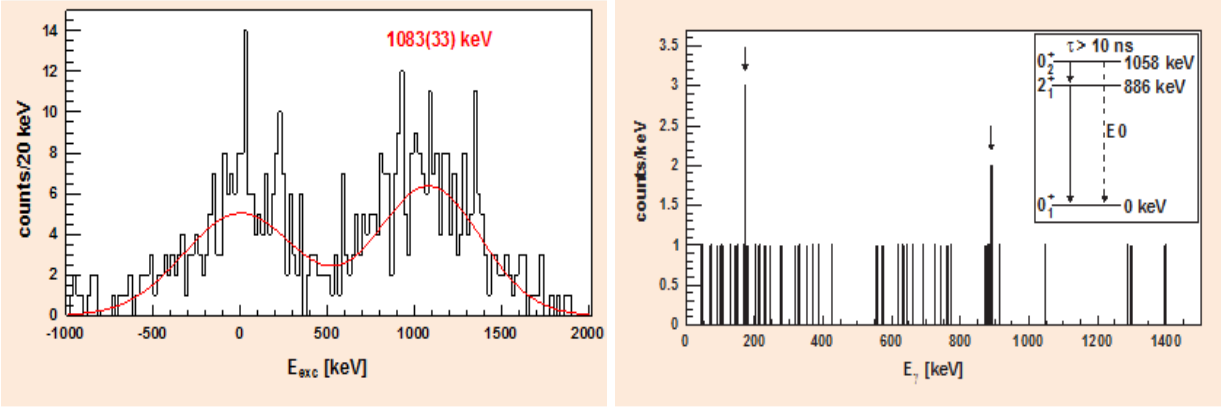

Fig. 13: Detailed spectroscopic data for ^{32}Mg (cf. Fig. 3, region C) from the ^{3}H(^{30}Mg,^{32}Mg)^{1}H, i.e., inverse (t,p), reaction. The upper frame shows the proton energy spectrum and the lower frame shows the γ rays in coincidence with protons from transfer to the excited state. The figures are taken from Wimmer et al. [13].

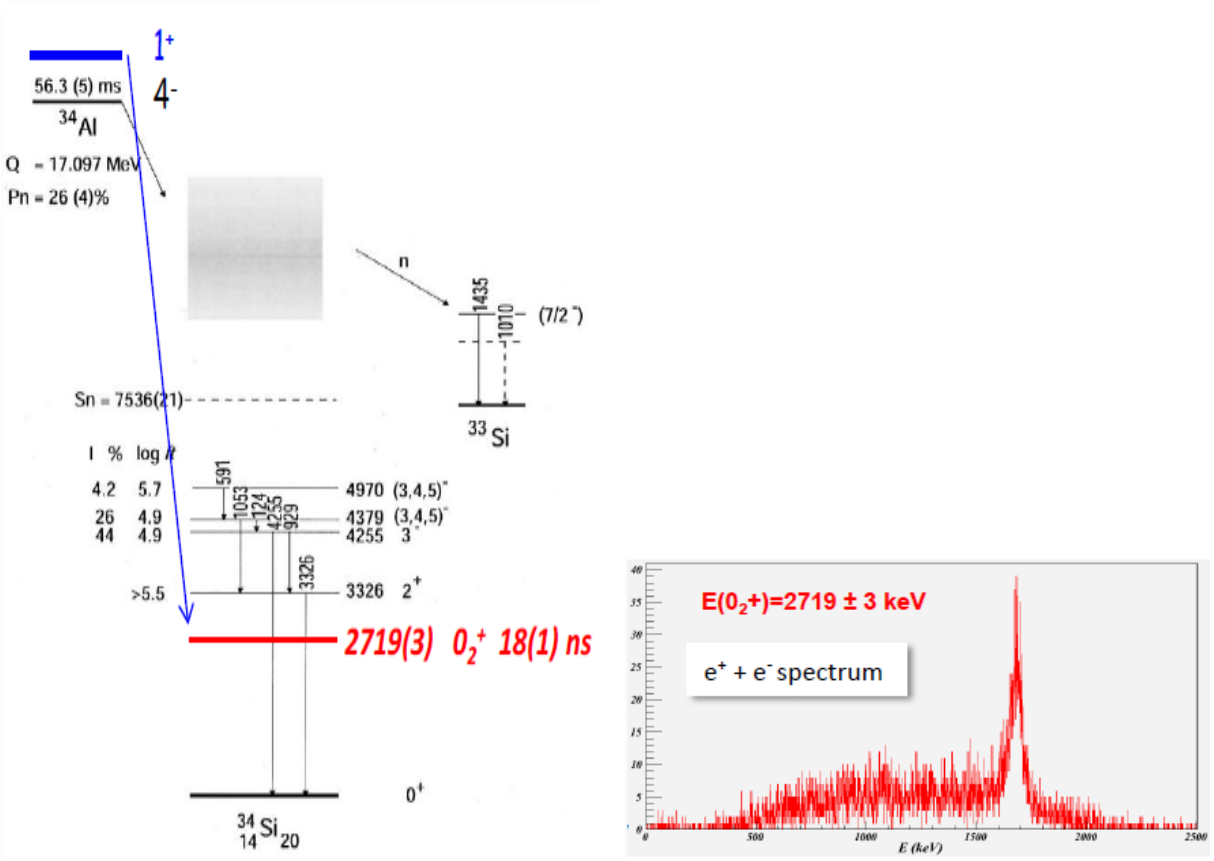

Fig. 14: Detailed spectroscopic data for ^{34}Si (cf. Fig. 3, region C) from the β decay of ^{34}Al^{mg}. The upper frame shows the decay scheme and the lower frame shows the internal-pair, e^+e^- spectrum that reveals the existence of a first excited state with spin-parity 0^+. The figures are taken from Rotaru et al. [14].

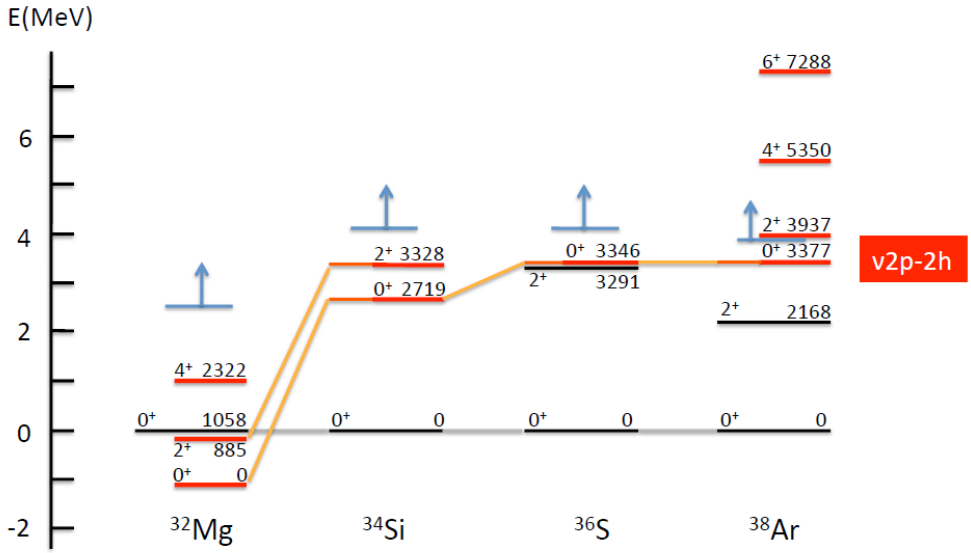

Fig. 15: Systematics of excited states in the N = 20 isotones (cf. Fig. 3, region C). The data are taken from Wimmer et al. [13], Rotaru et al. [14], and Nuclear Data Sheets.

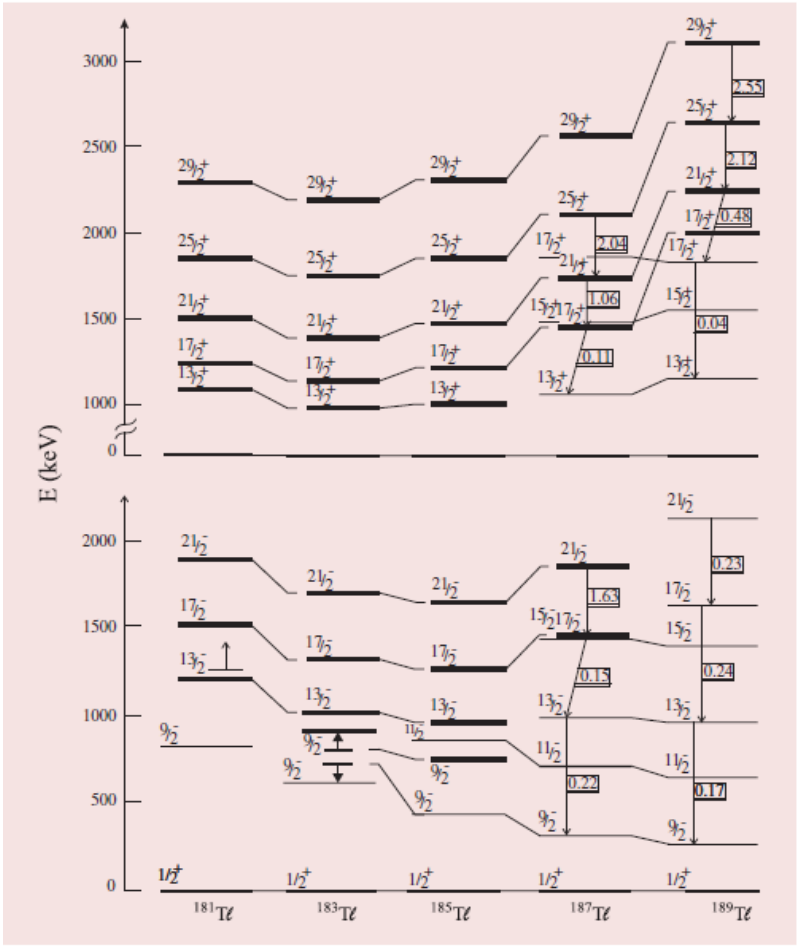

Fig. 16: Systematics of bands observed built on the lowest $9/2^-$ and $13/2^+$ states in the odd-Tl isotopes (cf. Fig. 3, region L). Strongly coupled bands with small B(E2) values and decoupled bands with large B(E2) values are observed (the values are given in $(e \cdot b)^2$ in the boxes. Mixing and repulsion of two $9/2^-$ configurations in ^{183}Tl is indicated. The figure is taken from Heyde and Wood [3].

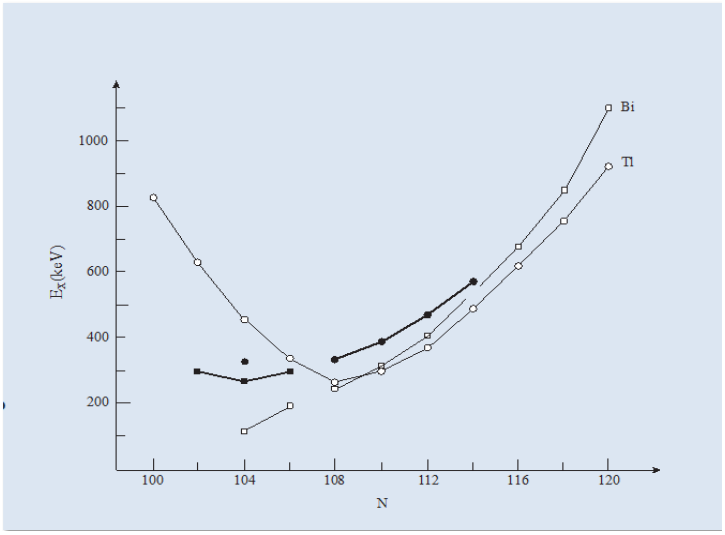

Fig. 17: Systematics of the odd-Tl(1p-2h), odd-Bi(2p-1h), and even-Pb(2p-2h) (cf. Fig. 3, region L) intruder-state energies (the even-Pb energies are divided by 2). Note the strong correlation of the three quantities: This is discussed further in the text. For the even-Pb isotopes, the candidate 4p-4h states are shown as solid squares. The figure is taken from Heyde and Wood.

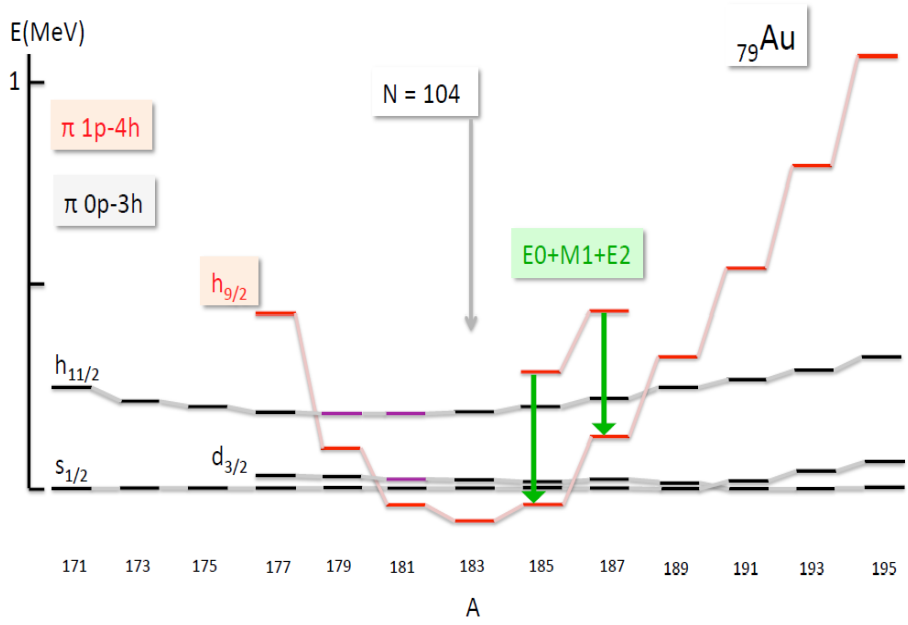

Fig. 18: Systematics of selected excited states in the odd-mass Au isotopes (cf. Fig. 3, region L). The states shown in black are the weakly deformed proton hole states characteristic of Z = 79 (π 3h); the states shown in red are deformed structures that arise from the excitation of a proton across the Z = 82 shell gap and are interpreted as π 1p-4h configurations. The states labeled as de-exciting by E0 + M1 + E2 transitions are discussed in the text. The data are taken from Venhart et al. [15] (see Figs. 31, 3, 33), Andreyev et al. [16], and Nuclear Data Sheets.

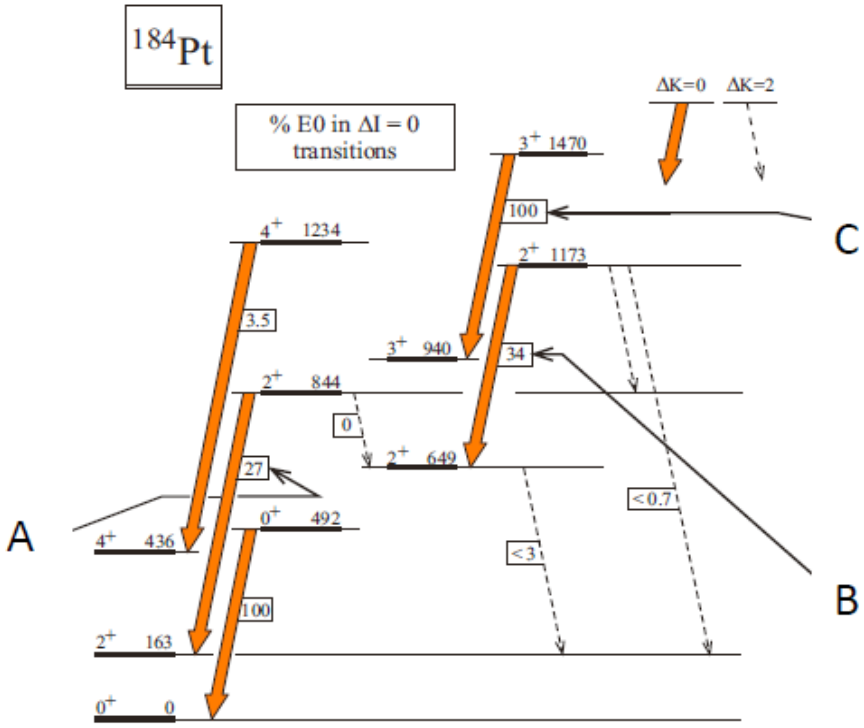

Fig. 19: Shape coexisting bands with K = 0 and K = 2 in ^{184}Pt (cf. Fig. 3, region L), as deduced from E0 transition patterns. Conversion electron and γ-ray spectra corresponding to transitions marked A, B, C are shown in Figs. 19, 20, and 21, respectively. The figure is adapted from Xu et al. [17].

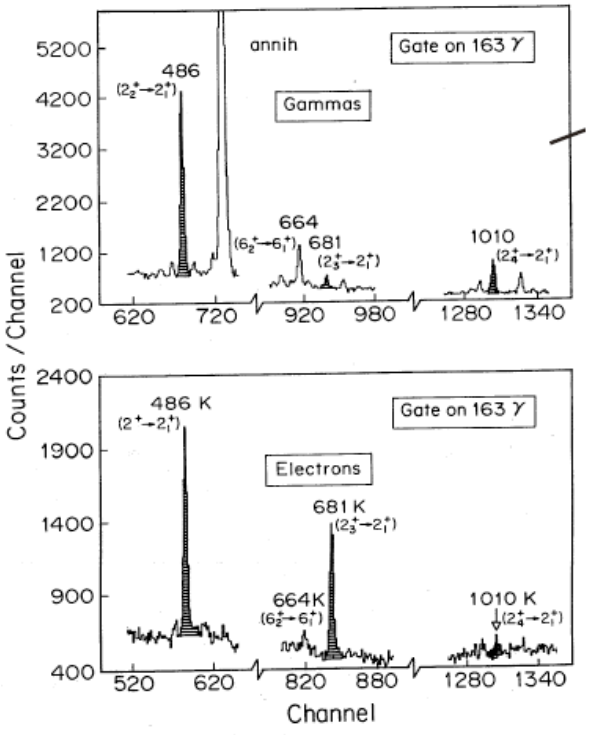

Fig. 20: Conversion electron and γ-ray spectra coincidence gated by the $2_1^+ \rightarrow 0_1^+$ γ-ray transition in ^{184}Pt. Note the highly converted nature of the $2_3^+ \rightarrow 2_1^+$ transition (cf. Fig. 19, transition A). The figure is taken from Xu et al. [17].

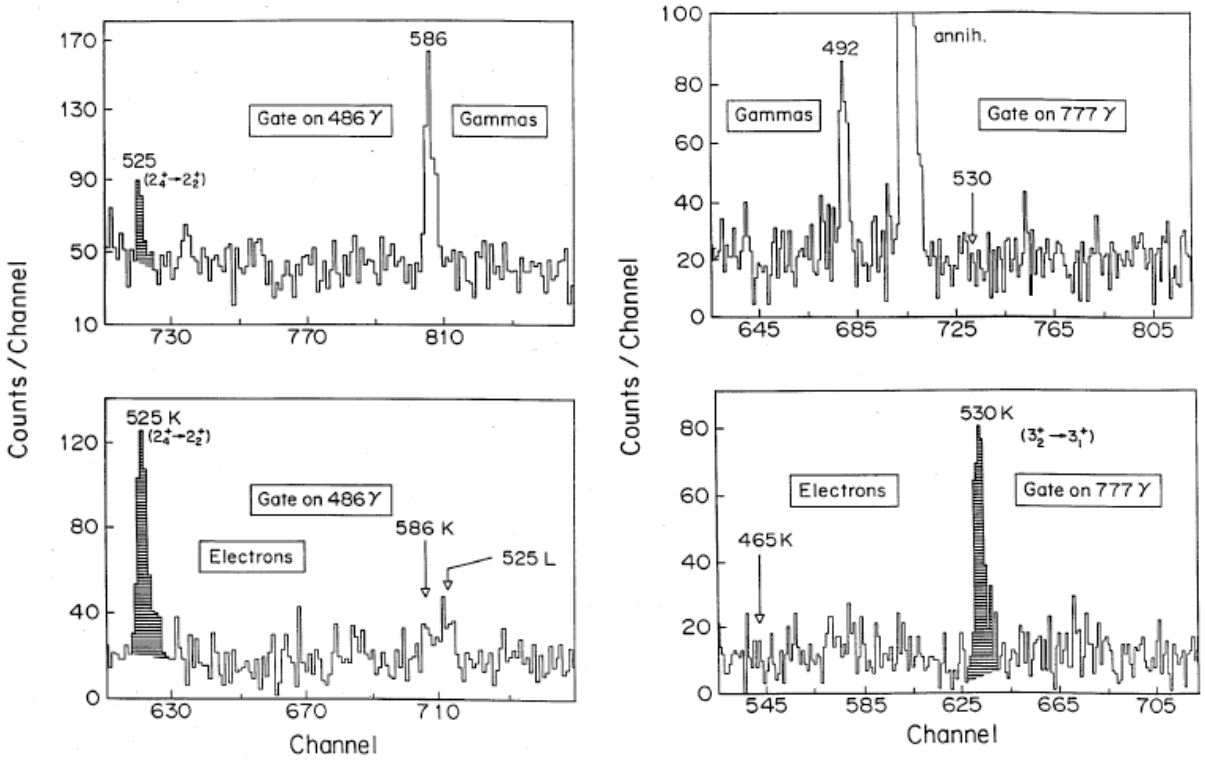

Fig. 21: Conversion electron and γ-ray spectra coincidence gated by the $2_2^+ \rightarrow 2_1^+$ γ-ray transition in ^{184}Pt. Note the highly converted nature of the $2_4^+ \rightarrow 2_2^+$ transition (cf. Fig. 19, transition B). The figure is taken from Xu et al. [17].

Fig. 22: Conversion electron and γ-ray spectra coincidence gated by the $3_1^+ \rightarrow 2_1^+$ γ-ray transition in ^{184}Pt. Note the highly converted nature of the $3_2^+ \rightarrow 3_1^+$ transition (cf. Fig. 19, transition C). The figure is taken from Xu et al. [17].

EXAMPLES OF EXTREME CHALLENGES IN THE ELUCIDATION OF SHAPE COEXISTENCE IN NUCLEI

The brief outline presented here of the manifestation of shape coexistence across the entire nuclear mass surface is designed to illustrate the breadth and depth of this facet of nuclear structure. It is also intended to show that detailed work is now possible; but much work needs to be carried out. One of the leading experimental probes for future work will be multi-step Coulomb excitation with radioactive beams (although much work with stable beams is also needed). The most detailed multi-step Coulex study with radioactive beams carried out so far is that of ^{74,76}Kr by Clement et al. [18] at GANIL. The γ-ray spectra obtained are shown in Fig. 23. The states excited in ^{74,76}Kr are shown in Fig. 24. The γ-ray yields lead

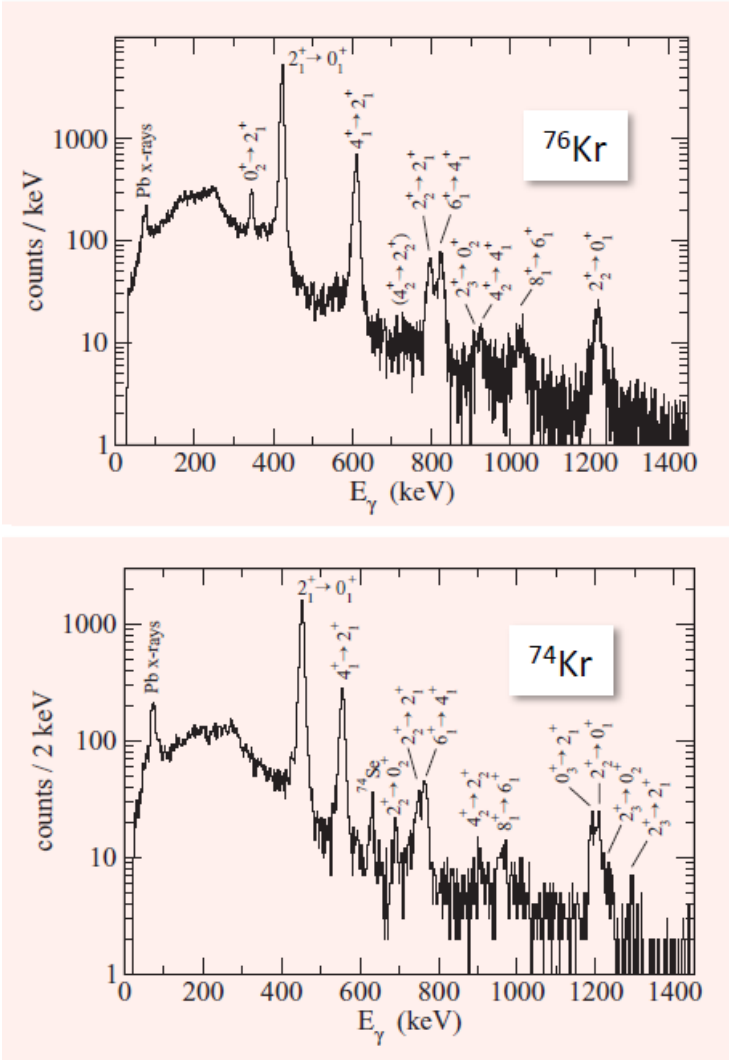

Fig. 23: The γ-ray spectra obtained by Coulomb excitation of ~4.5 MeV/u ^{74,76}Kr beams on a ^{208}Pb target. (cf. Fig. 3, region H). The γ-ray lines are labeled by the corresponding transitions in ^{74,76}Kr (cf. Fig. 24). The figures are adapted from a figure in Clement et al. [18].

to E2 matrix elements which can then be combined into products that define E2 centroids and fluctuation widths using the so-called Kumar-Cline sum rules [19,20]: these are shown for ^{74,76}Kr in Fig. 25. There are a sufficient number of E2 matrix elements determined, to infer centroids that support triaxial coexisting shapes for the 0_1^+ and 0_2^+ states in ^{74,76}Kr; but there are not enough to infer fluctuations, which need complete sums over products of four and six matrix elements to obtain quadrupole deformation and triaxiality fluctuations, respectively. It is evident that the Kumar-Cline sums reveal subtle manifestations of shape coexistence that cannot be "seen" by other methods.

The more subtle signature of shape coexistence manifested in E0 transition strengths has been outlined. Such information will be a vital complement to E2 matrix element information and the resulting Kumar-Cline sums. A manifestation of shape coexistence that is severely masked by mixing with respect to E2 transition

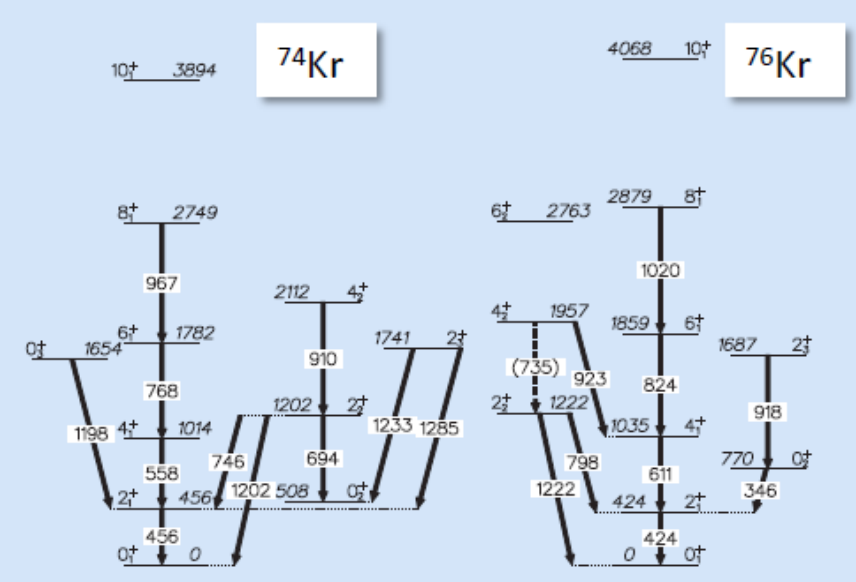

Fig. 24: The location of the γ-ray transitions observed in ^{74,76}Kr (cf. Fig. 3, region H) by Coulomb excitation (cf. Fig. 23). The figure is adapted from a figure in Clement et al. [18].

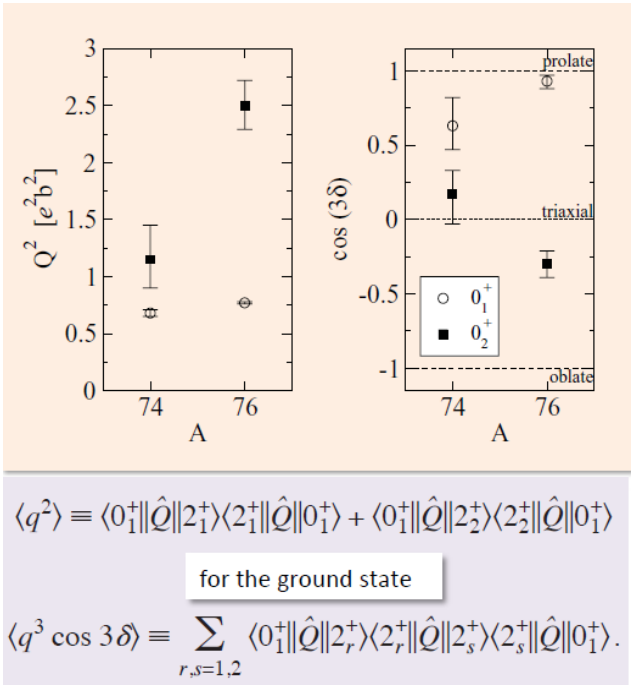

Fig. 25: Kumar-Cline sums for ^{74,76}Kr constructed from E2 matrix elements determined by Clement et al. [18]. The expressions for the sums that define the ground state deformation and its axial asymmetry are shown. The data are discussed in the text. The upper part of the figure is adapted from a figure in Clement et al. [18].

strengths but clearly visible from E0 transition strengths is depicted in Fig. 26, 26, 26. The nearly complete obscuration of the coexisting shapes, as manifested in excitation energies, is explained by the schematic view shown in Fig. 29, namely that this is due to quantum mechanical mixing of configurations with different deformations. The possible connection between shape coexistence in doubly even nuclei and odd-mass nuclei is briefly outlined in the previous section. If the connection is universal, it provides a powerful tool for the exploration of shape coexistence in nuclei. This potential connection is shown in a broad view in Fig. 30. The underlying connection is through the number of correlated pairs, cf. Fig. 17. This contradicts the popular view of "deformation-driving orbitals".

The study of odd-mass nuclei is highly demanding because of the high level density, especially at low

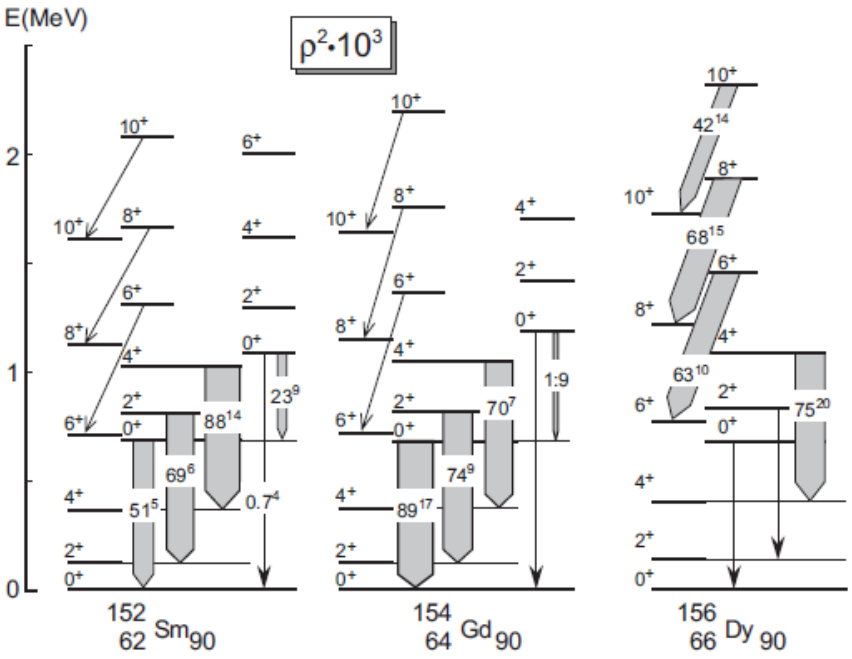

Fig. 26: Shape coexistence in the N = 90 isotones (cf. Fig. 3, region K) revealed by E0 transition strengths. The figure is similar to one in Heyde and Wood [3].

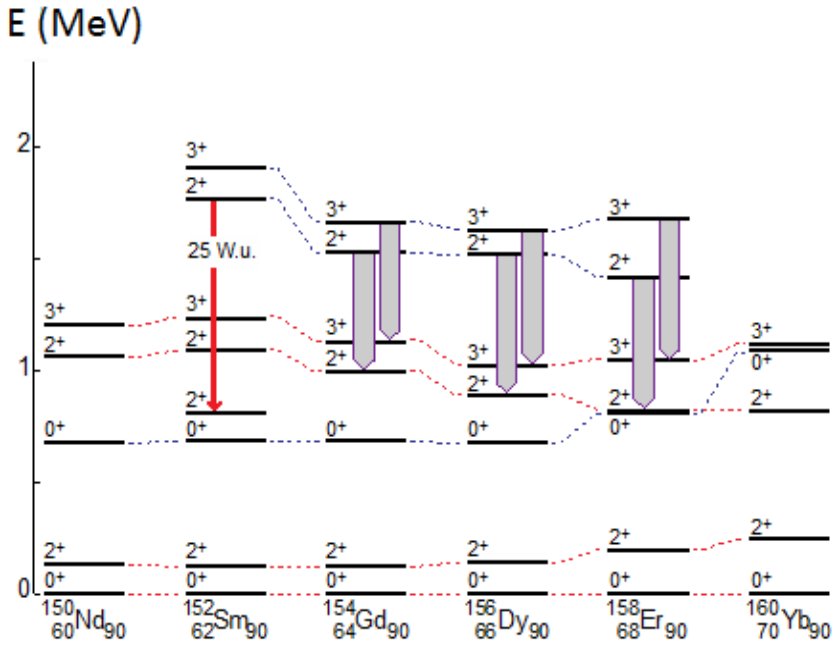

Fig. 27: Coexistence of K = 0 and K = 2 bands in the N = 90 isotones (cf. Fig. 3, region K) revealed by E0 transition strengths (cf. Figs. 19, 20, 21, 22 and see Fig. 28). The data are taken from work by Kulp et al. [21] and Nuclear data Sheets [17].

excitation energy. An example of an important odd-mass nucleus, ^{179}Au, for advancing our picture of the systematics of shape coexistence is shown in Figs. 31, 32, 33 and is based on the work of Venhart et al. [15]. This result provided a key step in the elucidation of the Au "parabola" shown in Fig. 18.

Figure 32 shows the α spectrum associated with ^{183}Tl decay (from an ISOLDE experiment) and the correlations between these α groups and γ rays (from a RITU at Jyväskylä in-beam experiment). Figure 33 shows the γ-ray spectrum following within 2 μs of the evaporation residue detection and within 15 s of the ensuing ^{179}Au ground-state α decay (from the RITU at Jyväskylä in-beam experiment). The narrow

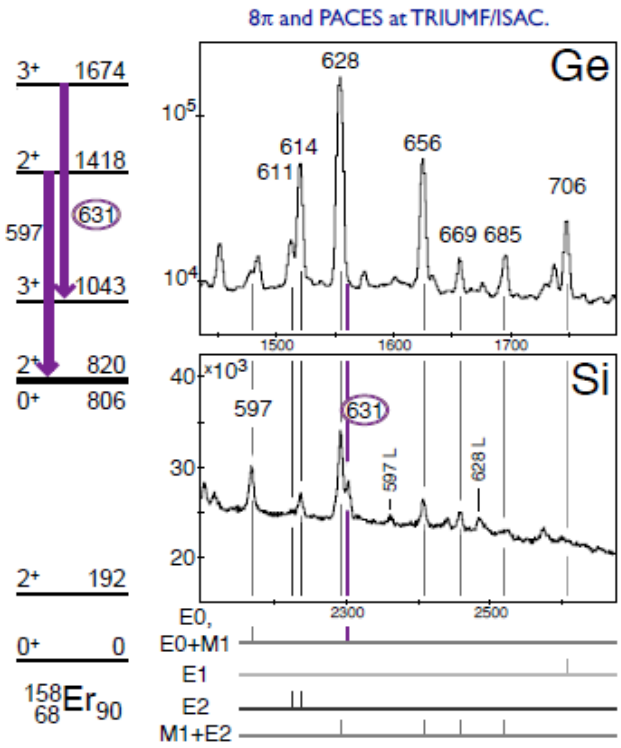

Fig. 28: Coexistence of K = 0 and K = 2 bands in the N = 90 isotone ^{158}Er (cf. Fig. 3, region K) revealed by E0 transition strengths (cf. Figs 19, 20, 21, 22 and see Fig. 27). The labelling of the spectra by Ge and Si designates that they are γ-ray and conversion-electron spectra obtained with Ge and Si semi-conductor detectors, respectively. Multipolarities of the corresponding transitions are shown by the " bar code ". The data are taken from work by Kulp et al. [21] and Nuclear Data Sheets [17].

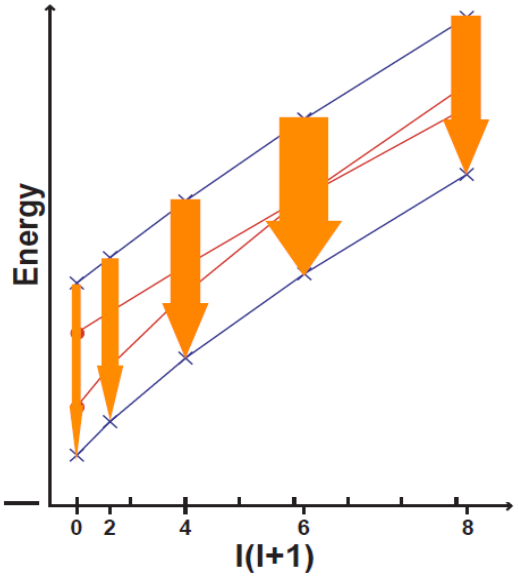

Fig. 29: Shape coexistence in the N = 90 isotones (cf. Fig. 3, region K) and how mixing causes excitation energies to appear as "identical bands" and produces E0 transition strength (orange arrows).

constraints on the time windows (and the energy window noted in the caption to Fig. 31) provided crucial simplifying features in what would otherwise have been a very complex set of spectra, for which extraction of decay information would have been extremely difficult or impossible.

Figure 32 also shows the employment of a quantitative analysis of the incidence of summing in the data using GEANT4 simulations. It is becoming evident that such summing analyses are mandatory for the execution of detailed, quantitative decay spectroscopy, especially when "close" geometry is used between the

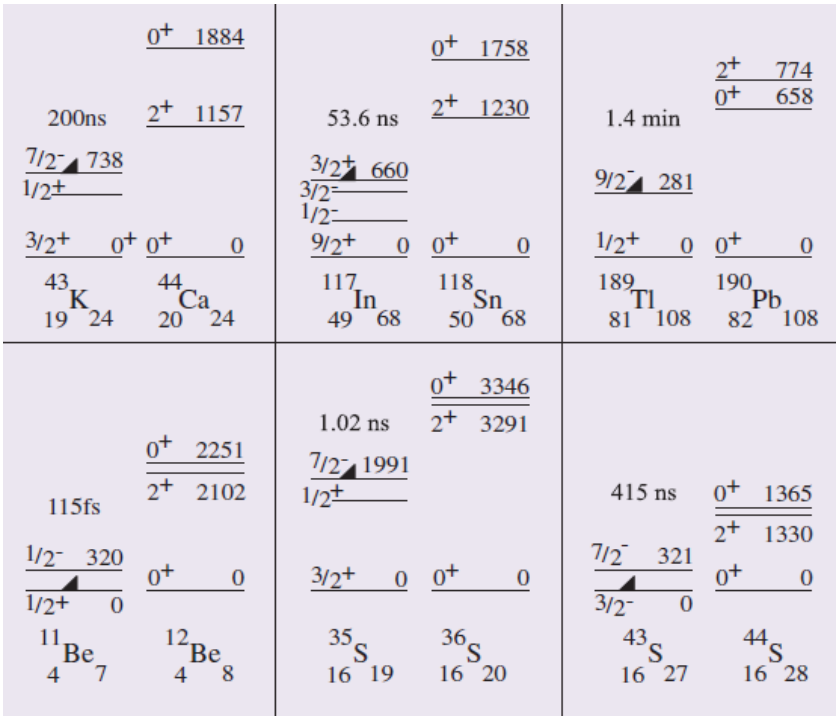

Fig. 30: The connection between shape coexistence in odd-mass and doubly even nuclei that are neighbors (cf. Fig. 3, regions E, J, L and B, C, D). The states marked by black triangles are 1p-2h states. The doubly even nuclei exhibit low-lying excited 0^+ states which are either established deformed structures (^{118}Sn, ^{190}Pb) or are candidates for deformed structures. The figure is taken from Heyde and Wood [3].

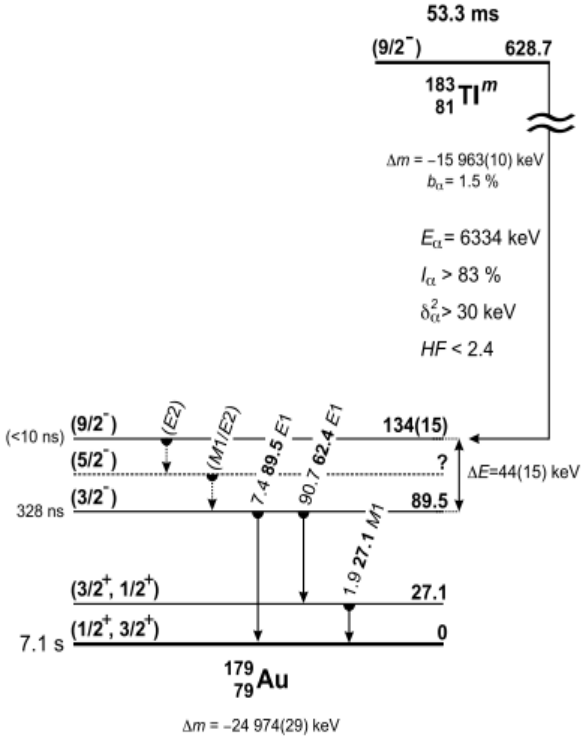

Fig. 31: The low-energy excitations of ^{179}Au as deduced from α decay of ^{183}Tl^m (53.3 ms) and ^{179}Au^m (328 ns). The mass of ^{179}Au and the α-decay energy of ^{183}Tl provided a very narrow constraint on the excitation energy "window" in ^{179}Au into which the observed γ rays (see Figs. 32, 33) had to be accommodated. The figure is taken from Venhart et al. [15].

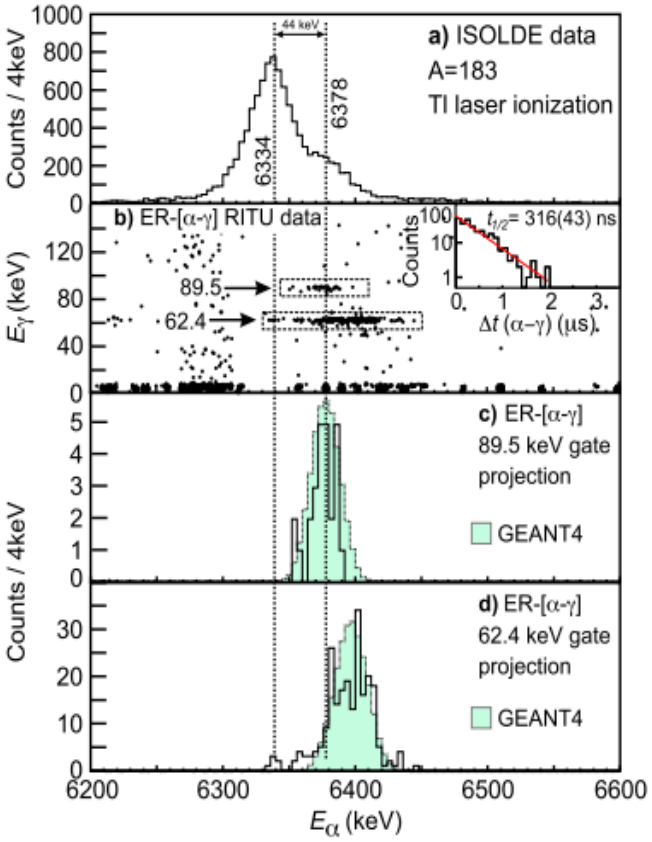

Fig. 32: The radiations deduced to be following the α decay of $^{183}\mathrm{Tl}^{m}$ (53.3 ms). The "offset" in the shaded green peaks reflects the summing between deposited energy (in the detector) from α particles and γ rays, as simulated by GEANT4. The figure is taken from Venhart et al. [15].

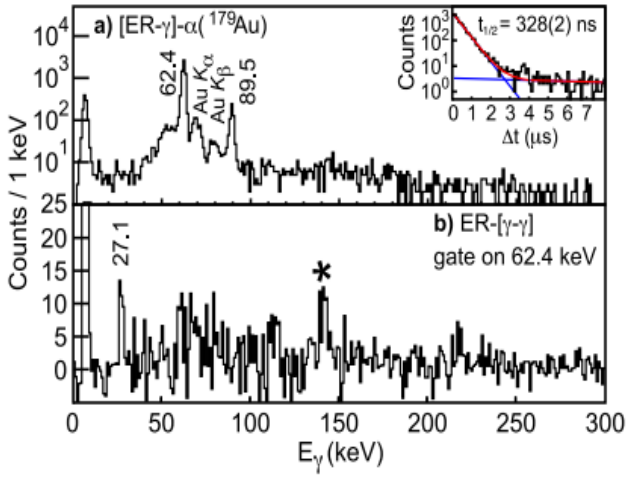

Fig. 33: The radiations deduced to be following the internal decay of $^{179}\mathrm{Au}^{m}$ (328 ns) and preceding the ground-state decay of ^{179}Au (7.1 s). The figure is taken from Venhart et al. [15].

decaying source and the detector. (Other details regarding these decays are found in Venhart et al. [15].)

SUMMARY AND CONCLUSIONS

This brief view of the outlook for studies of shape coexistence in nuclei is intended to show: a). shape coexistence in nuclei occurs everywhere, b). the manifestations of shape coexistence in nuclei may be subtle and the experimental work needed to identify its presence may be challenging,c). we possess a powerful arsenal of experimental equipment and techniques to advance this fundamental component of nuclear behavior.

Regarding future data needs, essentially all regions that exhibit evidence of shape coexistence need more detailed study (even regions where the isotopes are stable). Regions that appear not to exhibit shape coexistence also need study. For example, while the Z = 50 and 82 closed-shell regions exhibit well-established shape coexistence, for the N = 50 and 82 regions the evidence is much more fragmentary. This is because it occurs either at higher excitation energy (near stability) or (at low excitation energy) far from stability; some details of this can be found in Heyde et al. [1]. One region where data are now beginning to show the emergence of shape coexistence is in the Z = 28 (Ni) isotopes [22, 23] (and see Pauwels et al. [24]).

The most prominent systematic feature of the manifestation of shape coexistence in nuclei is the "parabolic" excitation energy pattern. Figures 2 and 18 highlight this. While the parabolas appear to be centered on mid-shell regions, there are subtle variations, cf. Fig. 15, 16, 17. Indeed, if the parabolic pattern is a universal one, then the energy pattern in Fig. 15 suggests two parabolas may be present. At a more subtle level, hints of two parabolas may be behind the patterns shown in Figs. 16 and 17. Two parabolas are also implicit in Fig. 18 as manifested in the states that feed the intruder states by E0 transitions, and are interpreted as "core" intruder configurations coupling to "particle" intruder configurations, i.e., "double" intruders. The parabolic energy pattern can be placed into a new perspective, as shown in Fig. 34. Case

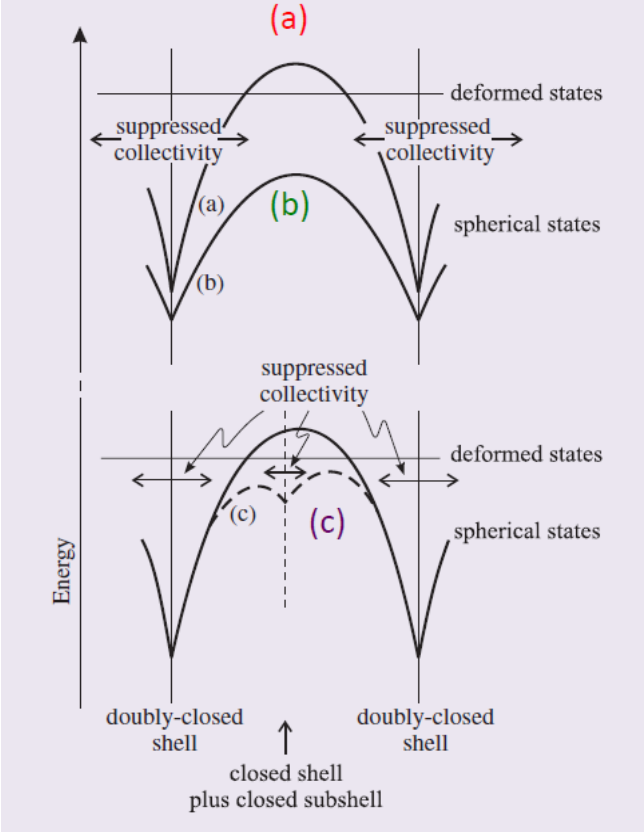

Fig. 34: The parabolic energy patterns of shape coexistence viewed from the perspective that deformation in nuclei is the norm and spherical shapes only dominate low-energy structure in isolated regions (called "closed shell"). Cases (a), (b), and (c) are discussed in the text. The figure is taken from Heyde and Wood [3].

(a) is the situation where deformed structures intrude to become the ground state at the middle of a singly closed shell, e.g., ^{32}Mg; case (b) is the situation where the ground states for a sequence of singly closed shell nuclei remain spherical, but deformed structures form excited intruder bands, e.g., the Sn isotopes; case (c) is the situation where a subshell may suppress intrusion of a deformed structure from becoming the ground state or a low-lying excited state, e.g., the N = 50, 82 isotones.

A greater challenge for future experiments will be the issues of shape coexistence in nuclei further from closed shells (and subshells) and whether or not spherical states occur in nuclei with deformed ground states (cf. Fig. 33). At present, very little is known about these issues.

The author wishes to acknowledge collaborations with Mitch Allmond (Oak Ridge National Lab), Paul Garrett (U. Guelph), Kris Heyde (U. Gent), Martin Venhart (Slovak Academy of Sciences), and Steve Yates (U. of Kentucky) in the development of these ideas.

REFERENCES

[1] K. Heyde, P. Van Isacker, M. Waroquier, J.L. Wood, and R.A. Meyer, Phys. Repts. **102**, 291 (1983).
[2] J.L. Wood, K. Heyde, W. Nazarewicz, M. Huyse, and P. Van Duppen, Phys. Repts. **215**, 101 (1992).
[3] K. Heyde and J.L. Wood, Rev. Mod. Phys. **83**, 1467 (2011).
[4] J. Elseviers *et al.*, Phys. Rev. C **84**, 034307 (2011).
[5] H.W. Fielding *et al.*, Nucl. Phys. A **281**, 389 (1977).
[6] J. Kantele *et al.*, Z. Phys. A **289**, 157 (1979).
[7] K. Heyde and R.A. Mayer, Phys. Rev. C **37**, 2170 (1988).
[8] J.L. Wood, E.F. Zganjar, C. De Coster, and K. Heyde, Nucl. Phys. A **651**, 323 (1999).
[9] T. Kidedi and R.H. Spear, At. Data Nucl. Data Tables **89**, 77 (2005).
[10] E. Elhami *et al.*, Phys.Rev. C **78**, 064303 (2008).
[11] A. Chakraborty *et al.*, Phys. Rev. Lett. **110**, 022504 (2013).
[12] N. Bree *et al.*, Phys. Rev. Lett. **112**, 162701 (2014).
[13] K. Wimmer *et al.*, Phys. Rev. Lett. **105**, 252501 (2010).
[14] F. Rotaru *et al.*, Phys. Rev. Lett. **109**, 092503 (2012).
[15] M. Venhart *et al.*, Phys. Lett. B **695**, 82 (2011).
[16] A. Andreyev *et al.*, Phys. Rev. C **73**, 044324 (2006).
[17] Y. Xu *et al.*, Phys. Rev. Lett. **68**, 3853 (1992).
[18] Clément *et al.*, Eur. Phys. J. Special Topic **150**, 117-120 (2007)
[19] K. Kumar, Phys. Rev. Lett. **28**, 249 (1972).
[20] D. Cline, Annu. Rev. Nucl. Part. Sci. **36**, 683 (1986).
[21] W.D. Kulp, priv. comm. (2007).
[22] F. Recchia *et al.*, Phys. Rev. C **88**, 041302(R) (2013).
[23] S. Suchyta *et al.*, Phys. Rev. C **89**, 021301(R) (2014).
[24] D. Pauwels, J.L. Wood, K. Heyde, M. Huyse, R. Julin, and P. Van Duppen, Phys. Rev. C **82**, 027304 (2010).

REACTIONS IN INVERSE KINEMATICS USING ACTIVE TARGETS

Giacomo Randisi[1]*

[1]Instituut voor Kern- en Stralingsfysica, KU Leuven, Celestijnenlaan 200d, BE-3001 Leuven

Abstract

Nuclear reactions in inverse kinematics with radioactive ion beams are nowadays extensively used to investigate the evolution of nuclear structure when moving far from stability. The choice of different types of reactions depends on the spectroscopic observables to be investigated and is also linked with the availability of radioactive ion beams. In the case of low intensity beams, the use of active targets allows to greatly increase the yields and still retain a good resolution, due to the high target thickness and the possibility to track the particles in the gas target. Active targets are particularly suited for the study of resonant elastic (inelastic) scattering, but they can also provide a unique way to measure direct reactions when other devices cannot overcome the low beam intensities. Interesting results have already been obtained with the existing devices, especially when studying extremely exotic structural properties, like neutron-unbound resonances. An overview of some key physics cases is presented, together with an outlook of the opportunities opening with the development of the next generation of these instruments.

INTRODUCTION

The extensive development of radioactive ion beams (RIB) in the last decades led to the discovery of several new phenomena connected to the evolution of nuclear structure when accessing nuclei with extreme neutron-to-proton ratios (nuclear halos [1, 2], disappearance or migration of the "classical" magic numbers far from stability [3, 4, 5]). Despite the progress made in the production and acceleration of radioactive beams, the production of intense radioactive beams is still a challenge, especially for very short-lived nuclei, and this is one of the primary objectives fixed by the scientific community for the next-generation RIB facilities like SPIRAL2, HIE-ISOLDE and ISAC2. When approaching the drip lines, due to the very low beam intensities, a compromise between target thickness and energy resolution is often necessary.

Several probes can be used to obtain information about the evolution of nuclear structure when approaching the drip lines, like direct reactions (one- and many-nucleon transfer, breakup), resonant reactions (resonant scattering, giant resonances) and nuclear decays (direct and β-delayed emission), giving access to complementary information.

Increasing the target thickness helps to improve the luminosity but it degrades the energy resolution, and is therefore detrimental when spectroscopic information is needed. Thus, when using thin solid targets, particle detector arrays become necessary to improve the solid angle coverage, especially in low-energy direct reactions in inverse kinematics. The use of coincidence techniques can often help to improve selectivity and resolution, but with a cost in terms of total efficiency.

An alternative solution is to use an active target, a gaseous ionization detector in which the atomic nuclei of the detection medium are also used as a target. Active targets are time projection chambers (TPC) [6], in which the incident particles and the reaction products are tracked inside the gas volume.

A uniform electric field acting in the gas volume, is used to make the electrons created by ionization to drift, with constant velocity, towards a region of amplification. In this region the number of electrons is then multiplied with a high gain factor (up to 10^5). The generated signals are collected onto a segmented pad plane which gives a two-dimensional charge projection of the particle tracks. The third dimension is obtained by deducing the drift time of the electrons generated along the tracks.

CHARACTERISTICS AND ADVANTAGES OF ACTIVE TARGETS

A major advantage when using an active target is the possibility to obtain a very high luminosity because of its high effective thickness, while still retaining a good energy resolution due to the reconstruction of the track vertex. A complete identification of the reaction kinematics can be obtained by tracking the particles and measuring their energies. For the particles that stop in the gas, the energy can be determined either by the ion range or the total detected charge, and their identification is achieved using the charge profile along

*Present address, GANIL, CEA/DSM - CNRS/IN2P3, BP 55027, F-14076 Caen Cedex, France. E-mail: randisi@ganil.fr.

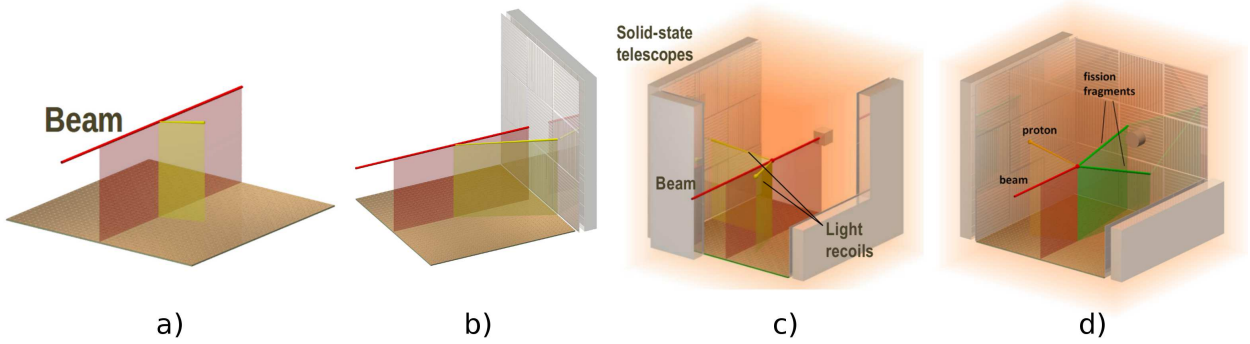

Fig. 1: Examples of various configurations of active targets for studying different physics cases: a) inelastic scattering, b) resonant elastic scattering, c) one-nucleon transfer reactions, b) transfer-induced fission reactions (courtesy of R. Raabe).

the pads (Bragg peak). Such a device also offers a very high solid angle coverage for the particles which are stopped in the gas volume. Particles escaping the gas volume can be detected and identified using auxiliary detectors (*i.e.* silicon detectors, scintillators). Other advantages of active targets are the low detection thresholds, the possibility to tune the gas pressure (and hence the explored energy range), the possibility to use different gases and gas mixtures as targets, and the portability of such devices.

Several types of active targets and TPCs have been operating over the past few years, like IKAR [7], MAYA [8] and the CENBG TPC [9], each with different characteristics depending on the physics cases. For a more extensive list of all the active targets used or under construction around the world see Ref. [10]. A series of pioneering results have been obtained using these devices. Some examples are the identification of the most neutron-rich unbound nucleus ^{7}H [11], the first measurement of the p(^{11}Li,^{9}Li)t reaction [12, 17] and the measurement of Isoscalar Giant Resonances in ^{56}Ni [14] and ^{68}Ni [15], obtained using the MAYA active target.

SELECTED PHYSICS CASES FOR MEASUREMENTS WITH ACTIVE TARGETS

The characteristics of the active target concept are very attractive for a variety of physics cases because of its versatility and its ability to operate with low intensity beams. Some of the most promising are briefly discussed below, together with the advantages and limitations which can be met.

Resonant Scattering

Resonant elastic scattering of exotic nuclei on a proton target can be performed to measure proton-unbound resonant states of astrophysical interest or to probe the structure of isobaric analogue states (IAS) for very neutron-rich nuclei. In the case of the former, the thick target method as been used extensively to measure proton excitation functions of light nuclei, and has provided precise structural information on proton-unbound states of astrophysical relevance [16]. Here the advantage of using an active target resides in the possibility of extending the measurements beyond zero-degrees, since the scattering angle can be determined from the track vertex (Fig. 1b). On the neutron-rich side, this method can be considered as complementary to (d,p) reactions but has the advantage of a much higher cross section for elastic scattering. Measurements of resonant scattering on an ^{A}Z nucleus on protons can populate isobaric analogue states (IAS) of the neutron-rich mirror $^{A+1}$Z which then gives insight on its structure. This technique is particularly attractive when applied to the study of neutron-unbound nuclei by measuring excited states above the proton emission threshold in the proton-rich isobar, as demonstrated in the measurement of IAS of the neutron-unbound ^{12}Li by using ^{11}Li+p resonant elastic scattering [17].

Giant Resonances

The measurement of isoscalar giant monopole (ISGMR) and dipole (ISGDR) resonances in nuclei close and far from stability constitutes a crucial input to determine the incompressibility modulus of nuclear matter [18]. While extensive experimental work has been carried out to measure these collective excitation modes for stable nuclei [19], information about the evolution of the incompressibility modulus in unstable nuclei and along different isotopic chains is limited. Recent measurements have attempted to determine this evolution for Nickel isotopes [14, 15]. The use of the MAYA active target was essential to couple the high luminosity of a gas target and the the possibility to detect low-energy recoil particles (Fig. 1a).

Transfer reactions

Active targets can also provide a unique way to study direct reactions when other devices cannot be used with very low beam intensities. One-nucleon transfer reactions, due to their sensitivity to single-particle states, have proven to be an important tool to probe the evolution of nuclear structure with increasing isospin [20, 21, 22]. Since the differential cross section for transfer to different states depends on the transferred angular momentum, a measurement of the angular distribution provides an indication of the spins and parities of the populated states. These measurements are usually performed using solid-state particle detector arrays covering the largest possible fraction of the solid angle. In inverse-kinematic (d,p) reactions, the light recoils are emitted at backward angles, thus it is necessary to use very thin targets, not only to obtain a good resolution, but also in order to be able to detect the low-energy recoils at large laboratory angles. These reasons, coupled to the relatively low ($\sim$ mbarn) cross-sections of these reactions in the energy range of few a MeV/nucleon required to probe low angular momentum transfer, impose a lower limit for beam intensities (around 10^4 pps), thus excluding the possibility to measure (d,p) cross sections with silicon arrays for very exotic nuclei. The advantage of the active target, with its very high effective thickness and ability to track the low-energy recoils at backward angles (Fig. 1c), brings a gain in resolution and allows these kinds of measurements for the most exotic nuclear beams.

Exotic decay modes

Exotic decay modes like ground-state two-proton radioactivity or the β-delayed particle emission are sensitive tools to probe the evolution of nuclear structure close to the drip lines. They also provide information on final-state proton-proton interactions [23]. Finally, two-proton radioactivity can also be considered as the time-reverse of two-proton capture reactions, which are believed to play a role in stellar nucleosynthesis [24]. Ground-state two-proton radioactivity of ^{45}Fe [25] and ^{54}Zn [26] was studied at GANIL using the CENBG TPC [9]. In these measurements, both the proton energies and their relative angles could be measured. An optical TPC, developed at the University of Warsaw [27], was used to study proton-proton angular correlations in ^{45}Fe [28] and has provided the first direct evidence for g.s. two-proton emission in ^{48}Ni [29].

Beta-delayed particle emission, on the other hand, is a key tool for the study of light neutron-rich nuclei (*i.e.* halo nuclei). For these nuclear systems, the high Q_β values of the progenitors and the low breakup thresholds of the daughters result in a non negligible part of the β-decay strength to be available for high-lying excited states in the continuum. Very rare decay channels with high thresholds (like deuteron and triton emission) are sensitive to the wave function of the parent nucleus [30, 31]. These studies have been carried out by observing the ions emitted after implanting the radioactive beam into a thin target or directly in a thin segmented silicon detector [32]. Even though very low thresholds can be reached for charged particles, complete kinematic studies of all of the individual channels can only be performed by tracking the decaying light ions. Such types of studies could be performed in the future by implanting the ion beams inside an active target.

NEW POSSIBILITIES WITH NEXT GENERATION ACTIVE TARGETS

Certain limitations of present active targets must be overcome in order to confront the most challenging physics cases. One of the most recurrent problems concerns the very high dynamic range that is required when dealing with simultaneous measurements of light and heavy reaction products. Another major problem concerns the vertex reconstruction, as it requires long tracks compared to the pad size or strip pitch. In the case of MAYA, low-energy events or large scattering angles are difficult to measure. This is the case for the reconstruction of low-energy, large-angle tracks obtained when measuring giant resonances, or when the light

backward recoils following nucleon-transfer reactions need to be measured. It is impossible to track more than two particles with an active target like MAYA, in which the amplification system is based on parallel wires. Finally, the current data acquisition systems set low limits for the maximum accepted counting rate, and do not allow for a multiple-level trigger required for certain kinds of reactions.

The next generation of active targets under construction, like ACTAR TPC at GANIL and AT-TPC at MSU, have been designed to overcome these limitations and to cover a wider range of possibilities with the most exotic radioactive beams. These detectors make use of new amplification systems based on Micro-Pattern Gaseous Detectors (MPGDs), characterized by a better intrinsic resolution, the possibility to operate at relatively high rates, moderate manufacturing cost and the possibility to be produced in different shapes and sizes. The most commonly used MPGD technologies are MICROMEGAS [33] and GEM [34], which can both be coupled to different detector geometries. This technology, coupled with highly-segmented pad planes and new electronics allows to obtain a very high granularity and to treat each pad independently. For this purpose, The General Electronics for TPCs (GET) project [35] has developed a new electronic system with an extended data readout bandwidth (10 Gb/s), being able to process up to 30 thousand channels and to provide a multi-level numeric trigger. This will allow different gain zones to be set in the pad plane to reach higher effective dynamic ranges (up to 10^3). At the same time, it will be possible to reconstruct multiple tracks and the multi-level trigger will allow for higher selectivity. Another improvement will be the use of gamma-ray detectors to increase the selectivity and resolution when dealing with high level densities. In that spirit, The SpecMAT project [36] will allow in the future to couple the concept of active target to a magnetic field and a gamma-ray detector array.

An array of new possibilities will open up with these devices. As an example, the robustness of shell gaps as well as the appearance of new shell-closures far from stability could be addressed using transfer reactions to probe the single-particle character of very exotic nuclear species, ranging from the light neutron-rich oxygen isotopes up to the region around the doubly-magic nucleus ^{132}Sn. A letter of intent has already been submitted to study shell evolution around ^{78}Ni through the ^{80}Zn(d,p) reaction at ISOLDE. In the region around ^{132}Sn, the high density of levels populated in the ^{134,135}Sn(d,p) reactions could be resolved using the SpecMAT gamma-ray detectors, in order to measure precise level schemes and spectroscopic factors and determine the evolution of the shell gap along the isotopic chain.

For resonant elastic scattering experiments, isobaric analogue states could be studied in neutron-rich nuclei which have been so far difficult to reach. This is the case for ^{27}Ne, whose neutron unbound states, important to measure the N=20 gap could be accessible through the ^{26}Ne+p reaction.

The ACTAR TPC detector will also be available in an elongated configuration, adapted to stop all of the products of interest produced by projectile fragmentation within the active volume of the chamber. Two-proton decay candidates like ^{59}Ge and ^{63}Se could be studied in the future with this geometry. Studies could also be performed on the β-delayed light-ion emission of light neutron-rich systems like ^{14}Be, ^{17}B and ^{22}C, providing detailed information on the halo wave function of the parent nuclei.

Finally, the study of the transfer-induced fission mechanism, recently proposed with the MAYA detector with a ^{238}U beam, could be extended to several proton-rich nuclei in the region around Z=82. These studies could provide a new method to measure fission barriers for exotic beams available with low intensities. An example is the ^{193}Tl(d,p) reaction, which has been proposed to be studied at HIE-ISOLDE in inverse kinematics with a ^{193}Tl beam at 5 MeV/nucleon using an active target, in order to obtain a complete kinematics measurement (energy and relative angles of the fission fragments and the proton recoil, Fig. 1d). This measurement will be feasible using ACTAR TPC filled with deuterium at 500 mbar and would allow a selective measurement of the excitation function over an extended range.

CONCLUSIONS

In summary, active targets have already been proven to be very effective tools for the study of many interesting phenomena in nuclear physics, especially with rare exotic beams. The capability of increasing the luminosity without degrading the overall resolution is one of the key characteristics of these instruments. The development of the next generation of these devices will open up new possibilities due to new amplification technologies and electronics, as well as the possibility to use magnetic fields to confine and unambiguously identify all of the reaction products.

ACKNOWLEDGMENT:

The ACTAR TPC and GET collaborations are gratefully acknowledged. Fruitful discussions with R. Raabe and G.F. Grinyer are also acknowledged. This work was supported in part by FWO-Vlaanderen (Belgium), by GOA/2010/010 (BOF KU Leuven), by the Interuniversity Attraction Poles Programme initiated by the Belgian Science Policy Office (BriX network P7/12) and by the European Commission within the Seventh Framework Programme through I3-ENSAR (contract no. RII3-CT-2010-262010).

REFERENCES

[1] I. Tanihata et al. Phys. Rev. Lett. **55**, 2676 (1985).
[2] P. G. Hansen, A. S. Jensen, and B. Jonson, Annu. Rev. Nucl. Part. Sci. **45**, 591 (1995).
[3] A. Navin et al. Phys. Rev. Lett. **85**, 266 (2000).
[4] A. Ozawa et al. Phys. Rev. Lett. **84**, 5493 (2000).
[5] O. Sorlin and M. G. Porquet, Prog. Part. Nucl. Phys. **61**, 602 (2008).
[6] J.A. MacDonald (ed.), The Time Projection Chamber, AIP Conf. Proc. Vol. **108**, New York (1984).
[7] S.R. Neumaier et al. Nucl. Phys. A **712**, 247 (2002).
[8] C.E. Demonchy et al. Nucl. Instrum. Meth. A **573**, 145 (2007).
[9] B. Blank Nucl. Instrum. Meth. B **266**, 4606 (2008).
[10] G.F. Grinyer, J. Pancin and T. Roger, EURISOL Report (2014), http://pro.ganil-spiral2.eu/laboratory/detectors/actar-tpc/.
[11] M. Caamaño et al., Phys. Rev. Lett.**99**, 062502 (2007).
[12] I. Tanihata et al., Phys. Rev. Lett. **100**, 192502 (2008).
[13] T. Roger et al., Phys. Rev. C **79**, 031603(R) (2009).
[14] C. Monrozeau et al., Phys. Rev. Lett. **100**, 042501 (2008).
[15] M. Vandebrouck et al., Phys. Rev. Lett. **113**, 032504 (2008).
[16] I. Stefan et al., Phys. Rev. C **90**, 014307 (2014).
[17] T. Roger, PhD Thesis (2009) , http://tel.archives-ouvertes.fr/tel-00424010.
[18] M. N. Harakeh and A. van der Woude, Giant Resonances: Fundamental high frequency modes of nuclear excitation (Oxford University Press, Oxford, 2001).
[19] T. Li, et al., Phys. Rev. Lett. **99**, 162503 (2007).
[20] W. N. Catford, et al., Eur. Phys. J. A **25** s01, 245 (2005).
[21] L. Gaudefroy, et al., Phys. Rev. Lett. **97**, 092501 (2006).
[22] K.L. Jones et al., Nature **465**, 454 (2010).
[23] B. Blank and M. Ploszajcak, Rep. Prog. Phys. **71**, 046361 (2008).
[24] H. Schatz et al., Phys. Rep. **294**, 167 (1998).
[25] J. Giovinazzo, et al., Phys. Rev. Lett. **99**, 102501 (2007).
[26] P. Ascher, et al., Phys. Rev. Lett. **107**, 102502 (2011).
[27] K. Miernik et al., Nucl. Instrum. Meth. A **581**, 194 (2007).
[28] K. Miernik et al., Phys. Rev. Lett. **99**, 192501 (2007).
[29] M. Pomorski et al., Phys. Rev. C **83**, 061303(R) (2011).
[30] K. Riisager et al., Phys. Lett. B **235**, 30 (1990).
[31] T. Nilsson, G. Nyman, and K. Riisager, Hyperfine Interact. **129**, 67 (2000).
[32] R. Raabe et al., Phys. Rev. Lett. **101**, 212501 (2008).
[33] Y.Giomataris et al., Nucl. Instrum. Meth. A **376**, 29 (1996).
[34] F. Sauli, Nucl. Instrum. Meth. A **386**, 531 (1997).
[35] E.C.Pollacco, et al., Physics Procedia **37**, 1799 (2012).
[36] R. Raabe, private communication.

SHAPE COEXISTENCE IN THE LEAD REGION FROM A GROUND-STATE PERSPECTIVE

Thomas Elias Cocolios[1,*]

[1]School of Physics & Astronomy, The University of Manchester, Oxford Road, Manchester M13 9PL, United Kingdom

Abstract

Ground-state properties are the basis upon which the nuclear levels are built. They are therefore essential building blocks to the understanding of any nuclear phenomenon at low energy, such as shape coexistence. Moreover, their study can determine the extent to which shape coexistence leads to the mixing of different configuration. In the region around ^{186}Pb, an extensive laser spectroscopy programme has been undertaken at the CERN ISOLDE radioactive ion beam facility at both the RILIS and CRIS experiments for the study of the even-Z $_{82}$Pb and $_{84}$Po isotopes, and the odd-Z $_{79}$Au, $_{81}$Tl, $_{83}$Bi, $_{85}$At, and $_{87}$Fr.

INTRODUCTION

Shape coexistence is found across the nuclear chart as different nuclear configurations give rise to different nuclear shapes in close proximity to one another [1]. A dramatic example is found in $^{186}_{82}Pb_{104}$ where the ground state and the two first excited states are $I^\pi = 0^+$ states, within less than 700 keV of each other, which are believed to be respectively spherical, oblate and prolate [2].

An extensive survey of the nuclear properties in this region has revealed many interesting features [3], such as the band structure of the even-A $_{80}$Hg isotopes. From the magic shell closure at $N = 126$ down to $N = 114$, the nuclear states are found to be very similar in energy and ordering, as expected in the vicinity of the magic shell closure at $Z = 82$. However, for $N \leq 112$, an intruding band is found with a prolate character. Its excitation energy decreases parabolically to a minimum at $N = 102$ [4], while the weakly oblate ground-state band remains mostly unaffected.

The $_{84}$Po isotopes have a mirrored configuration with respect to $_{80}$Hg across the $Z = 82$ magic shell closure. As such, many features of their nuclear levels are expected to be similar. In particular, the $_{84}$Po nuclear levels in the region from $N = 126$ down to $N = 116$ can be described as for the $_{80}$Hg isotopes, as well as the intrusion of a presumably prolate band [5]. A slight difference is found, however, in the ground-state band, as it appears to be affected by this intruding band, as seen in the lowering of the energy of 2^+, 4^+, 6^+, and 8^+ states for $N \leq 112$ [5].

Those excited band structures, and in particular the existence of many 0^+ states at low energy, provide a first insight into the phenomenon of shape coexistence. There are however many more nuclear observables that may be used to asses the nuclear configurations and their shapes, such as the ground-state properties, which will be discussed in this contribution, or the excited-state properties, e.g. from lifetime measurements [6] or Coulomb excitation studies [7].

Amongst the ground-state properties, the charge distribution and the electromagnetic moments are the most relevant to shape coexistence. Through the changes in the mean-square charge radii, it is possible to determine the shape of the ground state and long-lived isomers along nuclear isotopic chains. As an example, and important highlight, these studies have revealed a dramatic shape staggering in the $_{80}$Hg isotopes, where the even-A isotopes follow a weakly oblate trend, while the odd-A isotopes are prolate deformed for $N \leq 105$ [8]. In this case, the ground state does not exhibit configuration mixing, yet the staggering between the two configurations suggests a close proximity between the two different nuclear shapes.

The nuclear spin and electromagnetic moments provide additional information. The nuclear spin and magnetic dipole moment are very sensitive to the orbital occupancy of the valence nucleons, while the nuclear electric quadrupole moment is a probe of the static deformation of the nucleus, and thus its shape [9].

All those observables, namely the nuclear spin, nuclear electromagnetic moments, and changes in the mean-square charge radius, can be studied by means of laser spectroscopy [10, 11]. The electron is then used as a probe of the nucleus. The finite size of the nucleus has a perturbative effect on the electron energy level, typically to the order of 1 part in 10^6. High precision laser spectroscopy is required in order to achieve such a sensitive measurement on the electronic level.

In this contribution, the recent studies of the isotopes of $_{79}$Au, $_{81}$Tl, $_{82}$Pb, $_{83}$Bi, $_{84}$Po, $_{85}$At, and $_{87}$Fr around or towards $N = 104$ at CERN ISOLDE are reported.

*E-mail: thomas.cocolios@manchester.ac.uk

In-source laser spectroscopy

ISOLDE

The work reported in this contribution was performed at the CERN ISOLDE radioactive ion beam facility [12]. The radioactive isotopes are created by spallation reactions upon the impact of a 1.4 GeV proton beam (up to 2 μA on average) from the CERN PS-Booster onto a thick UC_x target (50 g/cm^2 of depleted ^{238}U). The target is maintained at high temperature ($\approx$ 2300 K) to enhance the diffusion and effusion of the reaction products towards the ion source.

The isotopes of interest are ionised using the Resonance Ionisation Laser Ion Source (RILIS) [13]. A series of laser beams are shone into the ion source so that resonant transitions excite a valence electron across the ionisation threshold of a given element. This approach is specific to a single element and provides high selectivity for the beam production. For the purpose of laser spectroscopy, one of these transitions is scanned across: upon resonance, the ionisation scheme is complete and the beam is ionised; off resonance, the scheme is incomplete and no beam is extracted [14]. The resonance spectrum is measured by monitoring the ion beam intensity as a function of the applied frequency.

Once ionised, the isotopes are accelerated up to 60 keV, separated in mass through a dipole magnet, and delivered to a detection setup. For the purpose of these studies, many setups have been used to address the various beam intensities, half-lives, decay properties, or beam purity.

The most intense beams, such as stable reference isotopes, or isotopes at the peak of the production cross section, are monitored using the current in a Faraday cup (FC) [15]. Some of the isotopes suffer however from high contamination or low production rate, and a more selective approach has to be undertaken.

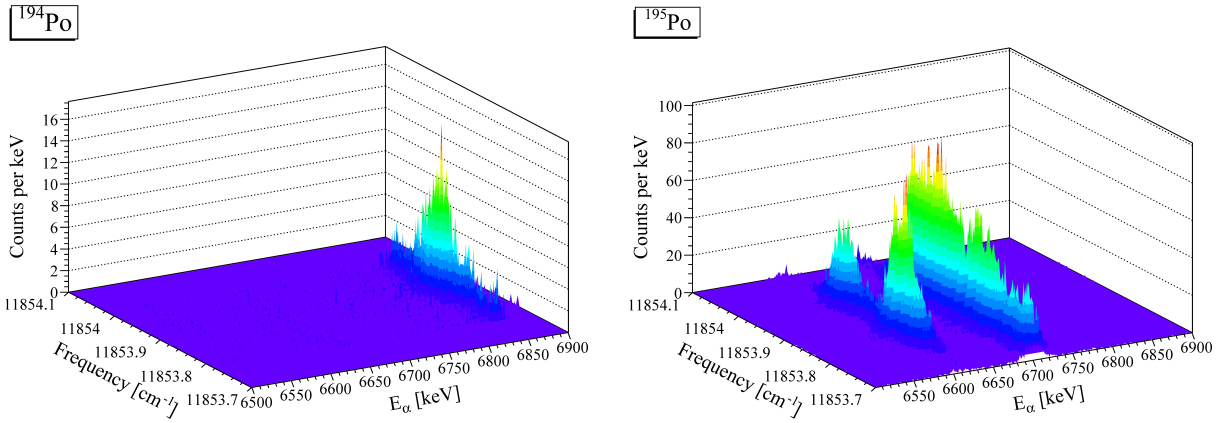

Fig. 1: Sample data from the Windmill: a set of α-decay energy spectra as a function of the applied laser frequency for ^{194}Po (left) and ^{195}Po (right). In the case of ^{195}Po, two different resonance spectra are found at different α-decay energies, corresponding to two isomers with $I^\pi = 3/2^-$ and $I^\pi = 13/2^+$ exhibiting different hyperfine structures.

One approach is to use the nuclear decay pattern of the isotope has an identification mechanism. Short-lived, α-decaying isotopes are studied with the Windmill decay setup [16], while $\beta\gamma$-decaying isotopes are studied with tape stations, such as the Orsay setup [17] or the ISOLDE yield station. A sample of the $_{84}$Po data is shown in Fig. 1. The half-life is a limiting factor for this approach, as long-lived isotopes might produce a low activity, resulting in poor statistics even if the beam intensity is high.

An alternative approach that combines selectivity and independence from the half-life has been found in the use of the ISOLTRAP Multi-Reflection Time-of-Flight Mass Spectrometer (MR-ToF-MS) [18]. By reflecting the ion beam across a short distance through many cycles, it is possible to let it travel up to 1 km, at the end of which the mono-energetic beam separates according to its mass, as the slightly heavier ions travel slower. It is then possible to count the isotopes with a multi-channel plate (MCP) detector and attribute each event to a different isotope based on its time of flight.

Even Z

The in-source laser spectroscopy technique has been used to study the even-Z isotopes $^{182-189}$Pb [22, 23]

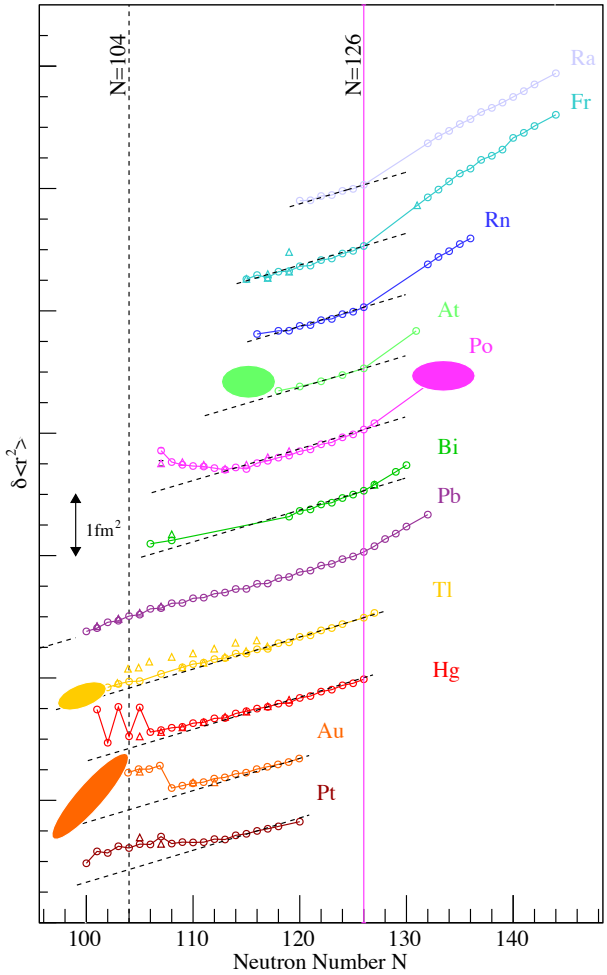

Fig. 2: Changes in the mean-square charge radii of the isotopes around $Z = 82$: $_{78}$Pt [19], $_{79}$Au [20], $_{80}$Hg [8], $_{81}$Tl [21], $_{82}$Pb [22, 23], $_{83}$Bi [24], $_{84}$Po [16, 25, 26], $_{85}$At [27], $_{86}$Rn [28], $_{87}$Fr [29, 30, 31], $_{88}$Ra [32]. Regions where results that are still under analysis are highlighted with an ellipse. The dotted lines along the data are the predictions for spherical nuclei [33]. The magic shell closure at $N = 126$ and the mid-shell at $N = 104$ are marked with vertical lines. The offset between the different isotopic chains is meant only for better display.

and $^{191-206,208-211,216-219}$Po [16, 25, 26, 34]. The resonance spectra and the discussion of the charge radii and electromagnetic moments may be found in the references. A compilation of the changes in the mean-square charge radii is shown in Fig. 2

The $_{82}$Pb isotopes remain close to the predictions from a spherical nucleus. This shows that, in spite of the proximity of the different shapes with each other, the ground-state of $_{82}$Pb around $N = 104$ is unaffected and maintains a pure spherical configuration [22]. The even-A $_{80}$Hg isotopes follow a similar trend, as their ground-state remain also unaffected by the proximity of the deformed shape, although the odd-A isotopes feature a prolate ground state [8]. Once again, however, the configurations are very pure and little mixing is expected between the different configurations.

The case of $_{84}$Po is in contrast to the picture presented by the $_{80}$Hg and $_{82}$Pb isotopes. A large departure in the charge radii is observed as early as $N = 116$ [25] and no shape staggering is observed between the even- and odd-A isotopes [26]. The electromagnetic moments of the odd-A isotopes suggest that the departure from the spherical trend arises from static deformation [16], although beyond mean-field calculations for the even-A isotopes suggest a rather soft nature of these isotopes with a strong mixing between oblate and prolate configurations [25]. The difference between the $_{80}$Hg and $_{84}$Po cases, while both possess the same number of valence nucleons, highlights the importance of the orbitals occupied by the nucleons.

Odd Z

The in-source laser spectroscopy programme at CERN ISOLDE has also recently addressed the odd-Z

isotopes $^{177-183}$Au, $^{179-184}$Tl, and $^{194-220}$At. The data are still under analysis.

The features of interest that will be addressed with these data will complement the study of the even-Z isotopes. The $_{79}$Au isotopes will be used to probe how far the prolate shapes extend beyond $N = 104$ [35]. The $_{81}$Tl isotopes will be used to determine whether a similar behaviour to that of $_{82}$Pb or $_{80}$Hg is followed, as well as the impact of isomerism arising from proton excitation across $Z = 82$. Finally, the $_{85}$At isotopes will be used to probe whether the early departure from sphericity in $_{84}$Pb is reproduced.

Collinear resonance ionisation spectroscopy

CRIS

Collinear resonance ionisation spectroscopy (CRIS) relies on the same principle as the in-source laser technique with the RILIS. The nuclear ground-state properties of a nucleus are determined by probing the electronic structure of the isotopes by means of resonance laser ionisation.

The specificity of the CRIS technique is that the excitation is performed in a collinear geometry on an accelerated beam [36]. In such a geometry, the broadening arising from the ion source temperature is compressed to a value below the natural linewidth of the atomic transition of interest, which allows greater precision to be reached than with in-source laser spectroscopy.

The radioactive ion beam is produced at ISOLDE using the same target and ion source configuration as for the RILIS. Any ISOLDE ion source may be used to deliver beams to the CRIS experiment; in the case of $_{87}$Fr, the surface ion source was chosen as the most practical and selective ion source. The beam is separated in mass through the high-resolution separator (HRS), cooled and bunched through ISCOOL [37], and delivered to the CRIS experiment. The bunched delivery is essential to overcome the duty cycle losses when using a pulsed laser beam system [38].

The CRIS beam line consists of a charge exchange cell where the ion beam is neutralised, a differential pumping region, an interaction region where the atom beam and the laser beams are overlapped, and a ion counting station equipped with an MCP detector [39, 40]. Similarly to the in-source study, additional selectivity may be required and a decay-spectroscopy station has been implemented as well [30, 41].

$_{87}$*Fr*

The CRIS experiment has been used to study the isotopes $^{202-206,218-219,229,231}$Fr [29, 30, 31]. The discussion of the data, their reduction to extract the nuclear observables, and the discussion of the changes in the mean-square charge radii and electromagnetic moments may be found in the references. Fig. 3 shows a sample of the CRIS $_{87}$Fr data. The changes in the mean-square charge radii are shown in Fig. 2.

The data exhibit a hint of departure from sphericity at $N = 116$ [29, 42] although the study of lighter isotopes is required to assert this observation.

A systematic study of the isomers in ^{206}Fr has revealed a dramatic shape staggering of the $I^\pi = 10^-$ isomer [30]. Although similar isomers are found in ^{202,204}Fr, as well as in $_{85}$At, $_{83}$Bi, and $_{81}$Tl, there are no evidence of such a deformed $I^\pi = 10^-$ state in any of these cases. This will be the subject of a forthcoming campaign at the CRIS experiment.

Shape changes are also found in odd-Z nuclei in this region as resulting from an intruding $I^\pi = 1/2^-$ state, arising from the excitation of a proton from the $p_{1/2}$ orbital across $Z = 82$. Such states have been observed in the neutron-rich isotopes ^{229,231}Fr [31] and pave the way to the forthcoming study of the neutron-deficient isotopes ^{201,203}Fr.

CONCLUSIONS & OUTLOOKS

An extensive programme has been on-going at CERN ISOLDE to study the ground-state properties of the isotopes around $Z = 82$ and characterise the extent of shape coexistence, and its impact on the ground-state of these isotopes. In the even-Z isotopes, the $_{82}$Pb isotopes remain spherical in spite of the variety of shapes present at low excitation energy. The $_{84}$Pb isotopes exhibit a completely different behaviour with respect to the $_{80}$Hg isotopes, although they mirror each other across $Z = 82$. New data is also available for the odd-A isotopes in the region, although most are still under analysis or require further studies to reach the region of interest.

Decay spectroscopy data were also acquired alongside the laser spectroscopy data [4, 17, 30, 46, 47]

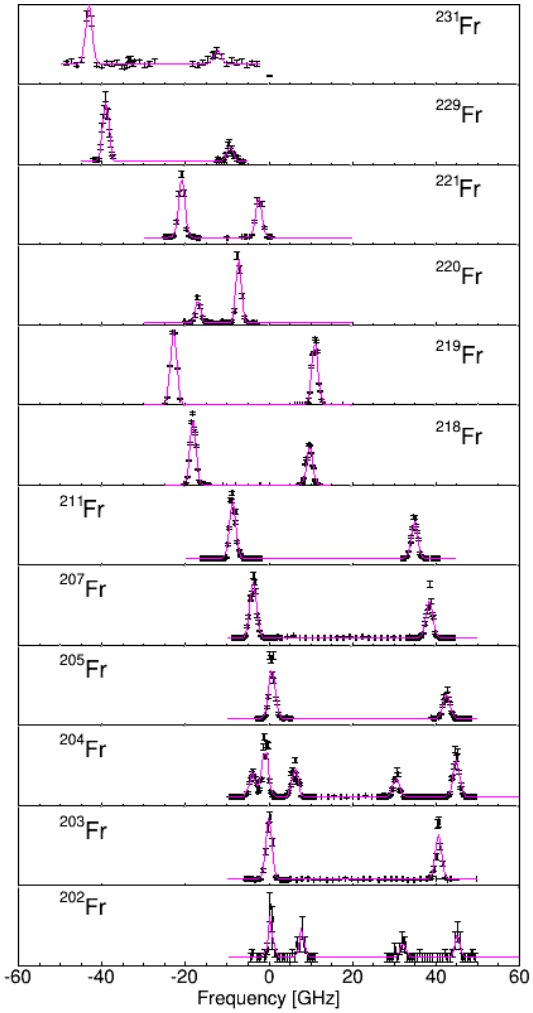

Fig. 3: Sample data from CRIS with the MCP detector.

and provide important complementary data on the low-excitation nuclear levels in the region. Additionally, Coulomb excitation experiments have been performed at REX ISOLDE on $_{80}$Hg [7], $_{82}$Pb, and $_{84}$Po. Transfer reactions and multiple Coulomb excitation studies are now foreseen at the HIE ISOLDE facility in the years to come.

ACKNOWLEDGMENT:
The author would like to acknowledge the contribution of the CRIS, ISOLTRAP, RILIS, and Windmill Collaborations to this work, and the ISOLDE Collaboration for providing excellent beams. This work was supported by FWO-Vlaanderen (Belgium), by GOA/2010/010 (BOF-KULeuven), by the IUAP-Belgian State Belgian Science Policy (BRIX network P7/12), by the UK Science and Technology Facilities Council (STFC), by the Slovak Research and Development Agency (contract No. APVV-0105-10), by the Slovak grant agency VEGA (Contract No. 1/0576/13), by the Bundesministerium für Bildung und Forschung (BMBF, Germany) within the Wolfgang-Gentner fellowship programme as well as through the consecutive project fundings of 06Mz9181I, 06Mz7177D and 05P12UMCIA, and by the European commission within FP7 (ENSAR No. 262010). The author was supported by STFC Ernest Rutherford Fellowship grant No. ST/J004189/1.

REFERENCES

[1] K. Heyde and J. L. Wood. Shape coexistence in atomic nuclei. *Rev. Mod. Phys.*, 83:1467–1521, 2011.
[2] A. N. Andreyev et al. A triplet of differently shaped spin-zero states in the atomic nucleus ^{186}Pb. *Nature*, 405:430–433, 2000.
[3] R. Julin, K. Helariutta, and M. Muikku. Intruder states in very neutron-deficient Hg, Pb and Po nuclei. *J. Phys. G*, 27:R109–R139, 2001.

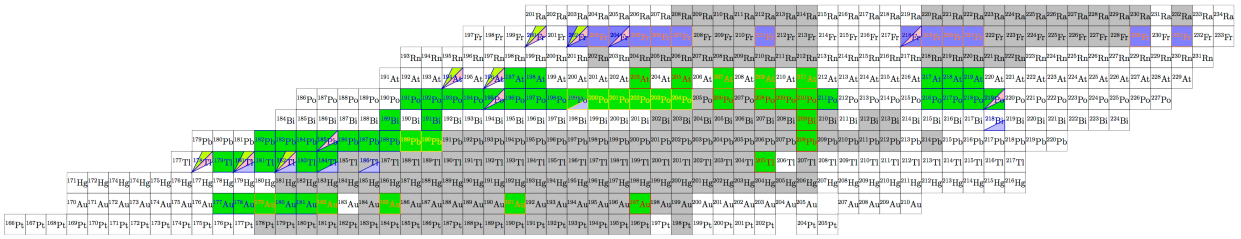

Fig. 4: Summary of the isotopes studied in this programme. Green isotopes were studied with the RILIS, blue isotopes with the CRIS experiment. Blue text refers to α detection, yellow text to $\beta\gamma$ detection, and red text to ion counting (FC or MCP). Blue triangles highlight β-decay spectroscopy studies, pink triangles α-decay spectroscopy studies, and light green triangles β-delayed fission studies [43, 44, 45].

[4] J. Elseviers et al. Shape coexistence in ^{180}Hg studied through the β decay of ^{180}Tl. *Phys. Rev. C*, 84:034307, 2011.

[5] K. Van de Vel et al. In-beam γ-ray spectroscopy of ^{190}Po: first observation of a low-lying prolate band in Po isotopes. *Eur. Phys. J. A*, 17:167–171, 2003.

[6] L. P. Gaffney et al. Shape coexistence in neutron-deficient Hg isotopes studied via lifetime measurements in ^{184,186}Hg and two-state mixing calculations. *Phys. Rev. C*, 89:024307, 2014.

[7] N. Bree et al. Shape coexistence in the neutron-deficient even-even $^{182-188}$Hg isotopes studied via Coulomb excitation. *Phys. Rev. Lett.*, 112:162701, 2014.

[8] G. Ulm et al. Isotope shift of ^{182}Hg and an update on nuclear moments and charge radii in the isotope range $^{181-206}$Hg. *Z. Phys. A*, 325:247–259, 1986.

[9] G.. Neyens. Nuclear magnetic and quadrupole moments for nuclear structure research on exotic nuclei. *Rep. Prog. Phys.*, 66:633–689, 2003.

[10] B. Cheal and K. T. Flanagan. Progress in laser spectroscopy at radioactive ion beam facilities. *J. Phys. G*, 37:113101, 2010.

[11] K. Blaum, J. Dilling, and W. Nörterhäuser. Precision atomic physics techniques for nuclear physics with radioactive beams. *Phys. Scripta*, T152:014017, 2013.

[12] B. Jonson and A. Richter. More than three decades of ISOLDE physics. *Hyperfine Interact.*, 129:1, 2000.

[13] V. N. Fedosseev, G. Huber, U. Köster, J. Lettry, V. I. Mishin, H. Ravn, and V. Sebastian. The ISOLDE laser ion source for exotic nuclei. *Hyperfine Interact.*, 127:409–416, 2000.

[14] V. N. Fedosseev, Yu. Kudryavtsev, and V. I. Mishin. Resonance laser ionization of atoms for nuclear physics. *Phys. Scripta*, 85:058104, 2012.

[15] B. A. Marsh et al. New developments of the in-source spectroscopy method at RILIS/ISOLDE. *Nucl. Inst. and Meth. B*, 317:550–556, 2013.

[16] M. D. Seliverstov, T. E. Cocolios, et al. Electromagnetic moments of odd-A $^{191-203,211}$Po isotopes. *Phys. Rev. C*, 89:034323, 2014.

[17] J. Sauvage et al. Nuclear structure of ^{189}Tl states studied via β^+/EC decay and laser spectroscopy of $^{189m+g}$Pb. *Eur. Phys. J. A*, 39:33–48, 2009.

[18] S. Kreim et al. Recent exploits of the ISOLTRAP mass spectrometer. *Nucl. Inst. and Meth. B*, 317:492–500, 2013.

[19] F. Le Blanc et al. Large odd-even radius staggering in the very light platinum isotopes from laser spectroscopy. *Phys. Rev. C*, 60:054310, 1999.

[20] F. Le Blanc et al. Nuclear moments and deformation change in ^{184}Au^{g,m} from laser spectroscopy. *Phys. Rev. Lett.*, 79:2213, 1997.

[21] A. E. Barzakh et al. Changes in the mean-square charge radii and magnetic moments of neutron-deficient Tl isotopes. *Phys. Rev. C*, 88:024315, 2013.

[22] H. De Witte et al. Nuclear charge radii of neutron deficient lead isotopes beyond N=104 mid-shell investigated by in-source laser spectroscopy. *Phys. Rev. Lett.*, 98:112502, 2007.

[23] M. D. Seliverstov et al. Charge radii and magnetic moments of odd-A $^{183-189}$Pb isotopes. *Eur. Phys. J. A*, 41:315–321, 2009.

[24] B. A. Marsh. *In-Source Laser resonance Ionization at ISOL Facilities*. PhD thesis, The University of Manchester, 2007.

[25] T. E. Cocolios, W. Dexters, M. D. Seliverstov, et al. Early onset of ground state deformation in neutron deficient polonium isotopes. *Phys. Rev. Lett.*, 106:052503, 2011.

[26] M. D. Seliverstov, T. E. Cocolios, et al. Charge radii of odd-A ^{191211}Po isotopes. *Phys. Lett. B*,

719:362–366, 2013.
[27] S. Rothe et al. Measurement of the first ionization potential of astatine by laser ionization spectroscopy. *Nature Comm.*, 4:1835, 2013.
[28] W. Borchers, R. Neugart, E. W. Otten, H. T. Duong, G. Ulm, and K. Wendt. Hyperfine structure and isotope shift investigations in $^{202-222}$Rn for the study of nuclear structure beyond $Z = 82$. *Hyperfine Interact.*, 34:25, 1987.
[29] K. T. Flanagan et al. Collinear resonance ionization spectroscopy of neutron-deficient francium isotopes. *Phys. Rev. Lett.*, 111:212501, 2013.
[30] K. M. Lynch et al. Decay-assisted laser spectroscopy of neutron-deficient francium. *Phys. Rev. X*, 4:011055, 2014.
[31] I. Budinčević et al. Laser spectroscopy of francium isotopes at the borders of the region of reflection asymmetry. *Phys. Rev. C*, 90:014317, 2014.
[32] K. Wendt, S. A. Ahmad, W. Klempt, R. Neugart, E. W. Otten, and H. H. Stroke. On the hyperfine structure and isotope shift of radium. *Z. Phys. D*, 4:227–241, 1987.
[33] W. D. Myers and K. H. Schmidt. An update on droplet-model charge distributions. *Nucl. Phys. A*, 410:61–73, 1983.
[34] D. A. Fink, T. E.. Cocolios, et al. In-source laser spectroscopy with the Laser Ion Source and Trap: First direct study of the ground-state properties of ^{217,219}Po. in preparation for Phys. Rev. X, 2015.
[35] J. L. Wood, E. F. Zganjar, C. De Coster, and K. Heyde. Electric monopole transitions from low energy excitations in nuclei. *Nucl. Phys. A*, 651:323–368, 199.
[36] Yu. A. Kudriavtsev and V. S. Letokhov. Laser method of highly selective detection of rare radioactive isotopes through multistep photoionization of accelerated atoms. *App. Phys. B*, 29:219, 1982.
[37] E. Mané et al. An ion cooler-buncher for high-sensitivity collinear laser spectroscopy at ISOLDE. *Eur. Phys. J. A*, 42:503–507, 2009.
[38] Ch. Schulz et al. Resonance ionization spectroscopy on a fast atomic ytterbium beam. *J. Phys. B*, 4831-4844:24, 1991.
[39] T. J. Procter et al. Development of the CRIS (collinear resonant ionisation spectroscopy) beam line. *J. Phys. Conf. Series*, 381:012070, 2012.
[40] T. E. Cocolios et al. The collinear resonance ionization spectroscopy (CRIS) experimental setup at CERN-ISOLDE. *Nucl. Inst. and Meth. B*, 317:565–569, 2013.
[41] M. M. Rajabali, K. M. Lynch, et al. A dedicated decay-spectroscopy station for the collinear resonance ionization experiment at ISOLDE. *Nucl. Inst. and Meth. A*, 707:35–39, 2013.
[42] A. Voss, M. Pearson, et al. First use of high-frequency intensity modulation of narrow-linewidth laser light and its application in determination of ^{206,205,204}Fr ground-state properties. *Phys. Rev. Lett.*, 111:122501, 2013.
[43] A. N. Andreyev, J. Elseviers, et al. New type of asymmetric fission in proton-rich nuclei. *Phys. Rev. Lett.*, 105:252502, 2010.
[44] J. Elseviers et al. β-delayed fission of ^{180}Tl. *Phys. Rev. C*, 88:044321, 2013.
[45] L. Ghys et al. Triple-humped fission-fragment mass distributions in the neutron-deficient lead region. *Phys. Rev. C*, 90:041301(R), 2014.
[46] T. E. Cocolios et al. Structure of ^{191}Po from α- and β-decay spectroscopy. *J. Phys. G*, 37:125103, 2010.
[47] T. E. Cocolios et al. Early onset of deformation in the neutron-deficient polonium isotopes. *J. Phys. Conf. Series*, 381:012072, 2012.

SHAPES AND COLLECTIVITY IN HEAVY NUCLEI – PROBED WITH RADIOACTIVE BEAMS AT REX-ISOLDE

J. Pakarinen[1,2]*
on behalf of the IS494 and S07 collaborations

[1]Department of Physics, University of Jyväskylä, FI-40014, Jyväskylä, Finland
[2]Helsinki Institute of Physics, FI-00014, Helsinki, Finland

Abstract

In recent years, a broad range of neutron deficient even-mass heavy nuclei around Z=82 have been studied in Coulomb excitation measurements employing the Miniball spectrometer and radioactive beams from REX-ISOLDE, CERN. These nuclei are of particular interest as they lie in a region where the intruding structures, associated with different deformed shapes, come down in energy close to the spherical ground state. These experiments alone can provide important information on nuclear structure, but complementary experiments using stable ion beams and fusion evaporation can provide essential constraints for detailed analysis of Coulomb excitation data.

INTRODUCTION

The atomic nucleus represents one of the fundamental building blocks of matter in the universe. It takes its place between the atom and the hadron in a chain of basic constituents that stretches from quarks to galaxies. Nuclei may consist of up to almost 300 nucleons, resulting in a rich variety of quantum phenomena. It is the task of nuclear structure physics to unravel this myriad of quantum structure and to find the ordering principles governing nuclei. This endeavour is very broad in scope, mirroring fields such as solid state physics, atomic structure physics and atomic collision physics in which the Coulomb interaction is accompanied by the much more complicated strong interaction. When it comes to the nuclear structure and dynamics, the Nuclear Physics European Collaboration Committee has formulated a list of key questions that are waiting for answers [1]:

- How can we describe the rich variety of low-energy structure and reactions of nuclei in terms of the fundamental interactions between individual particles?
- How can we predict the evolution of nuclear collective and single-particle properties as functions of mass, iso-spin, angular momentum and temperature?
- How do regular and simple patterns emerge in the structure of complex nuclei?
- What are the key variables governing the dynamics between colliding composite systems of nucleons?

A correspondingly versatile set of tools, both theoretical and experimental, are still required to advance our understanding of this diverse field. One of the richest regions where these questions can be addressed, is formed by very neutron-deficient nuclei with the proton number Z close to the magic 82 and the neutron number N close to 104 [2, 3, 4, 5, 6], where the interplay between single-particle motion, collectivity and pairing can be seen as a rich tapestry of coexisting nuclear shapes and exotic excitations [2].

Fundamentally, shapes are concrete and easy to understand. In nature, one can often find objects with symmetries that can be defined in terms of multipole order. For example, a spherical orange can be associated with monopole (λ=1) shape, whereas a melon typically finds a prolate, quadrupole deformed shape (λ=2). Similarly, these shapes can be found in atomic nuclei, but unlike typical macroscopic objects, atomic nuclei do not present a well-defined boundaries nor surface. However, lots of efforts have been put in to understanding what are the underlying forces that drive nucleus in to deformation. Relevant to this presentation, three different shapes have been defined in ^{188}Pb [7].

Collectivity is more difficult to be expressed quantitatively. Collective motion can be observed in many different domains. Stock market dynamics shows correlations over financial disciplines, whereas flocking is a fascinating phenomenon in nature. While the fluctuations of plasma represent the collective behaviour governed by the electromagnetic forces, a similar statistical approach can not be applied to the atomic

*E-mail: janne.pakarinen@jyu.fi

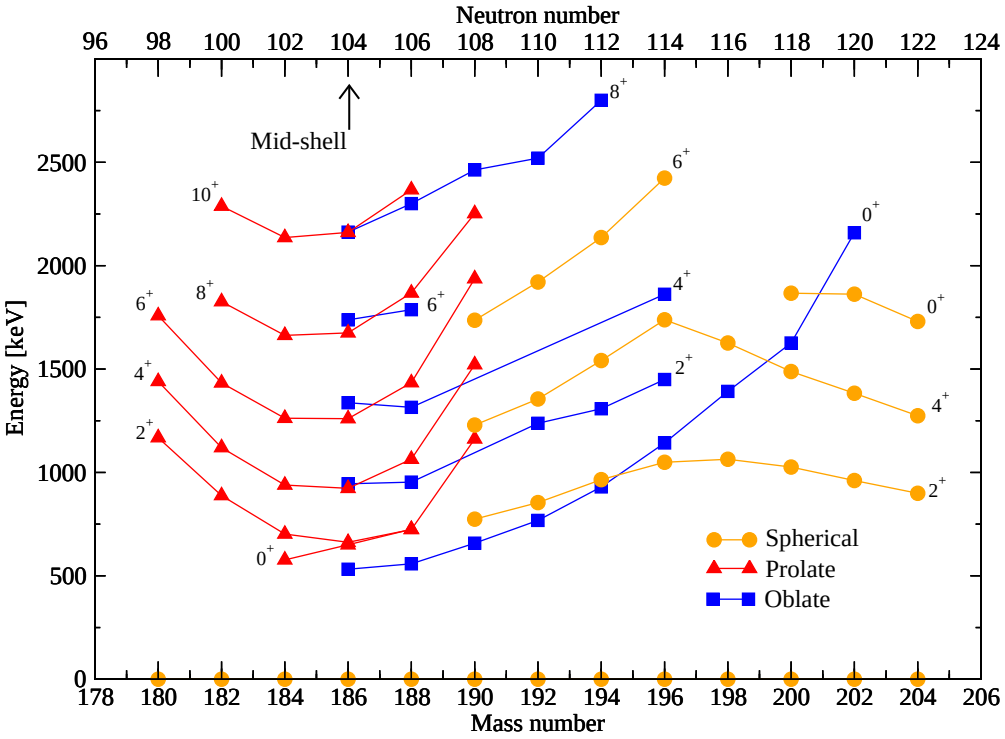

Fig. 1: Level energy systematics of the even-mass Pb isotopes. Data taken from [8] and references therein.

nucleus. Yet, the number of nucleons in atomic nuclei often results in a many body problem that can not be solved explicitly.

In this presentation, our recent efforts in studies of shapes and collectivity in ^{188}Pb have been briefly described.

^{188}Pb AS A CASE STUDY

The level energy systematics of even-mass Pb isotopes is shown in Fig. 1. The 0^+ state of the π(2p-2h) configuration is associated with an oblate shape. It intrudes down in energy close to the spherical ground state when approaching the neutron mid-shell at N=104 and becomes the first excited state already at A=194. The onset of prolate deformation, mainly associated with the π(4p-4h) configuration, can be seen around A=190 for states with $I^\pi \leq 4^+$. The prolate states with $I^\pi \geq 4^+$ form the yrast band at A=188.

However, there is no clear consensus regarding the level energies of the proposed oblate and prolate bandheads in ^{188}Pb. The first excited 0^+ state (oblate) has strong arguments both from the α-decay studies and in-beam work to be at 591keV [9, 10, 11] (it should be noted that its transition energy overlaps with the $4_2^+ \rightarrow 2_1^+$ transition energy), whereas two different candidates have been proposed for the 0_3^+ state [11, 12]. On the other hand, no evidence supporting the existence of the 0_3^+ state (prolate) was provided by Van de Vel [10]. Regardless of these ambiguities, it is evident that the light Pb isotopes provide a unique laboratory to study the three competing structures of different shapes below 1MeV. In order to establish a complete picture of shape coexistence in this nucleus and in this region, knowledge of transition probabilities from nuclear states assigned with different shapes is essential. Transition probabilities are very sensitive to the details of a nuclear wave function and, consequently, information about nuclear shape and configuration mixing can be inferred. Furthermore, the knowledge of the nuclear wave functions renders it possible to extract an effective nucleon-nucleon interaction to produce a realistic nuclear potential. Therefore, we have carried out two experiments to probe different shapes, collectivity and locations of the bandhead states in ^{188}Pb:

1. Coulomb excitation experiment using radioactive ion beam and

2. simultaneous in-beam γ-ray conversion electron spectroscopy employing fusion evaporation reaction.

The Coulomb excitation experiment was performed at the REX-ISOLDE facility, CERN [13]. The nuclei of interest were produced by bombarding a high temperature UC_x target with 1.4GeV, up to 2μA proton beam provided by PS-Booster and extracted employing the RILIS laser ion source [14]. Subsequently,

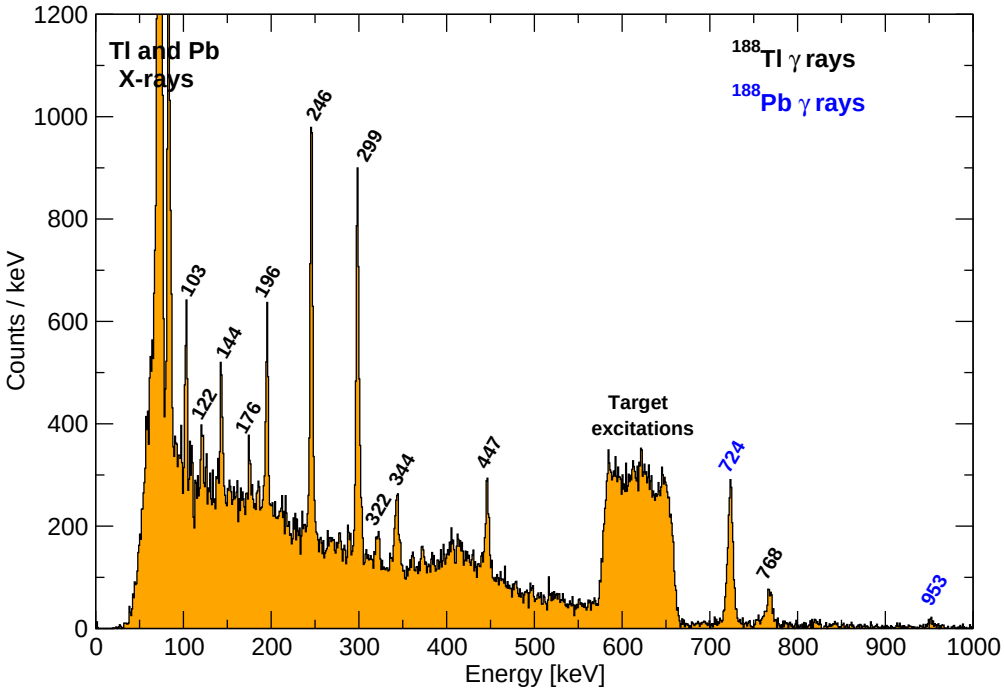

Fig. 2: γ-ray energy spectrum in coincidence with the scattered particles, Doppler corrected for the A=188 projectile nuclei, recorded in the IS494 experiment. Transitions belonging to ^{188}Pb and to the contaminant ^{188}Tl nuclei have been labelled in blue and black, respectively.

they were mass selected utilising the high resolution separator before being delivered to the REXTRAP-REXEBIS for charge breeding. Finally, the REX-ISOLDE post-accelerator was employed to deliver radioactive ion beams of ^{188}Pb at 2.82MeV/u to the Miniball spectrometer [15]. At Miniball, the radioactive beam was impinging on a 2mg/cm^2 thick ^{112}Cd target. The average beam intensity on the Miniball target was 3.2×10^5pps and the beam purity $\sim$55%. The scattered projectile- and target-like nuclei were detected with the CD detector at $\sim$30mm downstream from the target. The γ rays from the decay of the Coulomb excited states were recorded with the Miniball Ge-detector array [15]. The relatively high granularity of Miniball and the CD detector allowed for kinematic correction to be made.

The γ-ray energy spectrum in coincidence with scattered particles in the low centre-of-mass angles, Doppler corrected for projectile-like particles, is shown in Fig. 2. Two γ-ray lines can be associated with ^{188}Pb, whereas the other γ-ray lines originate from the excitation of ^{188}Tl impurities in beam. By using the laser on/off technique, one can extract the amount of target excitations arising from reactions with ^{188}Tl. Preliminary analysis suggests that the transition strengths for the first and second excited 2^+ states in ^{188}Pb isotopes can be extracted. The analysis is still in progress and final results will be published later.

A complementary experiment (S07), simultaneous in-beam γ-ray conversion electron spectroscopy was carried out in the Accelerator Laboratory of the University of Jyväskylä with a view on probing the enhanced E0 components of the inter-band transitions and the feeding and location of the bandhead 0^+ states. A beam of ^{32}S ions was accelerated to an energy of 165MeV and used to populate excited states in ^{188}Pb via the ^{160}Dy(^{32}S,4n)^{188}Pb fusion-evaporation reaction. The ^{160}Dy target had a thickness of 500μg/cm^2. The average beam current was 13pnA, yielding an average recoil implantation rate of 1.3kHz at the focal plane.

Prompt γ-rays and conversion electrons were observed using the SAGE spectrometer [16]. Fusion–evaporation residues were separated from the primary beam using the RITU gas-filled separator [17]. The GREAT spectrometer [18] was employed at the focal plane. Implanted evaporation residues and their subsequent α decays were detected by two double-sided silicon strip detectors (DSSDs) of high granularity. A transmission multiwire proportional counter placed upstream of the DSSDs was used to obtain energy loss and time-of-flight information for the recoils. Data were collected using the triggerless, fully digital total data readout data acquisition system [19]. The temporal and spatial correlations of the data were performed using the GRAIN software package [20].

Preliminary results are shown in Fig. 3. The top spectrum shows projection of recoil-gated γe^--matrix on to the γ-axis. In addition to transitions associated with ^{188}Pb, transitions arising from the decay of the excited states in other fusion evaporation reaction products can be seen. In the bottom, recoil-gated electron energy spectrum in coincidence with the 724keV γ-ray transition is shown. The most prominent electron

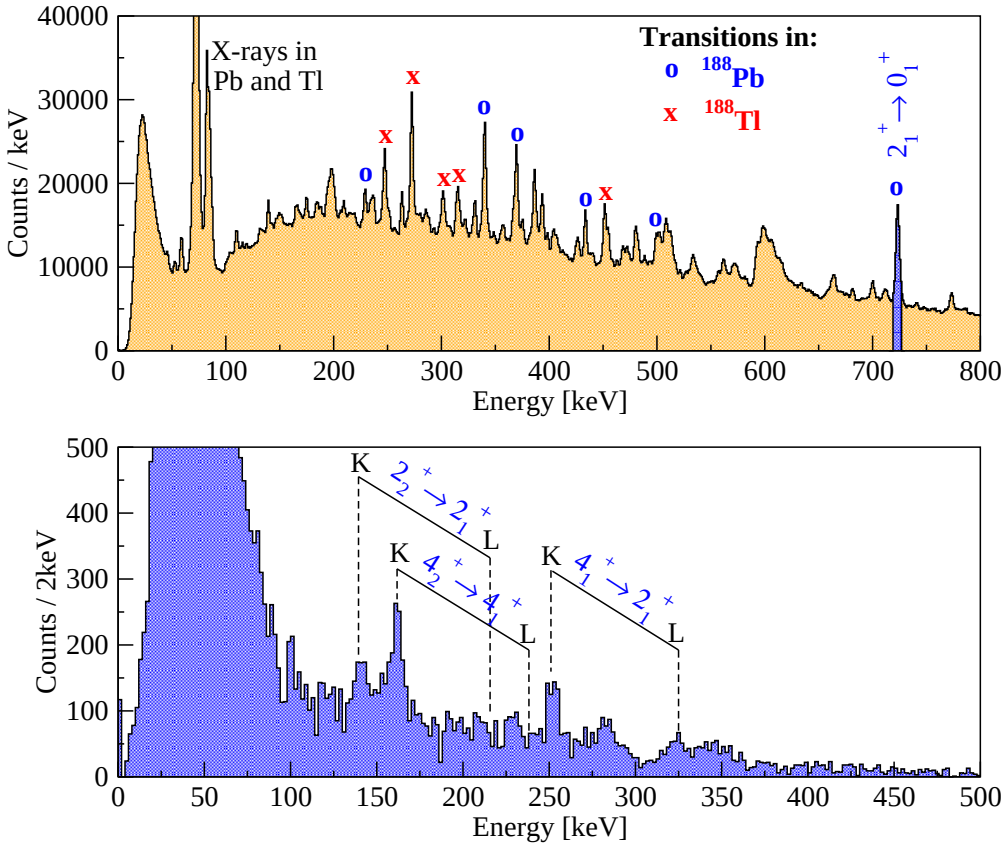

Fig. 3: SAGE data for ^{188}Pb. Top panel: projection of the recoil-gated γe^--matrix onto the γ-axis. Peaks associated with ^{188}Pb and ^{188}Tl have been labelled. Bottom panel: conversion electron energy spectrum obtained by gating on the yrast 2^+ to 0^+ transition (marked as blue on the top spectrum).

lines have been labelled. While for the yrast $4_1^+ \rightarrow 2_1^+$ transition both the K and L conversion electron peaks can be identified, only the K conversion electron peaks are clearly seen for the inter-band $2_1^+ \rightarrow 2_1^+$ and $4_1^+ \rightarrow 4_1^+$ transitions suggesting remarkable E0 components in these transitions. The precise values of the E0/M1/E2 multipole mixing ratios for the inter-band transitions can set vital constraints for the analysis of Coulomb excitation data using coupled-channel Coulomb excitation least-squares search code, GOSIA [21]. This will be even more important for the data obtained at HIE-ISOLDE, where higher beam energies will allow access to experiments with higher multistep Coulomb excitations cross-sections. Preliminary analysis of the ^{188}Pb SAGE data also shows evidence for the excited 0^+ state at 591keV, however, a real challenge in the analysis is to firmly associate events with ^{188}Pb. Our next objective in studies of the ^{188}Pb nucleus is to exploit the SPEDE spectrometer [22]. SPEDE will allow simultaneous γ-ray conversion electron spectroscopy employing Coulomb excitation in radioactive ion beams at HIE-ISOLDE.

CONCLUSIONS

Despite the huge amount of experimental and theoretical efforts, more studies are needed for better understanding of the shape coexistence, configuration mixing and collectivity in the neutron-deficient Z∼82 nuclei. The advent of radioactive ion beam facilities have allowed these nuclei to be investigated by employing the Coulomb excitation methods. Albeit the radioactive odd-mass ion beams in this region are available, the studies employing those beams remain unexplored. Meanwhile, the exploitation of transfer reactions in this region is seen as an important next step. The technical and methodological developments have pushed the frontier of nuclei accessible using stable ion beams further. As a result of recent progress, the number of feasible experimental cases has increased. The capability to probe further will advance our understanding of these intriguing exotic phenomena.

ACKNOWLEDGMENT:
The staff members of the REX-ISOLDE and JYFL facilities are gratefully acknowledged for providing smooth running conditions. This research project has been supported by a Marie Curie Career Integration Grant of

the European Community's 7th Framework Programme (project number 304033) and Academy of Finland (decision number 257562).

REFERENCES

[1] Perspectives of Nuclear Physics in Europe, NuPECC Long Range Plan 2010, www.nupexx.org
[2] K. Heyde and J. L. Wood, Rev. Mod. Phys. **83**, 1467 (2011).
[3] P. Van Duppen et al., Phys. Rev. Lett. **52**, 1974 (1984).
[4] A. N. Andreyev et al., Nature (London) **405**, 430 (2000).
[5] R. Julin, K. Helariutta, and M. Muikku, J. Phys. G **27**, R109 (2001).
[6] H. De Witte et al., Phys. Rev. Lett. **98**, 112502 (2007).
[7] G.D. Dracoulis et al., Phys. Rev. C **67**, 051301(R) (2003).
[8] J. Pakarinen et al. Phys. Rev C. **75**, 014302 (2007).
[9] A.N. Andreyev et al., J. Phys. G: Nucl. Part. Phys. **25**, 835 (1999).
[10] K. Van de Vel et al., Phys. Rev. C **68**, 054311 (2003).
[11] Y. Le Coz et al., EPJdirect A **3**, 1-6 (1999).
[12] R.G. Allatt et al., Phys Lett. B **437**, 29 (1998).
[13] O. Kester et al., Nucl. Instrum. Methods B **204**, 20 (2003).
[14] V. N. Fedoseyev et al., Hyperfine Interact. **127**, 409 (2000).
[15] N. Warr et al., Eur. Phys. J. A **49**, 40 (2013).
[16] J. Pakarinen et al., Eur. Phys. J. A **50**, 53 (2014).
[17] M. Leino et al., Nucl. Instrum. Methods Phys. Res. B **99**, 653 (1995).
[18] R. D. Page et al., Nucl. Instrum. Methods Phys. Res. B **204**, 634 (2003).
[19] I. H. Lazarus et al., IEEE Trans. Nucl. Sci. **48**, 567 (2001).
[20] P. Rahkila, Nucl. Instrum. Methods Phys. Res. A **595**, 637 (2008).
[21] D. Cline, Nucl. Phys. A **557**,615634 (1993).
[22] P. Papadakis et al., submitted to JPS Conference Proceedings, http://jpscp.jps.jp/ (2014)

COULOMB EXCITATION AND ONE-NEUTRON TRANSFER STUDIES OF STABLE AND RADIOACTIVE NUCLEI AT HRIBF-ORNL*

J.M. Allmond[1,†]

[1]Physics Division, Oak Ridge National Laboratory, Oak Ridge, Tennessee 37831, USA

Abstract

Several stable and radioactive nuclei ranging from $A = 58$ to 208 were recently studied in inverse kinematics by Coulomb excitation and heavy-ion induced one-neutron transfer at the Holifield Radioactive Ion Beam Facility of Oak Ridge National Laboratory. These studies used CsI(Tl) and HPGe detector arrays to detect scattered charged particles and emitted γ rays from the in-beam reactions. A Bragg-curve detector was used to measure the energy loss of the various beams through the targets and to measure the radioactive beam compositions. Stable nickel, strontium, zirconium, molybdenum, tin, tellurium, and lead isotopes and neutron-rich radioactive tin and tellurium isotopes were among the nuclei recently studied. Coulomb excitation was used to measure the electromagnetic moments of the first excited states and heavy-ion induced one-neutron transfer was used to measure the absolute cross sections and lifetimes of the excited single-particle states. A sample of these results are presented here with an emphasis on the tin isotopes. In particular, a survey of the Bragg-curve measurements, Doppler corrections, and inconclusive $i_{13/2}$ candidate in ^{133}Sn is presented.

INTRODUCTION

The advent of radioactive beams has brought about a revival in the interest of shell closures and the emergence of collectivity in atomic nuclei. A leading question has been - "Are the shell closures at Z or N equal to 2, 8, 20, 28, 50, 82, or 126 maintained for exotic nuclei with extreme proton-to-neutron ratios?". There has been progress towards this question for a few exotic regions. For instance, radioactive ^{132}Sn with $Z = 50$, $N = 82$ has been determined to be a good double-shell closure [1, 2, 3, 4]. On the other hand, a breakdown of the $N = 20$ shell closure in ^{31}Na [5] and ^{32}Mg [6], and $N = 28$ shell closure in ^{44}S [7, 8, 9, 10] has been observed.

Two powerful tools for probing the shell structure and collectivity of both stable and radioactive nuclei are Coulomb-excitation and heavy-ion induced transfer reactions in inverse kinematics using particle-γ coincidence spectroscopy. Advantages of these two techniques include: (1) relatively large cross sections, (2) use of thick, pure, self-supporting targets, (3) excellent energy resolution from Doppler-corrected γ rays, and (4) abundant spectroscopic information from particle-γ correlations. Safe Coulomb excitation can be used to measure the electromagnetic moments of excited states, which probe the shape and coherent motion of the nucleons. Sub-barrier heavy-ion induced transfer can be used to measure the absolute cross sections and lifetimes of excited states, which probe the purity of the single-particle states. These techniques were recently employed at the Holifield Radioactive Ion Beam Facility (HRIBF) of Oak Ridge National Laboratory (ORNL) to study the stable nickel, strontium, zirconium, molybdenum, tin, tellurium, and lead isotopes and neutron-rich radioactive tin and tellurium isotopes. Coulomb excitation results of ^{130,134}Te [11] and ^{58,60,62,64}Ni [12] were recently published. These studies were based on seminal single-step Coulomb excitation studies of radioactive Te isotopes by Radford *et al.* [13] and Stone *et al.* [14]. Sub-barrier heavy-ion induced transfer results with radioactive ^{132}Sn and stable ^{208}Pb beams were recently published [4]. This study was based on a seminal heavy-ion induced transfer study of radioactive ^{134}Te by Radford *et al.* [15] and Allmond *et al.* [16]. A sample of the recent Coulomb excitation and heavy-ion induced transfer results from HRIBF-ORNL are presented here with an emphasis on the tin isotopes. In particular, a survey of the Bragg-curve measurements, Doppler corrections, and inconclusive $i_{13/2}$ candidate in ^{133}Sn are presented.

EXPERIMENTAL SETUP

Stable and radioactive beams were provided by HRIBF-ORNL with energies ranging from 1.8 to 3.0 MeV per nucleon. A Bragg detector at zero degrees was used to measure the energy loss of the beam through the

†E-mail: allmondjm@ornl.gov

target and to measure the radioactive beam compositions. The Bragg detector was calibrated by measuring direct beam from the 25-MV tandem at multiple energies, which was achieved quickly by dropping charge states while keeping the magnetic rigidity fixed (i.e., using analog beams). Recoiling target nuclei were detected in the "bare" HyBall (BareBall) CsI(Tl) array [17], using the first four rings at laboratory angles 7°-14°, 14°-28°, 28°-44°, and 44°-60° relative to the beam direction. Coincident γ rays were detected in the CLARION array of 11 Compton suppressed, segmented HPGe Clover detectors [18], which was configured (nominally) with five detectors at 90°, four at 132°, and two at 154°. The Clover detectors were at a distance of 21.75 cm from the target with a total efficiency of 3.00(5)% at 1 MeV. The experimental trigger required either a scaled-down particle event or a particle-γ coincidence event. The trigger type was recorded for each event in a bit register to cleanly distinguish particles from the scaled-down trigger and particle-γ trigger. For stable beams, a relatively low beam intensity of $\sim$ 5 pA was used to prevent target degradation and to maintain a data acquisition livetime of $\geq$ 99%.

BRAGG DETECTOR MEASUREMENTS

The energy loss of a beam through a target, which can be measured with a Bragg-curve detector, is a critical component to absolute cross section measurements and comparison with theory. A tabulation of energy losses for various beam and target combinations is provided in Table 1. Energy loss calculations based on the nominal target thicknesses and stopping powers can result in up to 40% uncertainties. It is essential that the beam energy loss through the target be measured. A few example Bragg-curve measurements are provided below.

Tab. 1: Calculated versus measured energy losses for various beam and target combinations.

Beam	E_{beam} (MeV)	Target	Thickness (mg/cm^2)	E_{loss}^{calc} (MeV) [19]	E_{loss}^{exp} (MeV)
^{58}Ni	104.4	C	1.01	39	43(1)
^{60}Ni	108	C	1.01	39	42(1)
^{112}Sn	324.8	C	1.01	69	79(2)
^{114}Sn	330.6	C	1.01	69	78(2)
^{130}Te	390	C	1.01	72	86(1)
^{114}Sn	330.6	Ti	1.09	51	59(2)
^{124}Sn	395	Be	1.57	100	140(2)
^{208}Pb	624	Be	1.57	161	193(10)

The energy loss of a ^{114}Sn beam at 330.6 MeV through a natural carbon and titanium target is shown in Figure 1. The carbon target had a nominal thickness of 1.01 mg/cm^2 with a calculated energy loss of 69 MeV; the measured energy loss was 78(2) MeV. The titanium target had a nominal thickness of 1.09 mg/cm^2 with a calculated energy loss of 51 MeV [19]; the measured energy loss was 59(2) MeV.

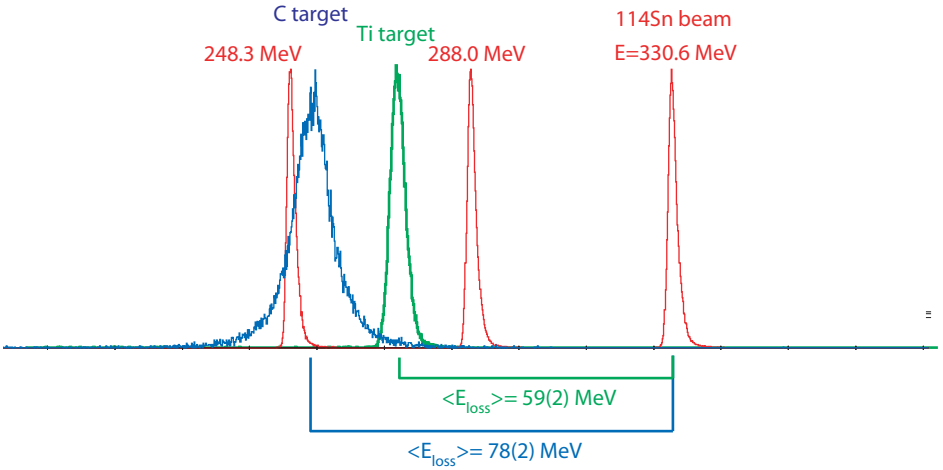

Fig. 1: Energy loss of a ^{114}Sn beam at 330.6 MeV through a natural carbon and titanium target.

The energy loss of a ^{124}Sn beam at 395 MeV through a natural beryllium target is shown in Figure 2.

Not only is the Bragg detector a useful way to measure the energy loss of the beam through the target but it is also a good way to determine the uniformity of the target. The beryllium target had a nominal thickness of 1.57 mg/cm^2 with a calculated energy loss of 100 MeV [19]; the measured energy loss was 140(2) MeV. The beryllium target thickness was remeasured using a scale and calipers but it was consistent to within a few percent of the nominal thickness quoted by the target manufacturer. The large discrepancies between calculated and measured energy losses are thought to be predominately from the uncertainty in the stopping powers.

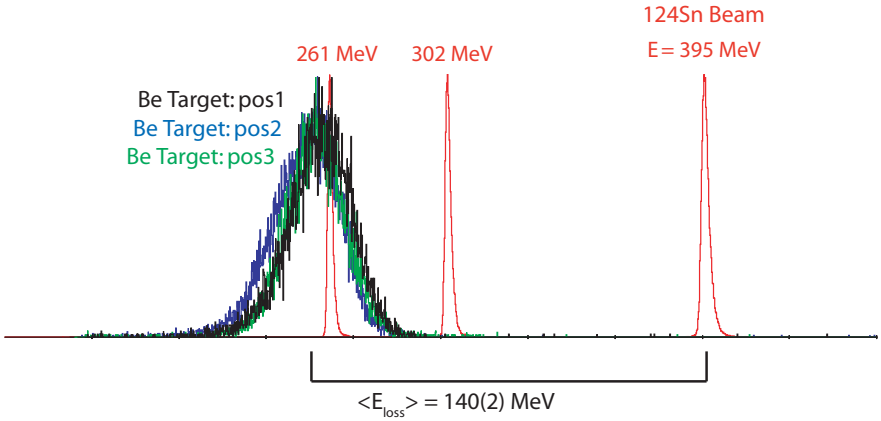

Fig. 2: Energy loss of a ^{124}Sn beam at 395 MeV through a natural beryllium target.

COULOMB EXCITATION

By measuring the absolute cross sections and particle-γ angular correlations of excited states following Coulomb excitation, a complete set of electromagnetic moments can be determined (cf. Refs. [20, 21]). These electromagnetic moments probe the shape of the nucleus and coherent motion of the valence nucleons. They also provide a sensitive test of the excited-state wavefunctions. The absolute cross sections can be obtained by measuring the Coulomb excitation to Rutherford yield, i.e., particle-γ to particle yield. Figure 3 shows a typical example of carbon recoils in the BareBall CsI(Tl) detector array. By using the angle of the detected target recoil in the CsI(Tl) array and the angle of the detected γ ray in the HPGe array, the angle between the projectile and γ ray can be calculated and compared to the observed γ-ray energy. Figure 4 shows the observed $2_1^+ \rightarrow 0_1^+$ γ-ray energies from ^{112}Sn as a function of $\cos\theta_{C-\gamma}$. A chi-square fit to the relativistic Doppler equation was used to determine the intrinsic $2_1^+ \rightarrow 0_1^+$ energy and $\beta = v/c$ values.

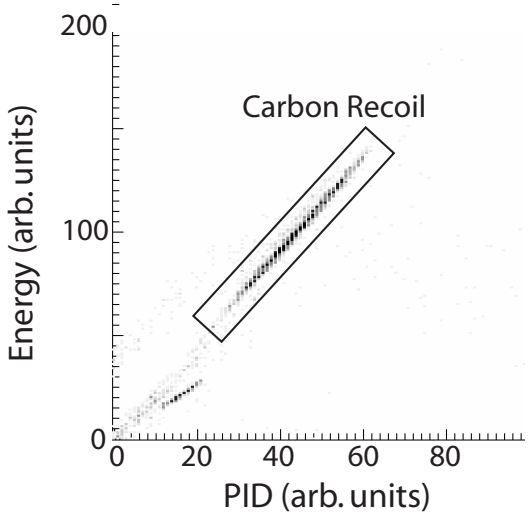

Fig. 3: A particle identification spectrum (PID) showing the Carbon recoils in the BareBall CsI(Tl) detector array.

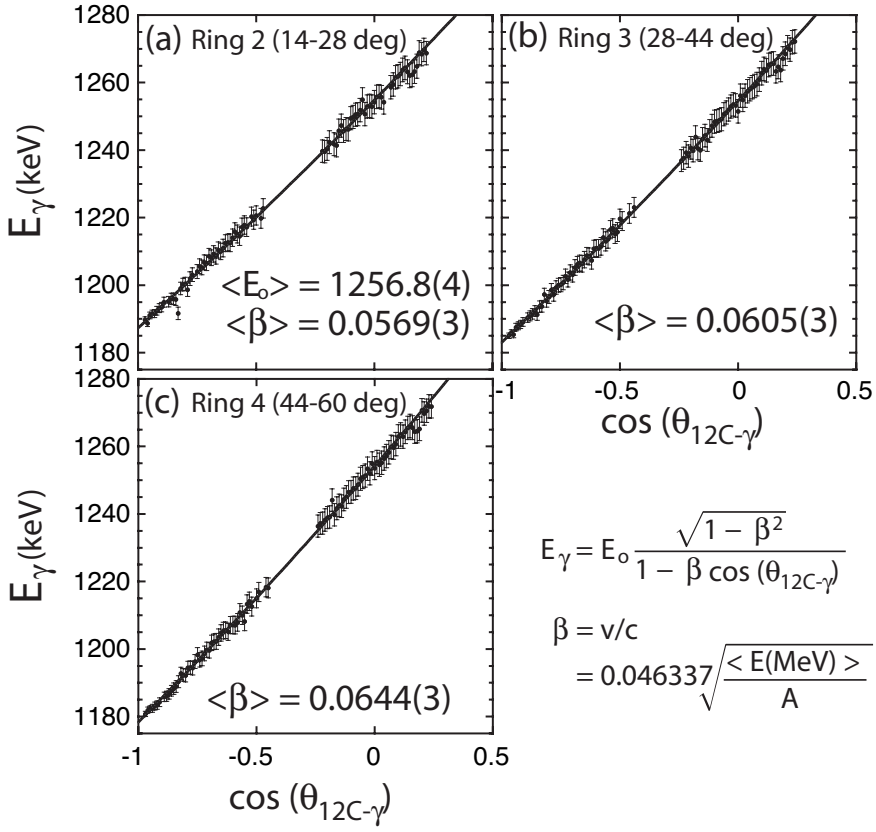

Fig. 4: Doppler shifts of the $2_1^+ \rightarrow 0_1^+$ γ-ray transition of ^{112}Sn following Coulomb excitation on a carbon target.

Figure 5 shows the Doppler corrected γ-ray spectrum of ^{112}Sn. Coulomb excitation on the low-Z carbon target resulted in mostly single-step excitation of the first 2^+ state. However, a small amount of two-step excitation to the first 3^- state is also observed. The Coulex results for the other Sn isotopes are nearly identical to these ^{112}Sn results. In addition, data were taken on a Ti target. Determination of $E2$, $E1$, and $M1$ matrix elements involving the 2_1^+ and 3_1^- states will be possible.

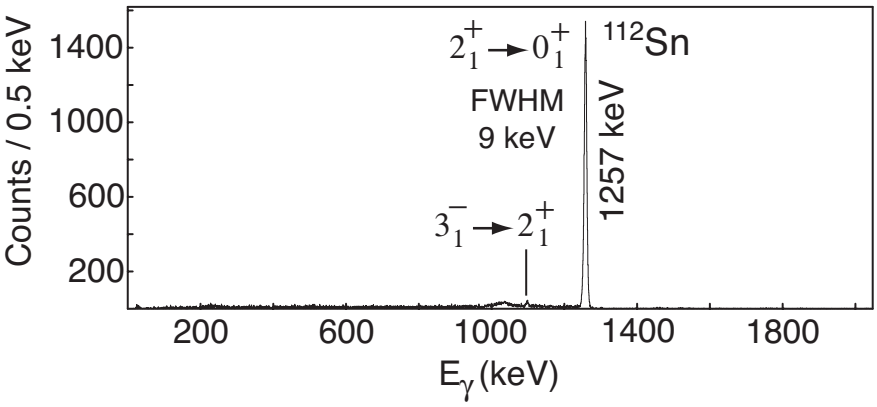

Fig. 5: Doppler-corrected γ-ray spectrum of ^{112}Sn following Coulomb excitation on a carbon target.

There are several advantages to performing Coulomb excitation in inverse kinematics with a low-Z carbon target, particularly for measuring high-precision absolute $B(E2; 0_1^+ \rightarrow 2_1^+)$ values, which include: (1) the excitation process is mostly single and two step, (2) the reorientation effect is minimized, (3) the target doesn't contribute to the gamma-ray background, (4) the uncertainties are not limited by a target $B(E2)$ uncertainty, and (5) the recoiling target nuclei are measured at backward center of mass angles where the Rutherford cross section is less sensitive to angle. Back angles minimize uncertainties related to geometry, and also maximize the ratio of Coulomb excitation to Rutherford scattering, which minimizes the non-prompt

(or random) particle-γ component. The cleanliness of the γ-ray spectrum in Fig. 5 is a testament to many of these points.

HEAVY-ION INDUCED TRANSFER

Single-neutron states in ^{133}Sn, which are analogous to single-electron states outside of closed atomic shells in alkali metals, were populated by the (^{9}Be,^{8}Be) one-neutron transfer reaction in inverse kinematics using sub-barrier energies and particle-γ coincidence spectroscopy [4]. Level energies, γ-ray transitions, absolute cross sections, spectroscopic factors, asymptotic normalization coefficients, and excited-state lifetimes were reported and compared with shell-model expectations. This was the first report on excited-state lifetimes of ^{133}Sn, which allowed for a unique test of the nuclear shell model and radioactive ^{132}Sn double-shell closure. An issue that remains inconclusive concerns the $i_{13/2}$ candidate. Additional evidence concerning this state is provided here.

The recoiling target-like particles from the ^{9}Be induced reactions on the ^{132}Sn radioactive beam are shown in Fig. 6. The one-neutron transfer channel is selected from the (^{9}Be,^{8}Be) reaction. Because ^{8}Be is unbound ($T_{1/2} = 8.2 \times 10^{-17}$ s [22]), two correlated alphas are detected. This provides a clean tag of the one-neutron transfer channel in the CsI(Tl) detector array.

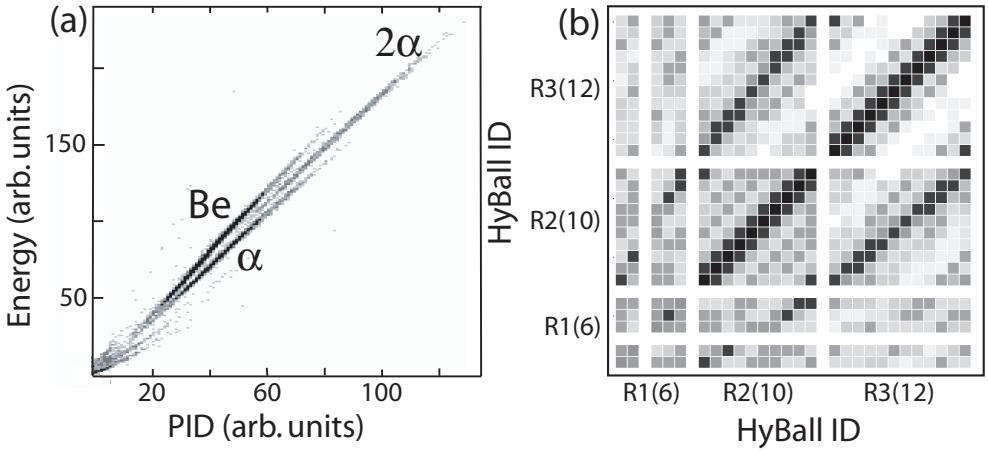

Fig. 6: (a) A particle identification spectrum (PID) from the ^{9}Be induced reactions on ^{132}Sn showing the target-like recoils in the BareBall CsI(Tl) detector array. (b) The particle detector hit pattern from the detection of two α particles.

The Doppler corrected γ-ray spectrum of ^{133}Sn following ^{132}Sn(^{9}Be,^{8}Beγ) is shown in Fig. 7. The 513- and 2792-keV γ-ray transitions from ^{133}Sn were previously unobserved. The 513-keV γ ray originates from a state at 1366.8(4) keV, which corresponds to the $p_{1/2}$ candidate state at 1363(31) keV in the (d,p) study of ^{133}Sn by Jones *et al.* [2]. The energy resolution of the state was dramatically improved by measuring the γ rays in coincidence with the particles. The only remaining single-neutron assignment for the 2792-keV γ-ray transition and state is $i_{13/2}$. However, the results for this assignment are inconclusive.

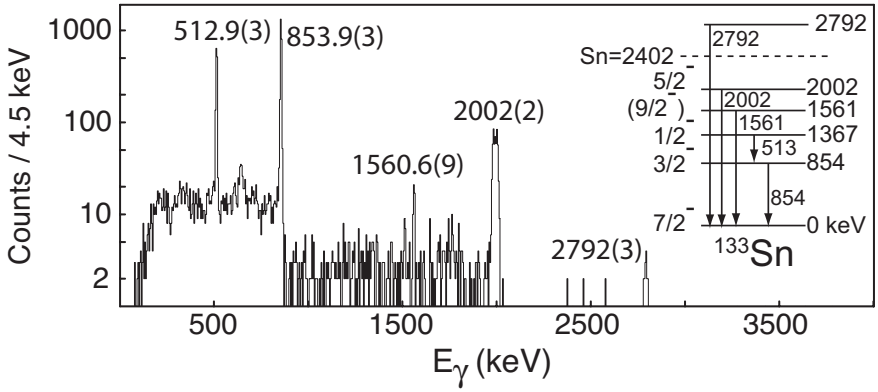

Fig. 7: The Doppler corrected γ-ray spectrum following ^{132}Sn(^{9}Be,^{8}Beγ)^{133}Sn.

The 2792-keV γ ray, Fig. 7, is a natural $\nu 1i_{13/2}$ candidate for ^{133}Sn. The energy is consistent with expectations from systematics, cf. Fig. 8. The energy is also consistent with the 2694(200)-keV prediction by Urban *et al.* [23]. However, 2792-keV is nearly 400 keV above the neutron separation energy of 2396(4) keV [24, 25, 3].

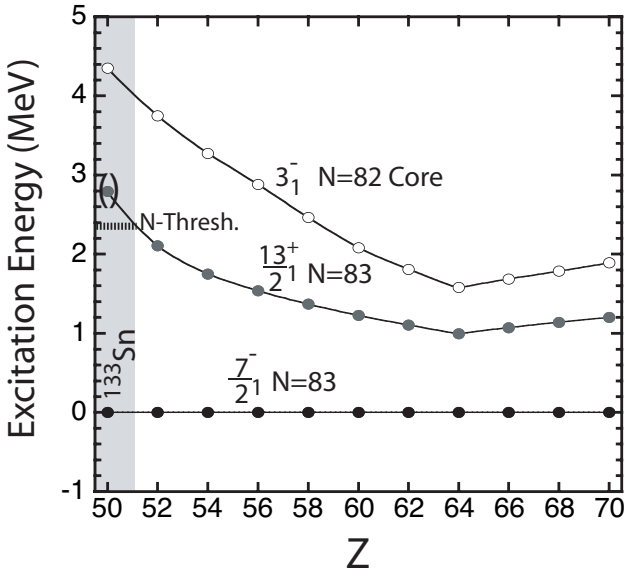

Fig. 8: The $7/2^-_1$ ($N = 83$), $13/2^+_1$ ($N = 83$), and 3^- ($N = 82$) core-excited octupole systematics from the present study and literature [22].

The γ-ray Doppler shift suggests that the 2792-keV transition originates from a state with a relatively long lifetime of $\tau > 1$ ps (cf. Fig. 9), which is consistent with expectations for an $E3$ decay but contradicts expectations for an unbound $\ell = 6$ neutron ($\tau \sim 0.1$ ps) that is nearly 400 keV above the neutron separation energy. The neutron-decay width should be much larger than the γ-decay width but a relatively large cross section was determined from the γ-ray intensity.

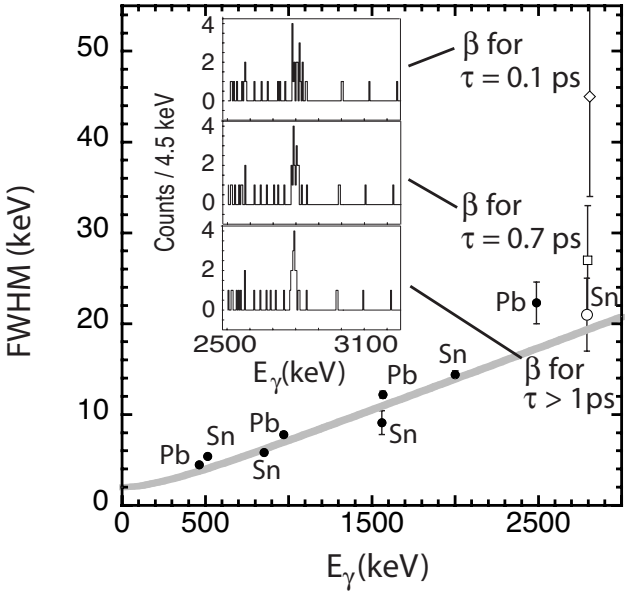

Fig. 9: The Doppler-correctd γ-ray spectra and FWHM values of the 2792-keV transition for different $\beta = v/c$ values (i.e., different lifetime assumptions).

A 2792-keV γ ray from an $(11/2^-)$ state in ^{133}Sb is reported in the literature [22]. This state could be populated by one-neutron transfer on a ^{132}Sb beam contaminant. However, there was no evidence for ^{132}Sb in the beam from either the Bragg detector or Coulomb excitation, which would produce a 163-keV γ ray (cf. Fig. 10).

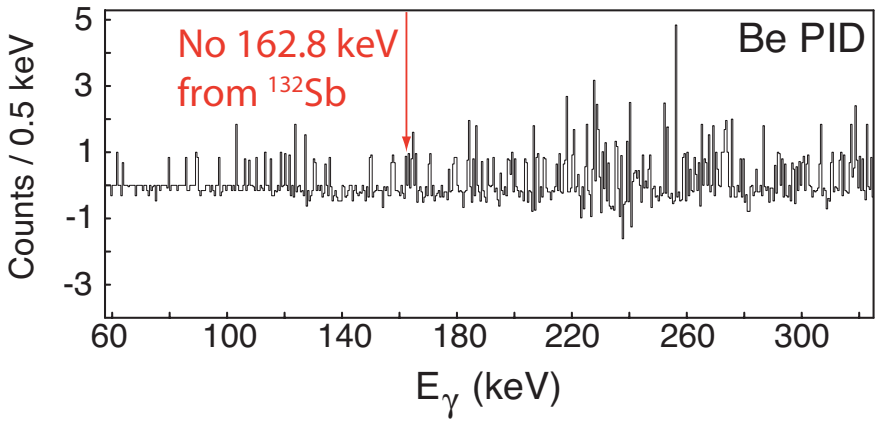

Fig. 10: Doppler-corrected, ^{9}Be-gated γ-ray spectrum showing the absence of a 163-keV γ ray from Coulomb excitation of ^{132}Sb.

Population of ^{133}Sb could be achieved by ^{132}Sn(^{9}Be,^{8}Li) but this channel would not lead to prompt detection of two correlated α particles (cf. Fig. 11). In addition, no γ rays were observed from the lower-lying states of ^{133}Sb [22].

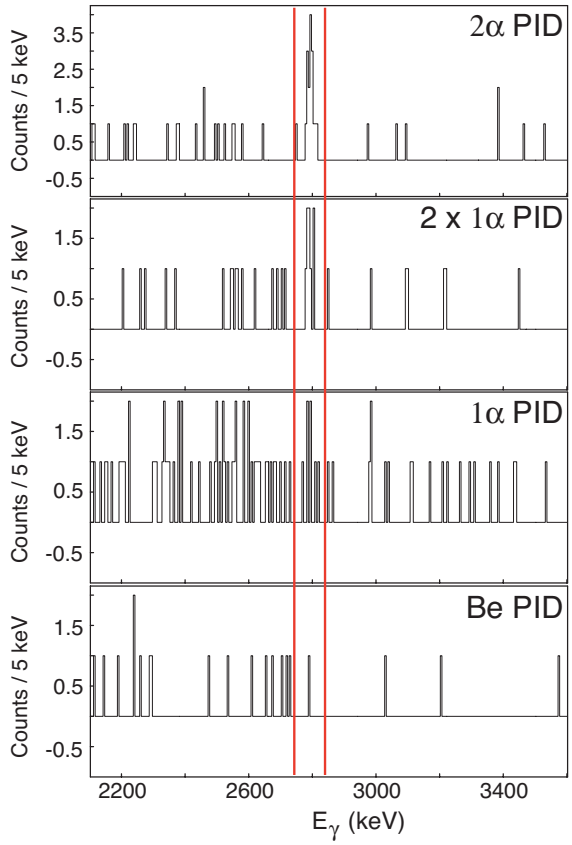

Fig. 11: The Doppler corrected γ-ray spectra for each particle-id gate in Fig. 6.

There appears to be no clear explanation for the observed 2792-keV γ-ray transition; a new experiment will be required to resolve the issue.

CONCLUSIONS

In summary, several stable and radioactive nuclei ranging from $A = 58$ to 208 were recently studied in inverse kinematics by Coulomb excitation and sub-barrier heavy-ion induced transfer at HRIBF-ORNL. For both techniques, absolute cross sections were measured by normalizing to Rutherford scattering. Beam

energy loss measurements with a Bragg-curve detector indicate that calculations based on target thicknesses and stopping powers are unreliable. The energy loss of the beam through the target must be measured for high-precision measurements. Overall, the present Coulomb-excitation and heavy-ion induced transfer studies have resulted in extensive, high-precision spectroscopic information that will challenge and constrain leading microscopic theories.

ACKNOWLEDGMENT:
I would like to thank the CLARION-BareBall collaboration and the HRIBF operations staff for making these studies possible. This material is based upon work supported by the U.S. Department of Energy, Office of Science, Office of Nuclear Physics and this research used resources of the Holifield Radioactive Ion Beam Facility of Oak Ridge National Laboratory, which is a DOE Office of Science User Facility.

REFERENCES

[1] J.R. Beene *et al.*, Nucl. Phys. **A746**, 471c (2004); D.C. Radford *et al.*, Nucl. Phys. **A752**, 264c (2005).
[2] K.L. Jones *et al.*, Nature, **465**, 454 (2010).
[3] J. Van Schelt *et al.*, Phys. Rev. Lett. **111**, 061102 (2013).
[4] J.M. Allmond *et al.*, Phys. Rev. Lett. **112**, 172701 (2014).
[5] C. Thibault *et al.*, Phys. Rev. C **12**, 644, (1975).
[6] D. Guillemaud-Mueller *et al.*, Nucl. Phys. **A426**, 37 (1984).
[7] O. Sorlin *et al.*, Phys. Rev. C **47**, 2941 (1993).
[8] H. Scheit *et al.*, Phys. Rev. Lett. **77**, 3967 (1996).
[9] T. Glasmacher *et al.*, Phys. Lett. B **395**, 163 (1997).
[10] D. Sohler *et al.*, Phys. Rev. C **66**, 054302 (2002).
[11] A.E. Stuchbery *et al.*, Phys. Rev. C **88**, 051304(R) (2013).
[12] J.M. Allmond *et al.*, Phys. Rev. C (accepted).
[13] D.C. Radford *et al.*, Phys. Rev. Lett. **88**, 222501 (2002).
[14] N. J. Stone *et al.*, Phys. Rev. Lett. **94**, 192501 (2005).
[15] D.C. Radford *et al.*, Eur. Phys. J. A **15**, 171 (2002).
[16] J.M. Allmond *et al.*, Phys. Rev. C **86**, 031307(R) (2012).
[17] A. Galindo-Uribarri, AIP Conf. Proc. **1271**, 180 (2010).
[18] C.J. Gross *et al.*, Nucl. Instrum. Methods Phys. Res. A **450**, 12 (2000).
[19] Energy loss and Straggling Tool, [Adapted from the computer program ENELOSS, written by H. Ernst (1981) with stopping power routines by K. Lesko (1984).]
[20] J.M. Allmond *et al.*, Phys. Rev. C **84**, 061303(R) (2011).
[21] J.M. Allmond *et al.*, Phys. Rev. C **87**, 054325 (2013).
[22] Evaluated Nuclear Structure Data File (ENSDF), http://www.nndc.bnl.gov/ensdf/.
[23] W. Urban *et al.*, Eur. Phys. J. A **5**, 239 (1999).
[24] M. Dworschak *et al.*, Phys. Rev. Lett. **100**, 072501 (2008).
[25] J. Hakala *et al.*, Phys. Rev. Lett. **109**, 032501 (2012).

SPECIFIC VISCOSITY OF HOT NUCLEAR MATTER

Y. G. Ma[1,*], D. Q. Fang[1,], J. XU[1,] and C. L. Zhou[1,]

[1]Shanghai Institute of Applied Physics, Chinese Academy of Sciences, Shanghai 201800, China
(Dated: December 24, 2014)

Abstract

The specific viscosity, defined as the ratio of shear viscosity over entropy density, is investigated in the vicinity of nuclear liquid-gas phase transition within the framework of the isospin-dependent quantum molecular dynamics model and the Boltzmann-Uehling-Uhlenbeck model. Different kinds of methods are employed to study the thermal and transport properties of the hot nuclear matter or the nuclear fireball formed in heavy-ion collisions. The results show that the specific viscosity first decreases with the increasing temperature (or collision energy), then reaches a saturation value or a minimum. The corresponding temperature of the minimum of the specific viscosity is around 10 MeV, which is consistent with that of the nuclear liquid-gas phase transition according to other relevant studies. It is proposed that the specific viscosity can be used as a proper probe of the nuclear liquid-gas phase transition. The correlation between the shear viscosity and the elliptic flow has also been studied, and it may shed light on extracting the shear viscosity in intermediate-energy heavy-ion collisions experimentally.

51.20.+d, 51.10.+y, 24.10.-i

INTRODUCTION

Due to van der Waals nature of nuclear force, liquid-gas phase transition (LGPT) could occur in heavy-ion collisions (HIC) at intermediate energies [1–8]. Studies on the phenomena of LGPT and its probes, like fragment size distribution, caloric curve, bimodality, and fragment rank distribution, etc., have become an important subject in HIC in the past years [3, 4, 9–12].

Viscosity describes the internal resistance to flow of a fluid, and might be thought of as a measure of the fluid friction. In ultra-relativistic HIC, the hydrodynamics model has been used to study the quark-gluon plasma (QGP) phase and the critical phenomenon [13–18]. The investigations show that the QGP has very small specific viscosity and behaves like a nearly perfect fluid. On the other hand, efforts have also been devoted to the study of viscosity for nuclear matter formed during HIC at intermediate energies [19–28]. It is found that the shear viscosity to entropy density ratio for matter such as H_2O, He, and Ne_2 has a minimum at or near the critical point of phase transition [14, 29]. This is an empirical observation for many kinds of substances. A lower bound of this ratio ($\eta/s \geq 1/4\pi$) is speculated to be valid universally according to certain gauge theory (Kovtun-Son-Starinets (KSS) bound) [30, 31]. However, the studies on the behavior of the specific viscosity in the vicinity of the liquid-gas phase transition are still lacking. In this paper, we summarized several interesting works that focus on the specific viscosity in intermediate-energy heavy-ion collisions or specific viscosity of hot nuclear matter close to the critical temperature of nuclear LGPT.

The paper is organized as follows. Section provides a brief introduction for the isospin-dependent quantum molecular dynamic (IQMD) model and the Boltzmann-Uehling-Uhlenbeck (BUU) model, which are used to simulate the dynamics of HIC at intermediate energies. Section introduces the various formalisms used to extract the thermal and transport properties of the hot nuclear matter formed in HIC. In section we present the calculation results and discussions. Finally a summary and outlook is given.

TRANSPORT MODELS

In this section we briefly review the main gradients of the two transport models used to study the dynamics of HIC and the specific shear viscosity of hot nuclear matter, i.e., the quantum molecular dynamics model and the Boltzmann-Uehling-Uhlenbeck model.

Quantum Molecular Dynamics Model

The quantum molecular dynamics model approach is a many-body theory that describes heavy-ion collisions from intermediate to relativistic energies. The isospin-dependent quantum molecular dynamics

*E-mail: ygma@sinap.ac.cn

model [32, 33] is developed from the QMD model by including the isospin degrees of freedom and Pauli blocking, etc. Each nucleon in the colliding system is described as a Gaussian wave packet, and the wave function of the ith nucleon is expressed as

$$\phi_i(\mathbf{r},t) = \frac{1}{(2\pi L)^{3/4}} \exp\left[-\frac{(\mathbf{r}-\mathbf{r_i}(t))^2}{4L} - \frac{i\mathbf{r}\cdot\mathbf{p_i}(t)}{\hbar}\right], \tag{1}$$

where $\mathbf{r}_i(t)$ and $\mathbf{p}_i(t)$ are the mean position and mean momentum, respectively, and the Gaussian width is set to be $L = 2.16$ fm^2 for Au + Au system. The centers of these Gaussian wave packets propagate in coordinate and momentum space according to the classical equations of motion:

$$\dot{\mathbf{p}}_i = -\frac{\partial\langle\mathbf{H}\rangle}{\partial\mathbf{r}_i}; \dot{\mathbf{r}}_i = \frac{\partial\langle\mathbf{H}\rangle}{\partial\mathbf{p}_i}, \tag{2}$$

where $\langle\mathbf{H}\rangle$ is the Hamiltonian of the system. The Wigner distribution function of the ith nucleon in phase space is thus given by

$$f_i(\mathbf{r},\mathbf{p},t) = \frac{1}{\pi^3\hbar^3} \exp\left[-\frac{(\mathbf{r}-\mathbf{r}_i(t))^2}{2L} - \frac{2L(\mathbf{p}-\mathbf{p}_i(t))^2}{\hbar^2}\right]. \tag{3}$$

From the above phase-space Wigner distribution, one can obtain the matter density as well as the kinetic energy density in the coordinate space by the sum over all the nucleons, and they are respectively expressed as

$$\begin{aligned}\rho(\mathbf{r},t) &= \sum_{i=1}^{A_T+A_P} \rho_i(\mathbf{r},t) \\ &= \sum_{i=1}^{A_T+A_P} \frac{1}{(2\pi L)^{3/2}} \exp\left[\frac{(\mathbf{r}-\mathbf{r}_i(t))^2}{2L}\right],\end{aligned} \tag{4}$$

and

$$\rho_K(\mathbf{r},t) = \sum_{i=1}^{A_T+A_P} \frac{\mathbf{p}_i(t)^2}{2m}\rho_i(\mathbf{r},t), \tag{5}$$

with A_T and A_P being the nucleon numbers of the target and the projectile, respectively.

The mean field used in IQMD model in the present study is:

$$U(\rho) = U_{\rm Sky} + U_{\rm Coul} + U_{\rm Yuk} + U_{\rm sym}, \tag{6}$$

where $U_{\rm Sky}$, $U_{\rm Coul}$, $U_{\rm Yuk}$, and $U_{\rm sym}$ are the Skyrme potential, the Coulomb potential, the Yukawa potential, and the isospin asymmetry potential, respectively [32]. The Skyrme potential has the form of :

$$U_{\rm Sky} = \alpha(\rho/\rho_0) + \beta(\rho/\rho_0)^\gamma, \tag{7}$$

where $\rho_0 = 0.16$ fm^{-3}, and ρ is the nucleon number density. In the present work, the parameter set α =-356 MeV, $\beta = 303$ MeV, and $\gamma = 7/6$ is used, which leads to a soft equation of state (EOS). $U^{\rm Yuk}$ is the long-range (surface) potential, and it takes the following form

$$\begin{aligned}U^{Yuk} &= (V_y/2)\sum_{i\neq j} exp(Lc^2)/r_{ij} \\ \times\ & [\exp(cr_{ij})erfc(\sqrt{L}c - r_{ij}/\sqrt{4L}) \\ -\ & \exp(cr_{ij})erfc(\sqrt{L}c + r_{ij}/\sqrt{4L})]\end{aligned} \tag{8}$$

with $V_y = 0.0074$ GeV, $c = 1.25$ fm^{-1}, and r_{ij} being the relative distance between two nucleons. The isospin asymmetry potential is written as

$$U_{sym} = 32\frac{\rho_n - \rho_p}{\rho_0}\tau_z, \tag{9}$$

where ρ_n and ρ_p are the neutron and proton densities, respectively, and $\tau_z = 1(-1)$ for neutrons (protons) is the isospin index.

Boltzmann-Uehling-Uhlenback Model

The BUU model is a one-body microscopic transport model based on the Boltzmann-Uehling-Uhlenbeck equation, which is expressed as [34]

$$\begin{aligned} &\frac{\partial f}{\partial t} + v \cdot \nabla_r f - \nabla_r U \cdot \nabla_p f = \frac{4}{(2\pi)^3} \int d^3p_2 d^3p_3 d\Omega \\ \times \quad &\frac{d\sigma_{NN}}{d\Omega} V_{12} [f_3 f_4 (1-f)(1-f_2) - f f_2 (1-f_3)(1-f_4)] \\ &\times \quad \delta^{(3)}(p + p_2 - p_3 - p_4). \end{aligned} \tag{10}$$

The above equation can be easily generalized to an isospin-dependent form, and it is usually solved with the method by Bertsch and Das Gupta [35]. $d\sigma_{NN}/d\Omega$ and V_{12} are the differential in-medium nucleon-nucleon (NN) cross section and relative velocity for the colliding nucleons, respectively, and U is the mean-field potential including the isospin-dependent term:

$$U(\rho, \tau_z) = a \left(\frac{\rho}{\rho_0} \right) + b \left(\frac{\rho}{\rho_0} \right)^{\sigma} + C_{sym} \frac{\rho_n - \rho_p}{\rho_0} \tau_z. \tag{11}$$

The coefficients a, b and σ are parameters for the nuclear equation of state, and there are two sets of parameters used in the study, namely the soft EOS with the incompressibility K of 200 MeV (a = -356 MeV, b = 303 MeV, and $\sigma = 7/6$), and the stiff EOS with K of 380 MeV (a = -124 MeV, b = 70.5 MeV, and $\sigma = 2$). $C_{sym} = 32$ MeV is the symmetry energy strength due to the density difference of neutrons and protons in nuclear medium.

FORMALISMS FOR THERMAL AND TRANSPORT PROPERTIES

In this section we briefly introduce the formalisms employed in calculating the thermodynamical properties of hot nuclear matter formed in HIC at intermediate-energies as well as different methods in studying its shear viscosity. The former contains the hot Thomas-Fermi formalism used in the study with the IQMD model and momentum fluctuation method for extracting the temperature with the BUU model, while the latter summarizes the Green-Kubo formula, Danielewicz's parameterization, the classical kinetic theory, and the relaxation time approach for the calculation of the shear viscosity.

Formalisms for Thermodynamical Quantities

Hot Thomas-Fermi Formalism

The hot Thomas-Fermi formalism (HTFF) is developed by Faessler and the collaborators [36–38]. In this approach, one starts from a microscopic picture of two interpenetrating pieces of nuclear matter and uses a deformed Fermi-Dirac distribution in momentum space. To extract the thermal properties of the hot nuclear matter, we first calculate the nuclear matter density and the kinetic energy density in coordinate space at each time step from the IQMD simulation. Afterwards, by employing the hot Thomas-Fermi formalism, we can obtain the corresponding thermal properties for every set of nuclear matter density and nuclear kinetic energy density [36, 37]. The advantage of HTFF is that one can study the time evolution of thermal properties such as the temperature, the entropy density, and the chemical potential in heavy-ion collisions. For more detailed information, we refer the reader to Refs. [36–38].

Momentum Fluctuation Method

The temperature of the hot nuclear matter can also be extracted from the momentum fluctuations of particles in the center-of-mass frame of the fragmenting source [39]. The variance σ^2 is obtained from the Q_z distribution through

$$\sigma^2 = \langle {Q_z}^2 \rangle - \langle Q_z \rangle^2, \tag{12}$$

where Q_z is the quadruple moment defined as $Q_z = 2{p_z}^2 - {p_x}^2 - {p_y}^2$, and p_x, p_y, and p_z are three components of the momentum vector extracted from the phase space. If $\langle Q_z \rangle$ equals to zero, the variance only depends

on $\langle Q_z^2 \rangle$, which can be calculated from

$$\langle {Q_z}^2 \rangle = \int d^3p (2{p_z}^2 - {p_x}^2 - {p_y}^2)^2 f(p). \tag{13}$$

Assuming a Maxwellian form of the particle momentum distribution, i.e.,

$$f(p) = \frac{1}{(2\pi mT)^{3/2}} \exp\left[-\frac{{p_x}^2 + {p_y}^2 + {p_z}^2}{2mT}\right], \tag{14}$$

we get

$$\langle {Q_z}^2 \rangle = 4m^2 A^2 T^2 \tag{15}$$

after Gaussian integration, where m is the mass of a nucleon and A is the mass number of the fragment. For a nucleonic system, we have $A = 1$ and can calculate the evolution of the temperature using this equation. Knowing the temperature, the entropy density can be calculated from the Gibbs formula, i.e.,

$$s = \frac{\varepsilon + P - \mu\rho}{T}, \tag{16}$$

where μ stands for the nucleon chemical potential, $P = \frac{1}{3V}\sum_{r_i<r_0}(p_i^2/E_i)$ is the pressure, and $\varepsilon = \frac{1}{V}\sum_{r_i<r_0} E_i$ is the energy density within a sphere of radius r_0 and volume V, which is used in the transport model calculation in the following discussions.

Formalisms for Shear Viscosity

Green-Kubo Formula

From the fluctuation-dissipation theory [40], the Green-Kubo formula for the shear viscosity is expressed as

$$\eta = \frac{1}{T}\int d^3r \int_0^\infty dt \langle \pi_{ij}(0,0)\pi_{ij}(\mathbf{r},t)\rangle, \tag{17}$$

where T is the temperature of the system, t is the post-equilibration time, and $\langle \pi_{ij}(0,0)\pi_{ij}(\mathbf{r},t)\rangle$ is the shear component of the energy momentum tensor. In the transport model calculation, the above average is taken on all the nucleons in the central region of the HIC, which are nearly in equilibrium. If the tensor correlation function follows $\langle \pi_{ij}(0)\pi_{ij}(t)\rangle \propto \exp(-1/\tau)$, Eq. (17) becomes

$$\eta = \frac{V}{T}\langle \pi_{ij}(0)^2 \rangle \tau, \tag{18}$$

where V is the volume of the central region in HIC and τ is the relaxation time of the system.

Danielewicz's Parameterization

In Refs. [41, 42] Danielewicz *et al.* studied the nuclear shear viscosity from the microscopic Boltzmann-Uehling-Ulenbeck equation, and the result is further parameterized as a function of density and temperature

$$\begin{aligned}\eta\left(\frac{\rho}{\rho_0}, T\right) &= \frac{1700}{T^2}\left(\frac{\rho}{\rho_0}\right)^2 + \frac{22}{1 + T^2 10^{-3}}\left(\frac{\rho}{\rho_0}\right)^{0.7} \\ &\quad + \frac{5.8\sqrt{T}}{1 + 160T^{-2}},\end{aligned} \tag{19}$$

where η is in MeV/fm^2c, T is in MeV, and the value of ρ_0 is set to be 0.168 fm^{-3}. The isospin effect in the study by Danielewicz *et al.* has been neglected. Extracting the density and the temperature in HIC with the hot Thomas-Fermi formulism, the time evolution of shear viscosity in HIC can be conveniently calculated by using the above parameterization.

Classical Kinetic Theory

From the classical kinetic theory, the shear viscosity η of the system is related to the mean free path of the particles [43]

$$\eta = \frac{1}{3}\rho m v \lambda, \tag{20}$$

where ρ, m, and v are the density, mass, and velocity of the nucleons, respectively, and the mean free path λ of nucleons can be expressed as

$$\lambda = \frac{A}{2N_{\rm coll}}v, \tag{21}$$

with $N_{\rm coll}$ being the collision number per unit time (or collision frequency).

Relaxation Time Approach

From the relaxation time approach, the shear viscosity is calculated by assuming that in the uniform nuclear system there exists a static flow field in the z direction with flow gradient in the x direction. The shear force, which is related to the nucleon flux as well as the momentum exchange between flow layers, is proportional to the flow gradient, and the proportional coefficient, i.e., the shear viscosity, turns out to be [27]

$$\eta = \sum_{\tau} -\frac{d}{(2\pi)^3}\int \tau_\tau(p)\frac{p_z^2 p_x^2}{p m_\tau^\star}\frac{dn_\tau}{dp}dp_x dp_y dp_z. \tag{22}$$

In the above, $d = 2$ is the spin degeneracy, $p = \sqrt{p_x^2 + p_y^2 + p_z^2}$ is the nucleon momentum, n_τ is the local momentum distribution

$$n_\tau(\vec{p}) = f_\tau(\vec{p})/d = \frac{1}{\exp\left[(\frac{p^2}{2m} + U_\tau(\vec{p}) - \mu_\tau)/T\right] + 1} \tag{23}$$

with μ_τ and T being the chemical potential and the temperature, respectively, and $U_\tau(\vec{p})$ being the mean-field potential from an isospin- and momentum-dependent effective nuclear interaction [44]. $p_x/m_\tau^\star$ is the nucleon velocity between flow layers, where $m_\tau^\star$ is the effective mass of nucleon as a result of the momentum-dependent potential. $\tau_\tau(p)$ is the relaxation time for a nucleon with isospin τ and momentum p, and it can be further expressed as

$$\frac{1}{\tau_\tau(p)} = \frac{1}{\tau_\tau^{same}(p)} + \frac{1}{\tau_\tau^{diff}(p)}, \tag{24}$$

with $\tau_\tau^{same(diff)}(p)$ being the average collision time for a nucleon with isospin τ and momentum p when colliding with other nucleons of same (different) isospin. For more detailed derivations and the expressions of the relaxation time by linearizing the isospin-dependent BUU equation, we refer the readers to Ref. [27]. The relaxation time depends not only on the medium properties such as the density, temperature, and isospin asymmetry but on the NN scattering cross section as well. The free-space proton-proton (neutron-neutron) and neutron-proton cross sections (σ_{NN}) is taken as the parameterized form from Ref. [45], while the in-medium cross section is modified by the effective mass through [46]

$$\sigma_{NN}^{medium} = \sigma_{NN}\left(\frac{\mu_{NN}^\star}{\mu_{NN}}\right)^2, \tag{25}$$

where μ_{NN} ($\mu_{NN}^\star$) is the free-space (in-medium) reduced mass of colliding nucleons. The reduced mass scaling of the in-medium cross section comes from the fact that the differential cross section is inversely proportional to the relative velocity between the two colliding nucleons [47], while the difference between the scattering T matrix in free space and in the nuclear medium is neglected.

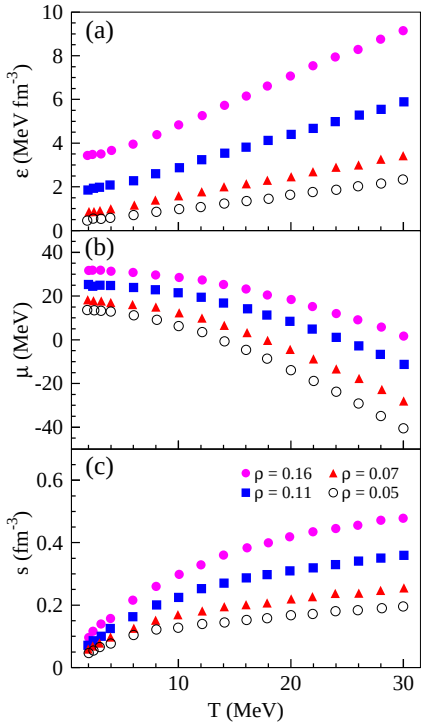

Fig. 1: (Color online) Temperature dependence of energy density (a), chemical potential per nucleon (b), and entropy density (c) for nuclear source at different densities ρ in fm^{-3}. Taken from Ref. [49].

RESULTS AND DISCUSSIONS

Shear Viscosity of Nuclear Matter

To begin with, we first review our studies of the shear viscosity of nuclear matter. In one approach, the finite-temperature nuclear source is constructed based on the IQMD model and the shear viscosity is calculated from the classical kinetic theory. In the other approach, one starts from the BUU equation with the relaxation time approximation and uses the Gibbs condition to construct the nuclear liquid-gas phase transition.

Finite-Temperature Nuclear Source

Usually the IQMD model is used to simulate the colliding process between two nuclei. However, only a single thermal source at $T > 0$ is needed for the study of initialized hot nuclear matter, and its thermal properties in the evolution process can be studied. The nuclear source with A nucleons is initialized using uniform density distribution with the radius given by $r_0 A^{1/3}$ (r_0 is the radius parameter). Then the initial coordinates of nucleons in the source are obtained by the Monte Carlo sampling method. In this work, the nuclear source with 50 protons and 62 neutrons (^{112}Sn) is chosen. The simulated temperature is $0 < T < 30$ MeV. Nevertheless, in order to study the density dependence, different radius parameters (r_0) are used to obtain different nuclear densities. The thermal properties could be calculated from the phase space information of the nucleons [24, 48]. However, the temperature and density of the system evolve with time when the nucleons propagate in the mean field in IQMD. The density distribution at any time can be calculated with the summation of all the nucleons, but the exact temperature T at time t is quite difficult to be extracted. To investigate the shear viscosity of nuclear matter at definite temperature and density, thermal properties and η are extracted from the phase-space information of nucleons at the very early stage ($1 < t < 5$ fm/c). During this period, the temperature of the system is almost as same as the initial value given by the input. In Fig. 1 (a)-(c), the temperature dependencies of the energy density ϵ, the chemical potential per nucleon μ, and the entropy density s are presented. As expected, the energy density increases with T as the probability of nucleons settled in high-energy levels is larger. Since the nuclear source studied is almost symmetric, the mean chemical potential of neutron and proton is presented in the figure. μ is

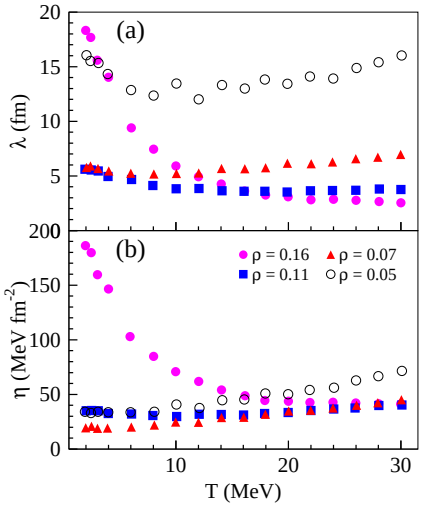

Fig. 2: (Color online) Temperature dependence of the mean free path (a) and the shear viscosity (b) for nuclear sources at different densities ρ in fm^{-3}. Taken from Ref. [49].

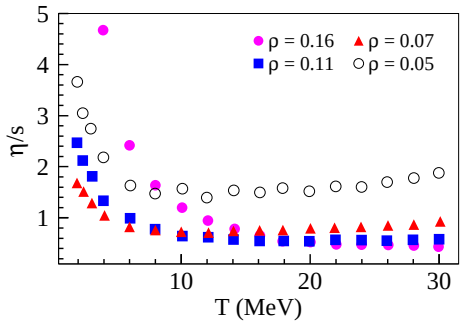

Fig. 3: (Color online) Temperature dependence of η/s for nuclear sources at different densities ρ in fm^{-3}. Taken from Ref. [49].

close to the Fermi energy when T is close to 0. Due to the Fermi-Dirac distribution for the momentum of nucleon, μ decreases with the increase of T, which makes more particles occupy the high-energy states. The entropy density increases with T, indicating that the system becomes more disordered with the increase of temperature. The energy density, chemical potential, and entropy density are proportional to the nuclear density as shown in the three panels.

The obtained mean free path λ is given in Fig. 2 (a). When the density is small, e.g., 0.05 and 0.07 fm^{-3}, the mean free path increases with increasing temperature. Interestingly, a totally opposite trend is observed for high-density case, and the larger the density, the smaller the mean free path is. This phenomenon could be caused by the collisions between nucleons, since the collision frequency is much larger when the nuclear matter is hotter. Consequently, the high collision frequency leads to a small mean free path. The shear viscosity is shown in Fig. 2 (b). At density $\rho = 0.16$ fm^{-3}, η decreases with T and becomes saturated to a value around 50 MeV fm^{-2}. At low densities, η decreases with T first but increase with T when T is larger than $8 \sim 10$ MeV.

The specific viscosity η/s is shown in Fig. 3. At densities $\rho = 0.11$ and 0.16 fm^{-3}, η/s decreases with the increase of T and becomes saturated to a value round 0.75 (about $7-8$ times of KSS bound) when T is larger than 20 MeV. But at low densities of $\rho = 0.07$ and 0.05 fm^{-3}, a minimum is seen at around 10 MeV. From the general relation between η/s and T, this minimum is related to the liquid-gas phase transition of nuclear matter.

Relaxation Time Approach

We first display the momentum dependence of the total relaxation time for a nucleon and that for the nucleon to collide with other ones of same or different isospin in symmetric and neutron-rich nuclear matter in Fig. 4. A smaller relaxation time means the nucleon on average experiences more frequent collisions. A constant cross section would make the relaxation time decrease with increasing momentum, as higher-

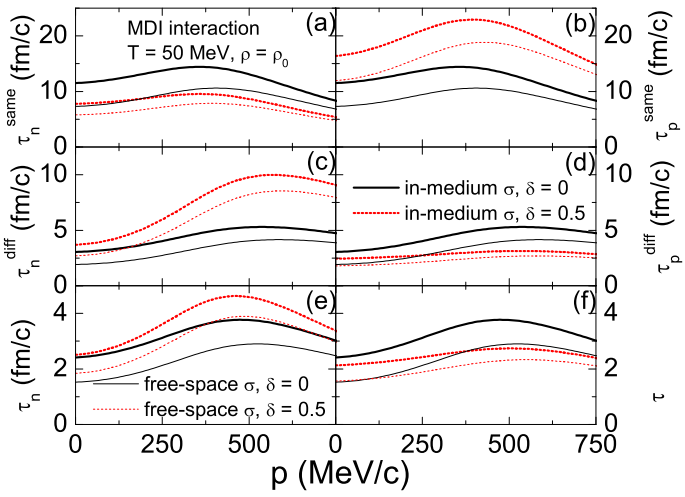

Fig. 4: (Color online) Momentum dependence of the total relaxation time and the relaxation time for the nucleon to collide with other ones of same or different isospin in symmetric ($\delta = 0$) and neutron-rich ($\delta = 0.5$) nuclear matter. Taken from Ref. [27].

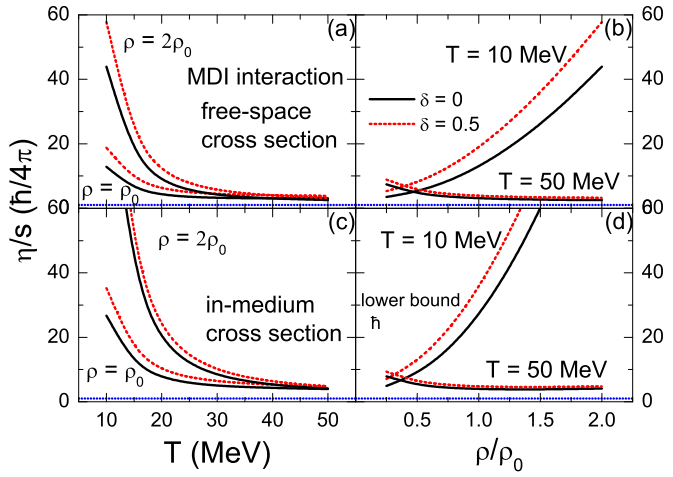

Fig. 5: (Color online) Specific viscosity as a function of the temperature at $\rho = \rho_0$ and $\rho = 2\rho_0$ (left panels) and that as a function of the density at $T = 10$ MeV and $T = 50$ MeV (right panels) for symmetric ($\delta = 0$) and neutron-rich ($\delta = 0.5$) nuclear matter from free-space cross sections (upper panels) and in-medium cross sections (lower panels). The lower bound of the specific viscosity is also shown by dotted lines for reference. No liquid-gas phase transition happens. Taken from Ref. [27].

momentum nucleons are more likely to collide with others. Using the energy-dependent free-space NN cross sections, there are peaks around $p = 500$ MeV, corresponding to the minimum values of the free cross sections as parameterized in Ref. [45]. Due to the smaller effective masses of nucleons in the nuclear medium, which leads to smaller in-medium NN cross sections, the relaxation times are larger. In symmetric nuclear matter, τ_τ, τ_τ^{same}, and τ_τ^{diff} are the same for nucleons of different isospins. In neutron-rich nuclear matter, τ_n^{same} are smaller while τ_p^{same} are larger compared with that in symmetric nuclear matter, due to larger chances for neutron-neutron collisions while smaller chances for proton-proton collisions. In addition, τ_n^{diff} becomes larger while τ_p^{diff} becomes smaller, due to a smaller number of protons and a larger number of neutrons to collide with, respectively. It is seen that there are always more chances for collisions between nucleons with different isospins than those with same isospin. The total relaxation time is dominated by the smaller one, i.e., τ^{diff}. Thus $\tau_n > \tau_p$ is found in neutron-rich nuclear matter, and they are both of the magnitude only

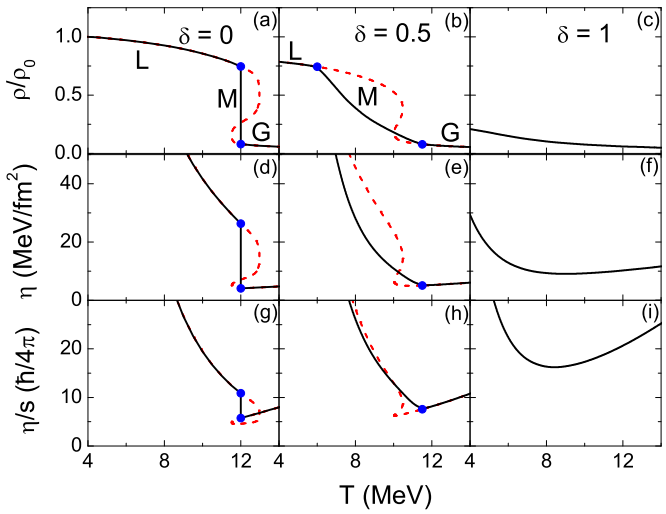

Fig. 6: (Color online) Temperature dependence of the average reduced number density (first row), the shear viscosity (second row), and the specific shear viscosity (third row) at the fixed pressure of $P = 0.1$ MeV/fm^3 for isospin symmetric matter ($\delta = 0$) (left column), neutron-rich matter ($\delta = 0.5$) (middle column), and pure neutron matter ($\delta = 1$) (right column). Solid lines are results including the liquid-gas phase transition with 'L', 'M', and 'G' representing the liquid phase, the mixed phase, and the gas phase, respectively. Dashed lines are results obtained by assuming the liquid-gas phase transition does not happen. Taken from Ref. [28].

a few fm/c at $\rho = \rho_0$ and $T = 50$ MeV.

The density and temperature dependence of the specific viscosity are shown in Fig. 5. Compared with the results from free-space NN cross sections, the specific viscosity from in-medium cross sections is much larger at lower temperatures and higher densities. The isospin effect on the specific viscosity is somehow smaller, compared with the results from free-space NN cross sections, due to the isospin-dependent modification on the in-medium cross sections. As the effective mass of neutrons is larger than that of protons in neutron-rich nuclear matter, the isospin effect on τ_n is smaller from in-medium cross sections than that from free-space cross sections. At $T = 50$ MeV, the specific viscosity is only about $4 \sim 5$ $(\hbar/4\pi)$, which is already close to the value of QGP extracted from the transverse momentum spectrum and elliptic flow using the viscous hydrodynamic model [50].

The above results are for the specific viscosity of uniform nuclear matter with a single phase, while the coexistence of the liquid and the gas phase of nuclear matter can be studied by constructing the binodal surface of the two phases with Gibbs condition. In the phase coexistence region with the liquid phase occupying a volume fraction λ, the average number and entropy densities can be expressed as

$$\rho = \lambda\rho_l + (1-\lambda)\rho_g, \tag{26}$$
$$s = \lambda s_l + (1-\lambda)s_g, \tag{27}$$

where $\rho_{l(g)}$ and $s_{l(g)}$ are the number and entropy densities of the liquid (gas) phase, respectively. The average shear viscosity of the mixed phase can then be expressed in terms of those in the liquid or the gas phase as

$$\eta = \lambda\eta_l + (1-\lambda)\eta_g. \tag{28}$$

Figure 6 displays the temperature dependence of the average reduced number density, the shear viscosity, and the specific viscosity, when the nucleonic matter is heated at the fixed pressure of $P = 0.1$ MeV/fm^3. As the temperature increases, the hot nucleonic matter undergoes a phase transition from the liquid phase at lower temperatures to the gas phase at higher temperatures if it has an isospin asymmetry $\delta = 0$ or $\delta = 0.5$ but has no phase transition if the isospin asymmetry is $\delta = 1$. The liquid-gas phase transition is of first order in symmetric nucleonic matter ($\delta = 0$) as shown in Fig. 26 of Ref. [51] by the sudden jump in the entropy per nucleon from the liquid phase to the gas phase as well as the discontinuity of the specific heat at the critical temperature. This leads to the sudden changes in all the thermodynamical quantities and the specific

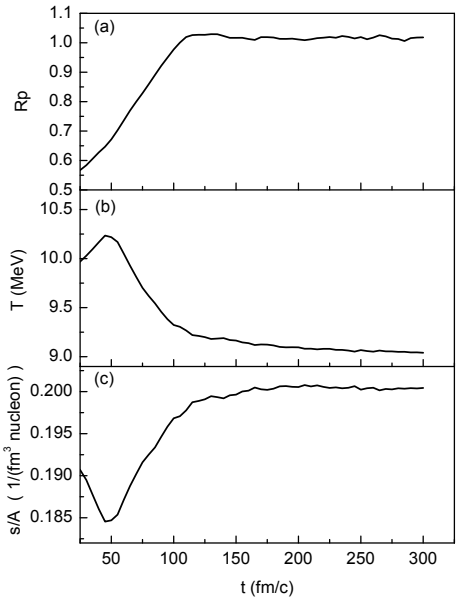

Fig. 7: (Color online) The anisotropy ratio R_p (a), temperature (b), and entropy density per nucleon (c) as a function of time after 24 fm/c for the head-on Au+Au collisions within a 5-fm-radius sphere at 50 AMeV. Taken from Ref. [24].

viscosity, while the latter evolves smoothly during the phase transition when it changes to a second-order one in neutron-rich matter ($\delta = 0.5$), confirming the expectation of Ref. [52]. Also, the liquid phase has a higher density and a lower temperature than the gas phase, leading to a stronger Pauli blocking effect in the liquid phase than in the gas phase. As a result, the liquid phase generally has a larger shear viscosity than the gas phase. For each phase, there are competing density and temperature effects on the evolution of the shear viscosity. An increase in temperature results in more frequent NN scatterings and weaker Pauli blocking effects, thus reducing the shear viscosity. On the other hand, the NN scattering cross section decreases with increasing center-of-mass energy of two colliding nucleons, which makes the shear viscosity increase with increasing temperature especially at very low densities. At higher densities, although the stronger Pauli blocking effect increases the shear viscosity, the smaller in-medium nucleon mass leads to a larger flux between flow layers and a larger relative velocity between two colliding nucleons, thus reducing the shear viscosity. Due to the combination of these effects together with the behavior of the entropy density with respect to temperature and density, the specific shear viscosity decreases in the liquid phase but increases in the gas phase with increasing temperature. The minimum of the specific shear viscosity is exactly located at the critical temperature when a first-order phase transition happens, while it is located at the boundary of the gas phase if the phase transition is of second order. Even for a pure neutron matter without a liquid-gas phase transition, the specific shear viscosity still shows a valley shape in its temperature dependence as a result of the competing effects discussed above.

Shear Viscosity in Heavy-Ion Collisions

We now move to the studies of the shear viscosity in intermediate-energy heavy-ion collisions simulated by the BUU and IQMD transport models. The shear viscosity is calculated by the Green-Kubo formula or Danielewicz's parametrization with the density and temperature extracted using the methods discussed in the previous section. Results with different NN cross sections are compared, and the correlation between the shear viscosity and the elliptic flow has also been studied.

Energy Dependence of Shear Viscosity

The head-on ^{197}Au+^{197}Au collision is simulated both in BUU and IQMD models for the consideration of equilibrium condition of the Green-Kubo formula. The heavier the collision system, the more NN collisions occur. Nevertheless, the smaller the impact parameter, the more frequently the NN scatterings happen. Both the size of the system and the impact parameter may affect the equilibration of the formed nuclear matter in HIC. In Fig. 7, the plotted results are based on the BUU model when the incident energy is 50

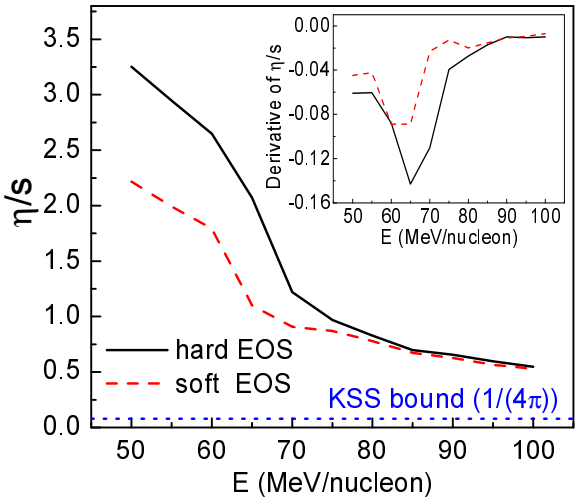

Fig. 8: (Color online) η/s as a function of beam energy for the head-on Au + Au collision in a spherical volume with a radius of 5 fm. The inset shows the derivative of η/s versus beam energy. Taken from Ref. [24].

MeV/u. The temperature is calculated from the momentum fluctuation method, while the entropy density is from the Gibbs formula. From panel (a), it is easy to see that anisotropy ratio R_p, which is a measure of the degree of equilibration reached in a heavy-ion reaction, increases from 0.5 to 1.0, reflecting that the systems is far from equilibrium from the very beginning and slowly approaches equilibrium as a result of the interactions between nucleons, and finally the system gets equilibrated after $t = 100$ fm/c. As for the temperature, it increases to a maximum value at about $t = 50$ fm/c and then decreases to a saturation value. As to the entropy per nucleon, it also reaches a saturation value after $t = 150$ fm/c. As expected, these three quantities reach their saturation values when a system reaches equilibrium since afterwards no dramatic changes happen for the thermal properties.

The value of η/s obtained from the Green-Kubo formula is plotted as a function of the incident energy after the system reaches equilibrium in Fig. 8, where two sets of nuclear equation of state are used. The η/s value shows a rapid fall as the increasing of the incident energy up to $E < 70$ MeV/u and then drops slowly to a value close to 0.5 when $E > 70$ MeV/u. Since the BUU equation is a one-body theory, fragmentation which originates from the fluctuation and correlation can not be treated properly in the present model. In this case, the specific viscosity decreases monotonically with increasing beam energy without a minimum value, and the phase transition behavior cannot be predicted in the BUU model.

In another study, the hot Thomas-Fermi formalisms are employed to study the thermal properties of the nuclear matter created in central intermediate-energy ^{197}Au+^{197}Au collisions based on the IQMD model. The time evolutions of temperature and entropy density are depicted in Fig. 9. Along the time scale of the collision, one can see that both values reach their maxima at about 20 fm/c and they evolve almost isochronously. After the compression stage the nuclear system begins to expand and some nucleons escape from the central region which is cooling down. The entropy density decreases more quickly than the temperature, and this is directly due to the quick escape of nucleons.

Figure 10(a) displays the extracted shear viscosity η as a function of the incident energy. It is very interesting to see that the shear viscosity alone also exhibits a minimum near 120 MeV/nucleon. Since the temperatures in post-equilibration stage are almost the same for the collisions at different energies, the value of the shear viscosity is mostly influenced by the tensor correlation, which reflects the fluctuation of dissipative fluxes. Figure 10(b) displays η/s as a function of the incident energy from 70 to 200 MeV/nucleon for the head-on Au + Au collisions. The η/s decreases quickly with the incident energy up to a platform of the minimum value at around 120 MeV/nucleon, and afterwards the curve weakly rises up. The minimum

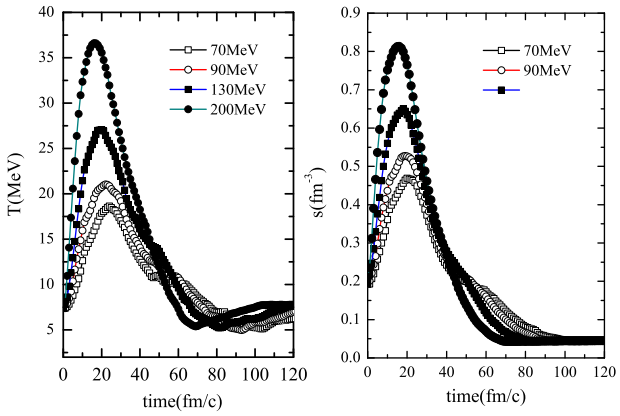

Fig. 9: (Color online) Time evolution of temperature (a) and entropy density (b) in the central region in heavy-ion collisions at different beam energies. Taken from Ref. [25].

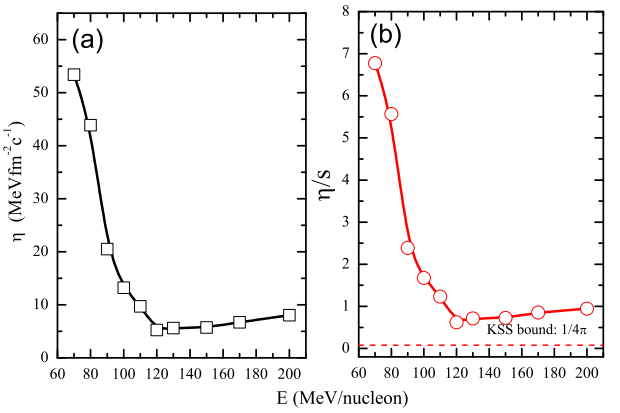

Fig. 10: (Color online) Shear viscosity η (a) and the specific shear viscosity η/s as a function of the incident energy for the head-on Au+Au collisions. Taken from Ref. [25].

value of the specific viscosity is around 0.6, i.e., about 7 times the KSS bound $(1/4\pi)$. As expected, all η/s values from the present study are larger than the KSS bound.

Shear Viscosity with Different Cross Sections

Since from a classical point of view the shear viscosity is inversely proportional to the NN scattering cross section, the in-medium behavior of which is less known, we have studied the specific viscosity η/s from different nucleon-nucleon cross sections by simply multiplying one coefficient C_σ in the IQMD model, i.e.,

$$\sigma_{NN} = C_\sigma \sigma_{NN}^{free}. \tag{29}$$

Three different situations are considered when C_σ is 0.5, 1.0, and 1.5, respectively. Consequently, the Danielewicz's parameterized function of the shear viscosity should be modified accordingly, i.e.,

$$\eta(\rho/\rho_0, T, C_\sigma) = \frac{\eta(\rho/\rho_0, T)}{C_\sigma}. \tag{30}$$

We can see that the larger the cross section, the smaller the shear viscosity is. It is intuitive that a larger NN cross section makes the transport of particle momentum more difficult.

Figure 11(a) shows the time evolution of the temperature with $C_\sigma = 1.0$ at different incident energies, and Fig. 11(b) shows the time evolution of the temperature when the incident energy is 130 MeV/nucleon but with different cross sections. For a given beam energy, the temperature increases at first, then reaches a local maximum about $t = 20$ fm/c and decreases till saturated at about $t = 80$ fm/c. The higher the

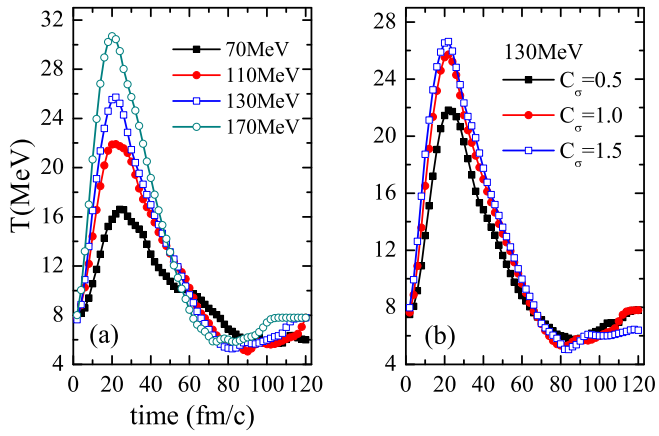

Fig. 11: (Color online) Time evolution of the temperature inside the central region at normal NN cross section at different incident energies (a), or at 130 MeV/nucleon but with different σ_{NN} (b). Taken from Ref. [26].

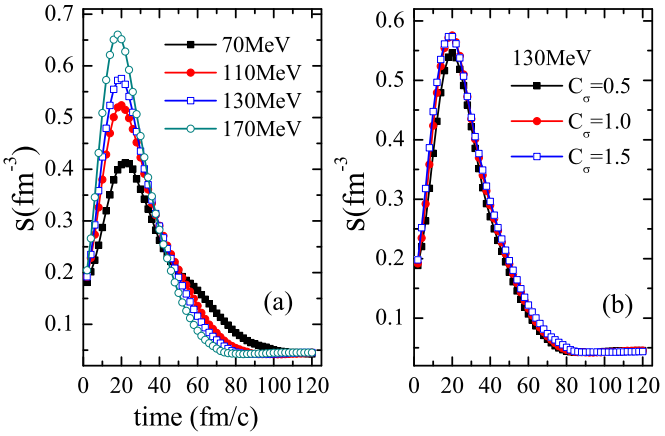

Fig. 12: (Color online) Same as Fig. 11 but for the entropy density. Taken from Ref. [26].

incident energy, the larger the maximum value of the temperature can be reached. The corresponding time for the maximum value of the temperature is a little earlier than that for the density and the kinetic density, according to our calculation. In panel (b), it is found that the larger cross section makes the system a little hotter. The reason is that there are more frequent NN collisions as σ_{NN} becomes larger, making the transformation from the longitudinal energy to the thermal energy more efficiently. The time evolution of the entropy density is plotted in Fig. 12. It is found that the entropy density almost synchronically evolves with the temperature. It is seen that the higher the incident energy and NN cross section, the larger the entropy density is.

Figure 13 displays the time evolution of shear viscosity, and one can see η shows an increase in the earlier stage and then drops with time. According the Danielewicz's parameterization, the shear viscosity depends on both the temperature and the density which vary with time. Roughly speaking, the shear viscosity increases in the compression stage and decreases as the system expands. Figure 13(b) shows that there is a big enhancement when the NN cross section is scaled by $C_\sigma = 0.5$, as demonstrated in Eq. (30), i.e., the smaller the NN cross section, the larger the shear viscosity is.

When the entropy density is taken into account, the ratio of the shear viscosity to the entropy density shows a minimum near the maximum compression point as shown in Fig. 14. From the hydrodynamical point of view, the smaller the η/s, the more perfect the matter looks like. In this sense, the nuclear matter becomes a more ideal-like liquid around the most compressible point in comparison with other evolution stages. But it is noteworthy that this minimum behavior of η/s is just a transient process. In addition, the extent of approaching an ideal-like liquid of the nuclear matter is growing up with the increase of beam

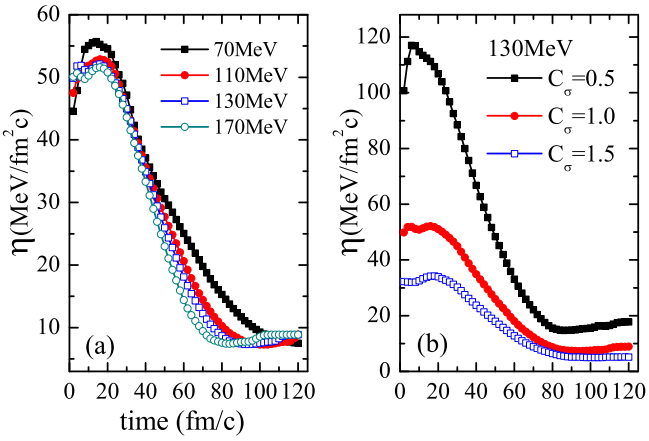

Fig. 13: (Color online) Same as Fig. 11 but for the shear viscosity η of the central fireball. Taken from Ref. [26].

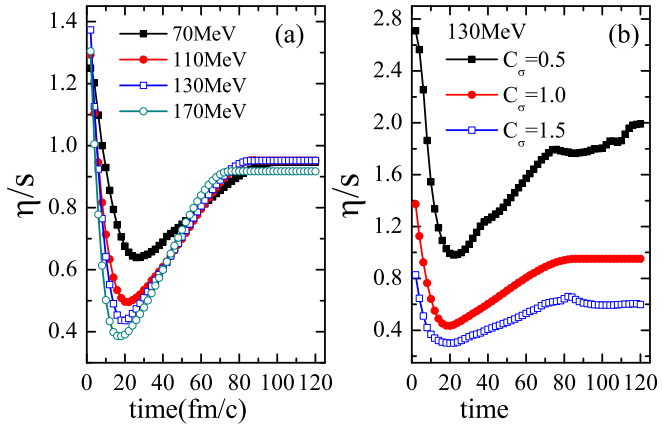

Fig. 14: (Color online) Same as Fig. 11 but for the ratio of the shear viscosity to the entropy density η/s of the central nuclear fireball. Taken from Ref. [26].

energy. In relativistic energy domain, the η/s of QGP becomes very small and close to $1/4\pi$ (KSS bound), even closer to a perfect liquid.

Figure 15 shows a correlation of the above average η/s versus the temperature for different given freeze-out densities (a) and with different σ_{NN} (b). From Fig. 15(a) we observe that there exhibits a local minimum of η/s with a value of 0.76 to 0.84 (about 9-10 times of KSS bound), depending on the freeze-out density in the range of 8 - 12 MeV of the temperature, and this phenomenon shall be related to the nuclear liquid-gas phase transition. With the increase of the freeze-out density, we observe that the minimal value of η/s decreases while its corresponding temperature increases. The latter can be understood by the transition temperature/pressure increases with the freeze-out density as expected by the pressure-density phase diagram [53, 54]. In contrast to the sensitivity of η/s to the freeze-out density, Fig. 15(b) demonstrates the time-averaged η/s when the system is given a freeze-out density of ρ/ρ_0 between 0.2 and 0.3. Again the larger the NN cross section, the smaller the η/s is, and the minimum of η/s is shifted to a higher temperature for a smaller NN cross section.

Correlation between Shear Viscosity and Elliptic Flow

In relativistic HIC, efforts have been made to extract the specific viscosity of the produced QGP from the correlation between the specific viscosity and the elliptic flow v_2, see, e.g., Ref. [50]. It would be interesting to see whether this correlation still holds in HIC at intermediate energies. However, it is known that the dynamics in intermediate-energy HIC is more complicated, as the expansion of the participant matter may

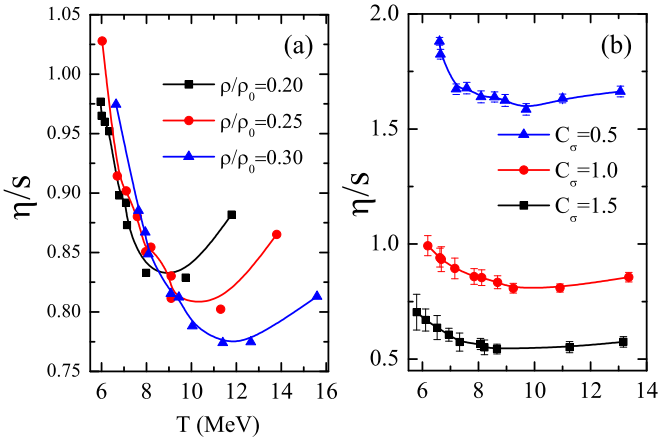

Fig. 15: (Color online) The average of η/s as a function of temperature at different freeze-out densities (a) and different cross sections (b). Taken from Ref. [26].

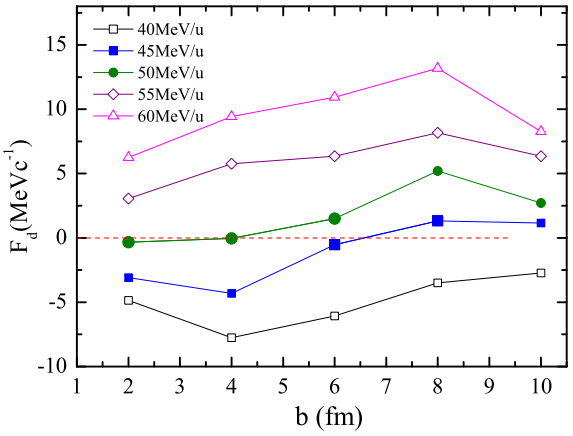

Fig. 16: (Color online) The extracted slope parameter F_d of the directed flow as a function of the impact parameter b in heavy-ion collisions at different beam energies. Taken from Ref. [56].

suffer from the blocking effect from the spectator, leading to a negative v_2 at intermediate energies but a positive one at higher or lower collision energies [55]. In this work we choose to study the correlation between the shear viscosity and v_2 at balance energy when the directed flow vanishes, to set a baseline on the collision geometry effect on v_2. For more detailed discussions on this argument, we refer the readers to Ref. [56].

The slope parameter of the directed flow in non-central heavy-ion collisions can be expressed as

$$F_d = \frac{d\langle p_x/A\rangle}{d(y/y_b)}, \tag{31}$$

where p_x is the projection of the transverse momentum in the reaction plane, A is the number of nucleons, and y/y_b is the particle rapidity y normalized by the beam rapidity y_b. The extracted F_d from the IQMD model versus the impact parameter b at different beam energies is shown in Fig. 16. The dashed line of $F_d = 0$ is plotted to guide eyes. With the increase of the impact parameter, it is seen that the $|F_d|$ generally increases, passes through a maximum value, and diminishes in most peripheral collisions. Besides, F_d is negative at lower energy of 40 MeV/u, positive at higher energies of $55-60$ MeV/u, and zero around $45-50$ MeV/u. The collision energies and impact parameters with F_d most close to 0 are: [50 MeV/u, 2 fm], [50 MeV/u, 4 fm], [50 MeV/u, 6 fm], [45 MeV/u, 6 fm], and [45 MeV/u, 8 fm], respectively. In these collisions, the effect from the mean field and NN scatterings cancel each other so that the influence of the blocking from the spectator matter on the elliptic flow are negligible. The elliptic flow is defined as the second-order

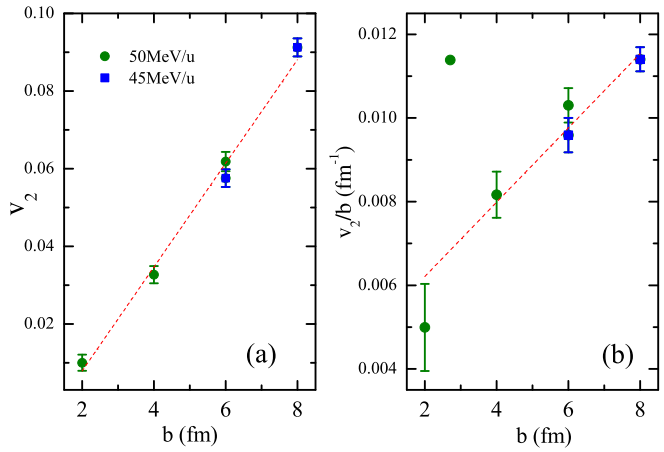

Fig. 17: (Color online) The elliptic flow and that scaled by the impact parameter at balance energies and corresponding impact parameters. The dashed lines are plotted to guide eyes. Taken from Ref. [56].

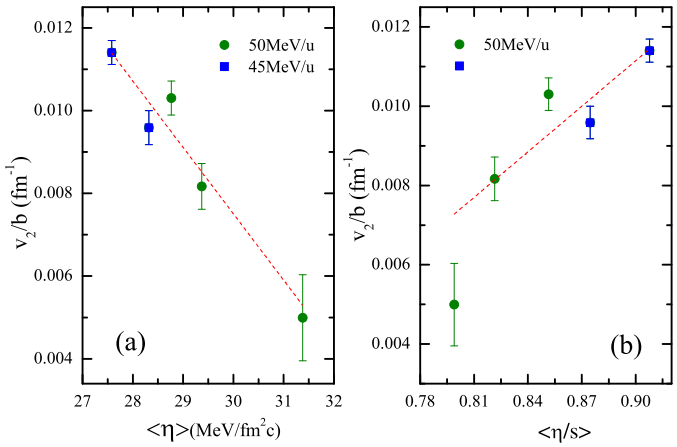

Fig. 18: (Color online) The scaled elliptic flow as a function of average shear viscosity and specific viscosity at balance energies and corresponding impact parameters. The dashed lines are plotted to guide eyes. Taken from Ref. [56].

harmonic coefficient of Fourier expansion of the particle azimuthal distribution

$$v_2 = \langle \cos(2\phi) \rangle = \left\langle \frac{p_x^2 - p_y^2}{p_x^2 + p_y^2} \right\rangle, \tag{32}$$

where ϕ is the azimuthal angle, p_x and p_y are the projections of the transverse momentum parallel and perpendicular to the reaction plane, respectively, and the bracket denotes the average over all the particles. The elliptic flow can be determined by the collective motion resulting from the rotation of the compound system, the expansion of the hot and compressed participant matter, and the possible modification by the shadowing effect of the cold spectator matter. Similar to the directed flow, generally the elliptic flow first increases with increasing impact parameter, reaches a maximum in mid-central collisions, and then decreases at large centralities. In this work the emitted light fragments of charge number $Z \leq 3$ including protons and neutrons at mid-rapidity $|y/y_b| \leq 0.1$ are employed to calculate the elliptic flow at freeze-out. The impact parameter dependence of v_2 and that scaled by the impact parameter is shown in panel (a) and panel (b) of Fig. 17, respectively. The positive value of v_2 indicates that an in-plane emission of particles is observed at balance energies. It is shown in panel (a) that v_2 increases linearly with increasing impact parameter, and the v_2 at [45 MeV/u, 8 fm] is about 10 times that at [50 MeV/u, 2 fm]. After scaled by the impact parameter, this difference is reduced to about 2 times as shown in panel (b), and we argue that the remaining difference is due to the viscous effect in intermediate-energy heavy-ion collisions.

Combing the results of the shear viscosity from Danielewicz's parameterization and entropy density from HTTF formalism with Fig. 17, the correlations between v_2/b and $\langle\eta\rangle$ as well as $\langle\eta/s\rangle$ are exhibited in panel (a) and (b) of Fig. 18, respectively. It is found that v_2/b decreases almost linearly with increasing average shear viscosity $\langle\eta\rangle$. This shows that a stronger interaction, which leads to a smaller shear viscosity, is more efficient in transforming the initial eccentricity to the final elliptic flow, consistent with the findings in heavy-ion collisions at ultra-relativistic energies. On the other hand, v_2/b somehow mostly increases with increasing average specific viscosity $\langle\eta/s\rangle$, different from that in ultra-relativistic heavy-ion collisions. This might be due to the stronger dissipation in the hadronic phase than in the partonic phase, which leads to a different behavior of the entropy density in the former case.

CONCLUSIONS

We summarized our recent studies on the specific viscosity η/s of hot nuclear matter with temperature around tens MeV based on an isospin-dependent quantum molecular dynamics (IQMD) model and a Boltzmann-Uehling-Uhlenbeck (BUU) model. Both the systems of intermediate-energy heavy-ion collisions as well as nuclear matter with different temperatures and densities are employed. Furthermore, the thermal and transport properties are also calculated from different methods, including the hot Thomas-Fermi formula, the momentum fluctuation, the Green-Kubo formula, Pawl Danielewicz's parameterized function, the classical kinetic theory, and the relaxation time approach. In the case of a hot nuclear source, the minimum of η/s exists when the density of nuclear matter is small (from 0.05 to 0.07 fm^{-3}), but a saturation value of η/s can be reached at higher densities. From the relaxation time approach together with the Gibbs condition for constructing the nuclear liquid-gas phase transition, the minimum of η/s is also observed in the vicinity of a first-order phase transition for symmetric nuclear matter or a second-order phase transition for asymmetric nuclear matter. It is found that the specific viscosity in heavy-ion collisions decreases with increasing temperature or incident energy then reaches a saturation value in the BUU transport model study or shows a minimum in the IQMD transport model study. Besides, the influence of the in-medium nucleon-nucleon cross section is also studied in the framework of the IQMD model. It is found that the larger the nucleon-nucleon cross section, the smaller the η/s is, which means that the nuclear matter behaves more like the ideal fluid. Furthermore, we have studied the correlation between the shear viscosity and the elliptic flow in non-central heavy-ion collisions at intermediate energies. Our study may shed light on measuring the shear viscosity of nuclear matter experimentally, which may serve as a signal of the occurrence of nuclear liquid-gas phase transition in intermediate-energy heavy-ion collisions.

This work is supported by the Major State Basic Research Development Program of China under contract Nos. 2014CB845401, 2013CB834405 and 2015CB856904, National Natural Science Foundation of China under contract Nos. 11421505, 11175231, and 11475243, Knowledge Innovation Project of CAS under Grant No. KJCX2-EW-N01, the "100-talent plan" of Shanghai Institute of Applied Physics under Grant No. Y290061011 from the Chinese Academy of Sciences, and the "Shanghai Pujiang Program" under Grant No. 13PJ1410600.

REFERENCES

[1] D. H. E. Gross, Rep. Prog. Phys. **53**, 605 (1990).
[2] J. P. Bondorf *et al.*, Phys. Rep. **257**, 133 (1995).
[3] J. Pochodzalla *et al.* (ALADIN Collaboration), Phys. Rev. Lett. **75**, 1040 (1995).
[4] Y. G. Ma, Phys. Rev. Lett. **83**, 3617 (1999); Eur. Phys. J. A **6**, 367 (1999).
[5] J. B. Natowitz *et al.*, Phys. Rev. Lett. **89**, 212701 (2002).
[6] S. Das Gupta, A. Z. Mekjian, and M. B. Tsang, Adv. Nucl. Phys. **26**, 89 (2001).
[7] B. Borderie and M. F. Rivet, Prog. Part. Nucl. Phys. **61**, 551 (2008).
[8] M. Veselsky and Y. G. Ma, Phys. Rev. C **87**, 034615 (2013).
[9] M. E. Fisher, Rep. Prog. Phys. **30**, 615 (1969); Physics **3**, 255 (1967).
[10] F. Gulminelli and M. D'Agostino, Eur. Phys. J. A **30**, 253 (2006).
[11] O. Lopez and M.F. Rivet, Eur. Phys. J. A **30**, 263 (2006).
[12] Y. G. Ma *et al.*, Phys. Rev. C **71**, 054606 (2005).
[13] N. Demir and S. A. Bass, Phys. Rev. Lett. **102**, 172302 (2009).
[14] R. Lacey *et al.*, Phys. Rev. Lett. **98**, 092301 (2007).
[15] J. W. Chen and E. Nakano, Phys. Lett. B **647**, 371 (2007).
[16] J. I. Kapusta and T. Springer, Phys. Rev. D **78**, 066017 (2008).
[17] A. Majumder, B. Müller, and X. N. Wang, Phys. Rev. Lett. **99**, 192301 (2007).
[18] J. Noronha-Hostler, J. Noronha, and C. Greiner, Phys. Rev. Lett. **103**, 172302 (2009).

[19] J. W. Chen, Y. H. Li, Y. F. Liu, and E. Nakano, Phys. Rev. D **76**, 114011 (2007).
[20] P. Danielewicz, Phys. Lett. B **146**, 168 (1984).
[21] L. Shi and P. Danielewicz, Phys. Rev. C **68**, 064604 (2003).
[22] S. Pal, Phys. Lett. B **684**, 211 (2010); Phys. Rev. C **81**, 051601(R) (2010).
[23] N. Auerbach and S. Shlomo, Phys. Rev. Lett. **103**, 172501 (2009).
[24] S. X. Li, D. Q. Fang, Y. G. Ma, and C. L. Zhou, Phys. Rev. C **84**, 024607 (2011); Nucl. Sci. Tech. **22**, 235 (2011).
[25] C. L. Zhou *et al.*, Euro. Phys. Lett. **98**, 66003 (2012).
[26] C. L. Zhou, Y. G. Ma, D. Q. Fang, and G. Q. Zhang, Phys. Rev. C **88**, 024604 (2013).
[27] J. Xu, Nucl. Sci. Tech. **24**, 050514 (2013); J. Xu, Phys. Rev. C **84**, 064603 (2011).
[28] J. Xu *et al.*, Phys. Lett. B **727**, 244 (2013).
[29] L. P. Csernai, J. I. Kapusta, and L. D. McLerran, Phys. Rev. Lett. **97**, 152303 (2006).
[30] P. K. Kovtun, D. T. Son, and A. O. Starinets, Phys. Rev. Lett. **94**, 111601 (2005).
[31] G. Policastro, D. T. Son, and A. O. Starinets, Phys. Rev.Lett. **87**, 081601 (2001).
[32] J. Aichelin, Phys. Rep. **202**, 233 (1991).
[33] C. Hartnack *et al.*, Eur. Phys. J. A **1**, 151 (1998).
[34] W. Bauer, G. F. Bertsch, W. Cassing, and U. Mosel, Phys. Rev. C**34**, 2127 (1986).
[35] G. F. Bertsch and S. Das Gupta, Phys. Rep. **160**, 189 (1988).
[36] D. T. Khoa, N. Ohtsuka, A. Faessler, *et al.*, Nucl. Phys.**A 542**, 671 (1992).
[37] T. Khoa, N. Ohtsuka, A. Faessler, *et al.*, Nucl. Phys.**A 548**, 102 (1992).
[38] P. K. Puri, N. Ohtsuka, E. Lehmann, *et al.*, 1992 GSI Scientific Report 93-1, GSI, Darmstadt, Germany, p. 126.
[39] S. Wuenschel, A. Bonasera, L.W. Maya *et al.*, Nucl. Phys. A **843**, 1 (2010); H. Zheng and A. Bonasera, Phys. Lett. B **696**, 178 (2011).
[40] R. Kubo, Rep. Prog. Phys. **29**, 255 (1966).
[41] P. Danielewicz, Phys. Lett. B **146**, 168 (1984).
[42] P. Danielewicz, B. Barker, and J. Li, AIP Conf. Proc. **1128**, 104 (2009).
[43] K. Huang, Statistical Mechanics, 2nd ed. (John Wiley & Sons, New York, 1987).
[44] C.B. Das, S. Das Gupta, C. Gale, and B.A. Li, Phys. Rev. C **67**, 034611 (2003).
[45] S.K. Charagi and S.K. Gupta, Phys. Rev. C **41**, 1610 (1990).
[46] B.A. Li and L.W. Chen, Phys. Rev. C **72**, 064611 (2005).
[47] V.R. Pandharipande and S.C. Pieper, Phys. Rev. C **45**, 791 (1992).
[48] A. Muronga, Phys. Rev. C **69**, 044901 (2004).
[49] D. Q. Fang *et al.*, Phys. Rev. C **89**, 047601 (2014).
[50] H.C. Song, S.A. Bass, U. Heinz, T. Hirano, and C. Shen, Phys. Rev. Lett. **106**, 192301 (2011).
[51] J. Xu, L. W. Chen, B. A. Li, and H. R. Ma, Phys. Rev. C **77**, 014302 (2008).
[52] J. W. Chen, Y. H. Li, Y. F. Liu, and E. Nakano, Phys. Rev. D **76**, 114011 (2007).
[53] S. Das Gupta, A. Z. Mekjian, and M.B. Tsang, Adv. Nucl. Phys. **26**, 89 (2001).
[54] Y. G. Ma, Q. M. Su, W. Q. Shen, J. S. Wang, D. Q. Fang, X. Z. Cai, H. Y. Zhang, and D. D. Han, Eur. Phys. J. A **4**, 217 (1999).
[55] P. Danielewicz, R. Lacey, and W. G. Lynch, Science **298**, 1592 (2002).
[56] C. L. Zhou *et al.*, Phys. Rev. C **90**, 057601 (2014).

NEUTRON-SKIN THICKNESS OF ^{208}Pb, AND SYMMETRY-ENERGY CONSTRAINTS FROM THE STUDY OF THE ANTI-ANALOG GIANT DIPOLE RESONANCE

A. Krasznahorkay[1,*] , M. Csatlós[1], L. Csige[1], T.K. Eriksen[2], F. Giacoppo[2], A. Görgen[2], T.W. Hagen[2], M.N. Harakeh[3,4], R. Julin[5], P. Koehler[2], N. Paar[6], S. Siem[2], L. Stuhl[1], T.G. Tornyi[1], D. Vretenar[6]

[1]Inst. for Nucl. Res. (MTA-Atomki), H-4001 Debrecen, P.O. Box 51, Hungary
[2]Department of Physics, University of Oslo, N-0316 Oslo, Norway
[3]KVI, University of Groningen, Groningen, The Netherlands
[4]GANIL, CEA/DSM-CNRS/IN2P3, 14076 Caen, France
[5]Department of Physics, University of Jyvškylä, Jyvškylä, FIN-40014, Finland
[6]Physics Department, Faculty of Science, University of Zagreb, Croatia

Abstract

The ^{208}Pb(p,$n\gamma\bar{p}$) ^{207}Pb reaction at a beam energy of 30 MeV has been used to excite the anti-analog of the giant dipole resonance (AGDR) and to measure its γ-decay to the isobaric analog state in coincidence with proton decay of IAS. The energy of the transition has also been calculated with the self-consistent relativistic random-phase approximation (RRPA), and found to be linearly correlated to the predicted value of the neutron-skin thickness (ΔR_{pn}). By comparing the theoretical results with the measured transition energy, the value of 0.190 $\pm$ 0.028 fm has been determined for ΔR_{pn} of ^{208}Pb, in agreement with previous experimental results. The AGDR excitation energy has also been used to calculate the symmetry energy at saturation ($J = 32.7\pm0.6$ MeV) and the slope of the symmetry energy ($L = 49.7\pm4.4$ MeV), resulting in more stringent constraints than most of the previous studies.

INTRODUCTION

There is a renewed interest in measuring the thickness of the neutron skin [1, 2, 3, 4], because it constrains the symmetry-energy term of the nuclear equation of state. The precise knowledge of the symmetry energy is essential not only for describing the structure of neutron-rich nuclei, but also for describing the properties of the neutron-rich matter in nuclear astrophysics.

The symmetry energy determines to a large extent, through the Equation of State (EoS), the proton fraction of neutron stars [5], the neutron skin in heavy nuclei [6] and enters as input in the analysis of heavy-ion reactions [7, 8]. Furnstahl [6] demonstrated that in heavy nuclei an almost linear empirical correlation exists between the neutron-skin thickness and theoretical predictions for the symmetry energy of the EoS in terms of various mean-field approaches. This observation has contributed to a revival of an accurate determination of the neutron-skin thickness in neutron-rich nuclei [9, 4, 3, 1]. In this work, we suggest a new method for measuring the neutron-skin thickness with unprecedented accuracy.

Recently, we have shown that the energy difference between the anti-analog giant dipole resonance (AGDR) and the isobaric analog state (IAS) is very sensitively related to the corresponding neutron-skin thickness [10]. We have also calculated the energy of the AGDR for the ^{208}Pb isotope using the state-of-the-art fully self-consistent relativistic proton-neutron quasi-particle random-phase approximation and compared to the available experimental data after correcting them for the admixture of the isovector spin giant dipole resonance (IVSGDR) [11].

Yasuda *et al.* [12] separated the AGDR from other excitations, such as the IVSGDR, by multipole decomposition analysis of the ^{208}Pb($\vec{p},\vec{n}$) reaction at a bombarding energy of E$_p$ =296 MeV. The polarization transfer observables were found to be useful for carrying out this separation. The energy difference between the AGDR and the IAS was determined to be $\Delta E_{AGDR-IAS} = 8.69 \pm 0.36$ MeV, where the uncertainty includes both statistical and systematic contributions. Using our theoretical results [11] a neutron-skin thickness of $\Delta R_{pn} = 0.216 \pm 0.046 \pm 0.015$ fm could be obtained, where the first and second uncertainties are the experimental and theoretical one, respectively.

The aim of the present work is to determine $\Delta E_{AGDR-IAS}$ with high precision by measuring the energy of the corresponding γ-transition. The direct γ-branching ratio of the AGDR to the IAS is expected to be similar to that of the isovector giant dipole resonance (IVGDR) to the ground-state (g.s.) in the parent nucleus, which can be calculated from the parameters of the IVGDR [13].

*E-mail: kraszna@atomki.hu

THE ANTI-ANALOG GIANT DIPOLE RESONANCE AND ITS γ-DECAY

Due to the isovector nature of the (p,n) reaction, the strength of the E1 excitation is distributed into T_0-1, T_0 and T_0+1 components, where T_0 is the g.s. isospin of the initial nucleus. The relevant Clebsch-Gordan coefficients [14] show, that the T_0-1 component (AGDR) is favored compared to the T_0 and T_0+1 ones by factors of about T_0, and $2T_0^2$, respectively. According to the work of Osterfeld [14], the non-spin-flip transition is preferred at low bombarding energies below 50 MeV.

Dipole resonances were excited earlier at such low energies in the ^{208}Pb(p,n) reaction by Sterrenburg *et al.* [15], and Nishihara *et al.* [16] at E_p= 45 MeV and 41 MeV, respectively. However, it was shown experimentally [17, 18] that the observed ΔL= 1 resonance was a superposition of all possible IVSGDR modes and the non-spin-flip dipole AGDR even at these low bombarding energies.

The expected γ-decay properties of the states excited in ^{208}Bi are shown in Fig. 1 together with the proton-decay branching ratios of the IAS [19, 20, 21].

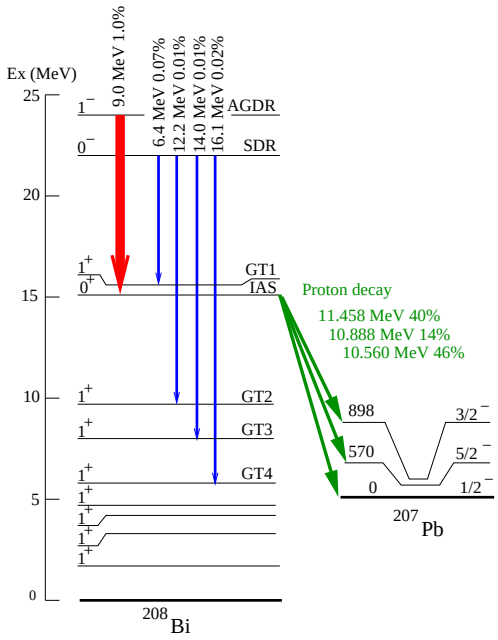

Fig. 1: Energy levels excited in the ^{208}Pb$(p,n)^{208}$Bi reaction and their expected γ-decay branching ratios (red and blue arrows). The energies and branching ratios of the proton decay of the IAS and GT resonance to the low-lying states in ^{207}Pb are also shown (green arrows).

Crawley and Miller [20] studied the ^{208}Pb(p,np)^{207}Bi reaction at many bombarding energies from 21.3 to 35 MeV by using a standard counter telescope of cooled silicon detectors for identifying the protons. Nice mono-energetic peeks have been observed at backward angles, which were identified as the proton decay of the IAS excited in ^{208}Bi to the low-lying states in ^{207}Bi.

The proton-decay of the IAS in ^{208}Bi was also investigated by Bhowmik et al., [22] by using the ^{208}Pb(p,np) ^{207}Bi reaction at E_p=25 MeV. They have measured the protons in coincidence with the neutrons and observed the same proton groups as Crawley and Miller [20] before. By measuring the time-of flight of the neutrons they could even set gates for different excitation energy regions around the IAS and well above to that. They could observe the same proton groups in coincidence with low-energy neutrons (E_n= 1.15-2.0 MeV) as in coincidence with the IAS neutrons. The excitation energy corresponding to E_n= 1.15-2.0 MeV is about E_x= 24-25 MeV, which is the energy of the AGDR. Such results suggested a relatively strong γ-transition between the AGDR and the IAS. The branching ratio of such transition can be bigger than the direct γ-branching ratio observed earlier from the IVGDR to the g.s. of ^{208}Pb ($B_\gamma \approx 1\%$) because of the bigger contribution of the statistical γ-transitions.

The observed γ-ray branching ratio of the IVGDR to the g.s. of ^{208}Pb is about 1% [13]. In contrast, in the investigation of the electromagnetic decay properties of the IVSGDR to the low-lying Gamow-Teller (GT) states by Rodin and Dieperink [23] the γ-decay branching ratio was found in the range of 10^{-4}.

EXPERIMENTAL METHODS AND RESULTS

The experiment, aiming at studying the neutron-skin thickness of ^{208}Pb, was performed at the Oslo Cyclotron Laboratory (OCL) with 30 MeV proton beam bombarding a 5.5-mg/cm^2 thick, self-supporting metallic ^{208}Pb target and a 1 mg/cm^2 thick ^{12}C target for energy calibration.

In the experiment, the proton-decay of the IAS was used as a signature of the de-excitation of the IAS. The γ-transition from the decay of the AGDR was measured in coincidence with such proton lines. These particle-γ coincidences were measured with the SiRi particle telescope and CACTUS γ-detector systems [24, 25]. The SiRi detectors were placed at backward angles, covering an angular range of Θ=126°-140° relative to the beam axis. The ΔE and E detectors had thicknesses of 130 μm and 1550 μm, respectively. The CACTUS array consists of 28 collimated 5"$\times$ 5" NaI(Tl) detectors with a total efficiency of 15.2% for E_γ= 1.33 MeV.

A typical proton spectrum is shown in Fig. 2. The proton transitions populating the low-lying states in ^{207}Pb are marked by arrows and used for gating the γ rays. Similar measurements has also been performed by using a ^{12}C target to check the background coming from the carbon buildup on the ^{208}Pb target.

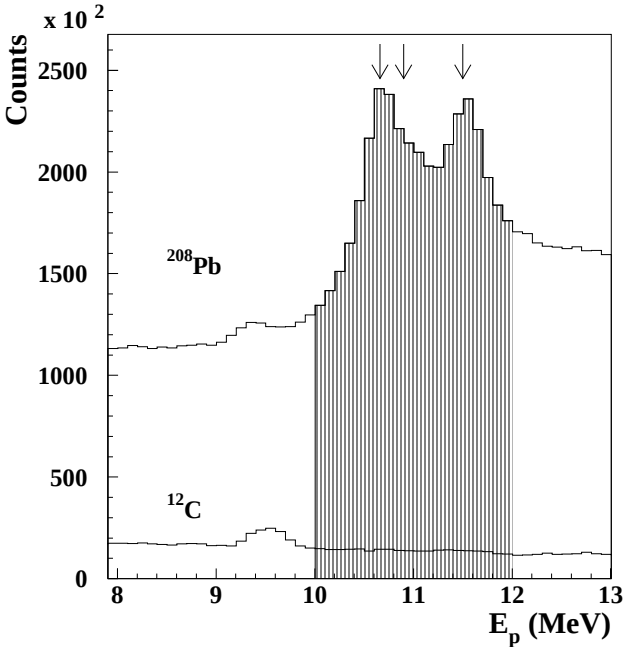

Fig. 2: Proton energy spectrum measured in coincidence with the γ-rays having energies between 0.5 and 10.0 MeV by using ^{208}Pb and ^{12}C targets.

The energy of the γ rays was measured in coincidence with the protons stemming from the decay of the IAS in ^{208}Bi. The random coincidence contribution was subtracted as well as the contribution of the proton decay of the GTR, which represents a broad ($\Gamma \approx$2.9 MeV) background in the proton spectrum.

The centroid of the γ transition was shifted towards lower energies as a result of the decreasing efficiency of the NaI detectors. In order to correct this effect, the spectrum was normalized with the detector response function that was extracted experimentally in Refs. [24, 25]. The γ-ray energy spectrum, as a result of these corrections, is presented in Fig. 3 together with the statistical error bars.

The double line at 4.44 MeV comes partly from carbon contamination of the target excited in the (p,$p\prime$) reaction. Similarly the broad transition around 13.3 MeV may come also from carbon contamination. Spectrum b) shows the γ-spectrum obtained by with a ^{12}C target, but otherwise with similar conditions like spectrum a). The strongest proton line we observed from the ^{12}C(p,p') reaction in the 8-13 MeV energy range has an energy of 9.6 MeV, which corresponds to the excitation of the 15.11 MeV state in ^{12}C. Spectrum c) shows the γ-spectrum measured in coincidence with such proton line. Unfortunately, the energy response of the CACTUS spectrometer was very nonlinear at that energy.

Additionally, NaI detectors are sensitive to low-energy neutrons [26]. These are captured mostly by iodine and the ^{127}I(n,γ) reaction produces γ-rays with an energy of E$_\gamma$=6.826 MeV, which interfere with the low-energy side of the AGDR $\rightarrow$ IAS transition. At higher neutron energies the neutron-capture cross section decreases drastically, and the response of the NaI detectors for MeV neutrons is constant as a function of

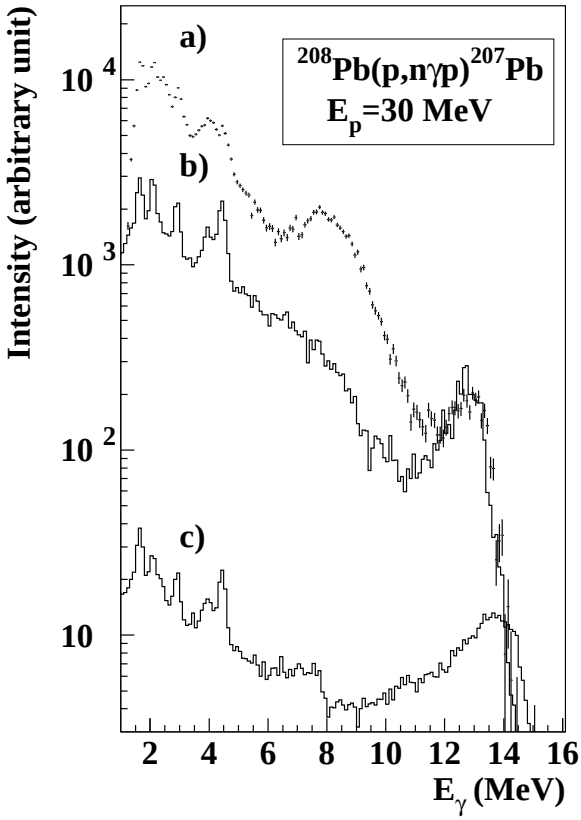

Fig. 3: a): The γ-ray energy spectrum measured in coincidence with protons of energy $10 \leq E_p \leq 12$ MeV using ^{208}Pb target. The random coincidences were subtracted and the spectrum was corrected for the efficiency of the NaI detectors. b): expected background measured by using a ^{12}C target, but the other conditions are the same like in case a). c): γ-ray energy spectrum measured in coincidence with protons of energy $9.1 \leq E_p \leq 9.9$ MeV using the ^{208}Pb target.

energy.

The NaI detectors of the CACTUS setup were placed relatively close (d=22 cm) to the target. Therefore, the time-of-flight method could not be used to discriminate safely against neutrons produced in the ^{208}Pb(p,n) reaction and also in the decay of the giant resonances. The effect of these neutrons had to be carefully treated. On the other hand, according to previous experimental studies [15, 16], neutrons from the ^{208}Pb(p,n) reaction are ejected predominantly to forward directions, and the cross section of this reaction drops by one order of magnitude beyond 30 degrees. Since the smallest angle of the NaI detectors of the CACTUS setup was 39° with respect to the beam direction, the ejected neutrons did not disturb the γ-spectrum considerably.

Giant resonances (including the AGDR) decay also by neutrons, which are detected by CACTUS with high efficiency. However, such neutron emission goes to the low-lying states of ^{207}Bi, and therefore such neutrons are not in coincidence with the proton-decay of the IAS in ^{208}Bi. These neutrons contributed to the random coincidences only, which were subtracted.

Since the random coincidences in the proton-gated γ spectrum around $E_\gamma = 7$ MeV is dominated by neutrons, it can be used to eliminate the neutron-related events from the real coincidences by subtracting it with a weighting factor, which is defined by the ratio of the corresponding time windows. In the resulting $p-\gamma$ coincidence spectrum, the peak observed at 8 MeV represents γ-rays from the AGDR $\rightarrow$ IAS transition only.

The energy distribution of the γ rays was fitted by a Gaussian curve and a second-order polynomial background as shown in Fig. 3. The obtained energy and width of the transition are $E_\gamma = 8.090 \pm 0.013$ MeV and Γ =2.2 MeV. However, the energy calibration of the CACTUS spectrometer has been performed with photopeaks having significantly smaller width than giant resonances. In order to determine the real energy of the resonance, GEANT Monte-Carlo simulations were performed and convoluted with a Gaussian function with the width of the resonance. This analytical procedure caused a reduction of 10% in the position

of the peak, which was taken into account when the final energy of the transition was extracted. As a result, the transition energy is $E_\gamma = 8.90 \pm 0.02$ MeV including only the statistical error.

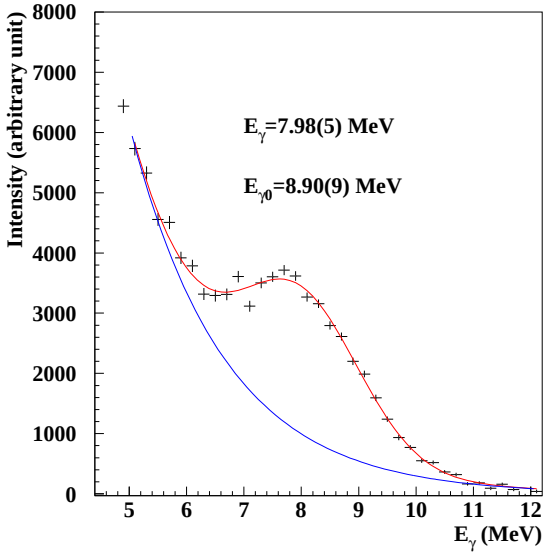

Fig. 4: The γ-ray energy spectrum measured in coincidence with protons. The solid line shows the result of the fit described in the text.

The contribution of the systematical error stems from the uncertainty of the energy calibration, which is estimated to be 1.0%, so the final transition energy is $E_{AGDR} - E_{IAS} = 8.90 \pm 0.09$ MeV. The energy and width of the transition agree well with the previously measured values of Refs. [15, 16] but having significantly smaller error bars.

THEORETICAL ANALYSIS

The AGDR and IAS excitation energies are calculated with the self-consistent relativistic proton-neutron random-phase approximation (pn-RRPA) [28, 29] based on the Relativistic Hartree (RH) model [27]. As in our previous studies of the AGDR [10, 11], the calculation is based on family of density-dependent meson-exchange (DD-ME) interactions, for which the constraint on the symmetry energy at saturation density has been systematically varied: J = 30, 32, 34, 36 and 38 MeV, and the remaining model parameters have been adjusted to accurately reproduce nuclear-matter properties (the saturation density, the compression modulus) and the binding energies and charge radii of a standard set of spherical nuclei [30]. These interactions were also used in Ref. [38] to study a possible correlation between the observed pygmy dipole strength (PDS) in ^{130,132}Sn and the corresponding values for the neutron-skin thickness. In addition, the relativistic functional DD-ME2 [31] will be also used in the calculation of the excitation energies of the AGDR with respect to the IAS. We note that the relativistic RPA with the DD-ME2 effective interaction predicts the dipole polarizability

$$\alpha_D = \frac{8\pi}{9} e^2 \; m_{-1} \tag{1}$$

(directly proportional to the inverse energy-weighted moment m_{-1}) for ^{208}Pb: α_D=20.8 fm^3, in agreement with the recently obtained experimental value: $\alpha_D = (20.1 \pm 0.6)$ fm^3 [4].

The results of the calculations for ^{208}Pb are shown in Fig. 5. The difference in the excitation energies of the AGDR and the IAS, calculated with the pn-RRPA based on the RH self-consistent solution for the g.s. of the target nucleus, is plotted as a function of the corresponding RH predictions for the neutron-skin thickness. For the excitation energy of the AGDR we take the centroid of the theoretical strength distribution, calculated in the energy interval above the IAS that corresponds to the measured spectrum of γ-ray energies: E$_\gamma$=6 to 14.8 MeV (Fig. 3). A single peak is calculated for the IAS. For the effective interactions with increasing value of the symmetry energy at saturation J = 30, 32, 34, 36 and 38 MeV (and correspondingly the slope of the symmetry energy at saturation [32]), one notices a linear decrease of $E(AGDR) - E(IAS)$ with increasing values of the neutron skin ΔR_{pn}. The value calculated with DD-ME2 (J = 32.3MeV) is denoted by a star.

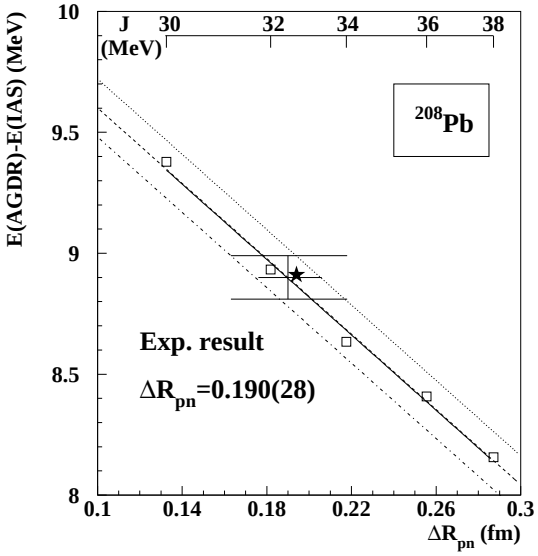

Fig. 5: The difference in the excitation energies of the AGDR and the IAS for the target nucleus ^{208}Pb, calculated with the pn-RRPA using five relativistic effective interactions characterized by the symmetry energy at saturation J = 30, 32, 34, 36 and 38 MeV (squares), and the interaction DD-ME2 (J = 32.3 MeV) (star). The theoretical values $E(AGDR) - E(IAS)$ are plotted as a function of the corresponding g.s. neutron-skin thickness ΔR_{pn}, and compared to the experimental value $E(AGDR) - E(IAS) = 8.90 \pm 0.09$ MeV.

The uncertainty of the theoretical predictions for the neutron-skin thickness is estimated around 10 %. This uncertainty was adopted for the differences between the neutron and proton radii for the nuclei ^{116}Sn, ^{124}Sn, and ^{208}Pb, when the parameters of the effective interactions with J = 30, 32, 34, 36 and 38 MeV, and DD-ME2 were adjusted [30, 31]. These interactions were also used to calculate the electric dipole polarizability and neutron-skin thickness of ^{208}Pb, ^{132}Sn and ^{48}Ca, in comparison to the predictions of more than 40 non-relativistic and relativistic mean-field effective interactions [2]. From the results presented in that work one can also assess the accuracy of the present calculation.

From the comparison to the experimental result for $E(AGDR) - E(IAS)$ we deduce the value of the neutron-skin thickness in ^{208}Pb: $\Delta R_{pn} = 0.190 \pm 0.028$ fm (including the 10% theoretical uncertainty). In Table I this value is compared to previous results obtained with a variety of experimental methods.

In parallel with our work the neutron-skin thickness has been extracted from coherent pion photoproduction cross sections [33]. The half-height radius and diffuseness of the neutron distribution are found to be 6.70±0.03(stat) fm and 0.55±0.01(stat)$^{+0.00}_{-0.025}$(sys) fm respectively, corresponding to a neutron skin thickness R_{pn} =0.15±0.03(stat)$^{+0.00}_{-0.03}$(sys) fm [33], which agrees well with our results.

The very good agreement with all available data supports the reliability of the method employed in the present study.

Tab. 1: The value of the neutron-skin thickness of ^{208}Pb determined in the present work compared to available data.

Method	Ref.	Date	ΔR_{pn} (fm)
(p,p) 0.8 GeV	[34]	1980	0.14 ± 0.04
(p,p) 0.65 GeV	[35]	1994	0.20 ± 0.04
($\alpha, \alpha\prime$) IVGDR 120 MeV	[13]	1994	0.19 ± 0.09
antiproton absorption	[36]	2001	0.18 ± 0.03
($\alpha, \alpha\prime$) IVGDR 200 MeV	[37]	2003	0.12 ± 0.07
pygmy res.	[38]	2007	0.180 ± 0.035
pygmy res.	[39]	2010	0.194 ± 0.024
($\vec{p}$,$\vec{p}\prime$)	[4]	2011	0.156 ± 0.025
parity viol. (e,e)	[1]	2012	0.33 ± 0.17
AGDR	pres. res.	2013	0.190 ± 0.028

CONSTRAINS ON THE SYMMETRY ENERGY FROM THE ENERGY DIFFERENCE OF THE AGDR AND THE IAS

In addition to correlating the excitation energy of the AGDR to the neutron skin, we have also used the AGDR to determine constraints on the symmetry energy at saturation density (J), and slope of the symmetry energy (L). Figure 5 shows that the J-L plot is particularly instructive because the AGDR constraint can be directly compared to those of the dipole polarizability and the pygmy resonances (PDR). It is important to note that constraints from AGDR, α_D, and PDR on this plot are obtained using the same family of energy density functionals, so one can determine whether different excitations probe the same property of the symmetry energy. From the AGDR analysis, we obtain constraints $J = 32.7 \pm 0.6$ MeV and $L = 49.7 \pm 4.4$ MeV.

Fig. 5 also shows a set of J-L constraints from a number of previous studies. A set of constraints from heavy ion collisions (HIC), within two standard deviations from the minimum, corresponding to a 95% confidence level, is confined by the two solid lines in the (L, J) plane [40]. The different rectangles in the figure denote the following constraints: from Quantum Monte Carlo (QMC) and neutron star [41], from nuclear binding energies (FRDM) [42], from isobaric analog states (IAS) [43, 44], from proton elastic scattering (^{208}Pb (p,p)) [45], from pygmy dipole resonances (PDR); LAND 2007 [38] and Carbone 2010 [39], from dipole polarizability experiment [4] and from the present result for the AGDR. The J-L constraints from α_D are reanalyzed using the same set of DD-ME effective interactions as in the study of AGDR. One can observe in figure that the mean values of J-L parameters obtained from the AGDR and α_D almost coincide, however, the AGDR provides more stringent constraints.

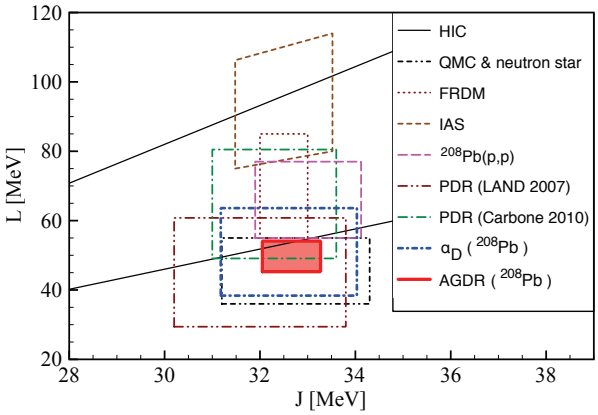

Fig. 6: (Color online) Constraints on the slope L and magnitude J of the symmetry energy at saturation density from different experiments compared to our present result (AGDR).

CONCLUSIONS

In this study we have analyzed the γ decay of the AGDR to the IAS excited in the ^{208}Pb(p,n$\gamma\bar{p}$) ^{207}Pb reaction. Using the experimental value obtained for the energy difference of the AGDR and the IAS, and comparing with the results of the RH+pn-RRPA model, we have been able to determine the corresponding neutron skin thickness in ^{208}Pb: $\Delta R_{pn} = 0.190 \pm 0.028$ fm. The agreement between the present result and values obtained in previous experiments using different methods is very good. In particular, the value obtained here is in accordance with results of a very recent high-resolution study of electric dipole polarizability α_D in ^{208}Pb [4], the correlation analysis of α_D and ΔR_{pn} [2], as well as with the Pb Radius Experiment (PREX) that used parity-violating elastic electron scattering at JLAB [1].

The measured energy difference between the AGDR and the IAS has also been used to constrain possible values of the symmetry energy at saturation density (J), and the slope of the symmetry energy (L). We have found good agreement between constraints that result from the AGDR and α_D, whereas the discrepancy with the constraint obtained from the pygmy resonance is probably due to the missing strength in PDR experiments [46]. Therefore, measurements of the AGDR might be important not only to constrain possible values of J and L, but also to understand differences between results obtained in various experiments. Since the mean values of J-L constraints obtained from the AGDR and α_D appear in excellent agreement, obviously the two very different collective modes of excitation in nuclei probe the same underlying physical content. The main advantage of the method based on the AGDR compared to the α_D analysis and most of the

previous studies is that it provides more stringent constraints on the symmetry energy parameters.

ACKNOWLEDGEMENTS

This work has been supported by the Hungarian OTKA Foundation No. K106035. This research was also supported by the European Union and the State of Hungary, co-financed by the European Social Fund in the framework of TÁMOP-4.2.2/B-10/1-2010-0024 and TÁMOP 4.2.4.A/2-11-1-2012-0001 'National Excellence Program'.

REFERENCES

[1] S. Abrahamyan et al., Phys. Rev. Lett. **108**, 112502 (2012).
[2] J. Piekarewicz et al., Phys. Rev.**C 85**, 041302 (2012).
[3] X. Roca-Maza, M. Centelles, X. Viñas, and M. Warda, Phys. Rev. Lett. **106**, 252501 (2011).
[4] A. Tamii et al., Phys. Rev. Lett. **107**, 062502 (2011).
[5] J. M. Lattimer and M. Prakash, Astrophys. J. **550**, 426 (2001); astro-ph/0002232.
[6] R. J. Furnstahl, Nucl. Phys. **A706**, 85 (2002).
[7] B. A. Li, C. M. Ko, and W. Bauer, Int. J. Mod. Phys. **E 7**, 147 (1998).
[8] Bao-An Li, Phys. Rev. Lett. **88**, 192701 (2002); Nucl. Phys. **A708**, 365 (2002).
[9] S. Terashima et al., Phys. Rev. **C 77**, 024317 (2008).
[10] A. Krasznahorkay et al., Phys. Lett. **B 720**, 428 (2013).
[11] A. Krasznahorkay et al., Phys. Scr. T **158**, 4018 (2013).
[12] J. Yasuda et al., Prog. Theor. Exp. Phys. 063D02 (2013).
[13] A. Krasznahorkay et al., Nucl. Phys. **A567**, 521 (1994).
[14] F. Osterfeld, Rev. Mod. Phys. **64**, 491 (1992).
[15] W.A. Sterrenburg, S.M. Austin, R.P. DeVito, A. Galonsky, Phys. Rev. Lett. **45**, 1839 (1980).
[16] S. Nishihara et al., Phys. Lett. **B 160**, 369 (1985).
[17] F. Osterfeld et al., Phys. Lett. **B 105**, 257 (1981).
[18] S. M. Austin et al., Phys. Rev. **C 63**, 034322 (2001).
[19] G.J. Igo et al., Phys. Rev. Lett. **22**, 724 (1969).
[20] G. M. Crawley and P. S. Miller, Phys. Rev. **C 6**, 306 (1972).
[21] A. Akimune et al., Phys. Lett. **B 323** (1994) 107.
[22] R. Bhowmik et al., Z. Physik A 280, 267 (1977).
[23] V. A. Rodin and A. E. L. Dieperink, Phys. Lett. **B 541**, 7 (2002).
[24] M. Guttormsen, A. Bürger, T. E. Hansen, and N. Lietaer, Nucl. Instrum. Meth. Phys. Res. **A 648**, 168 (2011).
[25] M. Guttormsen, A. Atac, G. Løvhøiden, S. Messelt, T. Ramsøy, J. Rekstad, T. F. Thorsteinsen, T. S. Tveter, and Z. Zelazny, Phys. Scr. **T32**, 54 (1990).
[26] O. Häusser et al., Nucl. Instrum Meth., **213** (1983) 301.
[27] D. Vretenar, A. V. Afanasjev, G. A. Lalazissis, and P. Ring, Phys. Rep. **409**, 101 (2005).
[28] N. Paar, P. Ring, T. Nikšić, and D. Vretenar, Phys. Rev. **C 67**, 034312 (2003).
[29] N. Paar, T. Nikšić, D. Vretenar, and P. Ring, Phys. Rev. **C 69**, 054303 (2004).
[30] D. Vretenar, T. Nikšić, and P. Ring, Phys. Rev.**C 68**, 024310 (2003).
[31] G. A. Lalazissis, T. Nikšić, D. Vretenar, and P. Ring, Phys. Rev. **C 71**, 024312 (2005).
[32] D. Vretenar, Y.F. Niu, N. Paar, J. Meng, Phys. Rev.**C 85**, 044317 (2012)
[33] C.M. Tarbert et al., arXiv:1311.0168v1 (2013).
[34] G.W. Hoffmann et al., Phys. Rev. **C 21**, 1488 (1980).
[35] V. E. Starodubsky and N. M. Hintz, Phys. Rev. **C 49**, 2118 (1994).
[36] A. Trzcinska et al., Phys. Rev. Lett. **87**, 082501 (2001).
[37] A. Krasznahorkay et al., Nucl. Phys. **A731**, 224 (2004).
[38] A. Klimkiewicz et al., Phys. Rev. **C 76**, 051603 (2007).
[39] A. Carbone et al., Phys. Rev. **C 81**, 041301 (2010).
[40] M.B. Tsang et al., Phys. Rev. **C 86**, 015803 (2012).
[41] A. W. Steiner and S. Gandolfi, Phys. Rev. Lett. **108**, 081102 (2012).
[42] P. Möller, W. D. Myers, H. Sagawa, and S. Yoshida, Phys. Rev. Lett. **108**, 052501 (2012).
[43] P. Danielewicz and J. Lee, AIP Conf. Proc. 1423, 29 (2012).
[44] P. Danielewicz and J. Lee, Nucl. Phys. **A818**, 36 (2009).
[45] J. Zenihiro et al., Phys. Rev. **C 82**, 044611 (2010); J. Zenihiro, Ph.D. Thesis, Kyoto University, 2011.
[46] N. Paar, J. Phys. G: Nucl. Part. Phys. 37, 064014 (2010).

SYMMETRY ENERGY: FROM NUCLEAR MATTER TO FINITE NUCLEI

V. M. Kolomietz[1] **and A. I. Sanzhur**[1]

[1]Institute for Nuclear Research, NAS of Ukraine, Prospekt Nauky 47, 03680 Kyiv, Ukraine

Abstract

We suggest a particular procedure of derivation of the beta-stability line and isotopic symmetry energy. The behavior of the symmetry energy coefficient $b(A, N-Z)$ is analyzed. We redefine the surface tension coefficient and the surface symmetry energy for an asymmetric nuclear Fermi-liquid drop with a finite diffuse layer. Following Gibbs-Tolman concept, we introduce the equimolar radius at which the surface tension is applied. The relation of the nuclear macroscopic characteristics like surface and symmetry energies, Tolman length, etc. to the bulk properties of nuclear matter is considered. The surface-to-volume symmetry energy ratio for several Skyrme-force parametrizations is obtained.

INTRODUCTION

Many static and dynamic features of nuclei are sensitive to the symmetry energy and the isospin degrees of freedom. The basic characteristics of isovector giant and isobar analog resonances [1], the isoscaling in nuclear fission and multifragmentation [2, 3, 4, 5, 6, 7, 8, 9] depend significantly on the isospin effects. The symmetry energy is also a key element for the derivation of the nuclear stability valley. The nuclear β-stability is determined by the balance of the isotopic symmetry, $E_{\rm sym}$, and the Coulomb, E_C, energies. However the extraction of both $E_{\rm sym}$ and E_C from the nuclear binding energy is not a simple problem because of their complicate dependency on the mass number $A = N + Z$ in finite nuclei with N neutrons and Z protons [10]. The standard procedure of extraction of the symmetry energy from a fit of mass formula to the experimental binding energies [11] is not free from ambiguities and does not allow one to separate the symmetry energy into the volume and surface contributions directly. In the present work, to study the structure of the β-stability line and both $E_{\rm sym}$ and E_C energies we use a particular procedure which is based on the dependence of the isospin shift of neutron-proton chemical potentials $\Delta\lambda(X) = \lambda_n - \lambda_p$ on the asymmetry parameter $X = (N - Z)/(N + Z)$ for nuclei beyond the β-stability line. This procedure allows us to represent the results for the A-dependence of the β-stability line and both energies $E_{\rm sym}$ and E_C in a transparent way, which can be easily used for the extraction of the smooth volume and surface contributions as well as their shell structure. Note also that our procedure of extraction of all values $E_C(A)$ and $E_{\rm sym}$ is partly model independent, that is, the theoretical models for calculations of the nuclear binding energy as well as the nucleon distributions are not involved. We only assume the commonly used parabolic dependence of the symmetry energy on the asymmetry parameter X. Due to the charge invariance of the nuclear forces this assumption is well justified for small values of X. A similar approach based on the isobaric multiplet mass equation [12] was used in Ref. [13] to study the Coulomb parameter within the modern nuclear mass model WS3.

The nucleus is a two component, charged system with a finite diffuse layer. This fact specifies a number of various peculiarities of the nuclear surface and symmetry energies: dependency on the density profile function, non-zero contribution to the surface symmetry energy, connection to the nuclear incompressibility, etc. The additional refinements appear due to the quantum effects arising from the smallness of nucleus. In particular, the curved interface creates the curvature correction to the surface energy $E_{\mathcal{S}}$ and the surface part of symmetry energy $E_{\rm sym}$ of order $A^{1/3}$ and can play the appreciable role in small nuclei as well as in neck region of fissionable nuclei. The presence of the finite diffuse layer in nuclei creates the problem of the correct definition of the radius and the surface of tension for a small drop with a diffuse interface. Two different radii have to be introduced in this case [14, 15]: the equimolar radius R_e, which gives the actual size of the corresponding sharp-surface droplet, and the radius of tension R_s, which derives, in particular, the capillary pressure. Bellow we will address this problem to the case of two-component nuclear drop. In general, the presence of the curved interface affects both the bulk and the surface properties. The curvature correction is usually negligible in heavy nuclei. However, this correction can be important in some nuclear processes. For example the yield of fragments at the nuclear multifragmentation or the probability of clusterization of nuclei from the freeze-out volume in heavy ion collisions [16]. In both above mentioned processes, small nuclei necessarily occur and the exponential dependence of the yield on the surface tension [17] should cause a sensitivity of both processes to the curvature correction. Moreover the dependency of the curvature interface effects on the isotopic asymmetry of small fragments can significantly enhance (or suppress) the yields of

neutron rich isotopes. In this paper we analyze of the interface effects in an asymmetric nuclear Fermi-liquid drop with a finite diffuse layer. We follow the ideology of the extended Thomas-Fermi approximation (ETFA) with effective Skyrme-like forces combining the ETFA and the direct variational method with respect to the nucleon densities, see Ref. [18]. The surface and symmetry energies were widely studied earlier taking into consideration also the finite surface thickness and the curvature corrections [19, 20, 21, 22, 23, 24]. Note also the applications of the ETFA with the Skyrme-type interactions to the studies of the nuclear bulk, surface and symmetry properties, see e.g. Refs. [25, 26, 27, 28]. In order to formulate proper definition for the drop radius, we use the concept of the dividing surface, originally introduced by Gibbs [14]. Following the Gibbs method, which is applied to the case of two component system, we introduce the superficial (surface) density as the difference (per unit area of dividing surface) between actual number of particles A and the number of bulk, $A_{\mathcal{V}}$, and neutron excess, $A_{-,\mathcal{V}}$, particles which a drop would contain if the particle densities were uniform.

STRUCTURE OF β-STABILITY LINE AND SYMMETRY ENERGY

Considering the asymmetric nuclei with a small asymmetry parameter $X = (N - Z)/A \ll 1$, the total energy per nucleon E/A can be represented in the following form of A, X-expansion,

$$E/A = e_0(A) + b(A)X^2 + E_C(X)/A \ , \tag{1}$$

where $e_0(A)$ includes both the bulk and the surface energies, $b(A)$ is the symmetry energy coefficient, $E_C(X)$ is the total Coulomb energy

$$E_C(X)/A = e_C(A)(1 - X)^2 \ . \tag{2}$$

Using the derivation of the chemical potential λ_q ($q = n$ for a neutron and $q = p$ for a proton)

$$\lambda_n = \left(\frac{\partial E}{\partial N}\right)_Z \ , \quad \lambda_p = \left(\frac{\partial E}{\partial Z}\right)_N \ , \tag{3}$$

one can write the condition of nuclear β-stability in the following form

$$\lambda_n - \lambda_p = 2\frac{\partial(E/A)}{\partial X}\bigg|_A = 0 \ . \tag{4}$$

The beta-stability line $X^*(A)$ is directly derived from Eqs. (1), (2) and (4) as

$$X^*(A) = \frac{e_C(A)}{b(A) + e_C(A)} \tag{5}$$

We point out that for finite nuclei, the beta-stability condition $\lambda_n - \lambda_p = 0$ is not necessary fulfilled explicitly because of the subshell structure in the discrete spectrum of the single particle levels near the Fermi energy for both the neutrons and the protons. Note also that, strictly speaking, the β-decay is forbidden if $|\lambda_n - \lambda_p| < m_e c^2$, where m_e is the electron (positron) mass, i.e., in general, the condition $\lambda_n - \lambda_p = 0$ for β-stability is too strong and we can expect more smooth behavior of $X^*(A)$ than the one given by Eq. (5).

Along the β-stability line, the binding energy per particle is given by

$$E^*/A = e_0(A) + b(A)X^{*\,2} + E_C(X^*)/A \ , \tag{6}$$

where the upper index "$*$" indicates that the corresponding quantity is determined by the variational conditions (5) taken for fixed A and $X = X^*$ on the beta-stability line. For any given value of mass number A, the binding energy per nucleon E/A can be extended beyond the beta-stability line as

$$E/A = E^*/A + b(A)(X - X^*)^2 + \Delta E_C(X)/A \ , \tag{7}$$

where $\Delta E_C(X) = E_C(X) - E_C(X^*)$. The symmetry energy coefficient $b(A)$ contains the A-independent bulk term, b_V, and the A-dependent surface contribution, $b_S A^{-1/3}$,

$$b(A) = b_V + b_S A^{-1/3}. \tag{8}$$

In general, the surface symmetry energy includes also the high order curvature correction $\propto A^{-2/3}$ [18].

Using Eq. (7), one can establish an important relation for the chemical potentials λ_q beyond the beta-stability line. Namely, for the fixed particle number A, we obtain from Eqs. (1), (6) and (5) the following relation

$$\Delta\lambda(A,X)/4 = (\lambda_n - \lambda_p)/4 = \frac{1}{2}\frac{\partial(E/A)}{\partial X}\bigg|_A = [b(A) + e_C(A)]\,X - e_C(A)\ . \tag{9}$$

On the other hand, the shift $\Delta\lambda(A,X)$ of the neutron-proton potentials can be evaluated numerically within the accuracy of $\sim 1/A^2$ using for the quantity of $\partial(E/A)/\partial X$ in Eq. (9) the experimental values of the binding energy per nucleon $\mathcal{B}(N,Z) = -E(N,Z)/A$. Namely,

$$\frac{\partial(E/A)}{\partial X}\bigg|_A = \frac{A}{4}\,[\,\mathcal{B}(N-1,Z+1) - \mathcal{B}(N+1,Z-1)\,]\ . \tag{10}$$

Since the difference (10) is taken for $\Delta Z = -\Delta N = 2$, the pairing effects do not affect the resulting accuracy. It was shown in Ref. [29] that the linear dependence of $\Delta\lambda(A,X)$ given by Eq. (9) at fixed particle number $A = \text{const}$ is reproduced quite well experimentally. This fact allows one to extract the values of $b(A)$, $e_C(A)$, and X^* for a given mass number A with acceptable accuracy.

Using Eqs. (9) and (10), we have evaluated the "experimental" values of quantities $X^*(A)$ and $b(A)$ along the Periodic Table of the Elements. From the beta-stability condition $\Delta\lambda(A,X) = 0$ and Eqs. (9) and (10) we can derive the asymmetry parameter $X^*(A)$. In Fig. 1, we have plotted the obtained "experimental" value of $X^*(A)$ (solid dots). The β-stability line $X^*(A)$ can be also evaluated theoretically using an appropriate equation of state (EOS). In our numerical calculations we have used the EOS from the extended Thomas-Fermi approximation (ETFA) with Skyrme forces [30]. The result of the typical microscopic calculation of $X^*(A)$ within the extended Thomas-Fermi approximation with Skyrme forces SLy230b is shown in Fig. 1 as the dashed line. The numerical results presented in Fig. 1 depends slightly only on the specific choice of Skyrme force parametrization. For comparison the dotted line in Fig. 1 shows the analogous result for Skyrme forces SkM.

The thin solid line in Fig. 1 was obtained by use the phenomenological Green-Engler formula [31]

$$X^*(A) = \frac{0.4\,A}{A + 200}\ . \tag{11}$$

The "experimental" curve (solid dots) $X^*(A)$ in Fig. 1 shows the non-monotonic (sawtooth) shape as a function of the mass number A. This behavior is the consequence of subshell structure of the single particle levels near the Fermi surface for both the neutrons and the protons. Because of this subshell structure, the Fermi levels for protons and neutrons can coincide (such a coincidence is the condition for the β-stability) by chance only creating the non-monotonic behavior of $X^*(A)$. Note that the non-monotonic subshell structure of the β-stability line is transparently discovered for the curve $X^*(A)$ only, i.e., for A-dependency of X^*. The traditional representation of β-stability line as $Z(N)$-dependency does not allow one to observe this phenomenon. The reason is that the shell oscillations appear against the small asymmetry parameter $X^*(A)$ which is close to zero. For the same reason the value of $X^*(A)$ requires more rigorous description than $Z(N)$.

We point out also that the traditionally used beta-stability line $Z(N)$ is given for a discrete set of the asymmetry parameter X and the mass number A which obey the condition $|\Delta\lambda(A,X)| < m_e c^2$. Under this condition the beta-stable nuclei represent rather eroded area than line as compared to the more tight definition $\Delta\lambda(A,X) = 0$. In Fig. 1 we have plotted the discrete points of the beta-stability line $Z(N)$ as the open circles. Each open circle in Fig. 1 corresponds to the stable isotope of maximum abundance for a certain value of charge number Z. As seen from Fig. 1, there is a correlation between the locations of solid dots and open circles. The location of the β-stability line defined by the condition $\Delta\lambda(A,X) = 0$ (solid dots) is obviously less scattered over the plot area, especially for light nuclei. In practical sense, the A-dependent β-stability line $X^*(A)$ is useful to extract the Coulomb energy parameter $e_C(A)$ and the symmetry energy $b(A)$ from the experimental data by use the chemical potential shifts $\Delta\lambda(A,X)$, see e.g. Eq. (9).

To show the origin of the subshell oscillations of $X^*(A)$ more transparently, we will consider the sequence of the nucleon magic numbers [32]: 8, 20, 28, 50, 82 and 126. From this sequence one should expect special behavior of the $X^*(A)$ nearby the following values of mass number $A = N + Z$: 28 (20+8), 48 (28+20), 78 (50+28), 132 (82+50) and 208 (126+82). The "experimental" beta-stability line (solid dots in Fig. 1) has the local maxima at mass numbers 24 (13+11), 48 (26+22), 84 (48+36), 133 (79+54) and 208 (126+82). We can see that mass numbers of local maxima in Fig. 1 does not exactly follow double magic numbers. Nevertheless, one can state that, at least approximately, there exists the correlation between the positions of maxima of sawtooth function $X^*(A)$ and double magic mass numbers.

The Coulomb energy parameter $e_C(A)$ in Eq. (9) can be easily evaluated for a given proton density distribution independently on the nuclear NN-interaction. In the simplest case, assuming a sharp proton distribution and neglecting the contribution from the quantum exchange term, one obtains $e_C(A) =$

$0.15Ae^2/R_C \propto A^{2/3}$, where R_C is the charge (Coulomb) radius of nucleus. In general, both the finite diffuse layer and the quantum exchange contributions must be taken into account. The last fact leads to more complicate A-dependence of $e_C(A)$. To extract such an actual A-dependency of the Coulomb parameter $e_C(A)$ which includes both above mentioned contributions, we will consider the values of the chemical potential shift $\Delta\lambda(A, X)$ at the fixed neutron excess, $A_- = N - Z = AX$ and the different particle numbers A. As seen from Eq. (9), for the zero's neutron excess $A_- = 0$ the value of $\Delta\lambda(A, X)$ is not affected by the symmetry energy b and it is completely determined by $e_C(A)$. Due to this fact, for nuclei with $A_- = 0$ the Coulomb parameter $e_C(A)$ can be evaluated precisely including all corrections caused by the finite diffuse layer, the quantum exchange effects, etc. The Coulomb parameter $e_C(A)$ can be represented by the smooth function

$$e_C(A) = C_1 A^{2/3} + C_2 A^{1/3} \tag{12}$$

with $C_1 = 0.207$, $C_2 = -0.174$ obtained using the fit to all available "experimental" data with $A_- = 0$. The use of Eq. (9) for the shift $\Delta\lambda(X)$ at fixed A allows us to determine the Coulomb parameter $e_C(A)$ for the whole region of mass number covered by experimental data. This was earlier done in Ref. [29] where the Coulomb parameter $e_C(A)$ was roughly estimated as $e_C(A) \approx 0.17A^{2/3}$. However, more precise evaluation is complicated because of the strong shell oscillations at $e_C(A)$. In contrast, the data for $e_C(A)$ obtained from (9) at fixed $A_- = 0$ do not show much shell structure. This fact is also supported by results of Ref. [13].

Note that the actual value of the Coulomb parameter $e_C(A)$ can deviate from its extrapolation given by Eq. (12) for heavy nuclei with $X \neq 0$. This deviation is caused by the fact that the proton distribution radius R_C is slightly dependent on the neutron excess ("neutron skin") in asymmetric nuclei. The origin of such dependency is the polarization effect. Namely, the saturation bulk density decreases with X for neutron-rich nuclei where more neutrons are pushed off to the "neutron skin" involving also the protons and increasing thereby the radius of proton distribution. Such kind of polarization effect of the neutron excess on the proton distribution can be estimated evaluating the X-dependency of the bulk density in asymmetric nuclei [33, 34, 35]. The estimation made in [30] shows that the influence of the neutron excess on the Coulomb radius R_C is negligible in asymmetric nuclei with $X \ll 1$ and the extrapolation formula (12) for the Coulomb energy parameter $e_C(A)$ can be used with high accuracy for heavy nuclei with $X \neq 0$.

Taking into account Eqs. (5), (8) and (12), we suggest the following new form for the β-stability line

$$X^*(A) = \frac{C_1 A^{2/3} + C_2 A^{1/3}}{C_1 A^{2/3} + C_2 A^{1/3} + b_V + b_S A^{-1/3}} \ . \tag{13}$$

Fitting $X^*(A)$ in Fig. 1 by formula (13), we can derive the smooth "experimental" parameters of the symmetry energy b_V and b_S. The corresponding smooth behavior of $X^*(A)$ is shown in Fig. 1 by solid thick line. This line was obtained as a best fit with the values of $b_{\rm sym,vol} = 27$ MeV and $b_{\rm sym,surf} = -23$ MeV which provide the surface-to-volume ratio $r_{S/V} = |b_S|/b_V \approx 0.85$. Note that the analysis made in Ref. [1] for the saddle point shapes of fissile nuclei gives the value for the surface symmetry coefficient of about $b_S \approx -25$ MeV.

Approximating the contribution of the Coulomb energy to $\Delta\lambda(A, X)$ by Eq. (12), one can extract $b(A)$ at fixed neutron excess $A_- \neq 0$ from the experimental values of $\Delta\lambda$ by means of Eq. (9). We have performed such kind of numerical calculations of the "experimental" symmetry energy coefficient $b(A)$ as a function of mass number A beyond the β-stability line for the values of the fixed neutron excess $A_- = 18$, 22, 26 and 30. The corresponding results are shown in Fig. 2. As seen from Fig. 2, qualitatively, $b(A)$ has canyon-like behavior for a given value of A_-. Such kind of canyon-like behavior of the symmetry energy correlates with the nuclear subshell structure. The width and the position of the bottom for the "canyon" depend on the neutron excess A_-. The left wall of the canyon corresponds to the proton closed shell and the right wall corresponds to the neutron shell closure. Such kind of features can be understood from Eq. (9) and the fact that the value of the nucleon chemical potential λ_q goes up sharply when one moves from the closed shell to the one which is far from closure. In Fig. 2 the walls are located symmetrically with respect to $A = 132$ which corresponds to both neutron and proton closed shell ($N = 82$, $Z = 50$). From $A_- = 18$ to $A_- = 30$ the shape of $b(A)$ changes to thinner and deeper canyon with the local minimum in the symmetry coefficient being located at mass number which corresponds to double (proton-neutron) magic number. One can conclude that the thin canyon-like structure of the symmetry energy coefficient $b(A)$ is caused by the shell effects in the single-particle level distribution near the nucleon Fermi energy.

ISOSPIN EFFECTS WITHIN GIBBS – TOLMAN APPROACH

We consider first the spherical nucleus at zero temperature, having the mass number $A = N + Z$, the neutron excess $A_- = N - Z$ and the asymmetry parameter $X = A_-/A$. The total binding energy of nucleus

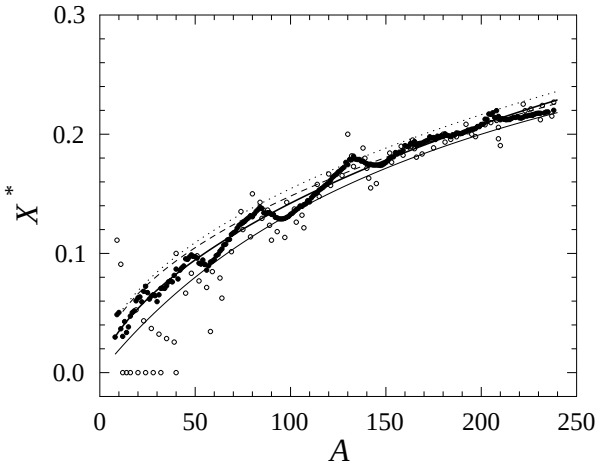

Fig. 1: Asymmetry parameter $X^*(A)$ versus the mass number A. Solid dots represent the data obtained from the condition $\Delta\lambda(A, X) = 0$. Open circles correspond to the stable isotopes of maximum abundance for different elements. Solid lines present $X^*(A)$ from Eq. (11) (thin) and from Eq. (13) with $b_V = 27$ MeV, $b_S = -23$ MeV (thick). The calculations using different Skyrme forces are shown by the dashed (SLy230b) and dotted (SkM) lines [30].

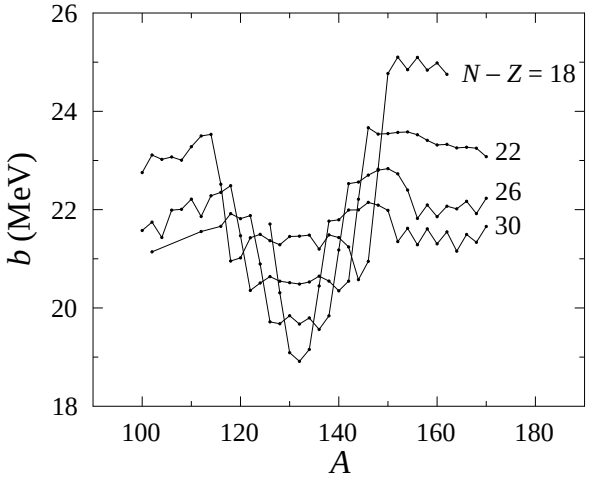

Fig. 2: The symmetry coefficient b vs mass number A at fixed neutron excess $A_- = N - Z$. The values of the neutron excess are specified by numbers near the curves.

is E. An actual nucleus has the finite diffuse layer of particle density distribution. Thereby, the nuclear size is badly specified. In order to formulate proper definition for the nuclear radius, we will use the concept of dividing surface of radius R, originally introduced by Gibbs [14]. Following Refs. [36, 14], we introduce the formal dividing surface of radius R, the corresponding volume $V = 4\pi R^3/3$ and the surface area $S = 4\pi R^2$. Note that the dividing surface is arbitrary but it should be located within the nuclear diffuse layer.

The energy of a nucleus E, as well as the mass number A and the neutron excess A_-, are spitted into the volume and surface parts,

$$E = E_V + E_S \ + E_C, \quad A = A_V + A_S \ , \quad A_- = A_{-,V} + A_{-,S}. \tag{14}$$

Here the Coulomb energy E_C is fixed and does not depend on the dividing radius R. The bulk energy E_V and the surface energies E_S can be written as [17, 36]

$$E_V = (-P + \lambda\varrho_V + \lambda_-\varrho_{-,V})\, V \quad \text{and} \quad E_S = (\sigma + \lambda\varrho_S + \lambda_-\varrho_{-,S})\, S. \tag{15}$$

Here P is the bulk pressure

$$P = -\left.\frac{\partial E_V}{\partial V}\right|_{A_V}, \tag{16}$$

σ is the surface tension and $\varrho_V = A_V/V$ and $\varrho_{-,V} = A_{-,V}/V$ are, respectively, the total (isoscalar) and the neutron excess (isovector) volume densities, $\varrho_S = A_S/S$ and $\varrho_{-,S} = A_{-,S}/S$ are the corresponding surface densities. We have used the isoscalar $\lambda = (\lambda_n + \lambda_p)/2$ and isovector $\lambda_- = (\lambda_n - \lambda_p)/2$ chemical potentials, where λ_n and λ_p are the chemical potentials of neutron and proton, respectively. The Coulomb energy E_C must be excluded from the chemical potentials λ and λ_- because of Eqs. (14) and (15). Namely,

$$\lambda_n = \left.\frac{\partial E}{\partial N}\right|_Z, \quad \lambda_p = \left.\frac{\partial E}{\partial Z}\right|_N - \lambda_C \ , \quad \text{where} \ \ \lambda_C = \left.\frac{\partial E_C}{\partial Z}\right|_N . \tag{17}$$

Note that the definition of λ_p in Eq. (17) differs from the previous one given by (3). Notation E_V stands for the nuclear matter energy of the uniform densities ϱ_V, $\varrho_{-,V}$ within the volume V. The state of the nuclear matter inside the specified volume V is chosen to have the chemical potentials μ and μ_- equal to that of the actual droplet. In more detail, from the equation of state for the nuclear matter one has chemical potentials

$\mu(\rho,\rho_-)$ and $\mu_-(\rho,\rho_-)$ as functions of the isoscalar, ρ, and isovector, ρ_-, densities. Then, the following conditions should be fulfilled:

$$\mu(\rho=\varrho_V,\ \rho_-=\varrho_{-,V})=\lambda\ ,\qquad \mu_-(\rho=\varrho_V,\ \rho_-=\varrho_{-,V})=\lambda_- \tag{18}$$

to derive the specific values of densities ϱ_V and $\varrho_{-,V}$.

The surface part of the energy E_S as well as the surface particle number A_S and the surface neutron excess $A_{-,S}$ are considered as the excess quantities responsible for "edge" effects with respect to the corresponding volume quantities. Using Eqs. (14), (15) one obtains

$$\sigma=\frac{E-\lambda A-\lambda_- A_-}{S}+\frac{PV}{S}-\frac{E_C}{S}=\frac{\Omega-\Omega_V}{S}\ . \tag{19}$$

Here the grand potential $\Omega=E-\lambda A-\lambda_- A_- -E_C$ and its volume part $\Omega_V=-PV=E_V-\lambda A_V-\lambda_- A_{-,V}$ were introduced. From Eq. (19) one can see how the value of the surface tension depends on the choice of the dividing radius R,

$$\sigma\,[R]=\frac{\Omega}{4\pi R^2}+\frac{1}{3}PR\ . \tag{20}$$

Taking the derivative from Eq. (20) with respect to the formal dividing radius R and using the fact that observables E, λ, λ_- and P should not depend on the choice of the dividing radius, one can rewrite Eq. (20) as

$$P=2\,\frac{\sigma\,[R]}{R}+\frac{\partial}{\partial R}\,\sigma\,[R]\ , \tag{21}$$

which is the generalized Laplace equation. The formal values of surface densities ϱ_S and $\varrho_{-,S}$ can be found from (14) as

$$\varrho_S[R]=\frac{A}{4\pi R^2}-\frac{1}{3}\varrho_V R\ ,\qquad \varrho_{-,S}[R]=\frac{A_-}{4\pi R^2}-\frac{1}{3}\varrho_{-,V}R\ . \tag{22}$$

In Eqs. (20) – (22) square brackets denote a formal dependence on the dividing radius R which is still arbitrary and may not correspond to the actual physical size of the nucleus. To derive the physical size quantity an additional condition should be imposed on the location of dividing surface. In general, the surface energy E_S for the arbitrary dividing surface includes the contributions from the surface tension σ and from the binding energy of particles within the surface layer. The latter contribution can be excluded for the special choice of dividing (equimolar) radius $R=R_e$ which satisfy the condition

$$\left(\varrho_S\lambda+\varrho_{-,S}\lambda_-\right)_{R=R_e}=0\ . \tag{23}$$

Here we use the notation R_e by the analogy with the equimolar dividing surface for the case of the one-component liquid [16, 36]. For the dividing radius defined by Eq. (23) the surface energy reads

$$E_S=\sigma_e S_e\ , \tag{24}$$

where $\sigma_e\equiv\sigma(R_e)$ and $S_e=4\pi R_e^2$. Using Eqs. (22), (23), the corresponding volume $V_e=4\pi R_e^3/3$ is written as

$$V_e=\frac{\lambda A+\lambda_- A_-}{\lambda\varrho_V+\lambda_-\varrho_{-,V}}\ . \tag{25}$$

As seen from Eqs. (18), (25), the droplet radius R_e is determined by the equation of state for the nuclear matter through the values of the droplet chemical potentials λ and λ_-.

The surface tension $\sigma\,[R]$ depends on the location of the dividing surface. Function $\sigma\,[R]$ has a minimum at certain radius $R=R_s$ (radius of the surface of tension [36]) which usually does not coincide with the equimolar radius R_e. The radius R_s (Laplace radius) denotes the location within the interface. Note that for $R=R_s$ the capillary pressure of Eq. (21) satisfies the classical Laplace relation

$$P=2\,\frac{\sigma\,[R]}{R}\bigg|_{R=R_s}\ . \tag{26}$$

The dependence of the surface tension $\sigma\,[R]$ of Eq. (20) on the location of the dividing surface for the nuclei ^{120}Sn and ^{208}Pb is shown in Fig. 3.

Following Gibbs and Tolman [14, 15], we will assume that the physical (measurable) value of the surface tension is that taken at the equimolar dividing surface. We assume, see also Ref. [36], that the surface tension $\sigma\equiv\sigma(R_e)$ approaches the planar limit σ_∞ as

$$\sigma(R_e)=\sigma_\infty\left(1-\frac{2\xi}{R_e}+\mathcal{O}(R_e^{-2})\right)\ , \tag{27}$$

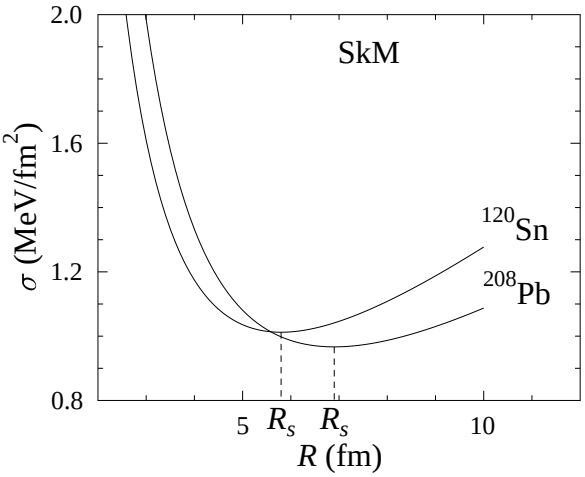

Fig. 3: Surface tension σ as a function of the dividing radius R for nuclei ^{120}Sn and ^{208}Pb. The calculation was performed using SkM force (see [37] for details). The Laplace radius R_s denotes the dividing radius where σ approaches the minimum value, i.e., the Laplace condition of Eq. (26) is satisfied.

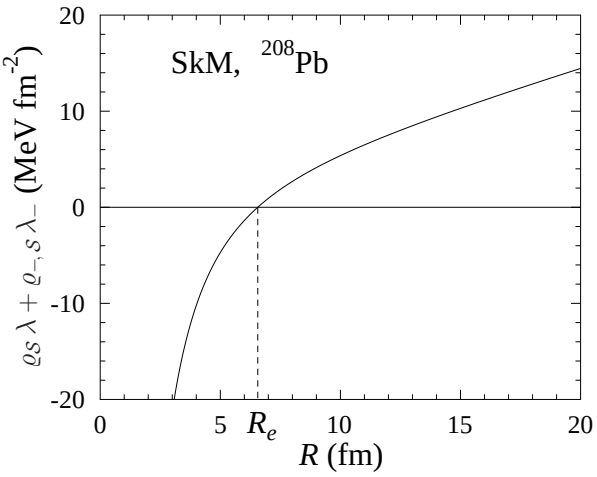

Fig. 4: Specific surface particle density $\varrho_S\lambda + \varrho_{-,S}\lambda_-$ versus dividing radius R for ^{208}Pb. The calculation was performed using the SkM force. R_e denotes the equimolar radius where $\varrho_S\lambda + \varrho_{-,S}\lambda_-$ becomes zero.

where ξ is the Tolman's length [15]. Taking Eq. (21) for $R = R_s$ and comparing with analogous one for $R = R_e$, one can establish the following important relation (see Eq. (45) in the next Section)

$$\xi = \lim_{A\to\infty} (R_e - R_s) \ + \mathcal{O}(X^2). \tag{28}$$

This result leads to the conclusion that to obtain the non-zero value of Tolman length ξ, and, consequently, the curvature correction $\Delta\sigma_{\rm curv} \neq 0$ for a curved surface, the nucleus must have a finite diffuse surface layer.

We perform the numerical calculations using Skyrme type of the effective nucleon-nucleon interaction. The energy and the chemical potentials for actual droplets can be calculated using a direct variational method within the extended Thomas-Fermi approximation [18, 37]. Using obtained chemical potentials we evaluate the equilibrium bulk densities ϱ_V and $\varrho_{-,V}$ from Eq. (18). For arbitrary dividing radius R and fixed asymmetry parameter X we evaluate then the volume, $A_V = 4\pi\varrho_V R^3/3$ and $A_{-,V} = 4\pi\varrho_{-,V}R^3/3$, the surface, $A_S = 4\pi\varrho_S R^2$ and $A_{-,S} = 4\pi\varrho_{-,S}R^2$, particle numbers and the volume part of equilibrium energy E_V. All evaluated values of $E_V[R]$, the bulk densities ϱ_V and $\varrho_{-,V}$ and the surface particle densities $\varrho_S[R]$ and $\varrho_{-,S}[R]$ depend on the radius R of dividing surface and asymmetry parameter X. The actual physical radius R_e of the droplet can be derived by the condition (23), i.e., by the requirements that the contribution to E_S from the bulk binding energy (term $\sim (\varrho_S\lambda + \varrho_{-,S}\lambda_-)$ in Eq. (15)) should be excluded from the surface energy E_S. In Fig. 4 we represent the calculation of the specific surface particle density $\varrho_S\lambda + \varrho_{-,S}\lambda_-$ as a function of the radius R of dividing surface. Equimolar dividing radius R_e in Fig. 4 defines the physical size of the sharp surface droplet and the surface at which the surface tension is applied, i.e., the equimolar surface where Eq. (24) is fulfilled.

Note that the value of equimolar radius R_e, which is derived by Eq. (25), is not considerably affected by the Coulomb interaction. We have also evaluated the values of R_e neglecting the Coulomb term, i.e., assuming $E_C = \lambda_C = 0$. The difference as compared with data obtained with Coulomb term included does not exceed 0.5% for A of about 200. Omitting the Coulomb energy contribution to the total energy E and evaluating the bulk energy E_V, one can obtain the surface part of energy $E_S = E - E_V$ and the surface tension coefficient $\sigma\,(R_e)$ (19) at the equimolar dividing surface for nuclei with different mass number $A \propto R_e^3$ and asymmetry parameter X. The dependence of the surface tension coefficient $\sigma\,(R_e)$ on the doubled inverse equimolar radius $2/R_e$ (see Eq. (27)) is shown in Fig. 5.

The surface tension $\sigma\,(R_e, X)$ approaches the planar limit $\sigma_\infty(X)$ in the limit of zero curvature $2/R_e \to 0$. As seen from Fig. 5, the planar limit $\sigma_\infty(X)$ depends on the asymmetry parameter. This dependence reflects the fact that the symmetry energy b in mass formula contains both the volume b_V and surface b_S contributions, see Refs. [38, 29]. In Fig. 6 we show the X-dependence of the surface tension $\sigma_\infty(X)$. This dependence can be approximated by

$$\sigma_\infty(X) = \sigma_0 + \sigma_- X^2 \ . \tag{29}$$

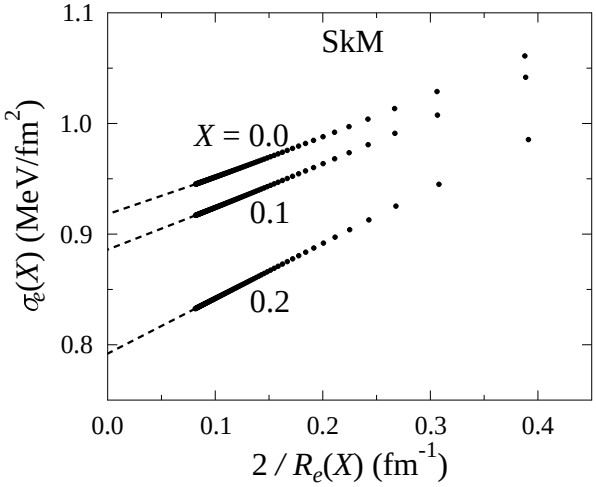

Fig. 5: The dependence of the surface tension coefficient $\sigma\,(R_e, X)$ on the equimolar radius R_e for different values of the asymmetry parameter X. The calculation was performed for Skyrme force SkM [37].

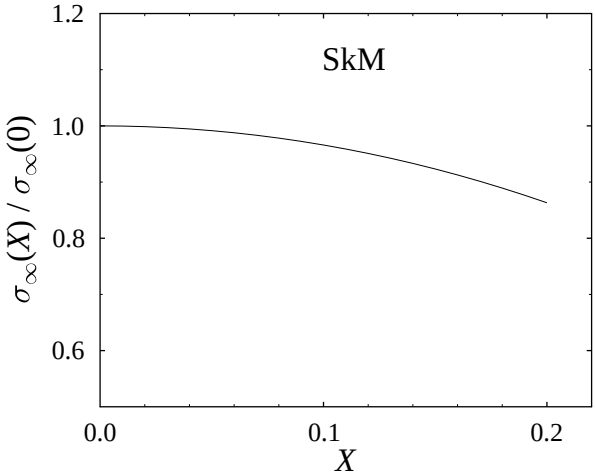

Fig. 6: Dependence of the planar surface tension $\sigma_\infty(X)$ on the asymmetry parameter X. The calculation was performed for Skyrme force SkM.

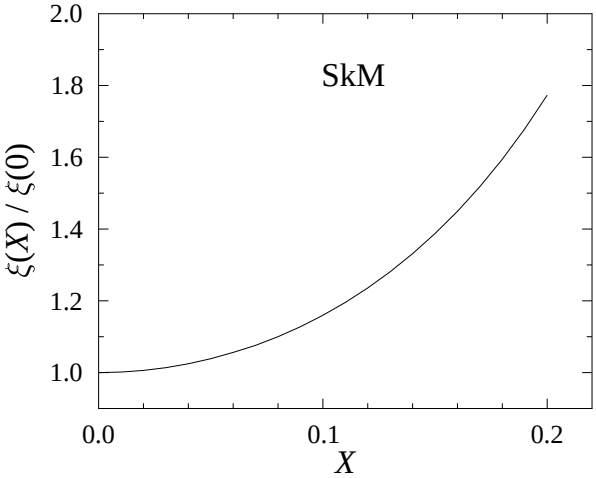

Fig. 7: Dependence of the Tolman length ξ on the asymmetry parameter X. The calculation was performed for Skyrme force SkM.

The dependence of parameters σ_0 and σ_- on the Skyrme force parametrization is shown in Table 1. The isovector term σ_- in the surface tension (29) is related to the surface contribution b_S to the symmetry energy (see the next Section, Eq. (42)). We evaluate the surface-to-volume ratio $r_{S/V} = |b_S/b_V| = 1.17 \div 1.47$ for Skyrme force parametrizations from Table 1. Note that in the previous theoretical calculations, the value of surface-to-volume ratio $r_{S/V}$ varies strongly within the interval $1.6 \leq r_{S/V} \leq 2.8$, see Refs. [38, 29, 39].

The slope of curves $\sigma\,(R_e)$ in Fig. 5 gives the Tolman length ξ, see Eq. (27). The value of the Tolman length ξ depends significantly on the asymmetry parameter X. In Fig. 7 we show such kind of dependence obtained from results of Fig. 5. As seen from Fig. 7, one can expect the enhancement of the curvature effects in neutron rich nuclei. The X-dependence of Tolman length ξ can be approximated as

$$\xi(X) = \xi_0 + \xi_- X^2 \ . \tag{30}$$

Both parameters ξ_0 and ξ_- as well as the surface tension parameter σ_- are rather sensitive to the Skyrme force parametrization, see Table 1.

NUCLEAR MATTER EQUATION OF STATE AND ($A^{-1/3}$, X)-EXPANSION FOR FINITE NUCLEI

We will consider the relation of the nuclear macroscopic characteristics (surface and symmetry energies, Tolman length, incompressibility, etc.) to the bulk properties of nuclear matter. Assuming a small deviations from the equilibrium, the equation of state (EOS) for an asymmetric nuclear matter can be written in the

form expansion around the saturation point. One has for the energy per particle (at zero temperature)

$$\mathcal{E}(\epsilon,x)=\frac{E_\infty}{A}=\mu_\infty+\frac{K_\infty}{18}\epsilon^2+b_\infty x^2+\dots\ , \tag{31}$$

where

$$\epsilon=\frac{\rho-\rho_\infty}{\rho_\infty}\ ,\ x=\frac{\rho_-}{\rho}\ ,\ \rho=\rho_n+\rho_p\ ,\ \rho_-=\rho_n-\rho_p\ ,$$

ρ_∞ is the matter saturation (equilibrium) density, μ_∞ is the chemical potential, K_∞ is the nuclear matter incompressibility and b_∞ is the symmetry energy coefficient (all values are taken at the saturation point $\epsilon=0$ and $x=0$). Coefficients of expansion (31) are determined through the derivatives of the energy per particle $\mathcal{E}(\epsilon,x)$ at the saturation point:

$$\mu_\infty=\left.\frac{E_\infty}{A}\right|_{\rm s.p.}\equiv\mathcal{E}^{(0,0)}\ ,\quad K_\infty=9\,\rho^2\left.\frac{\partial^2E_\infty/A}{\partial\rho^2}\right|_{\rm s.p.}\equiv 9\,\mathcal{E}^{(2,0)}\ ,\quad b_\infty=\frac{1}{2}\left.\frac{\partial^2E_\infty/A}{\partial x^2}\right|_{\rm s.p.}\equiv\frac{1}{2}\mathcal{E}^{(0,2)}\ . \tag{32}$$

Here we use the short notations s.p. $\equiv(\rho=\rho_\infty,\,x=0)$ and $\mathcal{E}^{(n,m)}\equiv\left.\dfrac{\partial^{n+m}\mathcal{E}}{\partial\epsilon^n\partial x^m}\right|_{\epsilon=0,\,x=0}$. Some coefficients $\mathcal{E}^{(n,m)}$ are vanishing. From the condition of minimum of $\mathcal{E}(\epsilon,x)$ at the saturation point one has $\mathcal{E}^{(1,0)}=\mathcal{E}^{(0,1)}=0$. Odd derivatives with respect to x, i.e., $\mathcal{E}^{(n,m)}$ for odd m, also vanish because of the charge symmetry of nuclear forces. Using $\mathcal{E}(\epsilon,x)$, one can also evaluate chemical potentials μ, μ_- and pressure P of the nuclear matter beyond the saturation point. Namely,

$$\mu(\epsilon,x)=\left.\frac{\partial E_\infty}{\partial A}\right|_{A_-,V}=\frac{\partial}{\partial\epsilon}(1+\epsilon)\mathcal{E}-x\frac{\partial\mathcal{E}}{\partial x}\ ,\quad \mu_-(\epsilon,x)=\left.\frac{\partial E_\infty}{\partial A_-}\right|_{A,V}=\frac{\partial\mathcal{E}}{\partial x}\ , \tag{33}$$

$$P(\epsilon,x)=-\left.\frac{\partial E_\infty}{\partial V}\right|_{A,A_-}=\rho_\infty(1+\epsilon)^2\frac{\partial\mathcal{E}}{\partial\epsilon}\ . \tag{34}$$

Similarly to Eq. (31), in a finite uncharged system the energy per particle E/A (we use $A=N+Z$, $A_-=N-Z$, $X=A_-/A$) of the finite droplet is usually presented as $(A^{-1/3},\,X)$-expansion around infinite matter using the leptodermous approximation

$$E/A=a_V+a_SA^{-1/3}+a_cA^{-2/3}+X^2(b_V+b_SA^{-1/3}+b_cA^{-2/3}) \tag{35}$$

where a_V, a_S and a_c are, respectively, the volume, surface and curvature energy coefficients, b_V, b_S and b_c are, respectively, the volume, surface and curvature symmetry coefficients. The nuclear chemical potentials λ and λ_- are derived as

$$\lambda(X,A^{-1/3})=E/A-\frac{1}{3}A^{-1/3}\frac{\partial\,E/A}{\partial A^{-1/3}}-X\frac{\partial\,E/A}{\partial X}\ ,\quad \lambda_-(X,A^{-1/3})=\frac{\partial\,E/A}{\partial X}\ . \tag{36}$$

Following Gibbs-Tolman method, one can derive the actual nuclear matter densities ρ and ρ_- from the conditions

$$\mu(\epsilon,x)=\lambda(X,A^{-1/3})\ ,\quad \mu_-(\epsilon,x)=\lambda_-(X,A^{-1/3})\ . \tag{37}$$

Using Eq. (37), one can establish the relation of the macroscopic energy coefficients in the mass formula expansion Eq. (35) to the nuclear matter parameters in EOS (31), see Eqs. (41) – (45) below. The results of numerical calculations of relevant quantities are represented in Tables 1 and 2.

We start from the nuclear matter EOS given by Eq. (31) and take into consideration the relations (32) and the following higher order coefficients

$$K_3=6K_\infty+27\,\rho^3\left.\frac{\partial^3E_\infty/A}{\partial\rho^3}\right|_{\rm s.p.}\equiv 27\left(\mathcal{E}^{(3,0)}+2\,\mathcal{E}^{(2,0)}\right)\ ,\quad L_\infty=\frac{3}{2}\,\rho\left.\frac{\partial^3E_\infty/A}{\partial\rho\partial x^2}\right|_{\rm s.p.}\equiv\frac{3}{2}\,\mathcal{E}^{(1,2)}\ , \tag{38}$$

$$K_{\rm sym}=\frac{9}{2}\,\rho^2\left.\frac{\partial^4E_\infty/A}{\partial\rho^2\partial x^2}\right|_{\rm s.p.}\equiv\frac{9}{2}\,\mathcal{E}^{(2,2)}\ , \tag{39}$$

for the expansion (31). Here K_3 is the bulk anharmonicity coefficient, L_∞ is the density-symmetry coefficient (symmetry energy slope parameter), $K_{\rm sym}$ is the symmetry energy curvature parameter. Using (27), we write also

$$\sigma\approx\sigma_\infty\,(1-2\xi/R_e)\ ,\quad \sigma_\infty\approx\sigma_0+\sigma_-X^2\ ,\quad \xi\approx\xi_0+\xi_-X^2\ , \tag{40}$$

and, taking the advantage of the large mass limit $E_\infty/A = E/A|_{X=\mathrm{const},\,A\to\infty}$, one has

$$a_V = \mu_\infty \ , \quad b_V = b_\infty \ . \tag{41}$$

Using the conditions (37) for the chemical potentials and both relations (36) and (33), we obtain $\rho/\rho_\infty \approx 1 + 6\,A^{-1/3} a_S/K_\infty - 3\,X^2 L_\infty/K_\infty$ and

$$a_S = 4\pi r_0^2 \sigma_0 \ , \quad b_S = 4\pi r_0^2 \left(\sigma_- + \frac{2L_\infty}{K_\infty}\,\sigma_0\right) \ , \quad a_c = -8\pi r_0 \sigma_0 \left(\xi_0 + \frac{3\,\sigma_0}{K_\infty \rho_\infty}\right) \ , \tag{42}$$

$$b_c = -8\pi r_0 \sigma_0 \left\{\xi_- + \left(\frac{L_\infty}{K_\infty} + \frac{\sigma_-}{\sigma_0}\right)\xi_0 + \frac{3\,\sigma_0}{K_\infty \rho_\infty}\left[\frac{L_\infty}{K_\infty}\left(4 + \frac{K_3}{K_\infty}\right) - \frac{K_{\rm sym}}{K_\infty}\right] + \frac{3\,\sigma_-}{K_\infty \rho_\infty}\left(2 + \frac{K_\infty \sigma_-}{2 b_\infty \sigma_0}\right)\right\} \ .$$

Here $r_0 = (4\pi\rho_\infty/3)^{-1/3}$ and we have assumed $A^{-1/3} \ll 1$. The equimolar, R_e, and Laplace, R_s, radii defined by Eqs. (25) and (26) read

$$R_e \approx r_0 A^{1/3} \left[1 - A^{-1/3}\frac{8\pi r_0^2 \sigma_0}{K_\infty}\right.$$

$$\left. + X^2 \left[\frac{L_\infty}{K_\infty} - A^{-1/3}\left\{\frac{8\pi r_0^2 \sigma_-}{K_\infty}\left(1 - \frac{L_\infty}{b_\infty} + \frac{K_\infty}{3\,\mu_\infty}\right) + \frac{8\pi r_0^2 \sigma_0}{K_\infty}\left[\frac{L_\infty}{K_\infty}\left(3 + \frac{K_3}{K_\infty}\right) - \frac{K_{\rm sym}}{K_\infty}\right]\right\}\right]\right] \ , \tag{43}$$

$$R_s \approx r_0 A^{1/3} \left[1 - A^{-1/3}\left(\frac{\xi_0}{r_0} + \frac{8\pi r_0^2 \sigma_0}{K_\infty}\right)\right.$$

$$\left. + X^2 \left[\frac{L_\infty}{K_\infty} - A^{-1/3}\left\{\frac{\xi_-}{r_0} + \frac{8\pi r_0^2 \sigma_-}{K_\infty}\left(1 + \frac{K_\infty}{2 b_\infty}\frac{\sigma_-}{\sigma_0}\right) + \frac{8\pi r_0^2 \sigma_0}{K_\infty}\left[\frac{L_\infty}{K_\infty}\left(3 + \frac{K_3}{K_\infty}\right) - \frac{K_{\rm sym}}{K_\infty}\right]\right\}\right]\right] \ . \tag{44}$$

Using the derivations of R_e and R_s, one obtains

$$R_e - R_s \approx \xi_0 + \left[\xi_- + \frac{3\sigma_-}{b_\infty \rho_\infty}\left(\frac{\sigma_-}{\sigma_0} + \frac{2L_\infty}{K_\infty} - \frac{2b_\infty}{3\mu_\infty}\right)\right] X^2 = \xi + \left[\frac{3\sigma_-}{b_\infty \rho_\infty}\left(\frac{\sigma_-}{\sigma_0} + \frac{2L_\infty}{K_\infty} - \frac{2b_\infty}{3\mu_\infty}\right)\right] X^2 \ . \tag{45}$$

To describe separately the neutron and proton density distributions we introduce the neutron radius, R_n, and the proton radius, R_p, as the dividing radii with zero value for the corresponding surface densities $\varrho_{n,\mathcal{S}} = (\varrho_{\mathcal{S}} + \varrho_{-,\mathcal{S}})/2$ and $\varrho_{p,\mathcal{S}} = (\varrho_{\mathcal{S}} - \varrho_{-,\mathcal{S}})/2$:

$$\varrho_{n,\mathcal{S}}|_{R=R_n} = 0 \ , \qquad \varrho_{p,\mathcal{S}}|_{R=R_p} = 0 \ .$$

The isovector shift of neutron-proton radii, $R_n - R_p$, is then written as

$$R_n - R_p \approx X\left[-\frac{2\,\sigma_-}{b_\infty \rho_\infty} + A^{-1/3}\left\{4\pi r_0^2 \sigma_0 \frac{4}{3 b_\infty}\left(\xi_- + \xi_0 \frac{\sigma_-}{\sigma_0}\right) + 4\pi r_0^2 \sigma_- \left[\frac{2\,\sigma_-}{b_\infty^2 \rho_\infty} + \frac{4\,\sigma_0}{b_\infty^2 \rho_\infty}\left(\frac{L_\infty}{K_\infty} + \frac{3 b_\infty}{K_\infty}\right)\right]\right\}\right] \ . \tag{46}$$

¿From Eq. (46) the value of neutron skin $\sqrt{\langle r_n^2\rangle} - \sqrt{\langle r_p^2\rangle}$ is given within the main order as

$$\sqrt{\langle r_n^2\rangle} - \sqrt{\langle r_p^2\rangle} \approx -\sqrt{\frac{3}{5}}\,\frac{2\,\sigma_- X}{b_\infty \rho_\infty} = \alpha X \ . \tag{47}$$

Here $\alpha = -2\sqrt{3/5}\,\sigma_-/(b_\infty \rho_\infty)$ is the neutron skin parameter. To describe the isospin dependence of surface energy within the droplet model the effective surface stiffness, Q, have been introduced [19]. At the large masses limit $A \to \infty$ the droplet model result reads

$$R_n - R_p \approx \frac{3}{2} r_0 \frac{b_\infty}{Q}\, X \ . \tag{48}$$

Using the main term on the right side of Eq. (46) together with Eq. (48) one obtains the surface stiffness Q as

$$Q = -\frac{9\,b_\infty^2}{16\pi r_0^2\,\sigma_-} \ . \tag{49}$$

The values of α and Q for different Skyrme forces are given in Table 3.

Tab. 1: Nuclear bulk parameters for different Skyrme forces. The planar surface values σ_0, σ_- and ξ_0, ξ_- were obtained by extrapolation $A \to \infty$, see Fig. 5.

	SkM	SkM*	SLy230b	T6
μ_∞ (MeV)	-15.77	-15.77	-15.97	-15.96
ρ_∞ (fm^{-3})	0.1603	0.1603	0.1595	0.1609
K_∞ (MeV)	216.6	216.6	229.9	235.9
K_3 (MeV)	913.5	913.5	1016.	1032.
$K_{\rm sym}$ (MeV)	-148.8	-155.9	-119.7	-211.5
b_∞ (MeV)	30.75	30.03	32.01	29.97
L_∞ (MeV)	49.34	45.78	45.97	30.86
σ_0 (MeV/fm^2)	0.9176	0.9601	1.006	1.021
ξ_0 (fm)	-0.3565	-0.3703	-0.3677	-0.3593
σ_- (MeV/fm^2)	-3.118	-3.094	-3.131	-2.413
ξ_- (fm)	-5.373	-5.163	-4.590	-2.944

Tab. 2: Mass formula coefficients for finite nuclei.

	SkM	SkM*	SLy230b	T6
a_V (MeV)	-15.8	-15.8	-16.0	-16.0
a_S (MeV)	15.0	15.7	16.5	16.7
a_c (MeV)	7.30	7.92	8.26	8.16
b_V (MeV)	30.8	30.0	32.0	30.0
b_S (MeV)	-44.2	-44.1	-44.9	-35.1
b_c (MeV)	35.7	35.1	28.6	17.3
$r_{S/V} = \lvert b_S/b_V \rvert$	1.44	1.47	1.40	1.17

Tab. 3: Neutron skin parameter α and surface stiffness Q for different Skyrme forces. The values of α and Q were calculated using Eqs. (47) and (49), respectively.

	SkM	SkM*	SLy230b	T6
α (fm)	0.980	0.996	0.950	0.775
Q (MeV)	41.6	40.0	44.8	51.2

CONCLUSIONS

We propose a new method of the evaluation of the A-dependency of β-stability line and both the Coulomb, $e_C(A)$, and the symmetry, $b(A)$, energies. Our method is model independent in a sense that it does not imply a theoretical model for the calculation of the nuclear binding energy. The method is based on the experimental data for the shift of the neutron-proton chemical potential $\Delta\lambda(A, X)$ for nuclei beyond β-stability line but at the fixed total particle number A. We show the presence of the thin structure (sawtooth shape) of β-stability line for the curve $X^*(A)$ which is not observed at the traditional presentation of β-stability line as $Z(N)$-dependency. We note that this non-monotonic behavior of β-stability line is the consequence of subshell structure of single particle levels near Fermi energy for both the neutrons and the protons. We demonstrate the correlation between the positions of maxima of function $X^*(A)$ and double magic nucleon numbers.

We have suggested the model independent method for calculation of the Coulomb energy parameter $e_C(A)$ which absorbs both the finite diffuse layer and the quantum exchange contributions. The last fact leads to more complicate A-dependence of $e_C(A)$ (see Eq. (12)) than the traditional one $e_C(A) \propto A^{2/3}$. We have established the dependence of β-stability line $X^*(A)$ on the Coulomb, $e_C(A)$, and the symmetry, $b(A)$, energies. That allowed us to redefine a smooth A-dependency of β-stability line (see Eq. (13)) which can be used instead the phenomenological one (11) given by Green and Engler [31]. One should note that it is difficult to determine b_V unambiguously. The reason is that the surface contribution cannot be neglected even for the heavy nuclei covered by the experimental data. Another reason is the different A-dependence for $b(A)$ used in the nuclear mass formula, see e.g. Ref. [38].

We have also observed the thin structure of the symmetry energy $b(A)$. The value of $b(A)$ has the canyon-like A-dependence for a fixed neutron excess $A_- = N - Z$. The width and the position of bottom for such a canyon-like shape depend on the neutron excess and are related to the subshell structure in the discrete spectrum of the single particle levels for both the neutrons and the protons. The canyon shape of $b(A)$ becomes thinner and deeper near double (proton-neutron) magic number.

Considering a small two-component, charged droplet with a finite diffuse layer, we have introduced a formal dividing surface of radius R which splits the droplet onto volume and surface parts. The corresponding splitting was also done for the binding energy E. Assuming that the dividing surface is located close to the interface, we are then able to derive the surface energy E_S. In general, the surface energy E_S includes the contributions from the surface tension σ and from the binding energy of A_S particles located within the surface layer. The equimolar surface and thereby the actual physical size of the droplet are derived by the condition $\varrho_S\lambda + \varrho_{-,S}\lambda_- = 0$ which means that the latter contribution is excluded from the surface energy providing $E_S \propto \sigma$.

In a small nucleus, the diffuse layer and the curved interface affect the surface properties significantly. In agreement with Gibbs–Tolman concept [15, 14], two different radii have to be introduced in this case. The

first radius, R_s, is the surface tension radius (Laplace radius) which provides the minimum of the surface tension coefficient σ and the fulfillment of the Laplace relation (26) for capillary pressure. The another one, R_e, is the equimolar radius which corresponds to the equimolar dividing surface due to the condition (23) and defines the physical size of the sharp surface droplet, i.e., the surface at which the surface tension is applied. The difference of two radii $R_e - R_s$ in an asymptotic limit of large system $A \to \infty$ derives the Tolman length ξ. That means the presence of curved surface is not sufficient for the presence of the curvature correction in the surface tension. The finite diffuse layer in the particle distribution is also required. We point out that the Gibbs–Tolman theory allows to treat a liquid drop within thermodynamics with minimum assumptions. Once the binding energy and chemical potential of the nucleus are known its equimolar radius, radius of tension and surface energy can be evaluated using the equation of state for the infinite nuclear matter. We have also established the relation of the macroscopic energy coefficients in the liquid drop model expansion Eq. (35) to the nuclear matter parameters.

The sign and the magnitude of the Tolman length ξ depend on the interparticle interaction. We have shown that the Tolman length is negative for a nuclear Fermi liquid drop. As a consequence, the curvature correction to the surface tension leads to the hindrance of the yield of light fragments at the nuclear multifragmentation in heavy ion collisions. We have also shown that the Tolman length is sensitive to the neutron excess and its absolute value growth significantly with growing asymmetry parameter X.

REFERENCES

[1] A. Bohr and B. Mottelson, *Nuclear Structure* (W.A. Benjamin, New York, 1975), Vol. II.
[2] M.B. Tsang, W.A. Friedman, C.K. Gelbke, *et al.*, Phys. Rev. Lett. **86** (2001) 5023.
[3] W.A. Friedman, Phys. Rev. C **69** (2004) 031601(R).
[4] M. Veselsky, G.A. Souliotis, and M. Jandel, Phys. Rev. C **69** (2004) 044607.
[5] T.X. Liu, X.D. Liu, M.J. van Goethem, W.G. Lynch, *et al.*, Phys. Rev. C **69** (2004) 014603.
[6] G.A. Souliotis, D.V. Shetty, M. Veselsky, *et al.*, Phys. Rev. C **68** (2003) 024605.
[7] M. Veselsky, G.A. Souliotis, and S.J. Yennello, Phys. Rev. C **69** (2004) 031602(R).
[8] E. Geraci, M. Bruno, M. D'Agostino, E. De Filippo, *et al.*, Nucl. Phys. **A732** (2004) 173.
[9] Y.G. Ma, K. Wang, X.Z. Cai, J.G. Chen, *et al.*, Phys. Rev. C **72** (2005) 064603.
[10] G. Audi, A.H. Wapstra and C. Thibault, Nucl. Phys. **A729** (2003) 337.
[11] J. Jänecke, T.W. O'Donnell and V.I. Goldanskii, Nucl. Phys. **A728** (2003) 23.
[12] W.E. Ormand, Phys. Rev. C **55** (1997) 2407.
[13] M. Liu, N. Wang, Y. Deng and X. Wu, Phys. Rev. C **84** (2011) 014333.
[14] J.W. Gibbs, in *The Collected Works* (Longmans, Green and Co., New York, 1928), Vol. I, p. 219.
[15] R.C. Tolman, J. Chem. Phys. **17**, 118, 333 (1949).
[16] V.M. Kolomietz, S.V. Lukyanov and A.I. Sanzhur, Phys. Rev. C 86 (2012) 024304
[17] L.D. Landau and E.M. Lifshitz, *Statistical Physics* (Pergamon Press, Oxford, 1958).
[18] V.M. Kolomietz and A.I. Sanzhur, Eur. Phys. J. **38**, 345 (2008).
[19] W.D. Myers and W.J. Swiatecki, Ann. Phys. (NY) **55**, 395 (1969).
[20] W.D. Myers, W.J. Swiatecki and C.S. Wang, Nucl. Phys. **A 436**, 185 (1985).
[21] M. Centelles, M. Del Estal and X. Viñas, Nucl. Phys. **A 635**, 193 (1998).
[22] M. Centelles, X. Roca-Maza, X. Viñas and M. Warda, Phys. Rev. C **82** 054314 (2010).
[23] X. Roca-Maza, M. Centelles, X. Viñas and M. Warda, Phys. Rev. Lett. **106** 252501 (2011).
[24] J.M. Lattimer, C.J. Pethick, D.G. Ravenhall and D.Q. Lamb, Nucl. Phys. **A 432**, 646 (1985).
[25] M. Brack, C. Guet and H.-B. Håkansson, Phys. Rep. **123**, 275 (1985).
[26] M. Centelles and X. Viñas, Nucl. Phys. **A 563**, 173 (1993).
[27] J. Treiner and H. Krivine, Ann. Phys. (NY) **170**, 406 (1986).
[28] K. Kolehmainen, M. Prakash , J.M. Lattimer and J. Treiner, Nucl. Phys. **A 439**, 535 (1985).
[29] V.M. Kolomietz and A.I. Sanzhur, Phys. Rev. C **81** (2010) 024324.
[30] V.M. Kolomietz and A.I. Sanzhur, Int. J. Mod. Phys. E **22** (2013) 135003.
[31] A.E.S. Green and N.A. Engler, Phys. Rev. **91** (1953) 40.
[32] A. Bohr and B. R. Mottelson, *Nuclear Structure* (W.A. Benjamin, New York, 1969), Vol. 1.
[33] V.M. Kolomietz, S.V. Lukyanov and A.I. Sanzhur, Phys. Rev. C **85** (2012) 034309.
[34] K. Oyamatsu, I. Tanichata, S. Sugahara, K. Sumiyoshi and H. Toki, Nucl. Phys. **A634** (1998) 3.
[35] K. Oyamatsu and K. Iida, Progr. Theor. Phys. **109** (2003) 631.
[36] J.S. Rowlinson and B. Widom, *Molecular Theory of Capillarity* (Clarendon Press, Oxford, 1982).
[37] V.M. Kolomietz and A.I. Sanzhur, Phys. Rev. C **88**, 044316 (2013).
[38] P. Danielewicz, Nucl. Phys. A727 (2003) 233.
[39] W. Satuła, R.A. Wyss and M. Rafalski, Phys. Rev. C **74**, 011301(R) (2006).

ANALYSIS OF THE FLOW SYSTEMATICS IN Au+Au COLLISIONS

Martin Veselsky[1,*], **Yu-Gang Ma** [2,†] **and Georgios A. Souliotis**[3,‡]

[1]Institute of Physics, Slovak Academy of Sciences, Dubravska cesta 9, 845 11 Bratislava, Slovakia
[2]Shanghai Institute of Applied Physics, Chinese Academy of Sciences, 2019 Jia-Luo Road, P.O. Box 800-204, Shanghai 201800, China
[3]Laboratory of Physical Chemistry, Department of Chemistry, National and Kapodistrian University of Athens, and Hellenic Institute of Nuclear Physics, Athens 15771, Greece

Abstract

The new implementation of the Boltzmann-Uehling-Uhlenbeck (BUU) equation, with in-medium nucleon-nucleon cross sections, derived from equation of state (EoS), used in the collision term, reproduces simultaneously both the directed and elliptic flow in semi-peripheral Au+Au collisions in the energy range from 400 AMeV to 10 AGeV. Based on this analysis, investigating the properties of nuclear matter at super-saturation densities, the range of feasible incompressibilities of the equation of state can be identified as $K_0 > 245MeV$, which is consistent with the recent re-analysis of the giant monopole resonance data, obtained close to saturation density, $K_0 = 250 - 310MeV$ (J.R. Stone et al., Phys. Rev. C 89, 044316 (2014)). Using such complementary result as an additional constraint, the range of the stiffness of density dependence of symmetry energy could be restricted to $\gamma = 0.7 - 1.25$, with the value of γ roughly increasing with increasing K_0. The implementation of BUU with EoS-dependent in-medium nucleon-nucleon cross sections, and thus with EoS-dependence for the first time implemented in the collision term, leads to physically relevant values of K_0 and γ, while the BUU with the free nucleon-nucleon cross sections can not describe correctly the global trends of flow observables.

INTRODUCTION

One of the main goals of intermediate-energy heavy-ion collisions (HIC) is to study properties of nuclear matter, especially to determine the nuclear equation of state (EoS). HIC provide a unique possibility to compress nuclear matter to a hot and dense phase within a laboratory environment. The pressures that result from the high densities achieved during such collisions strongly influence the motion of ejected matter and are sensitive to the EoS. With the hard work of the researchers over the last three decades, the EoS of symmetric nuclear matter was studied in detail by the study of giant resonances, collective flow as well as multifragmentation [1, 2, 3, 4]. The study of the EoS of isospin asymmetric nuclear matter is currently underway, particularly, for the density dependence of symmetry energy. Considerable progress has been made in determining the sub- and supra-saturation density behavior of the symmetry energy [5, 6, 7, 8, 9, 10, 11, 12]. The latter issue is still an unanswered question in spite of recent findings in term of neutron-proton elliptic flow ratio and difference [10, 11]. However, the former topic is understood to some extent [5, 6, 7, 8], although, more efforts are needed for precise measurements.

BOLTZMANN-UHLING-UHLENBECK EQUATION WITH EOS-DEPENDENT IN-MEDIUM NUCLEON-NUCLEON CROSS SECTIONS

A transport model is very useful to treat heavy ion collision dynamics and obtain important information of nuclear matter EoS as well as the symmetry energy. In intermediate energy heavy ion collisions, the Boltzmann-Uehling-Uhlenbeck (BUU) model is an extensively useful tool [13, 14], which takes both Pauli blocking and mean field into consideration. The BUU equation reads

$$\frac{\partial f}{\partial t} + v \cdot \nabla_r f - \nabla_r U \cdot \nabla_p f = \frac{4}{(2\pi)^3} \int d^3p_2 d^3p_3 d\Omega$$
$$\frac{d\sigma_{NN}}{d\Omega} v_{12} \times [f_3 f_4 (1-f)(1-f_2) - f f_2 (1-f_3)(1-f_4)]$$
$$\delta^3(p + p_2 - p_3 - p_4), \quad (1)$$

*E-mail: martin.veselsky@savba.sk
†E-mail: ygma@sinap.ac.cn
‡E-mail: soulioti@chem.uoa.gr

where $f=f(r,p,t)$ is the phase-space distribution function. It is solved with the test particle method of Wong [15], with the collision term as introduced by Cugnon, Mizutani and Vandermeulen [16]. In Eq.(1), $\frac{d\sigma_{NN}}{d\Omega}$ and v_{12} are in-medium nucleon-nucleon cross section and relative velocity for the colliding nucleons, respectively, and U is the single-particle mean field potential with the addition of the isospin-dependent symmetry energy term, which in its simplest form is usually expressed as

$$U = a\rho + b\rho^{\kappa} + 2a_s(\frac{\rho}{\rho_0})^{\gamma}\tau_z I, \tag{2}$$

where $I = (\rho_n - \rho_p)/\rho$, ρ_0 is the normal nuclear matter density; ρ, ρ_n, and ρ_p are the nucleon, neutron and proton densities, respectively; τ_z assumes value 1 for neutron and -1 for proton, coefficients a, b and κ represent properties of the symmetric nuclear matter while the last term, which describes the influence of the symmetry energy, can be obtained e.g. from simple Weizsacker formula, where a_s represents the coefficient of the symmetry energy term and γ is the exponent, describing the density dependence.

When considering influence of the symmetry energy on emission rates of nucleons in nucleus-nucleus collisions, one needs to understand whether and how the medium represented by the equation of state can influence relative probabilities of emission of protons and neutrons. Theoretical investigations of the density-dependence of in-medium nucleon-nucleon cross section were carried out for symmetric nuclear matter [17, 18], and significant influence of nuclear density on resulting in-medium cross sections was observed in their density, angular and energy dependencies. Using momentum-dependent interaction, ratios of in-medium to free nucleon-nucleon cross sections were evaluated via reduced nucleonic masses [19] and used for transport simulations. Still, transport simulation are mostly performed using parametrizations of the free nucleon-nucleon cross sections, eventually scaling them down empirically or using simple prescriptions for density-dependence of the scaling factor [20]. In the recent work [23], a prescription for estimation of the density-dependence of the in-medium nucleon-nucleon cross sections corresponding to the specific form of phenomenological nuclear equation of state was presented. Such possibility to establish a simple dependence of nucleon-nucleon cross sections on density, temperature and symmetry energy is potentially important for a wide range of problems in nuclear physics and astrophysics.

As demonstrated in [23], in order to find a relation between the equation of state and nucleon emission rates one can turn attention specifically to the Van der Waals equation of state. To proceed in this direction, the equation of state of nuclear matter can be formulated as an expression for the pressure which can be in general written as

$$p = \langle\frac{f_{5/2}(z)}{f_{3/2}(z)}\rangle\rho T + a\rho^2 + p_{pot}(\rho,T,I) + p_{kin}(\rho,T,I) \tag{3}$$

where $p_{pot}(\rho,T,I)$ represents the component of pressure related to single particle potential (with the exception of the pressure term $a\rho^2$ which is treated separately) and $p_{kin}(\rho,T,I)$ is caused by the kinetic term of the symmetry energy. The Fermi integrals $f_{5/2}(z)$, $f_{3/2}(z)$ reflect the Fermionic nature of nucleons. It is then possible to formally transform the above equations of state (and practically any other equation of state) into the form analogous to the Van der Waals equation. Then corresponding expression for the proper volume in the Van der Waals form will be

$$b' = \frac{1}{\rho}\ \frac{p_{pot}(\rho,T,I) + p_{kin}(\rho,T,I)}{\langle\frac{f_{5/2}(z)}{f_{3/2}(z)}\rangle\rho T + p_{pot}(\rho,T,I) + p_{kin}(\rho,T,I)} \tag{4}$$

which demonstrates immediately that for any form of equation of state it always exhibits a $1/\rho$-dependence at zero temperature. The expression $\langle\frac{f_{5/2}(z)}{f_{3/2}(z)}\rangle T$ is a classical temperature which can be estimated easily from the momentum distribution of nucleons.

ANALYSIS OF THE FLOW OBSERVABLES

The flow observables were introduced primarily as observables directly related to the equation of the state of nuclear matter. Essentially, different flow observables can be identified with the coefficients of the Fourier expansion of the azimuthal angular distribution relative to the reaction plane.

Flow observable, related to the first Fourier coefficient v_1 is usually called as directed flow. It can be alternatively expressed in terms of a slope of the momentum p_x (in the reaction plane) at mid rapidity. The systematics of this observable for protons observed in the semi-peripheral collisions (b=5.5-7.5 fm) of Au+Au at various beam energies was published in [21] and it exhibits an initial linear rise from zero to the maximum value of about 0.37 GeV/c at beam energy 400 AMeV, followed by linear decrease to the

value 0.1 at 10 AGeV. The positive values of the slope appear to signal that the stopping in the nuclear medium is not full and the effect of the attractive mean-field is stronger than stopping due to two-body nucleon-nucleon collisions. The elliptic flow is characterized by the value of the second Fourier coefficient v_2 and its systematics for the protons observed in the semi-peripheral collisions of Au+Au at mid-rapidity was published in the work [22]. Below 100 AMeV the elliptic flow is positive, reflecting the binary dissipative nature of the semi-peripheral collision at such beam energies, reflected in mostly in-plane proton emission. Furthermore, at approximately 150 AMeV the elliptic flow assumes negative value, reflecting the squeeze-out effect where the protons from the participant zone are emitted predominantly in the out-of plane direction. When combined, these two systematics provide a good set of experimental data for testing of the transport codes and for determination of the parameters of the equation of the state of nuclear matter.

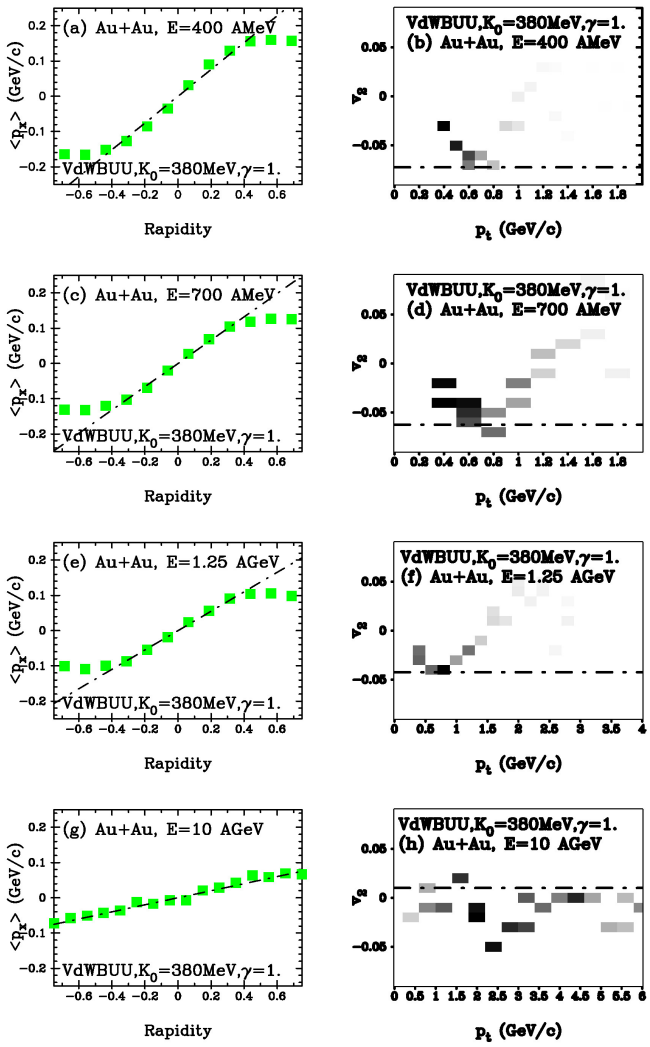

Fig. 1: Systematics of the proton directed flow (left panels, lines show experimentally observed slopes) and the transverse momentum dependence of the calculated proton elliptic flow at mid-rapidity versus the experimental value (boxes and the dash-dotted lines in right panels, respectively) in the collisions of Au+Au at beam energies ranging from 400 AMeV to 10 AGeV. Results were obtained using the VdWBUU simulation using the stiff EoS with $\kappa = 2$ and the symmetry energy potential parametrization with $\gamma = 1$.

A new variant of the transport code for simulation of the nucleus-nucleus collisions was introduced in the work [23]. At variance to previous codes used for the solution of the Boltzmann-Uhling-Uhlenbeck equation (BUU), the nucleon-nucleon cross sections used for evaluation of the collision term, are estimated directly from the equation of state used for evaluation of the mean-field potential. The method of estimation of the nucleon-nucleon cross sections is based on the formal transformation of the equation of state into the form of the Van der Waals equation of state and the cross sections is obtained using the proper volume, a parameter of the Van der Waals equation of state. Thus the whole calculation is based on the selected equation of state and there is no need to use free or empirically estimated in-medium cross sections. These simulations will

be described using the acronym VdWBUU, while the reference simulations using the free nucleon-nucleon cross sections of Cugnon [16] will be described as fBUU. In order to evaluate flow observables in the BUU simualtions, it is necessary to implement a method for selection of the free nucleons. Like in the work [23], in a standard variant, particles are considered as emitted when they are separated in the phase-space from any other particle and separation is large enough to assure that two particles are not part of a cluster (a condition $\Delta\vec{p}\Delta\vec{r} > 2h$ is implemented).

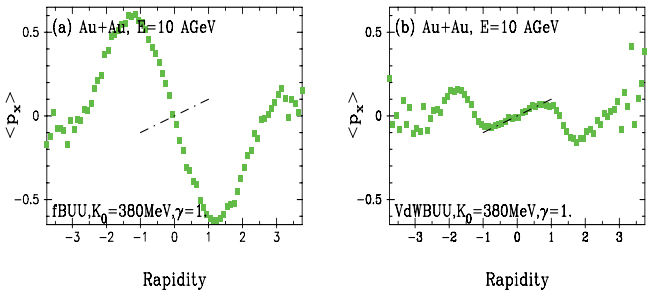

Fig. 2: Proton directed flow in the collisions of Au+Au at beam energy of 10 AGeV. Results were obtained using the simulation with and without EoS-dependent in-medium nucleon-nucleon cross sections (left and right panels, respectively) using the stiff EoS with $\kappa = 2$ and the symmetry energy potential parametrization with $\gamma = 1$. Lines show experimentally observed slope.

The equations of state used in many preceding works are typically two types of the mean field, the soft EoS with the compressibility K of 200 MeV (corresponding to the value $\kappa = 7/6$ in the equation (2)), and the hard EoS with K of 380 MeV ($\kappa = 2$), as first introduced in the work [13]. These two equations of the state can be considered as two extremes and many intermediate equations of the state are feasible, with the compressibility K depending linearly on κ, as shown in the equation

$$K = 9\kappa(B + \frac{\epsilon_F(\rho_0)}{5}) - \frac{6}{5}\epsilon_F(\rho_0) \tag{5}$$

where B is the binding energy at saturation density (with typically assumed value $B = 16$ MeV) and $\epsilon_F(\rho_0)$ is the Fermi energy at the saturation density ρ_0 (typically set to $\rho_0 = 0.16$ fm^{-3}). In the present work, the intermediate values of $\kappa = 4/3,\ 3/2,\ 5/3$ were used.

The density dependence of the symmetry energy is parameterized in a way that the symmetry energy term, corresponding to the potential term of the type, shown in equation (2), is complemented by an analogous term with $\gamma_k = 2/3$, representing the kinetic energy of the degenerate Fermi gas at zero temperature (with the corresponding coefficient asummed to be related to the Fermi energy as $a_k = \epsilon_F(\rho_0)/3$). In the present work, the density dependences of the symmetry potential ranging from the asy-soft ($\gamma = 1/2$) to asy-stiff ($\gamma = 2$) were used ($\gamma = 4/5, 1, 5/4, 3/2$ being the intermediate values). The relative weight of the two terms was set to keep the value of the symmetry energy coefficient at normal nuclear density at the value of 32 MeV.

For each case the simulation was performed using 180 event runs with 600 test particles in each run. For each simulation the emitted protons were selected as described above and the resulting flow observables were compared to the measured values. Since the measured values represent a compilation of results of many experiments, no specific filtering procedure, taking into account experimental angular and momentum coverage, was performed. It is simply assumed that if the calculated value, even e.g. a maximum value of the negative elliptic flow at a given transverse momentum, approaches the measured value, the corresponding choice of the parameters of the equation of the state is considered as viable, while if neither the inclusive data nor the subset approach the measured value, the corresponding choice of the parameters of the equation of the state is considered as excluded by the measured data.

As one of the viable variants of the calculations appears to be the VdWBUU simulation (with in-medium nucleon-nucleon cross sections) using the stiff EoS and the symmetry energy potential parametrization with $\gamma = 1$. Besides the selection criterion mentioned above, the low energy cutoff was set at transverse momentum 0.4 GeV/c, since low-energy particles below such cutoff represent essentially the initial transverse momenta randomly generated according to the zero temperature Fermionic momentum distribution. Furthermore, also the effect of Coulomb interaction, which affects primarily such low-energy particles, is not taken into account in the BUU. The results are shown in the Figure 1. As one can see the measured directed flow is reproduced well over the whole range of beam energy and thus over a range of the maximum densities of

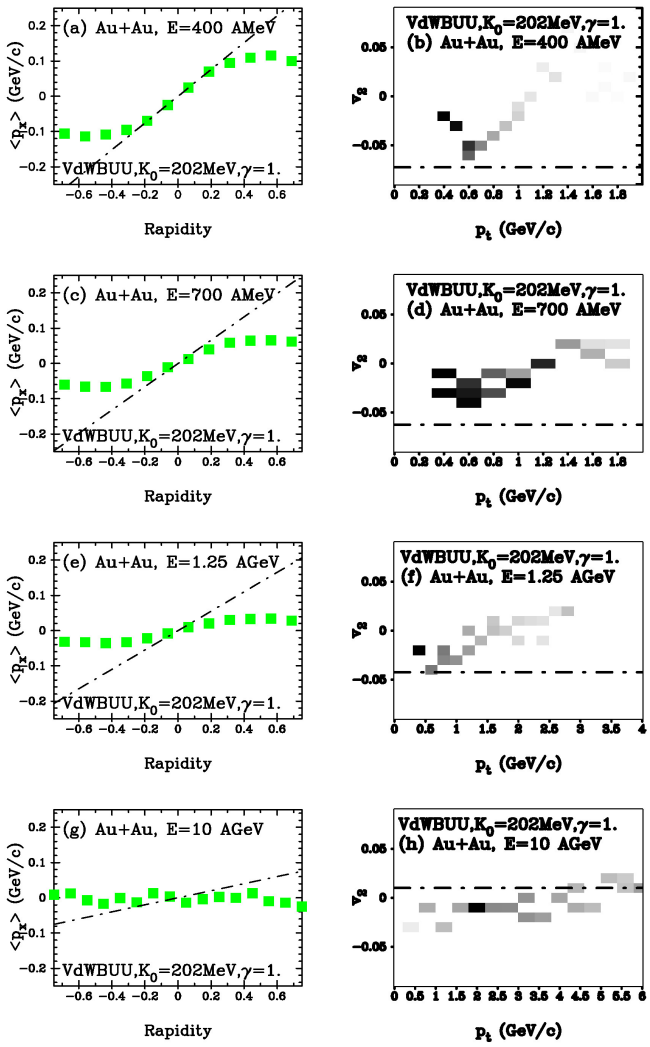

Fig. 3: Systematics of the proton directed flow (left panels, lines show experimentally observed slopes) and the transverse momentum dependence of the calculated proton elliptic flow at mid-rapidity versus the experimental value (boxes and the dash-dotted lines in right panels, respectively) in the collisions of Au+Au at beam energies ranging from 400 AMeV to 10 AGeV. Results were obtained using the VdWBUU simulation using the soft EoS with $\kappa = 7/6$ and the symmetry energy potential parametrization with $\gamma = 1$.

nuclear matter achieved in collisions. The maxima of the negative elliptic flow shown in the right panels reach the experimentally observed value. The agreement can be obviously improved by imposing more strict low-energy cutoff, which can be justified since the transport model describes only the pre-equilibrium stage of the collision and the properties of the low energy protons are influenced strongly by the secondary emission from the thermally equilibrated hot remnants of the first stage of collision. Also, especially at the lowest beam energies the behavior of the low energy particles depends also on the treatment of the Pauli principle, which is treated in an approximate way in the BUU simulation, and in the case of protons also by the Coulomb interaction which is not implemented in the model. The reproduction of the directed flow would not be affected by such cutoff, as can be understood when alternatively to the condition $\Delta\vec{p}\Delta\vec{r} > 2h$, one uses a widely used criterion, where the particle is considered as emitted when it is separated from any other particle in the space by distance of 3fm and in the momentum space by difference 0.3 GeV/c. This selection method was also implemented, and it does not affect the simulated values of directed flow, however the elliptic flow disappears almost fully.

To understand better the dramatic effect of the EoS-dependent in-medium nucleon-nucleon cross sections on directed flow, the results for the beam energy 10 AGeV with and without EoS-dependent in-medium nucleon-nucleon cross sections are compared in Figure 2 (the free nucleon-nucleon cross sections being used in the latter case). It is noteworhty that the free nucleon-nucleon cross sections lead to much stronger stopping and thus negative value of directed flow, while their reduction caused by density dependence leads

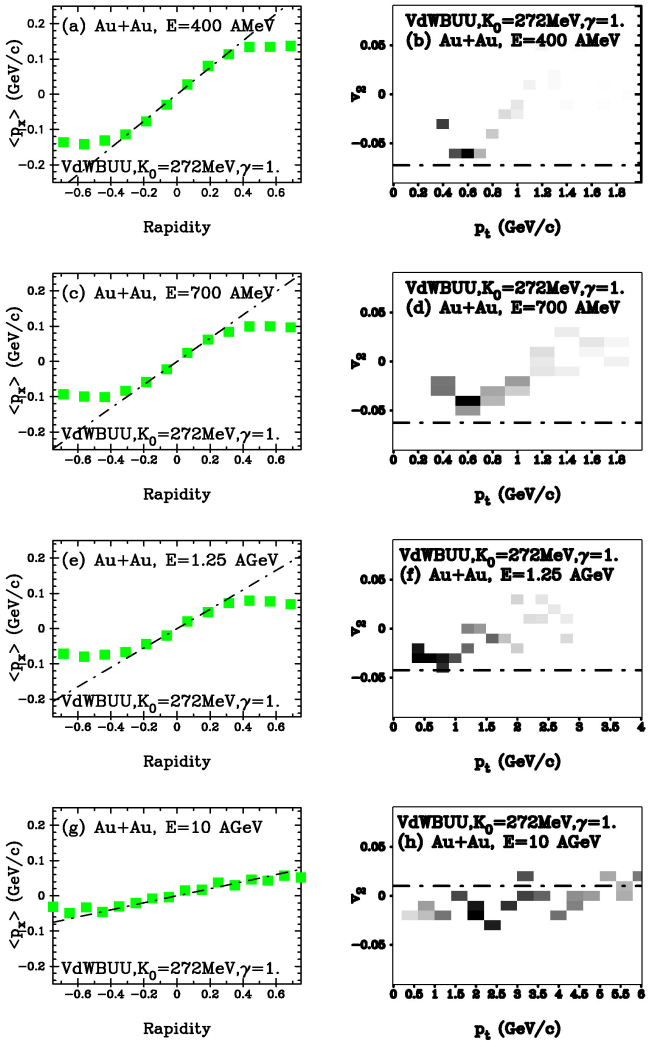

Fig. 4: Systematics of the proton directed flow (left panels, lines show experimentally observed slopes) and the momentum dependence of the calculated proton elliptic flow at mid-rapidity versus the experimental value (boxes and the dash-dotted line in right panels, respectively) in the collisions of Au+Au at beam energies ranging from 400 AMeV to 10 AGeV. Results were obtained using the VdWBUU simulation using the intermediate EoS with $\kappa = 3/2$ and the symmetry energy potential parametrization with $\gamma = 1$.

to reproduction of the measured value and thus correct description of dynamics in the participant zone leading to sidesplash behavior.

Another interesting observation is that other simulations with the stiff EoS and stiffer parametrizations of the density dependence of the symmetry energy up to the $\gamma = 2$ lead to a rather limited effect and all these symmetry energy parametrizations can be considered as viable. It appears to signal that the stiff equation of state with $\kappa = 2$ limits the effect of the density dependence of the symmetry energy. It can be understood since especially at high densities the contribution of symmetry energy to the total value of the potential is only a small part of the term corresponding to the stiff equation of state. Thus the effect of the density dependence of the symmetry energy can be expected to become more prominent when using the softer equations of the state.

As can be seen in Figure 3, simulations with the soft EoS (with $\kappa = 7/6$ and the compressibility $K = 200$ MeV) fail to reproduce both the directed flow and also elliptic flow. The directed flow is not reproduced from the beam energy 700 AMeV and above, the slopes of the transverse momentum are much less steep and such a soft equation of the state appears as excluded by the measured data on directed flow. The situation concerning the elliptic flow is less dramatic, still the observed agreement is worse than in the case of the stiff equation of the state. In this case the variation of the density dependence of the symmetry energy does not bring any improvement concerning the reproduction of the measured elliptic flow and thus the soft EoS with the compressibility $K = 200$ MeV appears to be excluded by the experimental directed flow and elliptic flow

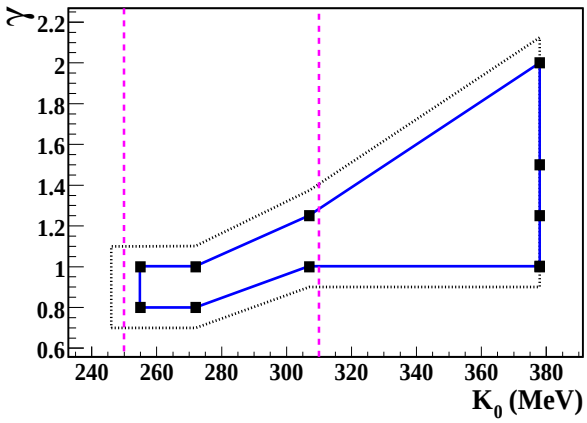

Fig. 5: The area marked by solid contour in the γ vs K_0 plot shows the values of the EoS and symmetry energy parameters, constrained by the analysis using the VdWBUU simulations (squares show the values where calculation was performed). Dotted contour shows the uncertainty where the values can not be conclusively excluded. Dashed lines shows the constrained values of K_0 from re-analysis of giant monopole resonance data [24].

systematics in the Au+Au collisions at the impact parameters b = 5.5 - 7.5 fm.

In Figure 4 are shown the results of the simulations with the intermediate EoS (with $\kappa = 3/2$ and the compressibility $K = 270$ MeV). This mode of simualtions leads to reasonable agreement with the measured directed flow and also the agreement with the measured elliptic flow is within the limits preventing to disregard this variant as viable. It is interesting to note that, compared to the stiff equation of the state, the effect of softening of the EoS is manifested in the shortening of linear parts of the transverse momentum dependence rather than by change of their slope. It might mean that especially at higher densities the effect of in-medium nucleon-nucleon cross sections dominates over the effect of mean-field potential.

The results of the analysis are summarized in the Figure 5. The approximately triangular areas marked by solid and dotted contour in the γ vs K_0 plot shows the combinations of the EoS incompressibilities and symmetry energy density dependencies, which lead to reasonable agreement (solid contour) or can not be conclusively ruled out as feasible for the description of properties of nuclear matter (dotted contour). The stiffer EoS apparently leads to weakening of the sensitivity to the density dependence of the symmetry energy. It appears that the density dependence with $\gamma = 1$ can be identified as a globally feasible value of the stiffness of the symmetry energy. The range of the possible stiffness of the EoS can be identified, based on the analysis presented here, as encompassing incompressibilities $K_0 > 245 MeV$. A reason why upper limit is not set can be understood from formula 4, which for high nucleonic densities tends to converge to the $1/\rho$-dependence and sensitivity to further stiffening is lost. It appears necessary to investigate further observables, which would eventually prove sensitive to effect of very stiff equation of state at super-saturation densities. Nevertheless, the constrained range, obtained by analysis of nuclear reactions occuring at super-saturation densities, appears to be in agreement with the results of recent re-analysis of the data from giant monopole resonance [24], a process occuring close to saturation density, where the range of $K_0 = 250$ - 310 MeV (shown as dotted area in Figure 5) was determined after modification of the fitting procedure, used to determine incompressibility, thus correcting the earlier constrained softer values between 200 - 240 MeV. Thus the values of incompressibility obtained at different density ranges appear to be in agreement, what may point toward existence of simple equation of state, which can be described by a single value of incompressibility K_0. When combining our results with results of the work [24], it is possible to set a stricter constraint on the values of γ, representing the stiffness of the density dependence of symmetry energy, which can be restricted to range $\gamma = 0.7 - 1.25$, with the value of γ roughly increasing with increasing value of K_0. The resulting values appear to be in agreement with results of earlier studies of nucleus-nucleus collisions [10, 19]. In order to obtain more strict constraints on γ, detailed simulations of experimental conditions and investigations of neutron flow observables might be necessary. Furthermore, the range of feasible incompressibilities is strongly correlated to the results of astrophysical evaluations of the radius of neutron stars. The values of $E_{sym}(\rho_0)$ and L constrained using radii of neutron stars depend rather weakly on the incompressibility of the EoS [25] and thus relatively stiffer equations of state appear appropriate, even if restrictions due to causality must be considered. Also, the recent re-analysis of the determination of the neutron star radii appears to lead to larger radii with lower limit around 14 km [26] and thus to favor

stiffer equation of the state. Furthermore, also the relatively thick neutron skin of ^{208}Pb, reported by the PREX experiment [27, 28], appears to favor a stiffer equation of state [29].

CONCLUSIONS

In summary, the new implementation of the BUU, the VdWBUU simulation (with EoS-dependent in-medium nucleon-nucleon cross sections) appears to reproduce simultaneously both the directed and elliptic flow in semi-peripheral Au+Au collisions in the energy range from 400 AMeV to 10 AGeV. Based on the analysis presented here, investigating the properties of nuclear matter at super-saturation densities, the range of feasible incompressibilities of the equation of state can be identified as $K_0 > 245MeV$, which is consistent with the results of recent re-analysis of the giant monopole resonance data, obtained at densities, close to saturation density, $K_0 = 250 - 310MeV$ [24]. Using such complementary result as an additional constraint, the range of the stiffness of density dependence of symmetry energy could be restricted to $\gamma = 0.7 - 1.25$, with the value of γ roughly increasing with increasing value of K_0. The implementation of BUU with EoS-dependent in-medium nucleon-nucleon cross sections, and thus with EoS-dependence for the first time implemented in the collision term, leads to physically relevant values of K_0 and γ, while the BUU with the free nucleon-nucleon cross sections can not describe correctly the global trends of flow observables.

ACKNOWLEDGMENT:

This work is supported by the Slovak Scientific Grant Agency under contracts 2/0105/11 and 2/0121/14, by the Slovak Research and Development Agency under contract APVV-0177-11 (M.V.), by the NSFC of China under contract Nos. 11035009, 10979074, the Knowledge Innovation Project of CAS under Grant No. KJCX2-EW-N01 (Y.G.M.) and by ELKE account No 70/4/11395 of the National and Kapodistrian University of Athens (G.S.).

REFERENCES

[1] D. H. Youngblood, H. L. Clark, and Y.-W. Lui, Phys. Rev. Lett. **82**, 691 (199 9). 06).
[2] J. B. Natowitz *et al.*, g, Phys. Rev. Lett. **89**, 212701 (2002).
[3] P. Danielewicz, R. Lacey, and W. G. Lynch, Science **298**, 1592 (2002).
[4] W. Reisdorf *el al.,* Nucl. Phys. A **876**, 1 (2012).
[5] M. B. Tsang *et al.*, Phys. Rev. Lett. **92**, 062701 (2004).
[6] M. A. Famiano *et al.*, Phys. Rev. Lett. **97**, 052701 (2006).
[7] M. B. Tsang *et al.*, Phys. Rev. Lett. **102**, 122701 (2009).
[8] S. Kumar *et al.*, Phys. Rev. C **84** , 044620 (2011).
[9] B. A. Li, L. W. Chen, and C. M. Ko, Phys. Rep. **464**, 113 (2008). (2009).
[10] P. Russotto *et al.*, Phys. Lett. B **697**, 471 (2011).
[11] M. D. Cozma, Phys. Lett. B **700**, 139 (2011).
[12] S. Gautam *et al.*, Phys. Rev. C **83**, 034606 (2011).
[13] G. F. Bertsch, H. Kruse, and S. Das Gupta, Phys. Rev. C **29**, 673 (1984).
[14] H. Kruse, B. V. Jacak, and H. Stöcker, Phys. Rev. Lett. **54**, 289 (1985).
[15] C. Y. Wong, Phys. Rev. C **25**, 1460 (1982).
[16] J. Cugnon, T. Mizutani, and J. Vandermeulen, Nucl. Phys. A **352**, 505 (1981).
[17] G. Q. Li, and R. Machleidt, Phys. Rev. C **48**, 1702 (1993); Phys. Rev. C **49**, 566 (1994).
[18] T. Alm, G. Ropke, and M. Schmidt, Phys. Rev. C **50**, 31 (1994); T. Alm, G. Ropke, W. Bauer, F. Daffin, and M. Schmidt, Nucl. Phys. A **587**, 815 (1995).
[19] B. A. Li, and L. W. Chen, Phys. Rev. C **72**, 064611 (2005).
[20] D. Klakow, G. Welke, and W. Bauer, Phys. Rev. C **48**, 1982 (1993).
[21] N. Herrmann, J. P. Wessels, and T. Wienold, Ann. Rev. Nucl. Part. Sci. 49 (1999) 581.
[22] A. Andronic, J. Lukasik, W. Reisdorf, and W. Trautmann, Eur. Phys. J. 30 (2006) 31.
[23] M. Veselsky, Y.G. Ma, Phys. Rev. C 87 (2013) 034615.
[24] J.R. Stone, N.J. Stone and S.A. Moszkowski, arXiv:1404.0744 [nucl-th].
[25] K. Hebeler, J.M. Lattimer, C.J. Pethick and A. Schwenk, arXiv:1303.4662 [astro-ph.SR].
[26] V. Suleimanov, J. Poutanen, M. Revnivtsev and K. Werner, Astrophys. J. 742 (2011) 122.
[27] S. Abrahamyan et al., Phys. Rev. Lett. **108**, 112502 (2012).
[28] C. Horowitz et al., Phys. Rev. C **85**, 032501 (2012).
[29] F.J. Fattoyev and J. Piekarewicz, arXiv:1306.6034 [nucl-th].

PLUNGER LIFETIME MEASUREMENTS AT JYFL

Tuomas Grahn[1,*]

[1]University of Jyväskylä, Department of Physics, Accelerator Laboratory, P. O. Box 35, FI-40014 University of Jyväskylä, Finland

Abstract

Recoil Distance Doppler-Shift (RDDS) mean lifetime τ measurements have been carried out with the JUROGAM I & II γ-ray spectrometers and the RITU recoil separator at the Accelerator Laboratory of the University of Jyväskylä. A dedicated plunger device for JUROGAM has been constructed and employed in a series of measurements in medium-heavy and heavy nuclei. These measurements have shed light on the collectitivity, deformation and configuration mixing of coexisting shapes. In addition, systematical measurements of development of collectivity in several nuclei have been carried out.

INTRODUCTION

Electromagnetic transition rates between the ground and excited states in atomic nuclei provide us with a delicate, model independent probe to the nuclear structure. Since the transition rate is directly proportional to the transition matrix element and as the electromagnetic operators are well understood one can, in principle, extract direct information about the nuclear wave function. Furthermore, by applying different models several quantites such as transition quadrupole moments and deformation parameters can be deduced.

The methods to measure transition rates vary according to the mean lifetime range of states under investigation [1]. Typically, when one deals with collective transitions in heavy nuclei, possible methods are Recoil Distance Doppler-Shift (RDDS) method, Coulomb excitation or direct (electronic) measurements of the lifetimes. Excited states of many neutron-deficient heavy nuclei can be produced with stable beam and target combinations in heavy-ion induced fusion reactions. Often when studying nuclei with production cross sections on the order of millibarn or less, high selectivity of the nuclei of interest is required. Such a selectivity can be obtained by coupling a recoil separator with a γ-ray and focal plane spectrometer. The present contribution reviews some results obtained with the RDDS method [2] and the plunger device with JUROGAM I & II.

EXPERIMENTAL METHOD

By utilising the heavy-ion beams delivered by the JYFL K130 cyclotron, the nuclei of interest are populated trough fusion-evaporation reactions. The beam intensity delivered to the target has typically been 1-5 pnA, mainly limited by heat deposited to a stretched target. Prompt γ rays have been detected with the JUROGAM Ge-detector array, consisting of 43 Eurogam Phase I type Compton-suppressed Ge detectors [3]. However, only 15 of the JUROGAM Ge detetors can be used in an RDDS analysis due to their suitable angular position (five at 158° and ten at 134° with respect to the beam direction). Recently, JUROGAM has been upgraded to the digitally instrumented JUROGAM II array, consisting of 15 Eurogam Phase I and 24 Eurogam clover detectors [4].

Spectroscopic studies close to the proton drip line require high selectivity due to low production cross sections in fusion-evaporation reactions of nuclei under investigation. This is also evident for many heavy nuclei with high neutron deficiency. To obtain this in RDDS measurements, the standard JUROGAM target chamber was replaced by the Köln plunger device, which houses the moveable target and a degrader foil [5]. Recently, Differential Plunger for Unbound Nuclear States (DPUNS), a plunger device dedicated for JUROGAM has been constructed [6]. The degrader foil that replaced the standard stopper foil is used in DPUNS in order to allow evaporation residues to recoil into the gas-filled RITU separator [7]. The principle of the RDDS method with the degrader foil in the plunger device is shown in Fig. 1. RITU separated the recoiling evaporation residues from unwanted particles such as scattered beam and fission products according to their magnetic rigidity. The recoils were transported to the focal plane of RITU and into the GREAT spectrometer [8]. At the entrance of GREAT the recoils passed through MultiWire Proportional Counter (MWPC) and were implanted into a pair of Double-sided silicon Strip Detectors (DSSDs). By combining

*E-mail: tuomas.grahn@jyu.fi

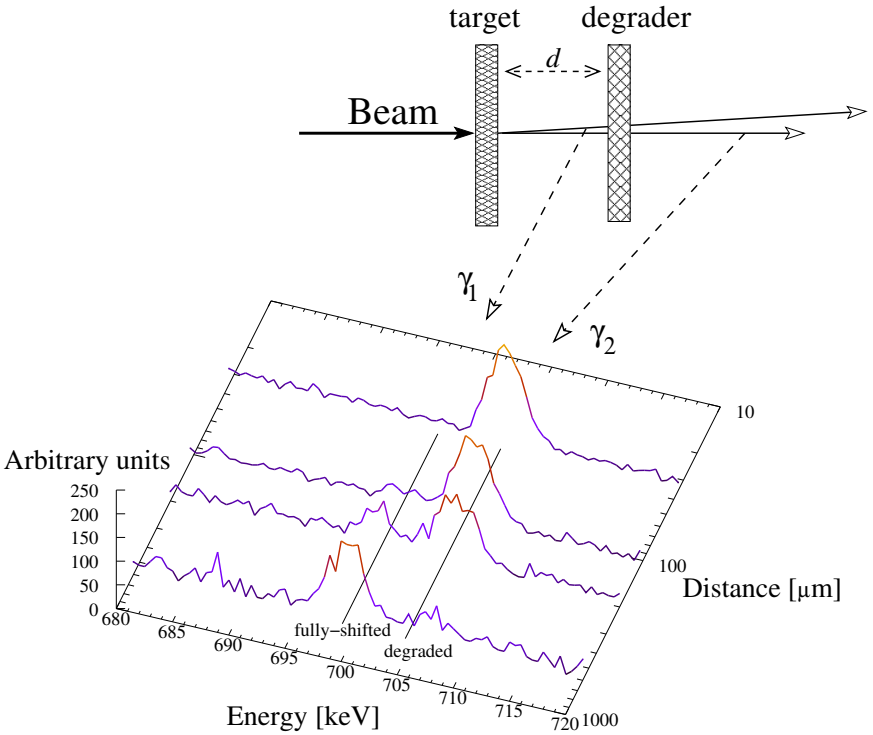

Fig. 1: The principle of the RDDS method with the degrader foil replacing the standard stopper foil in the plunger device. The γ rays emitted from a nucleus moving with different velocities undergo different Doppler shifts in energy when observed in a given angle θ with respect to the beam direction. By measuring the γ-ray intensities of the two components (fully-shifted and degraded) of the full energy γ-ray peak as a function of the target-to-degrader distance d, a mean lifetime τ can be extracted.

the energy loss in MWPC and the time-of-flight between the MWPC and DSSDs, selection of recoils were made (recoil gating hereafter). Consequently, recoil-gated prompt γ-ray spectra recorded with JUROGAM were constructed. Higher sensitivity, subject to favourable radioactive decay conditions, were obtained by demanding a characteristic radioactive decay following the recoil event in the same pixel of DSSDs within a given time window, following the principles of the Recoil-Decay Tagging (RDT) technique [9].

The use of the degrader foil sets certain limitations for feasibility of the experiments with the RDDS method. Due to the small angle scattering of the recoiling evaporation residues in the degrader foil, the solid angle covered by the recoils is increased, which in turn decreases the number of recoils entering RITU. It has been shown that use of 1 mg/cm^2 Mg degrader foil reduces the RITU transmission by a factor of 2/3. With such a foil, a sufficient velocity difference $\Delta v/c = 1\%$ is achieved. More detailed discussion about experimental conditions can be found e.g. in Ref. [10]

SHAPE COEXISTENCE AROUND $Z = 82$ AND $N = 104$

The shape coexistence, in which very different coexisting shapes (e.g. spherical, prolate and oblate) coexist with almost degenerate energies, has been a subject of both experimental and theoretical studies in the neutron-deficient Pb region [11]. It has been a common practice to base arguments of the shape coexistence on the observed level energies and in particular on observation of the parabolic pattern of intruder-state energies around the neutron mid shell at $N = 104$. Indeed, systematical in-beam γ-ray spectroscopy studies have been carried out providing invaluable data [12]. However, as the shape coexistence is closely intertwined with quadrupole collectivity, absolute fingerprints can only be be acquired through measurements of transition probabilities. Only until recently, data of such quantities have been scarce. Through developments of the selective tagging methods as described above, such measurements have become possible in very exotic nuclei such as ^{186}Pb [13].

By utilising the RDDS method, transition probability data have been obtained across the $Z = 82$ shell gap in the vicinity of $N = 104$. Furthermore, by applying rotational model [14] absolute values of transitional quadrupole moments Q_t can be obtained. The quadrupole moment is charge dependent and therefore it is necessary to take that into account when comparing $|Q_t|$ values of nuclei with different Z. In Fig. 2 quantities $< |Q_t| > /Z$ are plotted as a function of Z for the isotopes at or near $N = 104$. The $< |Q_t| >$ values are

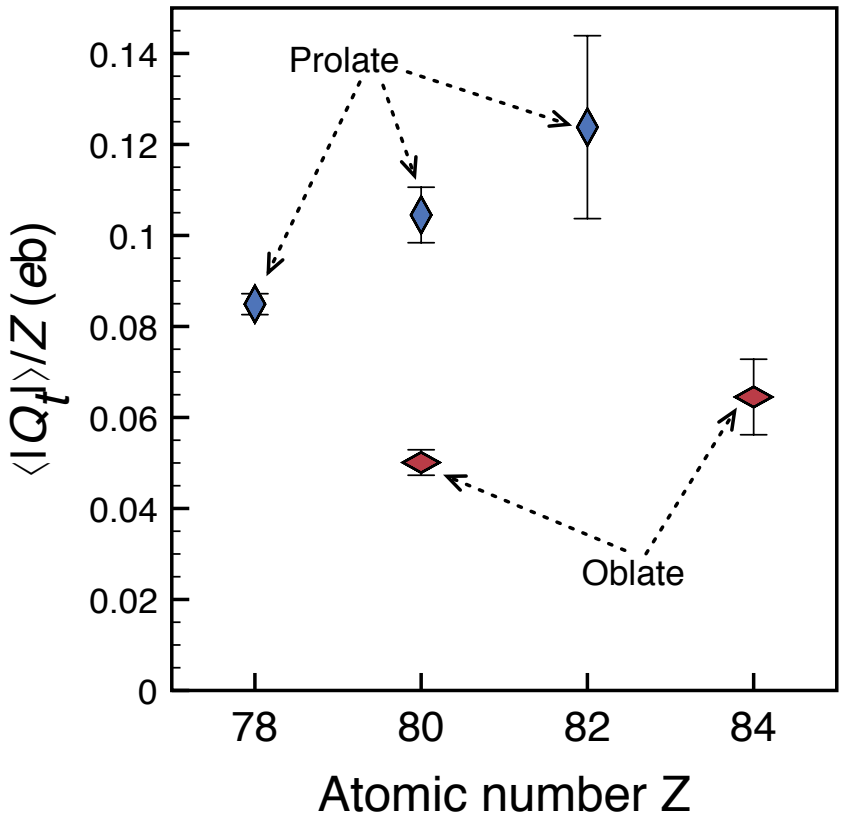

Fig. 2: The mean values of $|Q_t|$ of states associated with prolate and oblate deformation extracted from measured mean lifetime τ and normalised by their nuclear charge Z. The data associated with oblate deformation are taken from the 2^+ states in ^{180,182}Hg [16] and the 2^+ and 4^+ states in ^{194}Po [13]. The data for the prolate deformation are taken from the yrast states in ^{184}Pt and states with $I^\pi > 2^+$ in ^{180,182}Hg [16] and ^{186}Pb [13].

mean values of transitional qudrupole moments for states associated with prolate and oblate deformations.

From Fig. 2 it is astonishing to note that there could be an increasing trend of collectivity as a function of Z. This behaviour is in disagreement with the fact that the observed kinematic moments of inertia are identical for these bands [12] suggesting their similarity in terms of collectivity. Also for the oblate states a very modest increase in collectivity can be seen. However, some caution should be exercised before making any further conclusions. It is clear that more systematical transition probability measurements are required for in-depth understanding of shape coexistence in the neutron-deficient Pb region.

NUCLEI ABOVE $N = Z = 50$

Significant effort has been invested in the study of $N \approx Z$ nuclei residing just above the $Z = 50$ shell gap. For example, recent γ-ray spectroscopy studies of the neutron-deficient Te [17], I [18] and Xe [19] nuclei that have provided extensive level-energy systematics, suggest evidence of enhanced collectivity when approaching the $N = 50$ shell gap. The decreasing trend of energy of the 2^+ and 4^+ states from ^{114}Te is observed down to ^{108}Te, before increasing again slightly at ^{106}Te. This can be seen from the bottom panel of Fig. 3. It is interesting to note that a similar phenomenon has also been observed in the neutron-deficient I and Xe nuclei and the origins are probably related to those in the Te nuclei.

Such an observation prompted investigations of transition probabilities in this region of the nuclear chart. An RDDS lifetime measurement of the 2^+ state in ^{108}Te has been carried out at JUROGAM II and RITU [21]. In contrast to the level-energy systematics for these nuclei, and what has previously been measured in light Sn isotopes [22], the result does not provide evidence for any enhancement in the $B(E2; 2^+ \rightarrow 0^+)$ reduced transition probability in the light Te nuclei as the $N = 50$ shell gap is approached. This can be seen from the top panel of Fig. 3. The result clearly suggests that the decreasing trend of the level energies below $N = 62$ is therefore most likely not a deformation driven effect.

In addition, an RDDS lifetime measurement in ^{109}I were carried out by tagging γ-ray spectra with

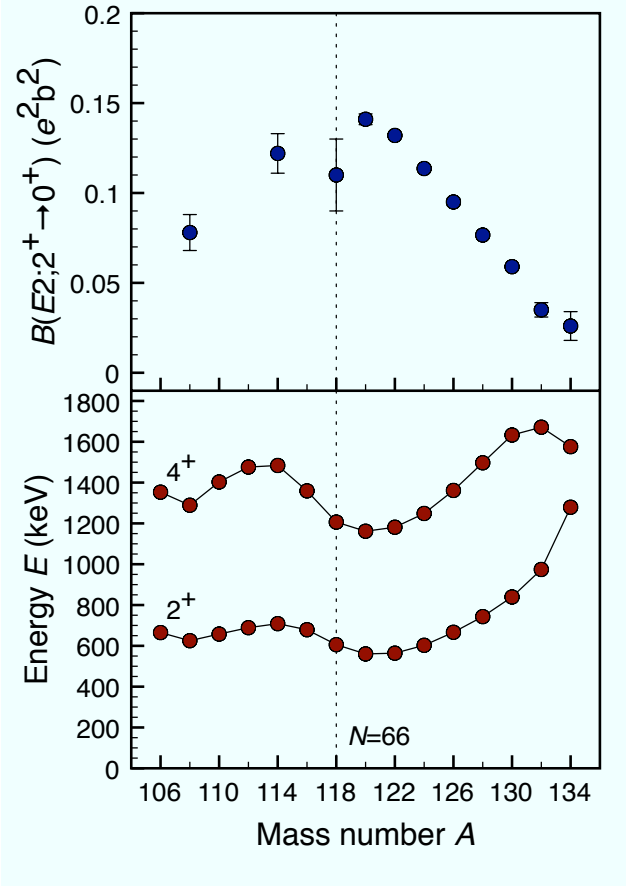

Fig. 3: Reduced transition prob-ability $B(E2; 2^+ \rightarrow 0^+)$ (top panel) and 2^+ and 4+ level-energy (bottom panel) systematics for even-mass Te isotopes. The experimental data marked with open circles are taken from Ref. [20]. The neutron mid shell at $N = 66$ is marked with the dotted vertical line.

characteristic proton-decay events of ^{109}I at the RITU focal plane, representing the first ever proton-tagged RDDS lifetime measurement [23]. The mean lifetime of the tentative $11/2^+$ was used to asses the nature of decoupling of the valence proton from its even-even ^{108}Te core.

CONCLUDING REMARKS

Recoil-Distance Doppler-Shift lifetime measurements by utilising selective tagging techniques have been carried out at the University of Jyväskylä. The JUROGAM I & II γ-ray spectrometers with the RITU separator have been used. The neutron-deficient nuclei with $52 \leq Z \leq 84$ have been probed. Collectivity and $Z = N = 50$ shell gap have been studied in Te and I nuclei by tagging the prompt γ rays with recoils, α or proton decays. In slightly heavier-mass nuclei recoil-isomer tagging has been exploited in measurements of lifetimes of states built on top of an isomeric state. Such studies have been carried out e.g. in ^{144}Ho [24]. Features of shape coexistence of several different collective configurations around the neutron mid shell at $N = 104$ in the Pt, Hg, Pb and Po nuclei have been probed trough lifetime measurements. Such measurements have also played important role in the analysis of Coulomb excitation data recorded with MINIBALL γ-ray spectrometer at CERN-ISOLDE [25].

REFERENCES

[1] P. J. Nolan and J. F. Sharpey-Shafer, Rep. Progr. Phys. **42**, 1 (1979).
[2] A. Dewald, O. Möller, P. Petkov, Prog. Part. Nucl. Phys. **67**, 786 (2012).
[3] C. W. Beausang *et al.*, Nucl. Inst. Methods Phys. Res. A **313**, 37 (1992).
[4] G. Duchene *et al.*, Nucl. Inst. Methods Phys. Res. A **432**, 90 (1999).
[5] L. Cleemann *et al.*, Nucl. Inst. Methods Phys. Res. **156**, 477 (1978).
[6] M. J. Taylor *et al.*, Nucl. Instrum. Meth. Phys. Res. A **707**, 143 (2013).
[7] M. Leino *et al.*, Nucl. Inst. Methods Phys. Res. B **99**, 653 (1995).
[8] R. D. Page *et al.*, Nucl. Inst. Methods Phys. Res. B **204**, 634 (2003).

[9] E. S. Paul *et al.*, Phys. Rev. C **51**, 78 (1995).
[10] T. Grahn *et al.*, Nucl. Phys. A **801**, 83 (2008).
[11] K. Heyde and J. L. Wood, Rev. Mod. Phys. **83**, 1467 (2011).
[12] R. Julin, K. Helariutta and M. Muikku, J. Phys. G: Nucl. Part. Phys. **27**, R109 (2001).
[13] T. Grahn *et al.*, Phys. Rev. Lett. **97**, 062501 (2006).
[14] A. Bohr and B. A. Mottelson, Nuclear Structure, Vol. 2: Nuclear Deformations, 1975 (Benjamin, New York, USA).
[15] U. Garg *et al.*, Phys. Lett. B **180**, 319 (1986).
[16] T. Grahn *et al.*, Phys. Rev. C **80**, 014324 (2009).
[17] B. Hadinia *et al.*, Phys. Rev. C **72** (2005) 041303(R).
[18] M. Petri *et al.*, Phys. Rev. C **76**, 054301 (2007).
[19] M. Sandzelius *et al.*, Phys. Rev. Lett. **99**, 022501 (2007).
[20] http://www.nndc.bnl.gov/ensdf/.
[21] T. B äck *et al.*, Phys. Rev. C **84**, 041306(R) (2011).
[22] A. Ekstr öm *et al.*, Phys. Rev. Lett. **101**, 012502 (2008).
[23] M. G. Procter *et al.*, Phys. Lett. B **704**, 118 (2011).
[24] P. J. R. Mason *et al.*, Phys. Lett. B **683**, 17 (2010).
[25] N. Bree *et al.*, Phys. Rev. Lett. **112**, 162701 (2014).

EXPERIMENTS ON PRODUCTION AND NUCLEAR STRUCTURE INVESTIGATIONS OF SUPERHEAVY ELEMENTS AT GSI

Fritz Peter Heßberger[1,2,*]

[1]GSI - Helmholtzzentrum für Schwerionenforschung GmbH, Planckstraße 1, 64291 Darmstadt, Germany
[2]Helmholtz Institut Mainz, Johann-Joachim-Becherweg, 55128 Mainz, Germany

Abstract

An extensive program on synthesis of superheavy elements (SHE) as well as on investigation of their nuclear structure and chemical properties has been performed at the UNILAC accelerator at GSI Helmholtzzentrum für Schwerionenforschung GmbH, Darmstadt, during the past three and a half decades. In recent years the program was focussed on attempts to synthesize the new elements 119 and 120 in the reactions ^{249}Bk(^{50}Ti,xn)$^{299-x}$119, ^{249}Cf(^{50}Ti,xn)$^{299-x}$120, and ^{248}Cm(^{54}Cr,xn)$^{302-x}$120. The present status of data evaluation revealed only upper production cross section limits.
Nuclear structure investigation concentrated on systematics of single particle levels in odd-mass nuclei, studies of two- and four-quasi-particle states forming K-isomers, determination of shell strengths around N = 152 and N = 162 within the isotone chains (N = 149-153) in odd-mass even-Z nuclei and along the isotope chains in odd-mass odd-Z nuclei (Z = 99-103).

INTRODUCTION

The quest for the heaviest atomic nucleus that can exist is a basic topic in nuclear physics research. The atomic nucleus is a quantum mechanical system consisting of protons carrying a positive electric charge and neutrons being electricly neutral. They interact via the Coulomb force and the so-called nuclear force. The latter is understood as the residuum of the strong interaction acting between the constitutents of the nucleons, the quarks, that can be felt outside the nucleons. The interplay between these two forces determines the properties of an atomic nucleus. While the Coulomb force is well understood, theoretical description of the nuclear force is difficult and has not been succeeded satisfactorily so far. It thus had become common already a couple of decades ago to approximate the nuclear force by a mean potential created by all the nucleons in which the latter act as quasi-free particles. This concept finally was the basis for the nuclear shell model [1, 2]. In practise, however, pure shell model calculations became extremely extensive with increasing nucleon number, so for heavy nuclei a combination of the liquid drop model and shell model calculations, known as macroscopic - microscopic models, became common (see e.g. [3, 4]). The liquid drop model, originally been suggested by C.F. von Weizsäcker [5], was used in improved versions to describe the gross properties of the nucleus, while the influence of the shell structure on the nuclear ground-state masses was taken into account by small energy corrections, often denoted as 'shell effects', calculated using a method suggested by V.M. Strutinsky [6].
Enhanced stability against radioactive decay is indicated by large negative values of the nuclear binding energy. Stabilization against spontaneous fission (sf) is of specific importance in the region of transactinide nuclei, as fission barriers (B_f) calculated on the basis of the liquid-drop model (see [7] for first theoretical treatment) were expected to vanish around $Z \approx 106$, determining the limit of nuclear stability. First theoretical studies on extrapolation of the nuclear shell model into regions far beyond the highest experimentally established magic proton and neutron numbers ($Z = 82$, $N = 126$) performed almost fifty years ago [8, 9] offered a different picture. They resulted in predicting $Z = 114$ and $N = 184$ as the next spherical shell closures, which should result in large shell correction energies for nuclei in that region leading to an enhanced stability and thus to expected long lifetimes. These results were the starting points for intense theoretical investigations to verify these numbers and to predict the shell strengths and possible decay properties of nuclei in that region, which soon were denoted as 'superheavy' (see e.g. [10]).
The results obtained from two advanced macroscopic - microscopic (MM) models [3, 4] are shown in fig. 1. One maximum is found around the $Z = 114$, $N = 184$, referring to spherical proton and neutron shell closures (as already predicted in [8, 9]). The other one is found around $Z = 108$, $N = 162$. Maximum shell correction energies are found nearly as high as at the spherical shell closures, but the nuclei are well deformed in their ground-state with quadrupole deformation parameters of $\beta_2 \approx 0.23$ in vicinity of the shell closures. While different MM approaches agreed in the location of the 'spherical' shells, significant differences were obtained in the shell correction energies itself as seen in fig. 1. Another feature evident from fig. 1 is the large

*E-mail: f.p.hessberger@gsi.de

extension of the region of high shell effects. Considering as a measure of that region, e.g., arbitrarily, the range $\delta E_{sh} \geq 0.8\,\delta E_{sh}(\max)$, we find in the SHE region the intervals N = 171-184 and Z = 112-120, or an extension of $\Delta N = 14$ and $\Delta Z = 9$ [4]. Around Z = 82, N = 126 these intervals are definitely smaller. One finds N = 123 - 128 and Z = 78 - 84, or $\Delta N = 6$ and $\Delta Z = 7$ [4]. Predicted half-lives varied considerably, depending on the size of shell effects and the competition between α- and β - decay and sf. Already in early calculations, the maximum half-lives were not expected at the shell closures (Z = 114, N = 184), but at somewhat lower values of Z and N [10] as shown in fig. 2 based on more recent predictions.

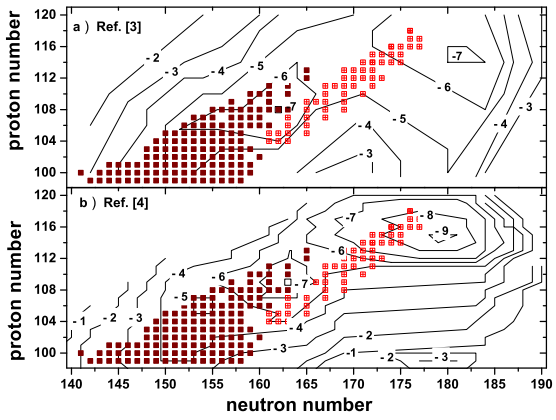

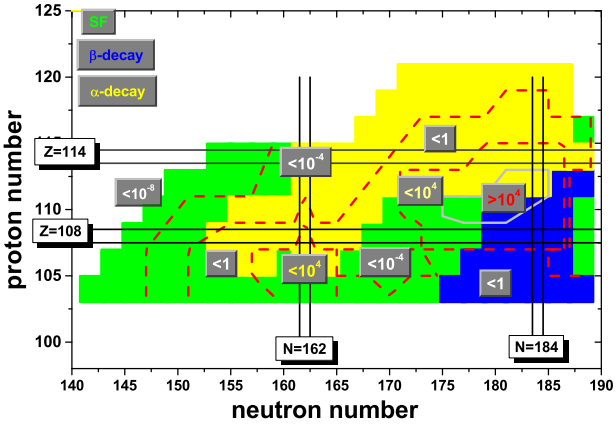

Fig. 1: left hand side: Ground-state shell correction energies of heavy nuclei (Z>100) as function of proton number Z and neutron number N, obtained from MM calculations by [3] (fig. 1a) or [4] (fig. 1b.). The squares represent the known nuclei, the subset of open squares with cross inside represent nuclei synthesized in actinide based fusion reactions using ^{48}Ca beams and their α decay products.

Fig. 2: right hand side: expected dominating decay modes and half-life ranges of SHE, yellow stands for α decay, green for sf, and blue for β^- decay. Alpha - halflives are calculated according to [11, 12] using the Q_α - values from [3], sf - half-lives are taken from [13, 14], and β^- half-lives from [15].

About a one and a half decades ago first results on predictions of proton and neutron shell closures in the transactinide region using completely different approaches were reported. They were obtained using self-consistent models like Skyrme-Hartree-Fock-Bogoliubov (SHFB) calculations or relativistic mean-field models (RMF) using NL3, NL-Z2 or NL-Z parametrisations [16, 17]. The RMF calculations resulted in N = 172 as the magic neutron number, while the Skyrme - force based calculations resulted in N = 184. The proton shell appeared at Z = 120 in the RMF and most of the SHFB calculations, while the SkI4 parametrization resulted in Z = 114, the SkP and SkM* parametrizations in Z = 126 as magic number [16]. Proton (Z) and neutron (N) numbers where the shells occur are strongly dependent on details in the description of the underlying forces as been discussed extensively by Bender et al. [18], especially from the values for the effective masses m^* and the stength of the spin - orbit interaction. High values $m^*/m \approx 1$ as used for SkP lead to a high level density at Z = 114 and Z = 120 and prefer a shell closure at Z = 126 [18]. A shell at Z = 114 on the other side, is located between the spin - orbit coupled states $2f_{7/2-}$ and $2f_{5/2-}$, while in addition the $1i_{13/2-}$ level has to be pushed down. It thus was discussed in [18] that Z = 114 is only magic in case of a large amplitude of the spin - orbit coupling as for the parametrization SkI4, which on the other hand overpredicts the spin - orbit coupling in ^{208}Pb by 80% [18].
Similar to the MM - calculations also these self-consistent calculations resulted in extended areas of large shell effects. It thus has been suspected recently if the concept of magicity is useful for superheavy nuclei [19]. As those calculations used effective nucleon-nucleon interactions the parametrization of the latter strongly determined the properties of the nuclei or, vice versa, from the properties of the nuclei (e.g. ground-state masses, deformations, nuclear structure) it seems possible to draw conclusions on the nuclear force and thus the strong interaction, which is not possible within the MM - models. As at least some of these parametrizations play also an important role in other topics in physics, a mutual influence from results of different topics is expected. This item has been already treated by E. Chabanat et al. [20, 21] who used Skyrme interactions to describe both, nuclear as well as neutron star properties, while recently M. Hempel presented results on mass - radius - relation and density - profiles of neutron stars using the SLy4 - force [23], which also had been used, e.g., to calculate low lying Nilsson levels in odd-mass einsteinium isotopes [22].

As superheavy elements are stabilized solely by shell effects their existence and properties are strongly dependent on details of the nuclear force. Under these circumstances it can be acted on the assumption that their properties and structure are sensitive probes for understanding the latter. So we here realize a motivation for SHE research that goes beyond the attempts to produce heavier and heavier elements, which finally is just one item in that field. The more global aspect of SHE research is to be part of the ambition to understand the basic interactions. It also comprises, among others, investigation of radiocactive decay modes, nuclear structure, atomic and chemical properties.
Yet, it is out of doubt that here we are faced with an ambitious project. A lot of effort from theoretical and experimental side is necessary to succeed and also new more powerful facilities are required.
Attempts to synthesize SHE in the laboratory or to find them in nature started already shortly after the first theoretical predictions. At GSI SHE - research as an essential part of the scientific program meanwhile has a tradition of nearly fourty years. Experimental techniques and sensitivity were developed and improved continuously and presently allow for the synthesis and identification of superheavy nuclei with production cross sections limits in the order of 50 fb that can be reached within reasonable irradiation times of about 150 days.
For many years the velocity filter SHIP [24] as well as chemical separation methods (see e.g. [25]) were the working horses. Recently the experimental possibilities were significantly extended by installation of the gas-filled separator TASCA [26] and the double Penningtrap spectrometer SHIPTRAP [27].
Highlights of this research program were the identification of the new elements with atomic numbers Z = 107-112 [28], detailed nuclear structure investigations [29, 30, 31] and discovery of new K isomers [32, 33, 34] in the transfermium region, first nuclear spectroscopy measurements in an experiment leading to Z = 115 as compound nucleus [35], confirmation of elements 116, 117 [36, 37], first chemical characterization of element 108 (hassium) [38], first direct mass measurements of $^{252-255}$No [39, 40, 41], ^{255,256}Lr [41] and identification of the deformed doubly magic nucleus ^{270}Hs [42].

Synthesis of Superheavy Elements

Most crucial for successful experiments on the synthesis of superheavy elements (SHE) is the proper choice of the reaction and the bombarding energies. Especially the latter is essential since maximum production cross-sections (σ) are restricted to a region of typically $\Delta E \approx \pm 4$ MeV as illustrated in fig.3, where experimental cross-sections for the production of ^{292,293}116 in bombardments of ^{248}Cm with ^{48}Ca are shown.

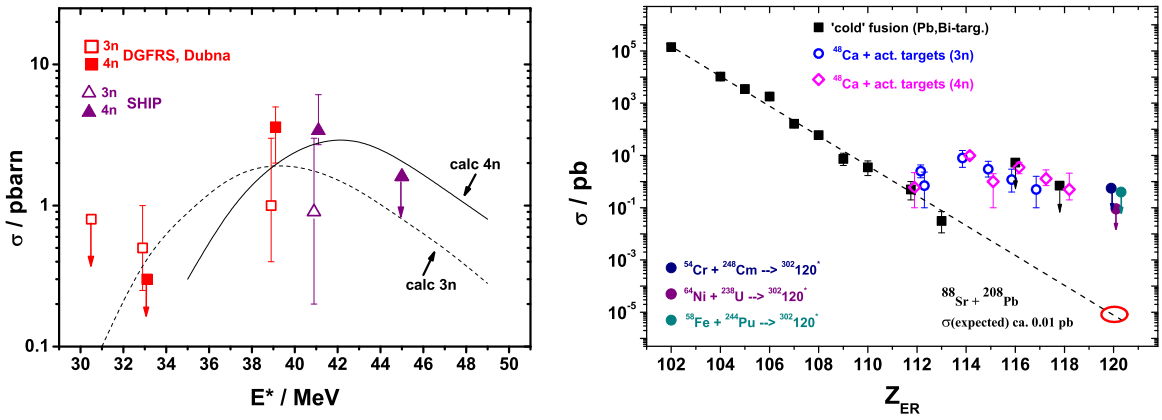

Fig. 3: (left side) Experimental and calculated production cross-sections for ^{292}Lv (4n) and ^{293}Lv (3n) in bombardments of ^{248}Cm with ^{48}Ca. 'DGFRS' - data are taken from [43], 'SHIP' - data from [36], calculated values from [44].

Fig. 4: (right side) Systematics of maximum production cross-sections in 'cold' fusion reactions and reactions using actinide targets. Data for element 120 are taken from [45] (^{54}Cr + ^{248}Cm), [46] ()^{64}Ni + ^{238}U), and [47] ()^{58}Fe + ^{244}Pu.)

To illustrate the difficulties connected with such experiments let us consider an average beam intensity of 1000 pnA (6.2×10^{12} projectiles/s), which is presently typical for SHE experiments, and a production cross-section $\sigma \approx 1$ pb, which results in a production of one atom per two days. Depending on the efficiency

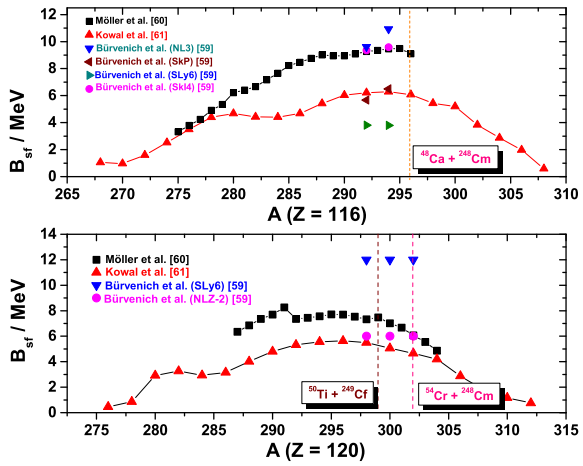

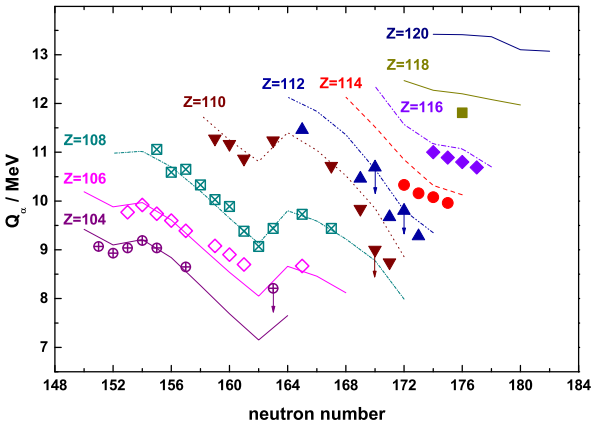

Fig. 5: (left side) Calculated fission barriers for livermorium (Z = 116) (upper figure) and element 120 (lower figure) isotopes. The underlying models are denoted in the figure.

Fig. 6: (right side) Comparison of Q_α - values obtained from MM calculations [3] and experimental values. For nucides with odd neutron number the latter are estimated from the highest α decay energy observed.

of the detection system, one decay chain per five to 10 days will be observed. One has, however, to consider that these are average values which are stongly influenced by statistical fluctuations. So in 'lucky cases' a couple of events may be observed within, e.g. ten days, but also no event may be observed within five week. Therefore, exploring regions with $\sigma << 1$ pb, negative results after several weeks of irradiation thus will not necessarily answer the question if the choice of the beam energy or the choice of the reaction (or both) were improper.

Using so-called 'cold' fusion reactions was the successful method to the discovery of elements bohrium (Z = 107) to copernicium (Z = 112) [28]; synthesis of element 113 in the reaction ^{70}Zn + ^{209}Bi was also claimed [48, 49, 50], but has not been affirmed by the IUPAC so far [51]. More successful for the production of elements with atomic numbers Z>112 have been so-called 'hot' fusion reactions of ^{48}Ca projectiles and actinide isotopes (e.g. ^{244}Pu, ^{248}Cm, ^{249}Cf) as target material. Using this method cross-sections remain quite stable in the range $\sigma \approx$ (1-10) pb at Z = (113-118), as shown in fig. 4.

Applying the 'cold' fusion reaction ^{88}Sr + ^{208}Pb one could expect $\sigma \approx 0.01$ fb for the so far unknown element 120 following the trend given by maximum formation cross-sections of elements Z = 102-113 (see fig. 3). Application of 'hot' fusion reactions thus seems more promising. However, to estimate cross-sections it is not straightforward to extrapolate the trend given from the synthesis of elements Z = 113-118. In these reactions ^{48}Ca projectiles were used. Going from synthesis of element 116 by ^{48}Ca + ^{248}Cm ($Z_p \times Z_t = 1920$) to element 118 by ^{48}Ca + ^{249}Cf ($Z_p \times Z_t = 1960$) leads to a slight increase of the Coulomb repulsion by ≈2%. As no target material heavier than californium (Z = 98) is presently available, synthesis of elements Z ≥ 119 requires heavier projectiles. For the most asymmetric possible reaction ^{50}Ti + ^{249}Cf leading to element 120 one obtains $Z_p \times Z_t = 2156$, i.e. a Coulomb repulsion 11% higher than for ^{48}Ca + ^{249}Cf, resulting in severe consequences for the fusion probability at energies around the (one dimensional) fusion barrier. A couple of theoretical studies to predict production cross-sections for elements Z = 119, 120 considering different reactions have been performed [44, 52, 53, 54, 55, 56, 57, 58]. Results often vary largely, e.g., between $\sigma \approx$ 10 - 80 fb for 3n,4n - cross-section for the reaction ^{54}Cr + ^{248}Cm leading to the compound nucleus ^{302}120 (except of [53] who predict 2-3 orders of magnitude higher values). Despite these differences calculations show a common trend of predicting the highest cross-sections for the most asymmetric reaction using ^{50}Ti as projectiles and californium isotopes of A = 249-251 as target material. Results are also strongly dependend on the underlying mass tables. Due to the relations $Q = (\Delta m_p + \Delta m_t - \Delta m_{CN})c^2$ and $E^* = E_{CM}$-Q (here $\Delta m_{CN}c^2$, $\Delta m_p c^2$, $\Delta m_t c^2$ denote the mass excesses of compound nucleus, projectile and target nuclei, E^* the excitation energy, and E_{CM} the center-of-mass energy). E^* and E_{CM} are thus connected via the Q-value. This means, depending on the used mass table a fixed excitation energy (related to the survival probability) is related to different center-of-mass energies (related to the fusion probability). Recently this issue was investigated theoretically for the reactions ^{48}Ca + ^{249}Bk → ^{297}117*, ^{50}Ti + ^{249}Cf → ^{299}120*, and ^{54}Cr + ^{248}Cm → ^{302}120* by Nasirov et al.[54]. We will come back to this feature later.

Besides fusion probability the survival probability is a crucial ingredient for the production cross-section. It is essentially determined by $(B_f - B_n)/T$ ((B_f = fission barrier, B_n = neutron binding energy, T = nuclear

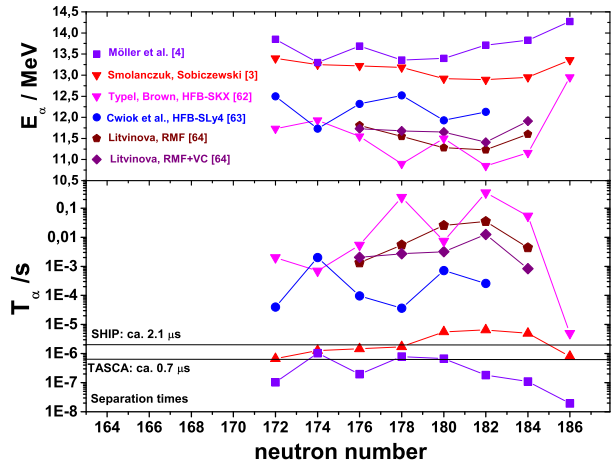

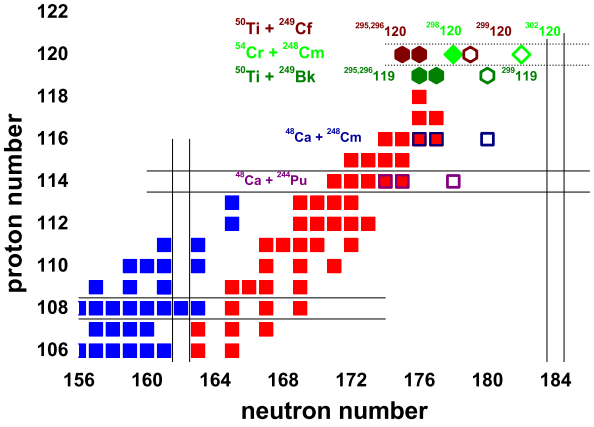

Fig. 7: (left side) Expected Q_α - values (upper part) and halflives (lower part) for element 120 isotopes at N = 172 - 186 obtained from different nuclear models.

Fig. 8: (right side) Reactions useed to synthesize elements flerovium (Z = 114), livermorium (Z = 116), Z = 119 and Z = 120 in the recent SHE campaign at GSI.

temperature). The feature concerning B_f is shown in fig. 5, where the values of B_f obtained from different models are compared. While B_f hights are quite stable within a mass range of $\Delta A \approx 10$, significant differences of up to 7 MeV are evident for the different models. An essentially wide spread of the values is obtained for the different parametrisations for the SHFB and RMF calculations [60]. Extremely high values ($B_f > 10$ MeV) are obtained using the SLy6 - parametrisation, resulting in Z = 120 as magic proton number [60]. Striking is also the large difference of values from the MM models [61, 13, 62], which is in the order of 2 MeV for Z = 116. It is finally a consequence of the larger shell correction energies at Z = 114, N = 184 obtained in [4] than in [3]. Recently Nasirov et al. [54] have theoretically investigated the influence of these differences on the production cross-sections of element 120 isotopes in reactions ^{50}Ti + ^{249}Cf and ^{54}Cr + ^{248}Cm. The higher ground-state mass excess (≈ 3.7 MeV) and lower B_f (≈ 2.2 MeV) value of the 'Warsaw group' [59, 62] of the compound nucleus ^{299}120 compared to [4, 61] lead to reduction of the cross-sections by ≈2 orders of magnitude for the 3n and 4n - deexcitation channels in the system ^{50}Ti + ^{249}Cf, which are most favorable in this reaction according to [54]. Due to the lower differences (≈ 2.8 MeV for the mass excess, ≈ 1.4 MeV for the fission barriers) between the values from the 'Warsaw group' [59, 62] and Möller et al.[4, 61] for the compound nucleus ^{302}120 the reduction factors are significantly lower, a factor of ≈30 for the 3n - channel and of ≈5 for the 4n - channel for the system ^{54}Cr + ^{248}Cm. Nevertheless production cross-sectons are thus pushed to values $\sigma < 2$ fb for both reactions, practically unreachable with presently existing experimental set-ups.

The other important feature of SHE production are the decay properties. While the even-even isotopes of copernicium (Z = 112) decay by sf with half-lives below 1 s, α decay prevails in the even-even isotopes of elements Z = 114-118, with half-lives decreasing from ≈1 s (^{288}114) to ≈2 ms (^{294}118) accompanied by an increase of the Q_α-value by ≈1.8 MeV. The overall trend is shown in fig. 6, where as an illustrative example the Q_α values for known even-Z isotopes of elements Z ≥ 104 are compared with predicted ones from [3]. The overall agreement between experimental and predicted values is quite fair; for the even-even isotopes of Z = 114, 116, 118 a mean deviation Q_α(exp)-Q_α(theo) = -0.32 MeV is found. For the two even-even isotopes of element 120 accessible in the envisaged reactions ^{249}Cf(^{50}Ti,3n)^{296}120 and ^{298}Cm(^{54}Cr,4n)^{298}120 Q_α values of 13.41 MeV and 13.37 MeV are expected, leading to half-lives of 1.5 μs and 1.7 μs according to [11, 12]. These values are already comparable with the flight times through SHIP (2.1 μs) or TASCA (0.7 μs).

E_α values and expected partial α decay halflives obtained from different models are compared in fig 7. Considerably higher (up to about 2 MeV) E_α - values are obtained from the MM models [3, 4], predicting Z = 114 as magic, compared to the SHFB SLy4 and RMF calculations predicting Z = 120 as magic [63, 64, 65]. The differences are reflected also in the expected half-lives which appear 3 - 6 orders of magnitude longer for the models preferring Z = 120 as magic. So the particular importance to produce element 120 isotopes is based on the fact, that their decay properties will be a stringent test for the existence of a spherical proton shell at Z = 120.

After successful penetration into the region Z > 112 by synthesizing element 114 isotopes at TASCA in the

reaction ^{48}Ca + ^{244}Pu [66, 67] and one year later element 116 isotopes in the reaction ^{48}Ca + ^{248}Cm at SHIP [36] an ambitious program to synthesize the new elements 119 and 120 was started at GSI.
In a preceeding first experiment, performed at SHIP, the reaction ^{64}Ni + ^{238}U $\rightarrow$ ^{302}120 was used. The irradiations were carried out in three experimental runs in the period april 2007 to october 2008. No events that could be attributed to decays starting from an element 120 isotope were observed. Beam doses of 1.2×10^{18} at $E^* = 32.3$ MeV and 21.1×10^{18} at $E^* = 35.9$-37.4 MeV were collected, which resulted in upper limits of 1.6 pb and 0.09 pb, respectively [46].
The recent campaign was performed in the years 2011/2012.
The second element 120 experiment at SHIP was the irradiation of ^{248}Cm with ^{54}Cr. It was carried out in the period april to may 2011. No events that could be attributed to decays starting from an element 120 isotope were observed. A beam dose of 7×10^{18} was collected, resulting in an upper cross-section limit of 0.56 pb [45].
At TASCA the reaction ^{50}Ti + ^{249}Cf $\rightarrow$ ^{299}120 was used. The irradiation was carried out at E_{lab} = 306 MeV in the period august to october 2011; a beam dose of 1.1×10^{19} at target was collected (preliminary value) [68]. Data are still under evaluation, but so far no events that could be attributed to decays starting from an element 120 isotope were reported.
The choice of the reactions may be under discussion. The upper cross-section limit for the ^{64}Ni + ^{238}U irradiation was typically more than an order of magnitude higher than the theoretical predictions (see references above, e.g. [44]). All these calculations, however, are based on fission barriers obtained from MM models that predict the proton shell at Z = 114. Self-consistent calculations that predict the proton shell at Z = 120 partly predict much higher fission barriers, e.g. SLy6 parametrization [60] (see fig. 5). So it was speculated that cross-sections could be enhanced significantly [46]. As this was experimentally not verified, it was concluded that values of $B_f \approx 12$ MeV are unrealistic in the range A = 298-302 [46]. It is, however, disputable to give upper limits for B_f on the basis of upper cross-section limits as done in [46]. Since evaporation residue cross-sections also sensitively depend on the fusion probability, different treatment of latter may lead to cross-section predictions differing by some orders of magnitude even when the same fission barriers are used [44, 53].
Production cross-sections for the reaction ^{50}Ti + ^{249}Cf are typically by a factor of roughly two higher than those for ^{54}Cr + ^{248}Cm. With respect to the uncertainties of mass and fission barrier predictions and treatment of the fusion probability in the vicinity of the fusion barrier this difference cannot be regarded as striking. Furthermore, the ^{248}Cm based reaction leads to a compound nucleus with N = 182 compared to N = 179 as reached with ^{50}Ti + ^{249}Cf resulting in the production of different evaporation residues. As exploration of decay properties in a mass range as wide as possible is required for each element to get detailed information about structure and stability of SHE investigation of both reactions is meaningful. It is, however, necessary to perform irradiations long enough to reach the region of predicted cross-sections (e.g. 20-50 fb predicted in [44]). Such times (>100 days) have not available so far.
To synthesize element 119 at TASCA the reaction ^{50}Ti + ^{249}Bk $\rightarrow$ ^{299}119 was applied. The irradiation was carried out at E_{lab} = 306 MeV in two experimental runs in the period april to september 2012; a beam dose of 4.2×10^{19} at target was collected (preliminary value) [68]. Data are still under evaluation, but so far no events that could be attributed to decays starting from an element 119 isotope were reported.

Nuclear Structure Investigations

Identification of new isotopes can be performed on the basis of few observed events. If at least one daughter product within the decay chain of an isotope is sufficiently known, often only one decay chain is already sufficient for a safe identification. Some gross properties as main decay modes, half-lives, Q_α - values can be estimated, with limited precision, even on the basis of some events. To get a deeper insight into the properties of a nucleus, however, detailed studies requiring the observation of at least more than one hundred events are necessary. Technical developments making high beam currents, efficient and fast separation devices and highly sensitive detector systems available enabled obout one and a half decades ago the access to detailed nuclear structure investigations in the region of transfermium elements by means of in-beam spectroscopy as well as by decay studies in the focal plane of the separator (see e.g. [69, 70]). The investigations at SHIP - GSI concentrated on neutron deficient isotopes in the vicinity of the deformed neutron shell at N = 152, which could be produced in 'cold' fusion reactions.
According to the nuclear shell model the orbitals $2g_{9/2}$, $1i_{11/2}$, $1j_{15/2}$, $3d_{5/2}$ $2g_{7/2}$, $4s_{1/2}$, and $3d_{3/2}$, are expected in the region between the established neutron shell at N = 126 and the predicted one at N = 184 [71]. A relatively large energy gap of ≈1.5 MeV should be present between the $1j_{15/2}$ and $3d_{5/2}$ orbitals. At deformation these orbitals split into the Nilsson levels. Some of them increase in energy at deformation,

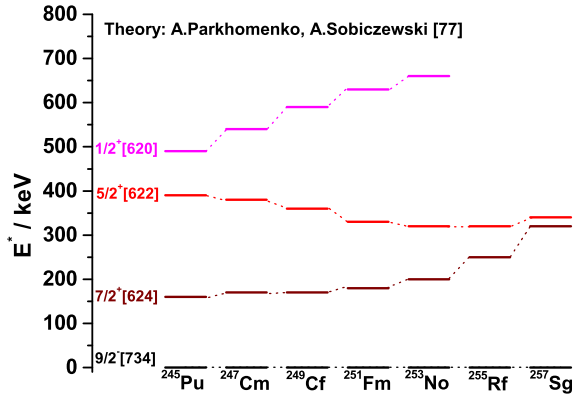

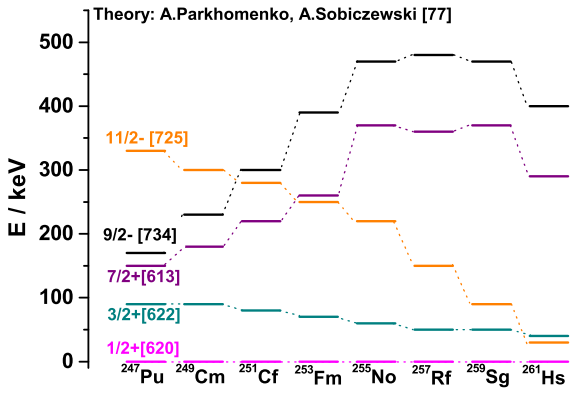

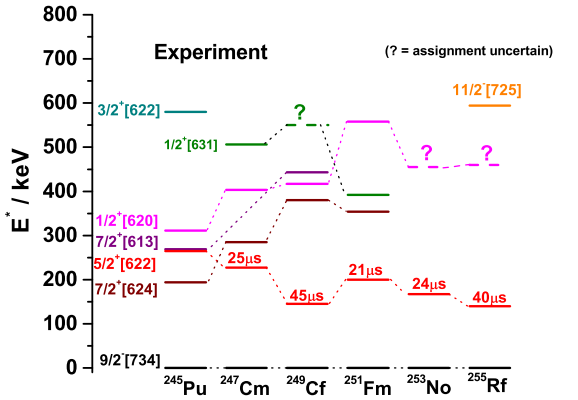

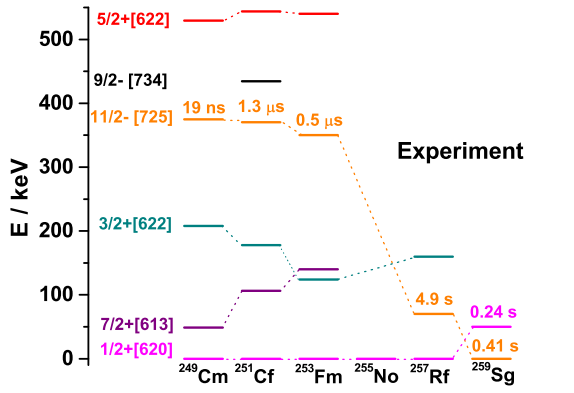

Fig. 9: (left side) Comparison of calculated [78] (upper figure) and experimental partial level schemes of N = 151 isotones

Fig. 10: (right side) Comparison of calculated [78] (upper figure) and experimental partial level schemes of N = 153 isotones

while others decrease, leading to shell gaps at N = 152 and N = 162 at large quadrupole deformations of $\beta_2 \approx 0.25$. Some of these Nilsson levels are located close to the Fermi surface at N ≈ 152. This region is presently accessible for detailed nuclear structure investigations up to Z = 106 (see e.g. [70]). Therefore those studies will have feedback to the energies and ordering of the neutron orbitals and thus on the strength and probably also on the location of the next spherical neutron shell. Vice versa, this is also valid for the protons. Recent experiments performed at SHIP concentrated on investigation of low lying levels in the N = 153 isotones ^{253}Fm [72], ^{255}No [73], ^{257}Rf [74, 75], and ^{259}Sg [76, 77] and their α - decay daughter products. The experimental results are shown and compared with theoretical predictions in figs. 9 and 10. Ground-states are assigned as $9/2^-[734]$ for the N=151 isotones and as $1/2^+[620]$ up to Z=104 for the N=153 isotones, in-line with the calculations [78]. These two levels are also predicted to be responsible for the shell gap at N = 152 in the deformation range around $\beta_2 \approx 0.27$ [71]. Indeed, experimental quadrupole deformation values are $\beta_2 = 0.28 \pm 0.02$ for ^{250}Fm, ^{252}No (N=,150) or $\beta_2 = 0.29 \pm 0.02$ for ^{254}No (N = 152) [70], while calculated values vary within $\beta_2 = 0.246$ - 0.32 for ^{254}No depending on the underlying nuclear model (see [70]).

Theory predicts $7/2^+[624]$ (arising from $2g_{9/2}$), $5/2^+[622]$ (arising from $1i_{11/2}$) and $1/2^+[620]$ (arising from $2g_{7/2}$) as the lowest lying excited levels in the N = 151 isotones. Indeed, these levels are also assigned at $E^*<500$ keV, but the ordering of the $7/2^+[624]$ and $5/2^+[622]$ levels is reversed. As a consequence the latter forms an isomeric state with some tens of microseconds half-life, decaying to the ground-state by M2 - transitions with E3 - admixtures (see e.g. [73, 72]). Recently such an isomer has also been identified in ^{255}Rf by measuring conversion electrons in delayed coincidence with α - decays of ^{259}Sg [77].

Most striking in the N=153 isotones is the predicted steep decrease of the $11/2^-[725]$ level with increasing proton number which is qualitatively in-line with the experimental results. In the lighter isotones ^{249}Cm, ^{251}Cf, and ^{253}Fm it forms a short-lived ($T_{1/2} < 2$ μs) isomer located some hundred keV above the ground-state and decaying by internal transitions [79, 72], while in ^{257}Rf it was identified as a low-lying isomer

with a half-life comparable to that of the ground-state decaying by α emission [74, 75]. In the next heavier N = 153 isotone, ^{259}Sg, it has been assigned as the ground-state [77]. The $11/2^-[725]$ level originates from the $1j_{15/2}$ orbital and is expected to increase with increasing quadrupole deformation, while the $1/2^+[620]$ level is expected to decrease with increasing deformation [71]. A change in the ground-state configuration thus could hint to decrease of the quadrupole deformation already from Z = 100 to Z = 106 for the N = 153 isotones, while MM calculations predict such a decrease starting from Z = 106 to Z = 108 [4]. Such an interpretation, however, is not straightforward as the considered nuclei also have significant hexadecapole (β_4) and hexacontatetrapole (β_6) deformation components [4, 80] and also a dependence of the energy difference between the $11/2^-[725]$ and $1/2^+[620]$ levels from β_4 and β_6 values has been discussed in [71].

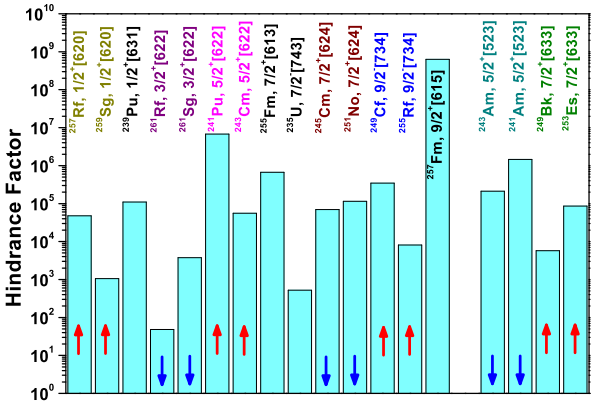

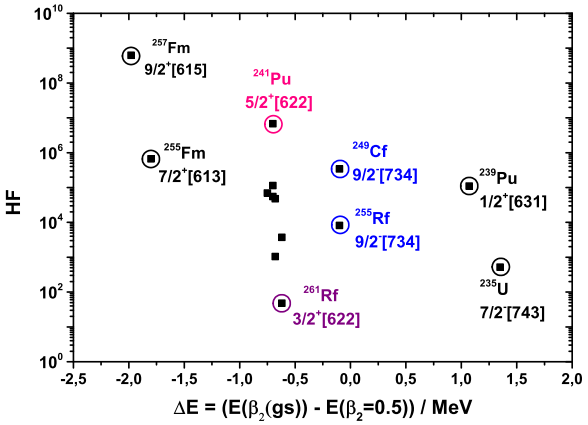

Fig. 11: (left side) Hindrance factors for spontaneous fission for nuclei where the configuration of the fissioning level is established and the fission halflives of the neighbouring even-even nuclei are experimentally known. Levels with parallel projection of spin and angular momentum are marked by arrows 'up', those with antiparallel projection by arrows 'down'.

Fig. 12: (right side) Plot of hindrance factors for spontaneous fission of even-Z odd-N nuclei in dependence of the energy difference of the fissioning Nilsson level at ground-state (β_2(gs)) and at ($\beta_2 = 0.5$). The single particle energies were taken from [71], the β_2(gs) are interpolated values from [80]. For better presentation only for a few cases isotope and Nilsson level assignments are given.

Spontaneous fission and nuclear structure

According to the nuclear drop model fission barriers are expected to vanish around Z = 106 (somewhat depending on the parametrization). Heavier nuclei thus exist only because of fission barriers created by the shell effects. Therefore spontaneous fission properties are a sensitive probe for shell stabilization of superheavy nuclei. For fission properties, among others as e.g. the effective inertia, not only the size of the shell effects play a role, but also their dependence from nuclear deformation or, in other words, their development along the fission path. For nuclei with odd proton and /or odd neutron numbers the change of the energy of the fissioning state along the fission path plays a dececive role, as due to spin and parity conservation at crossing points of Nilsson levels the unpaired nucleon cannot change the level as it is the case for nucleon pairs in even-even nuclei. This leads to an effective increase of the fission barrier, in literature denoted as specalization energy [81]. Quantitatively this influence can be expressed by a hindrance factor HF, defined as HF = T_{sf}(Z,N)/T_{ee}(Z,N) (eq. 1), where T_{sf} is the experimental fission half-life and T_{ee} the unhindered half-life defined as the geometric mean of the neighbouring even-even nuclei [82], e.g. for odd neutron number T_{ee}(Z,N) = (T_{sf}(N-1,Z) x T_{sf}(N+1,Z))$^{1/2}$ (eq. 2).
In fig. 11 the hindrance factors are shown for the cases where spin and parity of the fissioning Nilsson levels ($\Omega^\pi[Nn_z\Lambda]$) are experimentally established and where fission halflives of the neighbouring even-even nuclei are experimentally known. Evidently the hindrance factors vary in a range of about nine orders of magnitude, even strong differences for nuclei with the same fission configuration are evident. Also no direct relation between the spin and the hindrance factor is evident. Interesting, however, is that for the even-Z nuclei for levels with 'spin-up' projections hindrance factors are higher for the lighter nucleus, while for those with spin-down projections the hindrance factors for the heavier nuclei are larger. As only few cases are known, however, it presently seems not justified to claim already a 'systematics'.
A direct connection between the change of the single particle energies at deformation and the hindrance factor

is also not evident in general, but, as seen in fig. 12, some trend is visible. Here the differences between the single-particle energies at ground-state deformation and at certain elongation (somewhat arbitrarily $\beta_2 = 0.5$ was taken as reference) are plotted versus the hindrance factors. Negative energy differences denote levels upsloping in energy with deformation, positive values those levels downsloping in energy. Although straggling of the data is large a general decrease of the hindrance factors with increasing energy difference is indicated. In other word, strongly upsloping levels tend to lead to higher hindrance factors than less strongly upsloping or even downsloping levels. Seemingly, however, the situation is more complicated and there are some other factors influencing the fission hindrance. It should be noted, that the unusual high value for ^{257}Fm was explained already in [81] by a strong increase of the fission barrier due to the strong upsloping in energy of the $9/2^+[615]$ level, but in [82] the very low half-life of the neighbouring ^{258}Fm (0.3 ms), which indeed means a decrease of T_{sf} by more than seven order of magnitude from ^{256}Fm to ^{258}Fm, was considered as a possible reason, as in this specific case relation (eq. 2) either may not be not a good measure for $T_{ee}(^{257}\mathrm{Fm})$ or that the decrease of the outer fission barrier, which should be responsible for the short fission half-life of ^{258}Fm, may not yet be effective for ^{257}Fm.

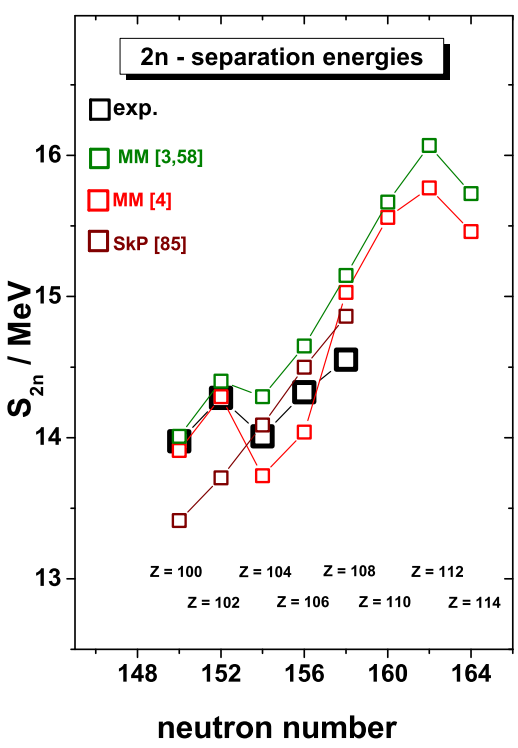

Fig. 13: (left side) Two - neutron separation energies along the N-Z = 50 isotope line.

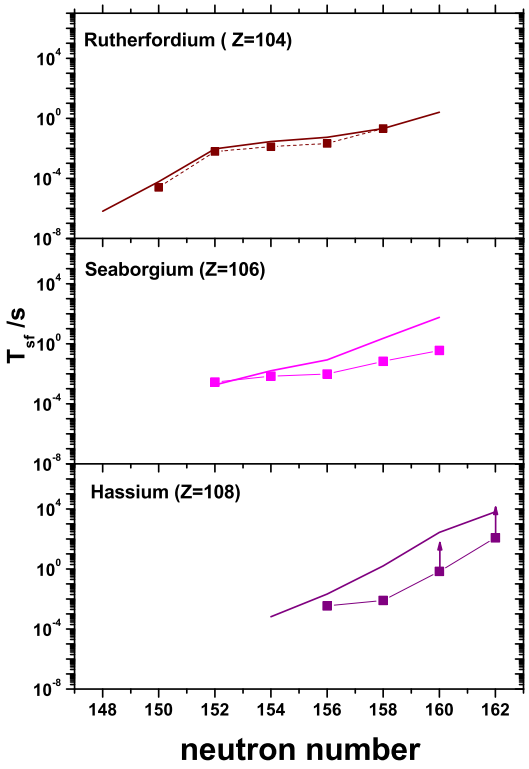

Fig. 14: (right side) Comparison of experimental and calculated fission halflives for even-even isotopes of rutherfordium, seaborgium and hassium. Experimental values are denoted by squares, theoretical values from [13] are given by thick lines. The thin lines are to guide the eye.

Investigation of shell strength

An important feature regarding nuclear stabilization by the shell structure is the shell strength; measures for it are usually the 2n- (or 2p) separation energies (S2n(N,Z)) or the shell gap parameter δ(N,Z) defined as the difference of the 2n separation energies (δ2n(N,Z) = S2n(N,Z) - S2n(N+2,Z)). The masses of nobelium and lawrencium isotopes measured directly with SHIPTRAP have been recently used to determine the strength of the N = 152 shell [41]; similary, the directly measured masses for ^{252}No and ^{252}No can be used to determine the ground-state masses of the α-decay precursers. For ^{252}No this chain has been known up to ^{264}Hs already for a quite long time [83], for ^{254}No, the recently discovered α-decay branches of ^{262}Sg [84] and ^{258}Rf [85] allow for a mass determination up to ^{270}Ds and hence for an experimental estimation of the 2n- separation energies for the even-even N-Z = 50 nuclei up to ^{266}Hs. The results are shown and compared

with the mass predictions of MM-model results of [3, 4] and with SkP - calculations [86] in fig. 13. The known shell gap at N = 152 is visible by a local maximum in the MM calculations, but is not indicated in the SkP calculations, which show a continuous increase with increasing neutron number in the considered range of nuclei. Beyond N = 154 the 2n- separation energies are increasing again due to the influence of the expected neutron shell at N = 162; obviously, the increase of the experimental values is smaller than predicted in the MM calculations. This might be accidental, maybe a 'local' effect, but it could be a hint that the N = 162 shell is weaker than predicted. Some indication for this assumption can be found also in the fission half-lives as shown in fig. 14; the agreement between the predicted values [13] and experimental values for ^{254,256,258,260}Rf and ^{258,260}Sg is better than a factor of three, while for ^{262}Sg the predicted value is already a factor of about six higher than the experimental one [13, 84]. In a recent experiment at SHIP a fission branch of $b_{sf} = 0.24 \pm 0.09$ has been established for ^{266}Hs [84] resulting in a partial fission half-life of $T_{sf} \approx 9$ ms, which is almost a factor of 200 lower than the predicted value $T_{sf} = 1.6$ s [13].

CONCLUSIONS

Superheavy elements represent a specific species of exotic nuclei. As liquid fission barriers have vanished, they owe their existence, stability and decay properties solely due to their shell structure, which is extremely sensitive to details of the nuclear force. Thus they represent a unique laboratory to study fundamental interactions.

Presently available facilities and experimental techniques allowed for the synthesis of elements up to Z = 118. 'Detailed' decay studies including measurement of γ rays were possible up to Z = 115 so far. Experiments aimed to the synthesis of heavier elements, also performed at GSI, did not show positive results on the basis of present status of data evaluation.

Experiments performed in recent years revealed a vast of new data allowing for a much deeper insight in ground-state and decay properties of SHE as well as in their nuclear structure. This certainly will serve also a basis for the development of advanced nuclear models. Still, the research work is rather at the beginning but is already fascinating enough to justify the demand for new facilities and set-ups allowing to increase sensitivity significantly, which is required to successfully synthesize new elements, to perform nuclear structure investigations of high quality in the region of the expected spherical proton and neutron shells and to investigate the properties of the nuclei there in detail. This will lead to new insights in understanding the existence and stability of our world.

REFERENCES

[1] M. Göppert-Mayer, Phys. Rev. **74**, 235 (1948).
[2] O. Haxel et al., Phys. Rev. **75**, 1769 (1949).
[3] R. Smolanczuk, A. Sobiczewski, Proc. EPS Conf. 'Low Energy Nuclear Dynamics', St. Petersburg 1995, eds. Yu.Ts. Oganessian et al., World Scientific, Singapore, New Jersey, London, Hong Kong 1995, 313 (1995).
[4] P. Möller et al., At. Data and Nucl. Data Tab. **59**, 185 (1995).
[5] C.F. von Weizsäcker, Z. Phys. **96** 461 (1935).
[6] V.M. Strutinsky, Nucl. Phys. A **95** 442 (1967).
[7] N. Bohr, J.A. Wheeler, Phys. Rev. **56** 426 (1939).
[8] A. Sobiczewski et al., Phys. Lett. **22**, 500 (1966).
[9] H. Meldner, Arkiv för fysik **36**, 593 (1967).
[10] S.G. Nilsson et al., Nucl. Phys. A **115**, 545 (1969).
[11] D.N. Poenaru et al., J. Physique Lett. **41**, 589 (1980).
[12] E. Rurarz, Acta Physica Polonica **14**, 917 (1983)
[13] R. Smolanczuk et al., Phys. Rev. **52**, 1871 (1995).
[14] R. Smolanczuk, Phys. Rev. C **56**, 812 (1997).
[15] A.V. Karpov et al., Int. Journ. of Modern Physics E **21**, 1250013 (2012).
[16] K. Rutz et al., Proc. of the Second Int, Conf. 'Fission and Properties of Neutron-Rich Nuclei', St. Andrews 1999,ed. J.H.Hamilton et al., (World Scientific, Singapore, New Jersey, London, Hong Kong, 2000), 449 (2000).
[17] M. Bender et al., Rev. of Mod. Physics **75**, 121 (2003).
[18] M. Bender et al., Phys. Rev. C **60**, 034304 (1999).
[19] W. Nazarewicz, Talk given at FUSHE12 (http.//www.ensarfp7.eu/projects/ecos/workshop-meetings/fushe2012/summaries-and-talks-1/fushe2012-nazariwicz).
[20] E. Chabanat et al., Nucl. Phys. A **627**, 710 (1997).
[21] E. Chabanat et al., Nucl. Phys. A **635**, 231 (1998).

[22] A. Chatillon et al., Eur. Phys. J. A **30**, 397 (2007).
[23] M. Hempel, Physik in unserer Zeit, **45**, 12 (2006).
[24] G. Münzenberg et al., Nucl. Instr. Meth. **161**, 65 (1979).
[25] M. Schädel et al., Eur. Phys. J. D **45**, 67 (2007).
[26] A. Semchenkov et al., Nucl. Instr. and Meth. in Phys. Res. B **266**, 4153 (2008).
[27] M. Block et al., Eur. Phys. J. D **45**, 39 (2007).
[28] S. Hofmann, G. Münzenberg, Rev. Mod. Phys. **72**, 773 (2000).
[29] F.P. Heßberger et al., Eur. Phys. J. A **26**, 233 (2005).
[30] F.P. Heßberger et al., Eur. Phys. J. A **30**, 561 (2006).
[31] F.P. Heßberger et al., Eur. Phys. J. D **45**, 33 (2007)
[32] S. Hofmann et al., Eur. Phys. J. A **10**, 5 (2001).
[33] B. Sulignano et al., Eur. Phys. J. A **33**, 327 (2007).
[34] F.P. Heßberger et al., Phys. of. At. Nuclei **70**, 1445 (2007).
[35] D. Rudolph et al., Phys. Rev. Lett. **111**, 112502 (2013).
[36] S. Hofmann et al., Eur. Phys. J. A **48:**62 (2012).
[37] J. Khuyagbaatar et al., Phys. Rev. Lett. **112**, 172501 (2014).
[38] Ch. E. Düllmann et al., Nature **418**, 859 (2002).
[39] M. Block et al., Nature **463**, 785 (2010).
[40] M. Dworschak et al., Phys. Rev. C**81**, 064312 (2010).
[41] E. Minaya Ramirez et al., Science **337**, 1207 (2012).
[42] J. Dvorak et al., Phys. Rev. Lett. **97**, 242501 (2006).
[43] Yu. Ts. Oganessian, J. Phys. G: Nucl. Part. Phys. **34**, R165 (2007).
[44] V. Zagrebaev, W. Greiner, Phys. Rev. C**78**, 034610 (2008).
[45] S. Hofmann et al., GSI Scientific Report 2011, **PHN-NUSTAR-SHE-01** 205 (2012).
[46] S. Hofmann et al., GSI Scientific Report 2008, **NUSTAR-SHE-01**, 131 (2009).
[47] Yu. Ts. Oganessian, Phys. Rev. C**79**, 024603 (2009).
[48] K. Morita et al., Journ. Phys. Soc. of Japan **75**, 2593 (2004).
[49] K. Morita et al., Journ. Phys. Soc. of Japan **76**, 045001 (2007).
[50] K. Morita et al., Journ. Phys. Soc. of Japan **81**, 103201 (2013).
[51] R.C. Barber et al., Pure Appl. Chem. **83**, 1485 (2011).
[52] G.G. Adamian et al., Eur. Phys. J. A **41**, 235 (2009).
[53] A.K. Nasirov et al., Phys. Rev. C **79**, 024606 (2009).
[54] A.K. Nasirov et al., Phys. Rev. C **84**, 044612 (2011).
[55] Z.H. Liu, Jing-Dong Bao, Phys. Rev. C **80**, 054608 (2009).
[56] K. Siwek-Wylczinska et al., Int. J. Mod. Phys. E **19**, 500 (2010).
[57] Yu-Jie Liang et al., Eur. Phys. J. A **48:**133 (2012).
[58] Nan Wang et al., Phys. Rev. C **85** 041601(R) (2012).
[59] I. Muntian et al., Phys. At. Nucl. **66**, 1015 (2003).
[60] T. Bürvenich et al., Phys. Rev. C **69**, 014307 (2004).
[61] P. Möller et al., Phys. Rev. C **79**, 064304 (2009).
[62] M. Kowal et al., Phys. Rev. C **82**, 014303 (2010).
[63] S. Typel, B.A. Brown, Phys. Rev. C **67**, 034313 (2001).
[64] S. Cwiok et al., Nature **433**, 705 (2005).
[65] E. Litvinova, Phys. Rev. C **85**, 021303(R) (2012).
[66] C.E. Düllmann et al., Phys. Rev. Lett. **104**, 252701 (2010).
[67] J. Gates et al., Phys. Rev. C **83**, 054618 (2011).
[68] J. Khuyagbaatar et al., GSI Scientific Report 2012 **PHN-ENNA-EXP-01**, 131 (2013).
[69] M. Leino, F.P. Heßberger, Annu. Rev. Nucl. Part. Sci. **54**, 175 (2004) .
[70] R.-D. Herzberg, P.T. Greenlees, Progr. in Part. and Nucl. Phys. **61**, 674 (2008) .
[71] R.R. Chasman et al., Rev. Mod. Phys. **49**, 833 (1977).
[72] S. Antalic et al., Eur. Phys. J. A **42:**62 (2011).
[73] F.P. Heßberger et al., Eur. Phys. J. A **29** 165 (2006).
[74] F.P. Heßberger et al., Z. Phys. A **359** 415 (1997).
[75] B. Streicher et al., Eur. Phys. J. A **45** 275 (2010).
[76] F.P. Heßberger et al., GSI Scientific Report 2012 **PHN-NUSTAR-SHE05**, 209 (2012).
[77] S. Antalic et al., submitted to Eur. Phys. J. A (2013).
[78] A. Parkhomenko, A. Sobiczewski, Acta Phys. Polonica B **36**, 3115 (2005).
[79] R.B. Firestone et al., Table of Isotopes (1996).
[80] A. Sobiczewski et al., Phys. Rev. C **67**, 034306 (2001).

[81] J. Randrup et al., Nucl. Phys. A **217**, 221 (1973).
[82] D.C. Hoffman et al., Nucl. Phys. A **502**, 21c (1989).
[83] F.P. Heßberger et al., Proc. Tours Symposium on Nuclear Physics III, Tours, France, September 1997, eds. M. Arnould, M. Lewitowicz, Yu. Ts. Oganessian, M. Ohta, H. Utsunomiya, T. Wada, AIP Conference Proceedings 425, Woodbury, New York, 3 (1998).
[84] D. Ackermann, Progr. of Theo. Phys. Suppl. **196**, 255 (1998).
[85] J. Gates et al. Phys. Rev. C **77**, 034603 (2008).
[86] J. Dobaczewski et al., arXiv:nucl-th/0404077v1 (2004)

HIGH-RESOLUTION DECONVOLUTION ALGORITHMS FOR ANALYSIS OF SPECTROSCOPIC DATA

Vladislav Matoušek[1,*] **and Miroslav Morháč**

[1]Institute of Physics, Slovak Academy of Sciences, Dubravska cesta 9, 845 11 Bratislava, Slovakia

Abstract

In this paper we present a set of deconvolution algorithms and study their decomposition capabilities from the resolution point of view. We illustrate their suitability for processing of spectrometric data. We have proposed an improvement in the efficiency by introducing a boosting operation into the deconvolution process. The study of the algorithms is accompanied by a set of examples illustrating their properties.

INTRODUCTION

Deconvolution methods are widely used techniques to improve the resolution in experimental spectroscopic data by mathematically removing the smearing effects of an imperfect instrument, using its resolution function. They can be successfully applied for the determination of positions and intensities of peaks and for the decomposition of multiplets in γ-ray spectroscopy.

From numerical point of view, the deconvolution is so called ill-posed problem, which means that many different functions solve a convolution equation within error bounds of experimental data. The estimates of the solution are sensitive to errors in the input data [1]. When employing standard algorithms to solve a convolution system, small errors or noise can cause enormous oscillations in the result. This implies that the regularization must be employed. Tikhonov first treated this problem on a strict mathematical basis by introducing the regularization theory and methods [2]. The regularization encompasses a class of solution techniques that modifies an ill-posed problem into a well-posed one, by approximation, so that a physically acceptable approximate solution can be obtained and the solution is sufficiently stable from the computational viewpoint [3]. Our endeavor in the deconvolution operation is to remove the influence of the response function, i.e., to deblur the data and in the ideal case to obtain a spectrum consisting of δ - functions like "peaks".

BRIEF OVERVIEW OF DECONVOLUTION METHODS

Stationary discrete system that satisfies the superposition principle can be described by convolution sum

$$y(i) = \sum_{k=0}^{i} x(k)\, h(i-k) + n(i) = x(i) * h(i) + n(i), \quad i = 0, 1, ..., N-1 \tag{1}$$

where $x(i)$ is the input into the system, $h(i)$ is its impulse function (response), $y(i)$ is the output from the system, $n(i)$ is additive noise and the mark * denotes the operation of the convolution. This system can be in matrix form written

$$y = Hx + n \tag{2}$$

where the matrix H has dimension $N \times M$, the vectors y, n have length N and the vector x has length M, while $N \geqslant M$ (overdetermined system).

Least Square Solution. To find least square solution of above given system of linear equations the functional

$$\parallel H\widehat{x} - y \parallel^2$$

should be minimized. Direct unconstrained least squares estimate of the vector x is

$$\hat{x} = (H^T H)^{-1} H^T y \tag{3}$$

*E-mail: Vladislav.Matousek@savba.sk

where $A = H^T H$ is the Toeplitz matrix. When employing this algorithm to solve a convolution system small errors or noise can cause enormous oscillations in the result. The problem of finding x, where H, y are known, is a discrete ill-posed problem [4], and requires regularization techniques to get adequate solution.

Several methods to regularize the solution of Eq. 2 were developed. Most methods used in inverse problems adopt both an extreme criterion to unfold data (for instance, those of least squares or the maximum entropy) and a regularization method to reduce the very large fluctuations of the unfolded spectrum. Three types of regularization methods are very often used:

- smoothing,
- constraints imposition (for example only non-negative data are accepted),
- choice of a prior information probability function - Bayesian statistical approach.

Tikhonov-Miller Regularization. To find a regularized approximate solution of Eq. 2, the functional

$$\| H\widehat{x} - y \|^2 + \alpha \| Q\widehat{x} \|^2 \tag{4}$$

must be minimized, Q and α are the regularization matrix and parameter, respectively. This solution can be obtained by solving the equation

$$\widehat{x} = \left(H^T H + \alpha Q^T Q\right)^{-1} H^T y \tag{5}$$

The solution of Eq. 5 for $\alpha = 0$ is often called the principal solution. It is a limiting case of what is called zero-th order or Tikhonov regularization for $Q = E$, unit matrix. Then we get

$$\widehat{x} = \left(H^T H + \alpha\right)^{-1} H^T y \tag{6}$$

Together with χ^2 also the sum of squares of elements of the estimated vector $\widehat{x}$ is minimized. There exist also some recommendations how to choose α, $(0 < \alpha < \infty)$. In [5] it is suggested to try

$$\alpha = Trace(H^T H)/Trace(Q^T Q).$$

Van Cittert Algorithm. The Van Cittert based algorithms [6] of deconvolution are widely applied in different areas, for example in spectroscopy, in image processing and others. The basic form of Van Cittert algorithm for discrete convolution system is

$$x^{(n+1)} = x^{(n)} + \mu\left(H^T H H^T y - H^T H H^T H x^{(n)}\right) = x^{(n)} + \mu\left(y' - A x^{(n)}\right) \tag{7}$$

where A is system Toeplitz matrix, n represents the number iterations and μ is the relaxation factor. The convergence condition of Eq. 7 is that the diagonal elements of the matrix A satisfy

$$A_{ii} > \sum_{j=0, j\neq i}^{N-1} A_{ij}, \quad i = 0, 1, ..., N-1$$

The relation between relaxation factor μ and Riley algorithm of deconvolution is apparent. The coefficient μ should satisfy the condition

$$0 < \mu < 2/\lambda_{\max}$$

where $\lambda_{\max}$ is the greatest eigenvalue of A.

Gold Algorithm. Further, if we choose the local variable relaxation factor

$$\mu_i = \frac{x^{(n)}(i)}{\sum_{m=0}^{M-1} A_{im} x^{(n)}(m)} \tag{8}$$

and we substitute it into Eq. 7 we get

$$x^{(n+1)}(i) = \frac{y'(i)}{\sum_{m=0}^{M-1} A_{im} x^{(n)}(m)} x^{(n)}(i) \tag{9}$$

This is the Gold deconvolution algorithm [7]. Its solution is always positive when the input data are positive, which makes the algorithm suitable for the use for naturally positive definite data, i.e., spectroscopic data. In the rest of the paper let us call it classic Gold deconvolution.

In practice, we have revealed that the second multiplication by the matrix $H^T H$ in Eq. 7, for Gold deconvolution, is redundant. On the contrary, its omitting gives result with better resolution. Then in Eq. 7 we set

$$A = H^T H, \quad y' = H^T y.$$

If we take the initial solution

$$\mathbf{x}^{(0)} = [1, 1, ..., 1]^T$$

and if all elements in the vectors **h**, **y** are positive (this requirement is fulfilled for spectroscopic data), this estimate is always positive [8]. It converges to the least square estimate in the constrained subspace of positive solutions.

Richardson-Lucy Algorithm. Richardson-Lucy like algorithms [9] use a statistical model for data formation and are based on the Bayes formula. The Bayesian approach consists of constructing the conditional probability density relationship

$$p(x|y) = \frac{p(y|x)p(x)}{p(y)}$$

where $p(y)$ is the probability of the output data and $p(x)$ is the probability of the input data, over all possible data realizations. The Bayes solution is found by maximizing the right part of the equation. The maximum likelihood (ML) solution maximizes only the density $p(y|x)$ over x. For discrete data the algorithm has the form

$$x^{(n+1)}(i) = x^{(n)}(i) \sum_{j=0}^{N-1} h(j,i) \frac{y(j)}{\sum\limits_{k=0}^{M-1} h(j,k)\, x^{(n)}(k)}, \quad i \in \langle 0, M-1 \rangle \tag{10}$$

This iterative method forces the deconvoluted spectra to be non-negative. The Richardson-Lucy iteration converges to the maximum likelihood solution for Poisson statistics in the data. It is also sometimes called the expectation maximization (EM) method.

Maximum A Posteriori Deconvolution Algorithm. The maximum a posteriori (MAP) solution maximizes x over the product $p(y|x)p(x)$. For discrete data the algorithm has the form

$$x^{(n+1)}(i) = x^{(n)}(i) \exp\left\{ \sum_{j=0}^{N-1} h(j,i) \left[\frac{y(j)}{\sum\limits_{k=0}^{M-1} h(j,k)\, x^{(n)}(k)} - 1 \right] \right\} \tag{11}$$

Positivity of the solution is assured by the exponential function. Moreover the non-linearity in Eq. 11 permits superresolution.

Blind Deconvolution. Up to this moment we assumed that we know the response function of the system $h(t)$. However sometimes we only suppose its shape or, respectively, we know theoretically its analytical form, which can substantially differ from the reality. In Eq. 1 one can observe that the operation of the convolution is commutative, which gives possibility of implementation of iterative algorithm of blind deconvolution scheme [11]:

1. Estimate an initial response function $h^{(0)}(i)$ from $y(i)$. This can be accomplished in different ways. For example, we choose the narrowest line lobe of $y(i)$. By Gaussian fitting of the selected part, we can get an initial estimate of the response function.

2. Accomplish the deconvolution using the estimated response function $h^{(0)}(i)$and given $y(i)$

   $$x^{(n)}(i) = y(i) * *h^{(n)}(i)$$

   where $**$ denotes the operation of deconvolution

3. Accomplish the deconvolution using the estimated spectral function for finding an improved estimation of the response function

   $$h^{(n+1)}(i) = y(i) * *x^{(n)}(i)$$

4. Repeat steps 2, 3 for improving the estimation of $x(i)$, $h(i)$.

In the steps 2, 3 one can use any of the above-presented deconvolution algorithms.

When using classic Gold algorithm in blind deconvolution scheme (Fig. 1) the resolution is practically the same like in the above mentioned forward classic Gold deconvolution. In Fig. 1(b) apparently the deconvolution deforms the shape of the response function. For the purposes of the deconvolution of spectroscopic data we can determine the response function with good fidelity.

From the point of view of application of the above mentioned deconvolution algorithms for processing of nuclear spectra the best results were achieved by Gold, Richardson-Lucy and MAP algorithms. Nevertheless, none of the algorithms is able to decompose the testing data to delta functions.

There exists immense number of variations of deconvolution algorithms applied in various scientific fields, e.g. astronomy, image processing, geophysics, optics etc. In this section we have introduced only basic classes of deconvolution algorithms that can be easily employed and implemented for the processing of spectrometric data.

BOOSTED DECONVOLUTION

Iterative positive definite deconvolutions (Gold, Richardson-Lucy and MAP.) converge to stable states. It is useless to increase the number of iterations, the result obtained practically does not change. To see and judge the course of the deconvolution procedure (Gold algorithm) we recorded the sum of weighted squares of errors per channel (denoted by letter Q) after each iteration step in the form of graph (Fig. 2).

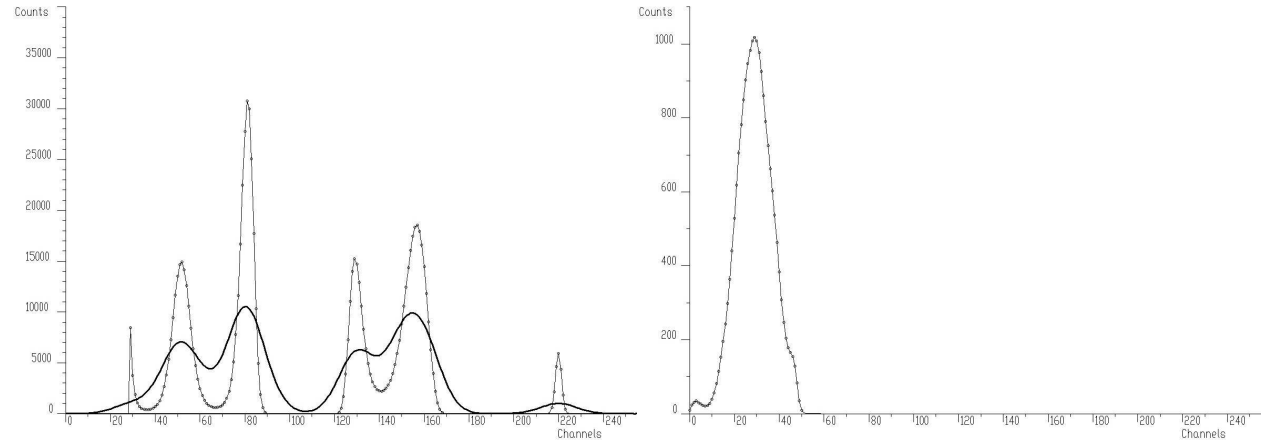

Fig. 1: Original spectrum (thick line) and deconvolved spectrum using blind Gold algorithm (thin line) after 1 000 iterations and 50 repetitions (a), deconvolved response function (b).

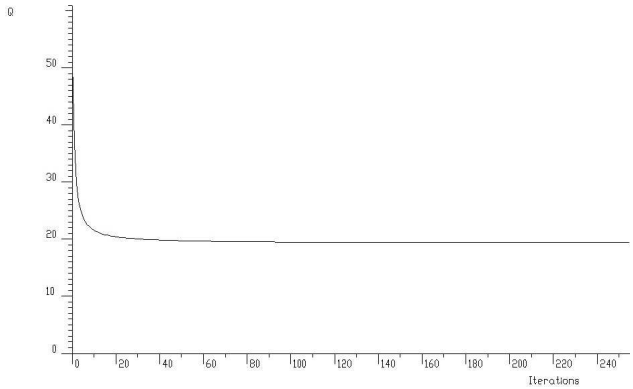

Fig. 2: Sum of weighted squares of errors per one channel in dependence on number of iterations.

Obviously, after initial decrease of Q at the beginning of the deconvolution operation during the following iteration steps it remains constant. Therefore, it is useless to continue in the iterations as it does not lead to sufficient improvement of the resolution. Instead of it we can stop iterations, apply a boosting operation and repeat this procedure. Boosting operation should decrease sigma of peaks. In other words when the

solution reaches its stable state it is necessary to change the particular solution $\mathbf{x}^{(L)}$ in a way and repeat again the deconvolution. To change the relations among elements of the particular solution we need to apply non-linear boosting function to it. The power function proved to work satisfactorily. Then, the algorithm of boosted Gold, Richardson-Lucy or MAP deconvolution is as follows:

1. Set the initial solution $\mathbf{x}^{(0)} = [1, 1, ..., 1]^T$.
2. Set required number of repetitions R and iterations L.
3. Set the number of repetitions $r = 1$.
4. According to either Eq. 9 (Gold), or Eq. 10 (Richardson-Lucy) or Eq. 11 (MAP) for $n = 0, 1, ..., L-1$ find solution $\mathbf{x}^{(L)}$.
5. If $r = R$ stop the calculation, else apply boosting operation, i.e., set
   $x^{(0)}(i) = \left[x^{(L)}(i)\right]^p$,where $i = 0, 1, ..., N-1$ (12)
   and p is boosting coefficient > 0,
   $$r = r + 1,$$
6. continue in 4.

The question is the choice of the boosting coefficient p in Eq. 12. Let us imagine the peak can be approximately described by a well-known Gaussian function

$$A \cdot e^{-\frac{(i-i_0)^2}{2\sigma^2}} \tag{12}$$

where A is amplitude, i_0 is position and σ represents width of the peak, respectively. By the application of the power function with the parameter p we get

$$A^p \cdot e^{-\frac{(i-i_0)^2}{2\left(\frac{\sigma}{\sqrt{p}}\right)^2}} \tag{13}$$

Clearly, if the coefficient p is greater than 1 the boosting operation increases the heights in favor of bigger peaks and decreases widths of peaks. However, if the coefficient is too big it relatively suppresses small peaks, which can later completely disappear from the deconvolved spectrum. Moreover, if two or more peaks are positioned closely to each other the exponential operation can produce new artificial peaks. For example let us imagine we have two peaks and $p = 2$. Then we get

$$\begin{aligned} &\left(A_1 \cdot e^{-\frac{(i-i_1)^2}{2\sigma^2}} + A_2 \cdot e^{-\frac{(i-i_2)^2}{2\sigma^2}}\right)^2 = \\ &A_1^2 \cdot e^{-\frac{(i-i_1)^2}{2\left(\frac{\sigma}{\sqrt{2}}\right)^2}} + A_2^2 \cdot e^{-\frac{(i-i_2)^2}{2\left(\frac{\sigma}{\sqrt{2}}\right)^2}} + 2 \cdot A_1 \cdot A_2 \cdot e^{-\frac{(i-i_1)^2+(i-i_2)^2}{2\sigma^2}} \end{aligned} \tag{14}$$

The third term on the right side of Eq. 15 represents fake peak with position between two original peaks. This can negatively influence the result of the boosted deconvolution.

Apparently when we want to boost peaks in the spectrum the parameter p should be greater than 1. Otherwise, the peaks would be suppressed (smoothed) and consequently the resolution would decrease. On the other hand, according to our experience, it should not be too big (greater than 2). When choosing it too big, small peaks will disappear from spectrum at the expense of big ones. One can conclude that the parameter p should be chosen from the range $p \in \langle 1, 2 \rangle$. Empirically we have found that reasonable results can be obtained with boosting coefficients $p \approx 1.1 - 1.2$.

Let us illustrate and compare the classic and boosting Gold deconvolution algorithms through the use of simple example. Let us have a convolution system with two unknowns

$$\mathbf{y} = H\mathbf{x} + \mathbf{n} = \begin{bmatrix} 3 \\ 17 \\ 4 \\ 0 \end{bmatrix} = \begin{bmatrix} 1 & 0 \\ 5 & 1 \\ 2 & 5 \\ 0 & 2 \end{bmatrix} \cdot \begin{bmatrix} x(0) \\ x(1) \end{bmatrix} \tag{15}$$

We have to minimize

$$\left\| \begin{bmatrix} 1 & 0 \\ 5 & 1 \\ 2 & 5 \\ 0 & 2 \end{bmatrix} \cdot \begin{bmatrix} x(0) \\ x(1) \end{bmatrix} - \begin{bmatrix} 3 \\ 17 \\ 4 \\ 0 \end{bmatrix} \right\|^2 = \begin{array}{l} 30x(0)^2 + 30x(0)x(1) + 27x(1)^2 \\ -192x(0) - 74x(1) + 314 \end{array} \tag{16}$$

which is called loss function. Least squares solution of the convolution system given by Eq. 16 according to Eq. 3 is

$$[3.444, -0.448]^T \tag{17}$$

It is optimal solution in the unconstrained space of two independent variables $x_0,\ x_1$. It contains negative value. However in the applications like spectroscopy, the negative values are unreasonable.

In Fig. 3 we show the loss function (Eq. 17) in two-dimensional space and both the unconstrained solution and the solution in the constrained to positive subspace. When employing the Gold deconvolution algorithm (Eq. 8) we get a sequence of iterations. The situation for the first 5 iterations (vectors $\mathbf{x}_0 - \mathbf{x}_4$) is shown in Fig. 3 as well. It converges rather slowly to the optimal solution in the positive subspace.

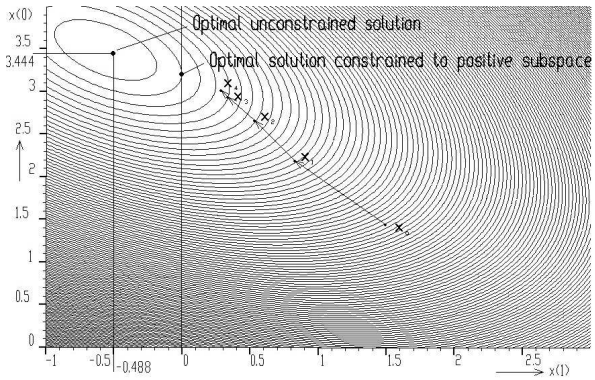

Fig. 3: Graphical illustration of loss function, optimal solutions in both unconstrained space and constrained positive subspace and the first 5 iterative solutions of Gold deconvolution. The arrows indicate the direction of iterations.

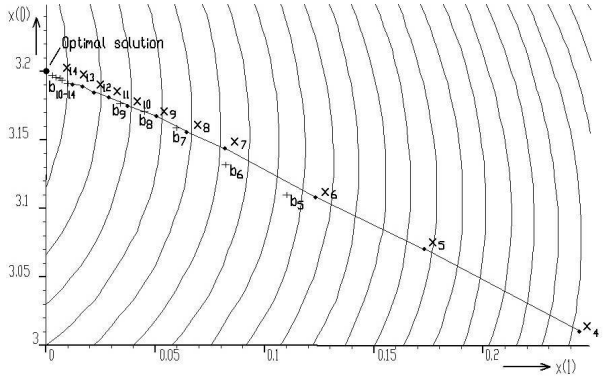

Fig. 4: Detailed view of loss function and iterative solutions for classic Gold deconvolution (vectors $\mathbf{x}$) and boosted Gold deconvolution (vectors $\mathbf{b}$).

In Fig. 4 we present detailed view for classic and boosted Gold deconvolution. Vectors $\mathbf{x}_0 - \mathbf{x}_{14}$ represent sequence of classic Gold deconvolution iterations. Vectors $\mathbf{b}$ represent sequence of boosted Gold deconvolution iterations. The boosted operation was carried out after every 5 iterations, so that the solutions $\mathbf{x}_0 - \mathbf{x}_4$ and $\mathbf{b}_0 - \mathbf{b}_4$ coincide. However, due to the boosting, the next iterations of boosted Gold deconvolution approach the optimal solution in positive subspace much faster than iterations of classic deconvolution.

Now let us investigate the properties of boosted deconvolutions using our testing synthetic spectrum from previous section. We stopped the iterations after every 200 steps, applied boosting operations according to the above given algorithm and repeated this procedure 50 times with boosting coefficient $p = 1.2$. Entirely it gives 10000 iteration steps. The result of the boosted one-fold Gold deconvolution is shown in Fig. 5.

Except for channel 80, it concentrates areas of peaks practically into one channel spikes. Anyway, there still remains the problem in the positions of some estimated peaks.

Further in Fig. 6 we present the result of boosted Richardson-Lucy algorithm (again 50 iterations, repeated 20 times with boosting coefficient $p = 1.2$). It decomposes completely (to one channel) all peaks in the spectrum.

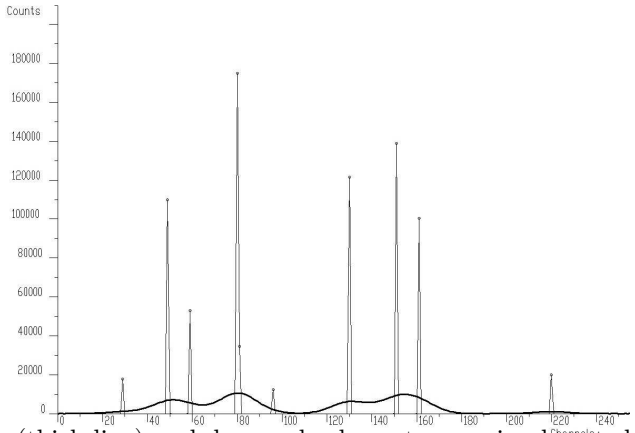

Fig. 5: Original spectrum (thick line) and deconvolved spectrum using boosted Gold algorithm (thin line) after 200 iterations and 50 repetitions ($p = 1.2$).

Finally in Fig. 7 we present the result of boosted MAP algorithm using the same parameters. Again it decomposes completely all peaks in the spectrum.

Further we have applied the sequence of above-mentioned methods also to experimental γ-ray spectra. However, before application of the deconvolution procedure we removed background from the spectrum using the background elimination algorithm with decreasing clipping interval presented in [12]. In Fig. 8 and Fig. 9 we give results after application of classic and boosted Gold deconvolution algorithms, respectively. Again, boosted Gold deconvolution decomposes the spectrum practically to δ functions. Application of boosted Richardson-Lucy and MAP deconvolution algorithms gives results practically identical to that given in Fig. 9.

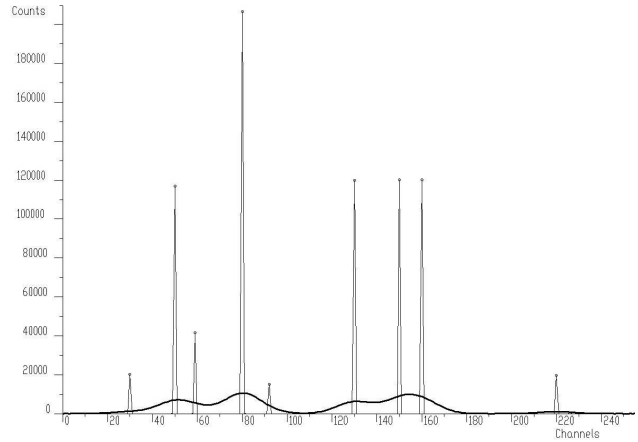

Fig. 6: Original spectrum (thick line) and deconvolved spectrum using boosted Richardson-Lucy algorithm (thin line) after 200 iterations and 50 repetitions ($p = 1.2$).

CONCLUSIONS

In the field of processing of spectroscopic information, the deconvolution methods represent an efficient tool to improve the resolution in the data. It is of great importance mainly in the tasks connected with decomposition of overlapped peaks (multiplets). In the work, we have discussed and analyzed a series of deconvolution methods.

We illustrated the behavior of the deconvolution methods using a testing synthetic spectrum. Though they improve substantially the resolution in the spectra they are not efficient enough to decompose closely

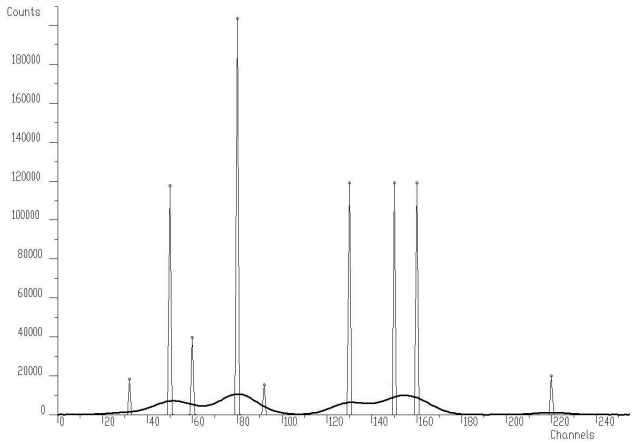

Fig. 7: Original spectrum (thick line) and deconvolved spectrum using boosted MAP algorithm (thin line) after 200 iterations and 50 repetitions ($p = 1.2$).

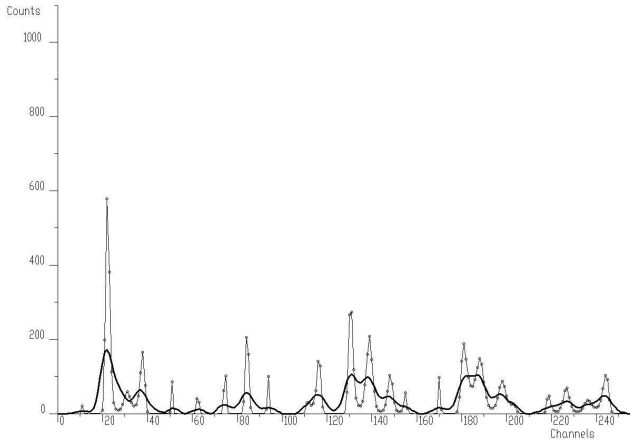

Fig. 8: Original γ-ray spectrum (thick line) and deconvolved spectrum using classic Gold algorithm (thin line) after 10 000 iterations.

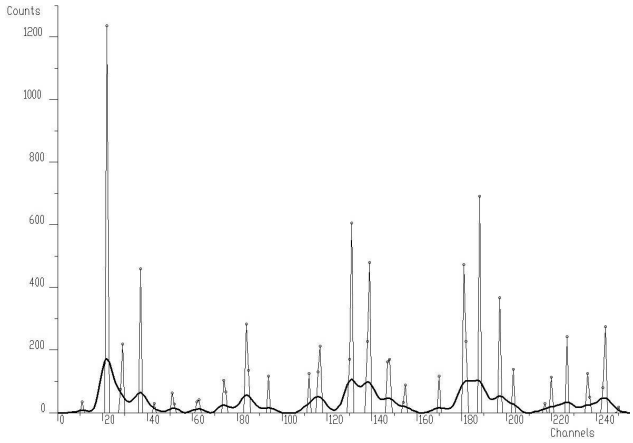

Fig. 9: Original γ-ray spectrum (thick line) and deconvolved spectrum using boosted Gold algorithm (thin line) after 200 iterations and 50 repetitions ($p = 1.2$).

positioned peaks.

Therefore in the subsequent section we proposed boosted deconvolution algorithms. We have studied the decomposition capabilities of boosted Gold, Richardson-Lucy and MAP algorithms, respectively. We have analyzed and compared achieved results. We can conclude that all three boosted algorithm are able to decompose the overlapped peaks practically to δ functions while concentrating the peak areas to one channel. Richardson-Lucy and MAP algorithms give slightly better result than one-fold Gold algorithm.

The deconvolution algorithms presented in this work were implemented in DaqProVis system [13]. Gold and Richardson-Lucy algorithms were also implemented in ROOT system [14] in the form of TSpectrum, TSpectrum2 and TSpectrum3 classes, developed in collaboration with CERN.

ACKNOWLEDGMENT:
This work was supported by the Slovak Research and Development Agency under the contract No. APVV-0177-11 and by Scientific Grant Agency through Project 2/0071/12 from Ministry of Education of Slovak Republic and the Slovak Academy of Sciences.

REFERENCES

[1] J. Weese et al, Nucl. Instr. Meth. Phys. Res. A **378**, 275 (1996).
[2] C. W. Groetch, The Theory of Tikhonov Regularization for Fredholm Equations of the First Kind, Boston: Pitman, 1984.
[3] M. Z. Nashed, IEEE Trans. Antenn. Propagat. **29**, 220 (1981).
[4] A. N. Tikhonov et al, Numerical Methods for the Solution of Ill-Posed Problems, Netherlands: Kluwer Academic Publishers, 1995.
[5] M. Morháč et al, Nucl. Instr. Meth. Phys. Res. A **401**, 385 (1997).
[6] G. E. Coote, Nucl. Instr. Meth. Phys. Res. B **130**, 118 (1997).
[7] R. Gold, ANL-6984 Report, Argonne: Argonne National Laboratories, 1964.
[8] M. Morháč, Nucl. Instr. Meth. Phys. Res. A **559**, 119 (2006).
[9] L. B. Lucy, Astronomical Journal **79**, 745 (1974).
[10] W. H. Richardson, J. Opt. Soc. Am. **62**, 55 (1972).
[11] D. T. Pham, Signal Processing **87**, 2045 (2007).
[12] M. Morháč and V. Matoušek, Applied Spectroscopy **62**, 91 (2008).
[13] M. Morháč et al, Nucl. Instr. Meth. Phys. Res. A **559**, 76 (2006).
[14] R. Brun et al, ROOT, An Object-Oriented Data Analysis Framework, Users Guide 3.02c, CERN (2002).

NEUTRON-RICH RARE ISOTOPE PRODUCTION IN PERIPHERAL HEAVY-ION COLLISIONS AT BEAM ENERGIES 15–25 MEV/NUCLEON

G.A. Souliotis[1,*], P.N. Fountas[1,†], M. Veselsky[2,‡] and A. Bonasera[3,4,§]

[1]Laboratory of Physical Chemistry, Department of Chemistry, National and Kapodistrian University of Athens, Athens 15771, Greece
[2]Institute of Physics, Slovak Academy of Sciences, Dubravska cesta 9, 845 11 Bratislava, Slovakia
[3]Cyclotron Institute, Texas A&M University, College Station, Texas 77843, USA
[4] Laboratori Nazionali del Sud, INFN, via Santa Sofia 62, I-95123 Catania, Italy

Abstract

We present a systematic study of the production cross sections of projectile-like fragments from collisions of ^{86}Kr projectiles with ^{64,58}Ni and ^{124,112}Sn targets at 15 and 25 MeV/nucleon with emphasis on the neutron-rich isotopes. Our recent experimental data are compared with calculations for the above collisions employing a hybrid approach. The dynamical stage of the projectile-target interaction was described with either the phenomenological deep-inelastic transfer (DIT) model or with the the microscopic constrained molecular dynamics model (CoMD). Subsequently, for the de-excitation of the projectile-like fragments, the statistical multifragmentation model (SMM) or the binary-decay code GEMINI were employed. An overall good agreement with the experimental results was obtained. We point out that our current understanding of the reaction mechanism at beam energies below the Fermi energy suggests that such nuclear reactions, involving peripheral nucleon exchange, can be exploited as a novel route to access extremely neutron-rich rare isotopes toward the r-process path and the hard-to-reach neutron drip-line. For this purpose, we believe that the use of re-accelerated neutron-rich radioactive beams may offer unique and exciting opportunities toward unexplored regions of the nuclear landscape.

INTRODUCTION

The exploration of the nuclear landscape toward the astrophysical r-process path and the neutron drip-line have recently received special attention by the nuclear physics community (see, e.g., [1, 2] and references therein). Closely related to this effort is the efficient production of very neutron-rich nuclides which constitutes a central issue in current and future rare isotope beam facilities (see, e.g., [3, 4, 5, 6, 7, 8, 9, 10, 11]).

Neutron-rich nuclides are mainly produced by spallation, fission and projectile fragmentation [12]. Spallation is an efficient mechanism to produce rare isotopes for ISOL-type techniques [13]. Projectile fission is appropriate in the region of light and heavy fission fragments (see, e.g., [14] for recent efforts on ^{238}U projectile fission). Finally, projectile fragmentation offers a universal approach to produce exotic nuclei at beam energies above 100 MeV/nucleon (see, e.g., [15, 16]). This approach is, nevertheless, based on the fact that optimum neutron excess in the fragments is achieved by stripping the maximum possible number of protons (and a minimum possible number of neutrons).

To reach a high neutron-excess in the products, apart from proton stripping, it may be necessary to capture neutrons from the target. Such a possibility is offered by reactions of nucleon exchange at beam energies from the Coulomb barrier [17, 18] to the Fermi energy (20–40 MeV/nucleon) [19, 20]. Detailed experimental data in this broad energy range are scarce at present [18, 21, 22]. In multinucleon transfer and deep-inelastic reactions near the Coulomb barrier [18], the low velocities of the fragments and the wide angular and ionic charge state distributions may limit the collection efficiency for the most neutron-rich products. The reactions in the Fermi energy regime combine the advantages of both low-energy (i.e., near and above the Coulomb barrier) and high-energy (i.e., above 100 MeV/nucleon) reactions. At this energy, the synergy of the projectile and the target enhances the N/Z of the fragments, while the velocities are high enough to allow efficient in-flight collection and separation.

Our initial experimental studies of projectile fragments from 25 MeV/nucleon reactions of ^{86}Kr on ^{64}Ni [19] and ^{124}Sn [20] indicated substantial production of neutron-rich fragments. Motivated by recent developments in several facilities that will offer either very intense primary beams [5, 8] at this energy range or re-accelerated rare isotope beams [4, 5, 8, 9], we continued our experimental studies at 15 MeV/nucleon [23].

*Corresponding author. E-mail: soulioti@chem.uoa.gr
†E-mail: pfountas@chem.uoa.gr
‡E-mail: Martin.Veselsky@savba.sk
§E-mail: abonasera@comp.tamu.edu

In this work, after a short overview of the experimental measurements, we present a systematic calculation of the production cross sections based on either the phenomenological deep-inelastic transfer (DIT) model or the microscopic constrained molecular dynamics model (CoMD). The good description of the experimental results with the CoMD code, as well as, with a properly modified version of the DIT code, suggest the possibility of using the present theoretical framework for the prediction of exotic nuclei employing radioactive beams that will soon be available in upcoming facilities. As an example, we present the production cros sections and the rates of neutron-rich nuclei using a radioactive beam of ^{92}Kr at 15 MeV/nucleon.

EXPERIMENTAL METHODS

A detailed presentation of the experimental results appear in [23] in which the mass spectrometric measurements of production cross sections of neutron-rich projectile fragments from the reactions of a 15 MeV/nucleon ^{86}Kr beam with ^{64}Ni, ^{58}Ni and ^{124}Sn, ^{112}Sn targets are given. We also note that the experimental results of the 25MeV/nucleon reactions and the relevant procedures are described in detail in our articles [19, 20, 21, 22]. We briefly mention that the use of the high-resolution recoil separator MARS in combination with standard Bρ–ΔE–E (magnetic rigidity, energy-loss, residual-energy) and time-of-flight techniques provided high-resolution information on the atomic number Z, the ionic charge q, the mass number A and the velocity distributions of the projectile fragments. Summation over q provided the yield distributions with respect to Z, A and velocity from which production cross sections were extracted. The measurements were performed inside the grazing angles of the corresponding reactions in a wide Bρ window that enabled efficient collection of heavy projectile residues produced in a broad range of energy damping, from quasielastic to deep-inelastic collisions.

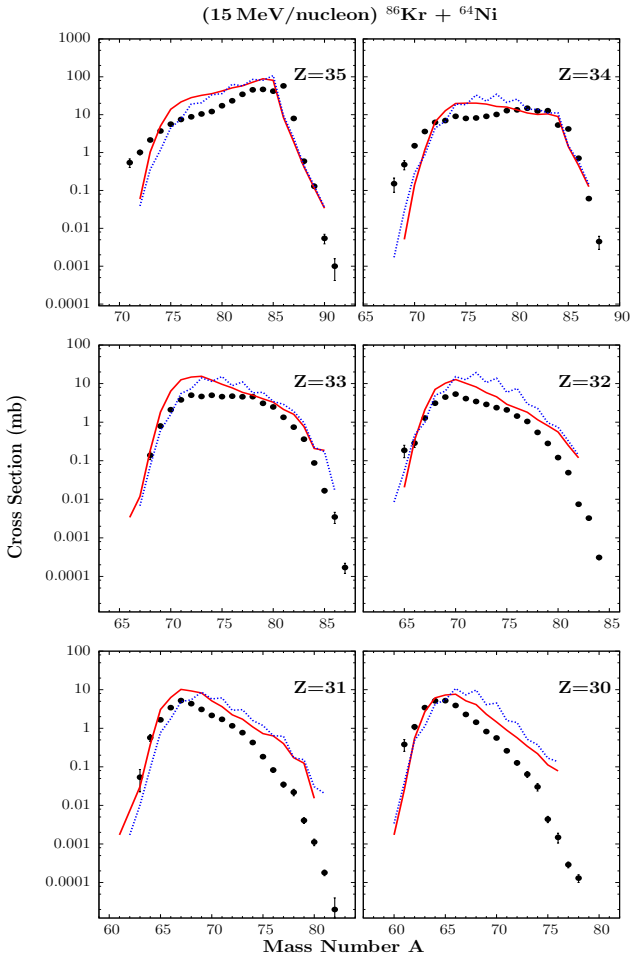

Fig. 1: (Color online) Experimental mass distributions (symbols) of elements with Z = 35–30 observed in the reaction ^{86}Kr(15 MeV/nucleon)+^{64}Ni [23] compared to the results of CoMD/SMM calculations (solid red line) and CoMD/GEMINI calculations (dotted blue line).

RESULTS AND COMPARISONS

In Fig. 1 we present the experimental mass distributions of elements with Z = 35–30 of the reaction ^{86}Kr(15 MeV/nucleon)+^{64}Ni [23] compared to the calculations with the CoMD code [24, 25] combined with the de-excitation codes SMM [26] (solid line) and GEMINI [27] (dotted line), used for the de-excitation of the quasiprojectiles emerging after the dynamical stage. The results of the calculations are in overall agreement with the experimental data especially for the isotopes close to the projectile with Z = 35–32. We also observe that the microscopic CoMD model is able to describe even the rare neutron-rich products from this reaction that are the products for our main interest. The overestimation of the cross sections for the products with Z = 31,30 is related to issues of the excitation energy as calculated by CoMD and are currently under further investigation. Subsequently, motivated by our previous studies [19, 20], we employed Tassan-Got's

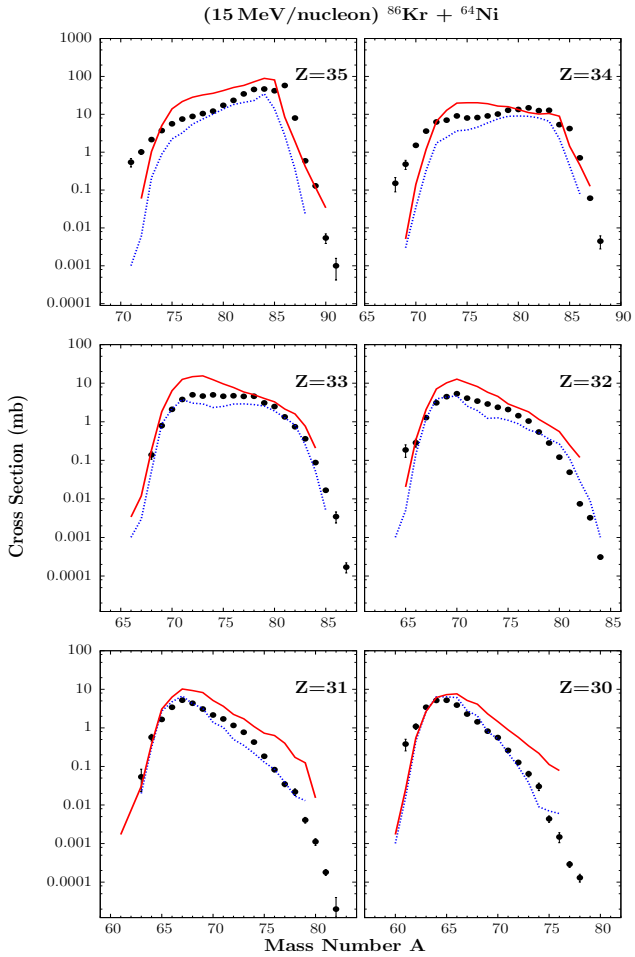

Fig. 2: (Color online) Experimental mass distributions (symbols) of elements with Z = 35–30 observed in the reaction ^{86}Kr(15 MeV/nucleon)+^{64}Ni [23] compared to the results of CoMD/SMM calculations (solid red line) and DITm/SMM calculations (dotted blue line).

phenomenological model of deep inelastic transfer (DIT) [28] coupled with SMM [26] or GEMINI [27]. The results of this standard version of DIT were not satisfactory. We thus proceeded with our modified version of the DIT model (DITm) [29] in which we have introduced a detailed description of the nuclear surface and the neutron skin of the involved nuclei. In Fig 2, we present the experimental mass distributions of elements with Z = 35–30 of the reaction ^{86}Kr(15 MeV/nucleon)+^{64}Ni [23] and compare them to the results of the modified DIT (DITm) calculations (dotted line) and to the results of the CoMD calculations (solid line) using SMM as the de-excitation code. From this figure we observe that the modified DIT code describes the experimental results rather well at these beam energies. Moreover, it can better describe the products further away from the projectile, that cannot be well described by CoMD, as we mentioned previously.

We mention that a thorough comparison of the data with the calculations for the 15 MeV/nucleon, as well as the 25 MeV/nucleon reactions has been performed that will appear in [31]. After this systematic comparison of the calulations with the experimental data of the stable ^{86}Kr beam, we proceeded to investigate what results we would obtain by using a neutron-rich radioactive beam, such as ^{92}Kr. In Fig. 3 we present

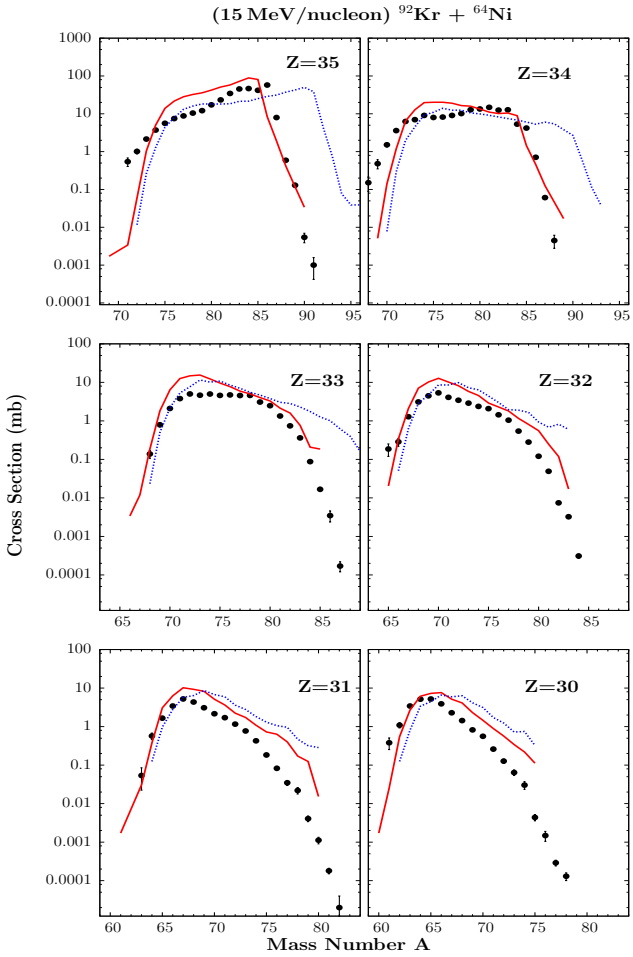

Fig. 3: (Color online) Experimental mass distributions (symbols) of elements with Z = 35–30 observed in the reaction ^{86}Kr(15 MeV/nucleon)+^{64}Ni [23], calculations CoMD/SMM for the reaction ^{86}Kr(15 MeV/nucleon)+^{64}Ni (solid red line), calculations CoMD/SMM for the reaction ^{92}Kr(15 MeV/nucleon)+^{64}Ni (dotted blue line).

again the experimental mass distributions (black symbols) of the reaction ^{86}Kr(15 MeV/nucleon)+^{64}Ni, the CoMD/SMM calculations for this reaction (solid line) and, furthermore, the CoMD/SMM calculations for the reaction ^{92}Kr(15 MeV/nucleon)+^{64}Ni (dotted line). We observe that by using the neutron-rich radioactive beam of ^{92}Kr, we obtain more neutron-rich products. This is primarily true for the isotopes near the projectile. We point out that, e.g., for bromine (Z=35), isotopes that have up to 15 more neutrons (A = 96) than the corresponding stable isotope (A = 81) can be obtained. This observation indicates that by using neutron-rich radioactive beams, and through the mechanism of peripheral multinucleon transfer, we will have the possibility to produce even more neutron-rich nuclides toward neutron drip line.

A comprehensive presentation of the CoMD/SMM calculated production cross sections of the projectile-like fragments from the above radioactive-beam reaction on the Z vs N plane is given in Fig. 4. In this figure, stable isotopes are represented by closed squares, whereas fragments obtained by the radioactive-beam reaction are given by the open circles (with sizes corresponding to cross-section ranges according to the figure key). The dashed (green) line gives the location of the neutron drip-line and the full (red) line indicates the expected path of the astrophysical rapid neutron-capture process (r-process), as calculated in [30]. In the figure we clearly observe that the neutron pickup products from the ^{92}Kr projectile reach and even exceed the path of the r-process near Z=30–36.

In Table I, we present the predicted cross-sections and the production rates of neutron rich isotopes from the reaction of the radioactive beam of ^{92}Kr (15 MeV/nucleon) with ^{64}Ni. For the rate calculations, the ^{92}Kr beam with intensity 0.5 pnA (3.1×10^9 particles/sec) is assumed to interact with a ^{64}Ni target of 20 mg/cm^2 thickness. We see that we have the possibility to produce extremely neutron-rich isotopes in these energies with the use of re-accelerated radioactive beams, such as ^{92}Kr, that will be available in upcoming rare-isotope facilities (e.g. [10, 11]).

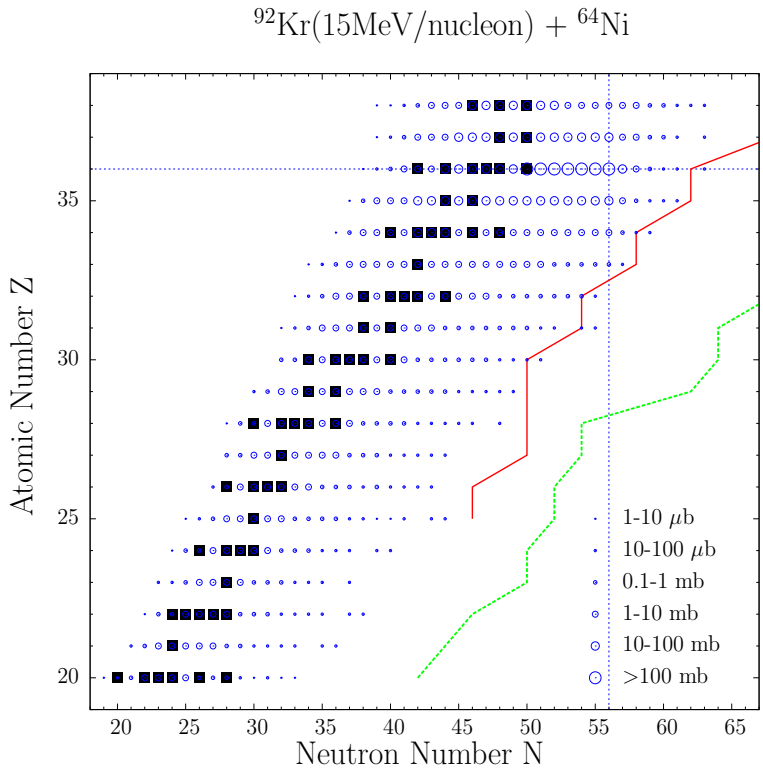

Fig. 4: (Color online) Representation of CoMD/SMM calculated production cross sections of projectile fragments from the radioactive-beam reaction ^{92}Kr (15 MeV/nucleon) + ^{64}Ni on the Z–N plane. The cross section ranges are shown by open circles according to the key. The closed squares show the stable isotopes. The solid (red) line shows the astrophysical r-process path and the dashed (green) line shows the location of the neutron drip-line. The horizontal and vertical dashed lines indicate, respectively, the proton and neutron number of the ^{92}Kr projectile.

SUMMARY AND CONCLUSIONS

In the present work, we perfomed a systematic study of the production cross sections of projectile-like fragments from collisions of ^{86}Kr projectiles with ^{64,58}Ni and ^{124,112}Sn targets at 15 and 25 MeV/nucleon with emphasis on the neutron-rich isotopes.

Our experimental data were compared with systematic calculations employing a two-step approach. The calculations for the dynamical stage of the projectile-target interaction were carried out using either the phenomenological deep-inelastic transfer (DIT) model or the the microscopic constrained molecular dynamics model (CoMD). For the de-excitation of the projectile-like fragments, the statistical multifragmentation model (SMM) or the binary-decay code GEMINI were employed. An overall good agreement with the experimental results was observed. With the current understanding of the reaction mechanism at these beam energies, we suggest that these nuclear reactions, involving peripheral nucleon exchange, be exploited as an efficient route to access neutron-rich rare isotopes toward the r-process path and the neutron drip-line. Therefore, future experiments in several accelerator facilities [12] can be planned that will enable a variety of nuclear structure and nuclear reaction studies in unexplored regions of the nuclear chart.

ACKNOWLEDGMENT:

We wish to thank S. Galanopoulos, Z. Kohley, A. Keksis, B. C. Stein, and S.J. Yennello for the help and support on the experimental work related to the heavy-residue measurements at 15–25 MeV/nucleon at Texas A&M. We are thankful to M. Papa for his version of the CoMD code, and to Hua Zheng for his rewritten version of the CoMD. We acknowledge the motivation and recent discussions on experimental aspects of RIB production with Y.K. Kwon and K. Tshoo of the KOBRA team of RISP. Financial support for this work was provided, in part, by ELKE Research Account No 70/4/11395 of the National and Kapodistrian University of Athens. M.V. was supported by the Slovak Scientific Grant Agency under contracts 2/0105/11 and 2/0121/14 and by the Slovak Research and Development Agency under contract APVV-0177-11.

Tab. 1: Cross sections and rate estimates (last column) of very neutron-rich isotopes from the reaction ^{92}Kr (15 MeV/nucleon) + ^{64}Ni. For the rates, a radioactive beam of ^{92}Kr with intensity 0.5 pnA (3.1×10^9 particles/sec) is assumed to interact with a ^{64}Ni target of 20 mg/cm^2 thickness.

Rare Isotope	Reaction Channel	Cross Section (mb)	Rate (sec^{-1})
^{93}Kr	-0p+1n	18.8	1.1×10^4
^{94}Kr	-0p+2n	2.3	1.3×10^3
^{95}Kr	-0p+3n	0.63	3.8×10^2
^{96}Kr	-0p+4n	0.2	1.2×10^2
^{92}Br	-1p+1n	4.5	2.7×10^3
^{93}Br	-1p+2n	0.75	4.5×10^2
^{94}Br	-1p+3n	0.078	47
^{95}Br	-1p+4n	0.040	23
^{96}Br	-1p+5n	0.008	5
^{90}Se	-2p+0n	2.7	1.6×10^3
^{91}Se	-2p+1n	0.6	3.5×10^2
^{92}Se	-2p+2n	0.12	70
^{93}Se	-2p+3n	0.04	23

REFERENCES

[1] J. Erler et al, Nature **486**, 509 (2011).
[2] J. Äystö, W. Nazarewicz, M. Pfützner, C. Signorini, eds, Proceedings of the 5th Int. Conference on Exotic Nuclei and Atomic Masses (ENAM08), Ryn, Poland, Sept. 7–13 (2008); Eur. Phys. J. A **42** (2009).
[3] D. F. Geesaman et al. Ann. Rev. Nucl. Part. Sci. **56**, 53 (2006)
[4] FRIB main page: www.frib.msu.edu
[5] GANIL main page: www.ganil.fr
[6] GSI main page: www.gsi.de
[7] RIBF main page: www.rarf.riken.go.jp/Eng/facilities/RIBF.html
[8] ATLAS main page: www.phy.anl.gov/atlas/facility/index.html
[9] EURISOL main page: www.eurisol.org
[10] RISP main page: www.risp.re.kr/eng/pMainPage.do
[11] K. Tshoo, Y. K. Kim, Y. K. Kwon et al, Nucl. Instrum. Meth. B **317**, 242 (2013).
[12] Y. Blumenfeld, T. Nilsson and P. Van Duppen, Phys. Scr. T152 014023 (2013).
[13] A. Kelić, M. V. Ricciardi, K. -H. Schmidt, BgNS Transactions, **13**, 98 (2009).
[14] H. Alvarez-Pol et al., Phys. Rev. C **82**, 041602 (2010).
[15] O. B. Tarasov et al., Phys. Rev. C **80**, 034609 (2009).
[16] S. Lukyanov et al., Phys. Rev. C **80**, 014609 (2009).
[17] V. V. Volkov, Phys. Rep. **44**, 93 (1978).
[18] L. Corradi, G. Pollarolo, S. Szilner, J. Phys. G **36**, 113101 (2009).
[19] G. A. Souliotis et al., Phys. Lett. B **543**, 163 (2002).
[20] G. A. Souliotis et al., Phys. Rev. Lett. **91**, 022701 (2003).
[21] G. A. Souliotis et al., Nucl. Instrum. Methods **B 204** 166 (2003).
[22] G. A. Souliotis et al., Nucl. Instum. Methods **B 266**, 4692 (2008).
[23] G. A. Souliotis et al., Phys. Rev. C **84**, 064607 (2011).
[24] M. Papa et al., Phys. Rev. **C 64**, 024612 (2001).
[25] M. Papa et al, J. Comp. Phys. **208**, 403 (2005).
[26] J. Bondorf et al., Phys. Rep. **257**, 133 (1995).
[27] R. Charity et al., Nucl. Phys. **A 483**, 391 (1988); Phys. Rev. **C 58**, 1073 (1998).
[28] L. Tassan-Got and C. Stephan, Nucl. Phys. **A 524**, 121 (1991).
[29] M. Veselsky and G.A. Souliotis, Nucl. Phys. **A 765**, 252 (2006).
[30] P. Moller, J.R. Nix and K.L. Kratz, At. Data Nucl. Data Tables **66**, 131 (1997).
[31] P.N. Fountas, G.A. Souliotis, M. Veselsky and A. Bonasera, Phys. Rev. C accepted (2014).

MICROSCOPIC CALCULATIONS OF LOW-ENERGY FISSION WITH THE CONSTRAINED MOLECULAR DYNAMICS (CoMD) MODEL

N. Vonta[1,*], G.A. Souliotis[1,†], M. Veselsky[2,‡] and A. Bonasera[3,4,§]

[1]Laboratory of Physical Chemistry, Department of Chemistry, National and Kapodistrian University of Athens, Athens 15771, Greece
[2]Institute of Physics, Slovak Academy of Sciences, Dubravska cesta 9, 845 11 Bratislava, Slovakia
[3]Cyclotron Institute, Texas A&M University, College Station, Texas 77843, USA
[4] Laboratori Nazionali del Sud, INFN, via Santa Sofia 62, I-95123 Catania, Italy

Abstract

The investigation of the mechanism of nuclear fission is a topic of current experimental and theoretical interest. In this work, we initiated a systematic study of low and intermediate energy fission calculations using the Constrained Molecular Dynamics (CoMD) code. The code implements an effective interaction with a soft isoscalar part and with several forms of the density dependence of the nucleon symmetry potential. In addition, CoMD imposes a constraint in the phase space occupation for each nucleon restoring the Pauli principle at each time step of the evolution of the nuclear system. Proper choice of the surface parameter of the effective interaction has been made to describe fission. In this work, we present CoMD calculations for several proton-incuded fission reactions at low and intermediate energy and compare them with recent experimental data. We found that the CoMD code is able to describe the complicated many-body dynamics of the fission process especially for intermediate and higher-energy fission reactions.

INTRODUCTION

The microscopic description of the mechanism of nuclear fission is a topic of intense nuclear research. Understanding of nuclear fission, apart from the theoretical many-body point of view, is of practical importance for energy generation, isotope production, as well as for the transmutation of nuclear waste. Furthermore, nuclear fission is essentially the process that defines the upper limit of the periodic table of the elements and plays a vital role in the production of heavy elements via the astrophysical r-process [1]. Motivated by the present state of affairs regarding fission research, we initiated a systematic study of low and intermediate energy fission using the Constrained Molecular Dynamics (CoMD) code of A. Bonasera and M. Papa [4, 5].

THEORETICAL FRAMEWORK

The Constrained Molecular Dynamics (CoMD) code is based on the gereral approach of molecular dynamics as applied to nuclear systems [2, 3]. The nucleons are assumed to be localized gaussian wavepackets in coordinate and momentum space. A simplified effective nucleon-nucleon interaction is implemented with a nuclear-matter compressibility of K=200 (soft EOS) with several forms of the density dependence of the nucleon-nucleon symmetry potential. In addition, a constraint is imposed in the phase space occupation for each nucleon, restoring the Pauli principle at each time step of the collision. Proper choice of the surface parameter of the effective interaction was made to describe fission.

In the calculations of the present work, the CoMD code was used essentially with its standard parameters. The soft density-dependent isoscalar potential was chosen (K=200). For the isovector part, several forms of the density dependence of the nucleon-nucleon symmetry potential are implemented. Two of them were used in the present work: the "standard" symmetry potential [red (solid) lines] and the "soft" symmetry potential [blue (dotted) lines] in the figures that follow. These forms correspond to a dependence of the symmetry potential on the 1 and the 1/2 power of the density, respectively. The surface term of the potential was set to zero to describe fission. For a given reaction, a total of approximately 5000 events were collected. For each event, the impact parameter of the collision was chosen in the range b = 0–6 fm, following a triangular distribution. Each event was followed up to 15000 fm/c and the phase space coordinates were registered

*E-mail: nikolettav@chem.uoa.gr
†Corresponding author. E-mail: soulioti@chem.uoa.gr
‡E-mail: Martin.Veselsky@savba.sk
§E-mail: abonasera@comp.tamu.edu

every 50 fm/c. At each time step, fragments were recognized with the minimum spanning tree method ([4, 5], and their properties were reported. Thus, information on the evolution of the fissioning system and the properties of the resulting fission fragments were obtained. In this way, the moment of scission of the deformed heavy nucleus could be determined. We allowed 2000 fm/c after scission for the nascent fission fragments to deexcite and we reported and analyzed their properties.

RESULTS AND COMPARISONS

Motivated by the present bibliography concerning the nuclear fission of uranium isotopes, we performed calculations related to the proton induced fission of ^{235}U, at 10 MeV, 30 MeV, 60 eV and 100 MeV. Moreover, calculations have been performed for the proton induced fission of ^{238}U, at 100 MeV and 660 MeV energies.

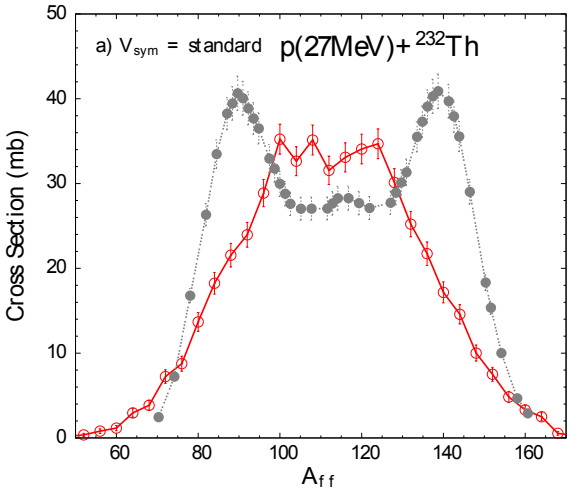

Fig. 1: (Color online) Normalized mass distributions (cross sections) of fission fragments from p (27 MeV) + ^{232}Th. Full points (grey): experimental data [6]. Open points: CoMD calculations with the standard symmetry potential.

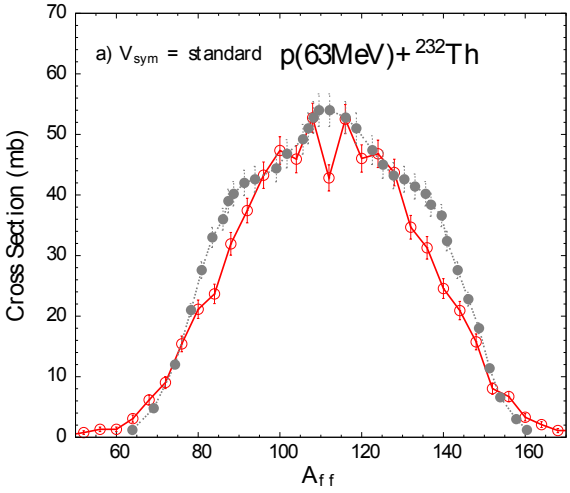

Fig. 2: (Color online) Normalized mass distributions (cross sections) of fission fragments from p (63 MeV) + ^{232}Th. Full points (grey): experimental data [6]. Open points: CoMD calculations with the standard symmetry potential.

In Fig. 1, in the experimental data of the reaction p (27 MeV) + ^{232}Th, we observe the asymmetric nature of the fission of ^{232}Th. In contrast, the CoMD calculations result in a symmetric distribution with a flat top. The main reason is that the nucleon-nucleon interaction in the CoMD model does not include spin dependence, and thus the resulting mean field potential has no spin-orbit contribution. Consequently, the

model cannot reproduce the correct shell effects necessary to describe the asymmetric low-energy fission of ^{232}Th.

When the proton energy increases (Fig. 2), it is expected that the shell effects will fade and the fissioning system will preferentially undergo symmetric fission. The mass yields for the same reaction at proton energy 63 MeV is presented. The experimental mass yield becomes more symmetric at this energy and the calculated yield curve is in better agreement with the data.

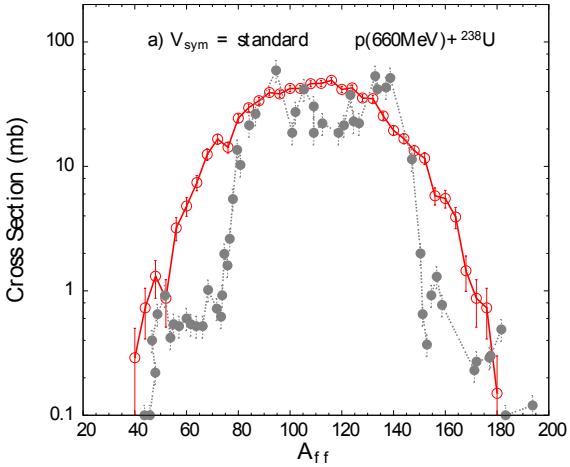

Fig. 3: (Color online) Normalized mass distributions (cross sections) of fission fragments from p (660 MeV) + ^{238}U. Full points (grey): experimental data [8, 9, 10]. Open points: CoMD calculations with the standard symmetry potential.

In Fig. 3, the mass distribution of proton induced fission of ^{238}U at 660 MeV is presented and it is in good agreement with the experimental data [8, 9, 10]. We observe, mostly the symmetric fission mode, due to the vanishing of the shell effects. Moreover, the calculations are able to describe satisfactorily the superasymmetric fission, which has been experimentallly seen at fission fragment masses ∼40–80 and ∼140–180.

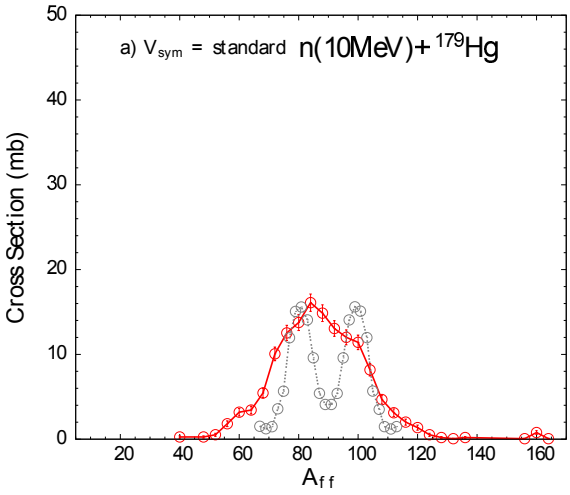

Fig. 4: (Color online) a) Normalized mass distributions (cross sections) of fission fragments from n (10 MeV) + ^{179}Hg. Full points (grey): experimental data [11, 12]. Open points: CoMD calculations with the standard symmetry potential.

In Fig. 4, we present the mass distribution for the neutron induced fission of ^{180}Hg at 10 MeV. The experimental data [11, 12] are compared with the calculations. The work of [12] introduces a new type of asymmetric fission in proton-rich nuclei. It is related to the exotic process of β-delayed fission of ^{180}Tl. The experimental data represent the fission fragment mass distribution of the β-decay daughter nucleus ^{180}Hg, which is asymmetric. The asymmetric nature is surprising due to the fact that the nucleus ^{180}Tl is expected

to be divided into two fragments of ^{90}Zr, with magic number of neutrons N=50 and semi-magic of protons Z=40, which are supposed to be more stable. The data of [11] are in arbitrary units and in order to be compared with the calculations, an appropriate scaling of the distribution has been made (multiplication factor 180). In the experimental data, the asymmetric nature of the fission is obvious. On the contrary, the CoMD calculations cannot describe correctly the shell effects and for this reason, the distribution is symmetric.

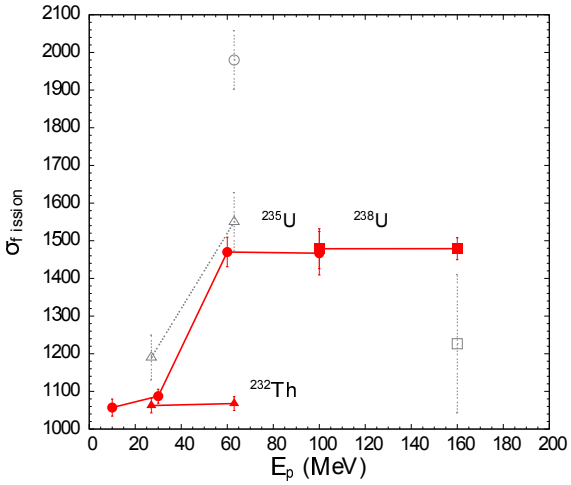

Fig. 5: (Color online) Calculated total fission cross section with respect to proton energy E_p. The CoMD calculations are carried out with the standard symmetry potential and are shown with full (red) symbols connected with full (red) lines. The reactions are indicated as follows: triangles: p (27, 63 MeV) + ^{232}Th, circles: p (10, 30, 60, 100 MeV) + ^{235}U, squares: p (100, 660 MeV) + ^{238}U. Some experimental data are shown with open symbols as follows: triangles: p (27, 63 MeV) + ^{232}Th [6], circles: p (60 MeV) + ^{235}U [7], square: p (660 MeV) + ^{238}U [9, 10]. The point at E_p=660 MeV is displayed at E_p=160 MeV.

Apart from the fission fragment mass distributions, we investigated other fission fragment properties. The results are mostly with the standard symmetry potential. For the following figures, the red closed circles represent the proton induced fission of ^{235}U at 10 MeV, 30 MeV, 60 MeV, 100 MeV. Moreover, the red closed squares represent the proton induced fission of ^{238}U at 100 MeV 660 MeV, whilst the red closed triangles represent the proton induced fission of ^{232}Th at 27 MeV 63 MeV. The blue points are with the soft symmetry potential. The experimental data are the open grey symbols (circles, squares and triangles) and they follow the same structure which has been adopted for the calculations.

The total fission cross section is presented in Fig. 5 in reference to the various proton energies for the proton induced fission of ^{232}Th, ^{235}U and ^{238}U. Concerning the fission of thorium, we observe that increasing the excitation energy there is only a slight increase. However, the experimental data show a jump of approximately 30%.

In Fig. 6, we present the correlation between the excitation energy and the ratio of the fission cross section over the residue cross section. For the fission of ^{232}Th we observe an increase in this ratio towards higher excitation energy. Hence, at 63 MeV beam energy, our calculations show higher probability for fission, in reference to the energy 27 MeV. Moreover, for the fission of the ^{235}U and ^{238}U, the probability of getting fission decreases at excitation energies, starting from 30 MeV to 100 MeV and from 100 MeV to 660 MeV respectively. Furthermore, a sensitivity of the calculations concerning the symmetry potential choice is depicted. For the soft potential choice, the aforementioned ratio increases and this means that this choice leads to an increasing probability of getting fission, especially for the proton induced fission of ^{235}U at various proton energies.

It is very difficult to estimate the fission time from experimental data. Because of the fact that the CoMD is a dynamical microscopic code, we can naturally obtain the dynamical path of the process and therefore determine the fission time. In Fig. 7, the fission time is plotted versus the proton energy of the indicated reactions. We performed the calculations under the restrictions that the fissioning system be a) Z=91, for ^{232}Th b) Z=93, for ^{235}U and ^{238}U, which are represented by the open circles, squares and triangles (open symbols). Moreover, the closed symbols refer to the CoMD calculations where the full ensemble of the fissioning nuclei is taken into account. For this ensemble, we noticed that the code emits on average two pre-scission protons. The general trend shows that the fission time decreases with the increase of the excitation energy. We observe that the open symbols are lower than the closed ones. The general trend

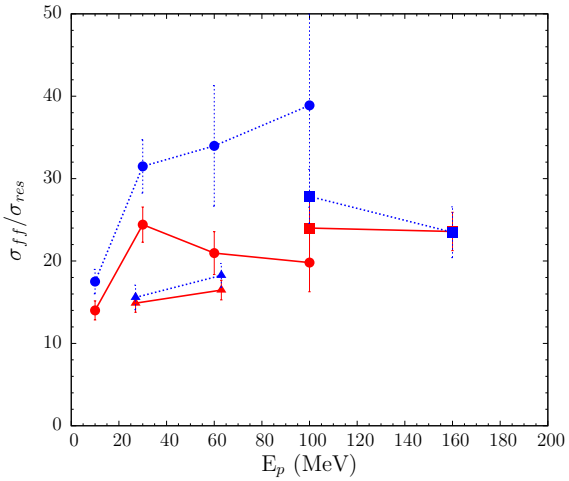

Fig. 6: (Color online) Calculated ratio of the fission cross section over residue cross section with respect to proton energy. CoMD calculations with the standard symmetry potential are with full (red) symbols connected with full (red) lines. Calculations with the soft symmetry potential are with full (blue) symbols connected with dotted (blue) lines. The reactions are indicated as follows: triangles: p (27, 63 MeV) + ^{232}Th, circles: p (10, 30, 60, 100 MeV) + ^{235}U, squares: p (100, 660 MeV) + ^{238}U. The points at E_p=660 MeV are displayed at E_p=160 MeV.

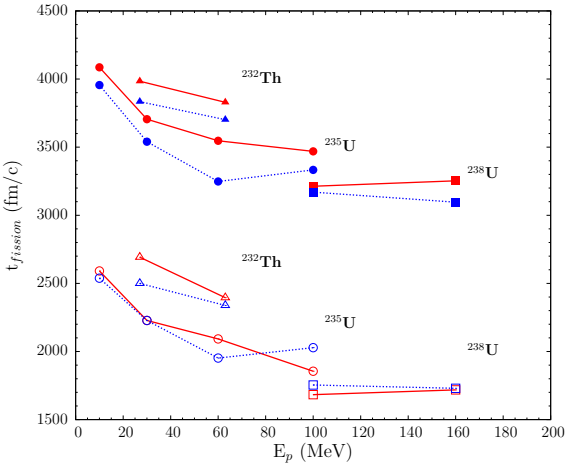

Fig. 7: (Color online) Calculated fission time with respect to incident proton energy. CoMD calculations with the standard symmetry potential are with (red) symbols connected with full (red) lilnes. Calculations with the soft symmetry potential are with (blue) symbols connected with dotted (blue) lines. The full symbols (upper half of the figure) are with the full ensemble of the fissioning nuclei, whereas the open symbols (lower half) are with the selection of the fissioning system not to emit any pre-scission protons (see text). The reactions are indicated as follows: triangles: p (27, 63 MeV) + ^{232}Th, circles: p (10, 30, 60, 100 MeV) + ^{235}U, squares: p (100, 660 MeV) + ^{238}U. The points at E_p=660 MeV are displayed at E_p=160 MeV.

shows that the fission time decreases when the proton energy increases. Additionally, the choice of Z for the fissioning system leads to a decrease of the fission time. When this choice is made, the total Coulomb energy is larger (since no pre-scission protons are emitted) and thus, the fissioning system is more fissionable.

DISCUSSION AND CONCLUSIONS

In the present work we employed the semi-classical microscopic code CoMD to describe mostly proton induced fission, in a variety of energies on ^{232}Th, ^{235}U and ^{238}U nuclei. We chose these nuclei because of the availability of recent literature data and because of their significance in current applications of fission. We found that the CoMD code in its present implementation is able to describe fission at higher energies where the shell effects are washed out. We mention that the effective nucleon-nucleon interaction employed in the code has no spin dependence and thus the resulting mean field has no spin-orbit contribution. We are exploring possibilities of adding such a dependence on the potential to give us the ability to adequately describe the characteristics of low energy fission.

We note that the total fission cross sections were rather well reproduced and the ratio of total fission cross sections over residue cross sections appears satisfactory. Interestingly, this ratio shows a sensitivity on the choice of the symmetry potential. Concerning the mean total energies and the neutron multiplicities, we mention that they are rather adequately reproduced [13]. Finally, information on the fission time scale is obtained from the present calculations. The obtained fission times show a dependence on the excitation energy of the fissioning nucleus, as well as on the choice of the symmetry potential.

In closing, we point out that the CoMD code gives results that are not dependent on the specific dynamics being explored and, thus, offers valuable predictive power for the different modes of fission without adjustable parameters. Consequently, the code can be used for the study of fission of either very neutron-rich or very neutron-deficient nuclei, which have not been studied experimentally to date. Furthermore, this possibility can be exploited to study the fission of very exotic nuclei related to the end point of the r-process, namely the process of fission recycling.

ACKNOWLEDGMENT:
We are thankful to M. Papa for his version of the CoMD code, and to Hua Zheng for his rewritten version of the CoMD. We wish to acknowledge the motivation and recent discussions on experimental aspects of fission with Y.K. Kwon and K. Tshoo of the KOBRA team of RISP. Financial support for this work was provided, in part, by ELKE Research Account No 70/4/11395 of the National and Kapodistrian University of Athens. M.V. was supported by the Slovak Scientific Grant Agency under contracts 2/0105/11 and 2/0121/14 and by the Slovak Research and Development Agency under contract APVV-0177-11.

REFERENCES

[1] J. Erler et al, Nature **486**, 509 (2011).
[2] A. Bonasera, F. Gulminelli, J. Molitoris, Phys. Rep. **243**, 1 (1994).
[3] J. Aichelin, Phys. Rep. **202**, 233 (1991).
[4] M. Papa et al., Phys. Rev. **C 64**, 024612 (2001).
[5] M. Papa et al, J. Comp. Phys. **208**, 403 (2005).
[6] P. Demetriou et al., Phys. Rev. **C 82**, 054606 (2010).
[7] M. C. Duijvestijn et al., Phys. Rev. **C 64**, 014607 (2001).
[8] A. Deppman et al., Phys. Rev. **C 88**, 064609 (2013).
[9] G.S. Karapetyan et al., Phys. Atom. Nucl. **C 72**, 911 (2009).
[10] A.R. Balabekyan et al., Phys. Atom. Nucl. **C 73**, 1814 (2010).
[11] A.V. Andreev et al., Phys. Rev. **C 88**, 047604 (2013).
[12] A.N. Andreyev et al., Phys. Rev. Lett. **105**, 252502 (2010)
[13] N. Vonta, G.A. Souliotis, M. Veselsky, A. Bonasera, Phys. Rev. C submitted (2014).

Abstracts

EXPERIMENTAL STUDIES ON EXOTIC STRUCTURE IN PROTON RICH NUCLEI

Deqing Fang
Shanghai Institute of Applied Physic, Shanghai, China

E-mail: dqfang@sinap.ac.cn

The exotic structure and properties for proton rich nuclei ^{23}Al and ^{22}Mg have been studied experimentally. A d-wave valance proton and enlarged core in ^{23}Al were deduced from the reaction cross section and fragment momentum distribution measurements. Measurements on two-proton correlation function for ^{23}Al and ^{22}Mg were also performed, spectrum of relative momentum and open angle between two protons are obtained. Emission source size is extracted. From p-p relative momentum and opening angles spectrum in different excitation energies, we observed strong component of ^{2}He-like cluster emission from high excitation energy states of ^{22}Mg. For ^{23}Al, sequential proton decay is dominate.

REACTIONS INDUCED BY LIGHT EXOTIC NUCLEI AT LOW ENERGIES

Rubens Lichtenthaler
Universidade de Sao Paulo, Brazil

E-mail: rubens@if.usp.br

Elastic scattering and reactions induced by light exotic nuclei such, as ^{6}He on different targets will be presented. The measurements have been performed in the RIBRAS facility of the University of Sao Paulo. Elastic scattering angular distributions allow a study of the nuclear potentials of exotic nuclei systems. In addition they provide the total reaction cross sections which have been compared with stable systems. Excitations functions of exotic projectiles on light targets have been measured by the thick target method and provide spectroscopic information of light nuclei such as ^{7}Li and its analog isobaric ^{7}He. The result of recent experiments will be presented.

SHAPE COEXISTENCE IN THE NEUTRON-DEFICIENT, EVEN-EVEN $^{182-188}$Hg ISOTOPES

Kasia Wrzosek-Lipska
Instituutvoor Kern-en Stralingsfysica, KU Leuven

E-mail: kasia.wrzoseklipska@fys.kuleuven.be

Shape coexistence whereby two or more shapes coexist at low excitation energy in the atomic nucleus is an intriguing phenomenon. In the region around the light lead isotopes, with proton number Z=82, a substantial amount of information has been collected using a wide spectrum of experimental probes like decay studies, optical spectroscopy studies and in-beam spectroscopy investigations. However, direct experimental information on the exact nature of the deformation or on the mixing of the different shape coexisting states is limited. In order to probe the electromagnetic properties of yrast and non-yrast states of the radioactive even-even $^{182-188}$Hg isotopes Coulomb excitation experiments were performed with 2.85 MeV/A Hg beams from REX-ISOLDE. Detailed analysis of the observed γ-ray transitions depopulating Coulomb excited states of investigated nuclei combined with recent results from life-time measurements and beta decay studies of Tl isotopes enable to extract, for a first time, a set of *E*2 reduced matrix elements coupling low-lying states of $^{182-188}$Hg. Based on the experimentally obtained magnitudes and relative signs of *E*2 matrix elements information on the deformation of the ground and first excited 0+ states was obtained. Results show that the ground state of light mercury isotopes is slightly deformed, and of oblate nature, while the deformation of the excited 0^+ states of ^{182,184}Hg is larger and hinting towards a triaxial character. Experimental results were compared to the state-of-the-art beyond mean field and IBM-CM predictions and were interpreted within a two-state mixing model. The presence of two different topologies in the light mercury isotopes that coexist and mix at low excitation energy has been firmly established.

PROBING NUCLEAR STRUCTURE WITH FAST NEUTRONS

Steven W. Yates
University of Kentucky, Lexington, Kentucky, USA

E-mail: yates@uky.edu

In most measurements at the University of Kentucky Accelerator Laboratory (UKAL), high-quality, pulsed/bunched proton or deuteron beams are utilized to produce nearly monoenergetic, time-bunched fast neutrons with nanosecond pulses from reactions on ^{2}H, ^{3}H, and ^{7}Li targets. These neutrons are employed in high-precision measurements, which utilize neutron, γ-ray, or coincidence detection.

Inelastic neutron scattering with the detection of emitted γ rays, *i.e.*, the (n,n′γ) reaction, has been exploited for many years at the UKAL to study the structure of stable and long-lived nuclei [1]. Scrutiny of the properties of nuclei at low energy and low spin complements advances in nuclear structure achieved by studying nuclei at extreme conditions of temperature and angular momentum or in regions far from stability. Experimental innovations at the UKAL–*e.g.*, the development of capabilities to measure lifetimes in heavy nuclei with the Doppler-shift attenuation method (DSAM) following inelastic neutron scattering [2]–have played a key role in our success, and collimated neutron "beams" have been employed in γ-γ coincidence measurements with an array of HPGe detectors in a close geometry [3]. Such developments have permitted us to address important questions in nuclear structure, and we are frequently able to obtain information about non-yrast states, which are inaccessible with other reactions.

Our research is focused on timely, relavant topics in nuclear structure, which are explored with fast-neutron-induced reactions, neutron-emitting reactions, and fast-neutron scattering. This broad-based program currently includes selected studies in forefront areas, such as nuclear structure relevant to neutrinoless double-β decay, nuclei undergoing shape transitions, deformed structures and shape coexistence, and nuclear structure contributions in support of searches for electric dipole moments. Lifetime determinations and coincidence measurements provide crucial information in many of these investigations. Examples of recent work will be discussed.

This material is based upon work supported by the U. S. National Science Foundation under Grant No. PHY-1305801, and this research is being performed using funding received from the DOE Office of Nuclear Energy's Nuclear Energy University Programs.

[1] P. E. Garrett, N. Warr, and S. W. Yates, J. Res. Natl. Inst. Stand. Technol. **105**, 141 (2000).

[2] T. Belgya, G. Molnár, and S. W. Yates, Nucl. Phys. **A607**, 43 (1996).

[3] C. A. McGrath, P. E. Garrett, M. F. Villani, and S. W. Yates, Nucl. Instrum. Methods Phys. Res. **A421**, 458 (1999).

THE IMPORTANCE OF COMPLEMENTARITY IN NUCLEAR STRUCTURE STUDIES

Paul Garrett
Dept. of Physics, University of Guelph, Guelph, Canada

E-mail: pgarrett@physics.uoguelph.ca

Our understanding of nuclear structure progresses rather slowly, from first observation of a phenomena to a clear understanding of its origin and nature. A classic example of this is the study of ^{32}Mg; from the first report of its 2^+state in 1979 via the β-decay of ^{32}Na, to the recent observation of shape-coexistence via the two-neutron-transfer reaction, the intervening years saw much speculation on its structure. In an era of radioactive beams where there is much excitement on probing nuclei at the limits of existence, it is with stable nuclei, or nuclei near stability, that can be studied by the variety of reactions that will continue to pose the greatest challenge to nuclear theory.

Despite decades of experimental research, there are only a handful of nuclei that have high-quality data available from a wide variety of experimental probes. Especially important in this regard are experiments that can provide level lifetimes or $B(E\lambda)$ values, such as the (n,n$'\gamma$) reaction, Coulomb excitation, and inelastic scattering, sensitivity to weak decay transition branches at high excitation energy, such as βdecay, and information of specific components in the wave functions, such as transfer reactions. This presentation will focus on some key examples, drawn from the Zr, Cd, and Xe regions, where new complementary data have refined or changed outright previous interpretations, and resulted in new insights in nuclear structure.

THE NEUTRON DETECTOR ARRAY DESCANT

Vinzenz Bildstein
University of Guelph, Canada

E-mail: vbildste@uoguelph.ca

The DESCANT array at TRIUMF is designed to track neutrons from RIB experiments. DESCANT is comprised of 70 close-packed deuterated liquid organic scintillators coupled to digital fast read-out ADC modules. This configuration will permit online pulse-shape discrimination between neutron and γ-ray events. The anisotropy of the n-d scattering will allow to distinguish higher neutron multiplicities from scattering within the array and to determine the neutron energy spectrum directly from the pulse-height spectrum without using TOF. Comparative type-testing of candidate small deuterated scintillators to non-deuterated scintillators have been performed at the University of Kentucky. Results of these type-testing measurements will be presented together with first designs of the firmware written for the fast sampling ADC modules.

CLUSTER EMISSION WITH SPIN VARIABLES WITHIN THE DENSITY APPROACH TO THE IWAMOTO-HARADA COALESCENCE/PICKUP MODEL

Emil Běták
Institute of Physics, Slovak Academy of Sciences, Bratislava, Slovakia

E-mail: emil.betak@savba.sk

The original Iwamoto-Harada model for pre-equilibrium cluster emission [1] was formulated using the overlap of the cluster and the nucleus in momentum space. Transforming it into level densities is not a straightforward task, however, five years before Iwamoto and Harada, physically the same model was presented at Balaton conference on reaction models (and the corresponding Proceedings), where all idea is expressed in terms of level densities [2]. At that time, only the densities without spin were used. The introduction of spin variables into exciton model [3] of pre –equilibrium decay and the consequent application to nucleon and gamma emissions [3], stimulated further developments. One of them was the code PEGAS [4], based on a huge set of coupled master equations. However, no spin formulation has been presented – to our best knowledge – concerning cluster emission till recently, when first attempts used for the first emission only have been presented [5]. Now we updated that effort and we are able to handle (using the same simplifications as in [5]) pre-equlibrium cluster emission with spin at later stages of a reaction too.

[1] A. Iwamoto, K. Harada, Phys. Rev. C **26**, 1821 (1982).

[2] J. Dobeš, E. Běták, in *Proc. Internat. Conf. Reaction Models, Balatonfured 1977*, ed. L. P. Csernai, Budapest 1977, p. 195

[3] P. Obložinský, Phys. Rev. C **35**, 407 (1987); P. Obložinský, M. B. Chadwick, *ibid.***42**, 1652 (1990).

[4] E. Běták, P. Obložinský, *Report INDC(SLK)-001,* IAEA Vienna 1993.

[5] E. Běták, EPJ Web Conf. **21**, 09004 (2012).

SYMMETRY TERM FROM HIGH ENERGY EXPERIMENTS

Jerzy Łukasik
Institute of Nuclear Physics PAN, Krakow, Poland

E-mail: jerzy.lukasik@ifj.edu.pl

Current status of experimental activities, observables and challenges related to the determination of the equation of state of asymmetric nuclear matter will be presented. These will include the results from the reanalysis of the GSI ^{197}Au+^{197}Au neutron/proton flow data, pion production results and the status of the ASY-EOS experimental data analysis (Au+Au, Ru+Ru, Zr+Zr), as well as some perspectives.

STATUS OF SYMMETRY ENERGY WITH DIFFERENT DYNAMICAL MODELS IN INTERMEDIATE ENERGY HEAVY-ION REACTION REGION

Sanjeev Kumar
Amity University, Noida (Delhi NCR), India

E-mail: sanjeev1283@gmail.com

When someone talks about symmetry energy, the question in mind comes are:

1. whether it is at sub saturation or supra-saturation density region
2. what is the feasibility of the results obtained with dynamical and statistical models in the contest with the experimental data.

Keeping in view the above two major points, the review of the symmetry energy by highlightening the importance of different symmetry energy sensitive observables at intermediate incident will be presented.

ASTROPHYSICAL CONSTRAINTS ON THE NUCLEAR EQUATION OF STATE

Evgeni E. Kolomeitsev
MatejBel University, BanskáBystrica, Slovakia

E-mail: E.Kolomeitsev@gsi.de

A neutron star is the unique place where the nuclear matter is sustained under extremely high densities for a very long time. Observable characteristics of a neutron star such as the star radius, mass, rotation period, or cooling history can be used to constrain the nuclear equation of state at high densities. So, the recent determination of the neutron star mass of about 2 solar masses requires the EoS to be sufficiently stiff. The composition of a neutron star, which depends on the nuclear symmetry energy, could be constrained using information about a star cooling. We discuss a set of astrophysical tests, which a realistic equation of state must pass. A possibility for exotic phases in the neutron star core, hyperons, meson condensates, quark matter is analyzed.

NEW APPROACHES TO THE EFFECTIVE DENSITY DEPENDENCE IN THE RELATIVISTIC MEAN-FIELD THEORY

Kristian Petrík
Institute of Physics, Slovak Academy of Sciences, Bratislava, Slovakia

E-mail: kristian.petrik@savba.sk

The density dependent relativistic hadron field (DDRHF) theory is introduced with several forms of density dependence of an effective nuclear interaction in order to study the dense nuclear matter that is likely to be found inside the compact stars. DDRHF models are easily applicable, although not parameter free. Various parametrizationsare thus extracted from the more fundamental Dirac-Brueckner-Hartree-Fock (DBHF) calculations. We have compared and analyzed the most important differences among them and found that the high-density extrapolations are strongly dependent on the choice of the density dependence. This has significant effects on the internal properties and structure of compact stars. According to observational data of the newly observed pulsars with masses around $2M_{\odot}$, one has to introduce new techniques in the DDRHF theory to satisfactorily describe such a high mass of a neutron star. We discuss theoretical prospects considering this issue as well.

SYMMETRY ENERGY, NUCLEAR RADII, AND NEUTRON STARS

Štefan Gmuca
Institute of Physics, Slovak Academy of Sciences, Bratislava, Slovakia

E-mail: stefan.gmuca@savba.sk

Neutron stars are valuable laboratories for the study of equation of state of dense nuclearmatter. The recent high precision observations of pulsars with as high masses as $2M_{\odot}$werereported with a suggestion that many nuclear models which consider exotic core could beruled out. In addition, various constraints on neutron star radii were published. The largestmass measurements are strongly inuencing the high{density equation of state because of theexistence of the neutron star maximum mass. The ensemble of mass and radius observationscan realistically restrict the properties of dense matter and, in particular, the behavior of thenuclear symmetry energy near the nuclear saturation density. The neutron skin of heavy nucleias well as neutron star properties are believed to be highly sensitive to the poorly constraineddensity dependence of the symmetry energy. The present paper is devoted to study thecorrelation between the neutron{skin thickness of ^{208}Pb and properties and composition ofneutron stars.

RADIATIVE FUSION REACTIONS IN SUB-BARRIER REGION

Andrey S. Zubov
Laboratory of Theorical Physics, Joint Institute for Nuclear Research

E-mail: azubov@theor.jinr.ru

Using the statistical approach, we study the possibility of radiative fusion reaction ^{208}Pb(^{48}Ca, 0n)^{256}No. The evaporation residue cross sections for this reaction are estimated using different approaches to the sub-barrier capture process. We reveal the dependence of fission barriers on angular momentum in this region of nuclear chat by describing the relative intensities of $E2$-transitions between the rotational states, the entry spin distributions of residual nuclei, and excitation functions for the reactions ^{208}Pb(^{48}Ca,2n)^{254}No, ^{206}Pb(^{48}Ca,2n)^{252}No, and ^{204}Hg(^{48}Ca, 2n)^{250}Fm. The calculated cross section for the radiative fusion reaction ^{90}Zr(^{90}Zr,0n)^{180}Hg, which was considered as a test for our approach, is in an agreement with the experimental data.

NUCLEAR STRUCTURE STUDIES OF HEAVY NUCLEI

Paul T. Greenlees
University of Jyväskylä, Finland

E-mail: paul.greenlees@jyu.fi

The investigation of the structure and stability of the heaviest elements has been a constant theme in nuclear physics research since the 1940's. In the last decade or so, a wealth of new data has been produced, both in terms of new elements (up to Z=118) and in detailed spectroscopic studies of nuclei with masses above 240. Such studies provide data concerning nuclear parameters such as masses, decay modes, half-lives, moments of inertia, single-particle properties, etc., in systems with the highest possible number of protons. The main focus of current experiments is the search for the next closed proton- and neutron- shells beyond the doubly magic ^{208}Pb. This search can be made directly, by producing nuclei in the region of interest (Z>112 and N>176), or indirectly through the study of lighter deformed nuclei where the orbitals of interest at sphericity are active at the Fermi surface. Nuclei in the region of ^{254}No are produced with cross-sections large enough to allow in-beam studies using recoil-decay tagging techniques. Advances in digital electronics and data acquisition have led to the observational limit in this region being pushed down to the level of ten nanobarns, as demonstrated by recent studies of ^{246}Fm and ^{256}Rf. In addition, the capabilities of focal plane spectrometer devices have been greatly improved, which has recently allowed the structure of a number of high-K isomeric states to be determined in a systematic manner. New instruments such as the recently commissioned SAGE combined conversion-electron and gamma-ray spectrometer provide additional information such as conversion coefficients to aid determination of transition multipolarities. Examples of recent highlights in in-beam studies of heavy elements will be presented.

SPECTROSCOPY OF ^{193}Bi

Andrej Herzáň
University of Jyväskylä, Finland

E-mail: andrej.a.herzan@jyu.fi

An experiment aiming to study the shape co-existence in ^{193}Bi has been performed at the Accelerator laboratory of the University of Jyväskylä, Finland (JYFL). The ^{193}Bi nuclei were produced via the fusion-evaporation reaction ^{165}Ho(^{32}S,4n)^{193}Bi at the bombarding energy of 152 MeV. The experimental set-up of this TDR experiment consisted of the fully digitized JUROGAM2 γ-ray spectrometer, followed by the gas-filled high-transmission recoil separator RITU [1,2] coupled with the GREAT focal plane spectrometer system [3]. Many new states have been found, hugely extending the previously known level scheme of ^{193}Bi [4]. Both the ground state band and the π$i_{13/}$band have been extended to higher spin and energy, where the π$i_{13/2}$ band was also found to be feeding the previously, only tentatively placed long-lived isomeric state, of which the feeding pattern together with its main characteristics have been now resolved. The previously floating dipole band ("shears band"?) [4] has now been extended and connected to lower lying states, revealing many new non- yrast states of this nucleus. Moreover, the band built on top of the alpha- decaying $1/2^+$ intruder state [4] has been examined and further modified. A superdeformed band almost identical to that present in the neighboring isotope ^{191}Bi has been identified. As in ^{191}Bi this band decays to the proton $1/2^+$ intruder band, however no connecting links have been found yet.

[1] M. Leino*et al.*, Nucl. Instr. and Meth.B **99**, 653 (1995).

[2] J. Saréne*t al.*, Nucl. Instr. and Meth.A **654**, 508 (2011).

[3] R.D Page *et al.*, Nucl. Instr. and Meth.B **204**, 634 (2003).

[4] P. Nieminen*et al.*, Phys. Rev. C **69**, 064326 (2004).

NUCLEAR STRUCTURE OF ODD-Au NUCLEI: IN-BEAM STUDY OF ^{177}Au

Martin Venhart
Institute of Physics, Slovak Academy of Sciences, Bratislava, Slovakia

E-mail: mvenhart@cern.ch

In the talk results of in-beam spectroscopy of 177Au will be presented. The experiment was performed at the University of Jyväskylä and employed digitized Jurogam2 array coupled with the RITU gas-filled separator and the GREAT focal plane array. Unique splitting of yrast cascade feeding two different isomers was observed. Strongly-coupled band associated with unique-parity $h_{11/2}$ proton configuration was observed together with corresponding E0 transition. These data allow valuable insight into structure of 0^+ intruder configuration in ^{178}Hg core. Implications of these results on the systematics of odd-Au will be discussed.

PROJECT OF NEW TANDEM-DRIVEN NEUTRON FACILITY IN SLOVAKIA

Martin Venhart
Institute of Physics, Slovak Academy of Sciences, Bratislava, Slovakia

E-mail: mvenhart@cern.ch

Project of new laboratory is ongoing in town of Piešťany in Slovakia. The laboratory is supported by Structural Funds of European Commission. In short talk will be presented physics program, current status and future plans.

LIST OF PARTICIPANTS

Fuad Ali (University of Liverpool)	faa@ns.ph.liv.ac.uk
James Mitchel Allmond (ORNL Oak Ridge)	jmallmond@gmail.com
Emil Běták (Institute of Physics of SAS)	Emil.Betak@savba.sk
Vincenz Bildstein (University of Guelph)	vbildste@uoguelph.ca
Thomas Elias Cocolios (University of Manchester)	thomas.cocolios@manchester.ac.uk
Deqing Fang (SINAP Shanghai)	dqfang@sinap.ac.cn
Paul Garrett (University of Guelph)	pgarrett@physics.uoguelph.ca
Štefan Gmuca (Institute of Physics of SAS)	Stefan.Gmuca@savba.sk
Tuomas Grahn (JYFL Jyvaskyla)	tuomas.grahn@jyu.fi
Paul Greenlees (JYFL Jyvaskyla)	paul.greenlees@jyu.fi
Andrej Herzáň (JYFL Jyvaskyla)	andrej.a.herzan@jyu.fi
Fritz Heßberger (GSI Darmstadt)	f.p.hessberger@gsi.de
Attila Krasznahorkay (ATOMKI Debrecen)	kraszna@atomki.hu
Evgeni Kolomeitsev (UMB Banská Bystrica)	E.Kolomeitsev@gsi.de
Sanjeev Kumar (Amity University New Delhi)	sanjeev1283@gmail.com
Jerzy Lukasik (IFJ PAN Krakow)	jerzy.lukasik@ifj.edu.pl
Yu-Gang Ma (SINAP Shanghai)	ygma@sinap.ac.cn
Vladislav Matoušek (Institute of Physics of SAS)	Vladislav.Matousek@savba.sk
Janne Pakarinen (JYFL Jyvaskyla)	janne.pakarinen@phys.jyu.fi
Kristian Petrík (Institute of Physics of SAS)	Kristian.Petrik@savba.sk
Giacomo Randisi (KU Leuven)	giacomo.randisi@fys.kuleuven.be
Andrii Sanzhur (INR Kiev)	sanjour@kinr.kiev.ua
George Souliotis (University of Athens)	soulioti@chem.uoa.gr
Martin Venhart (Institute of Physics of SAS)	Martin.Venhart@savba.sk
Martin Veselský (Institute of Physics of SAS)	Martin.Veselsky@savba.sk
Nikoletta Vonta (University of Athens)	nikolettav@chem.uoa.gr
John Wood (Georgia Tech Atlanta)	john.wood@physics.gatech.edu
Kasia Wrzosek-Lipska (KU Leuven)	kasia.wrzoseklipska@fys.kuleuven.be
Steven Yates (University of Kentucky)	yates@uky.edu
Andrey Zubov (JINR Dubna)	azubov@theor.jinr.ru

CONFERENCE PHOTO

SPONSORS

Slovenské elektrárne, a.s.
member of the Enel Group

Slovak Research
and Development Agency

Slovak Physics Society

ISBN 978-80-971975-0-6